

DISSERTATION

EXTREME ULTRAVIOLET LASER IONIZATION MASS SPECTROMETRY: PROBING  
MATERIALS AT THE MICRO AND NANO SCALES

Submitted by

Lydia Alexandra Rush

Department of Electrical and Computer Engineering

In partial fulfillment of the requirements

For the Degree of Doctor of Philosophy

Colorado State University

Fort Collins, Colorado

Fall 2023

Doctoral Committee:

Advisor: Carmen S. Menoni  
Co-Advisor: Andrew M. Duffin

Delphine K. Farmer  
Mario C. Marconi  
Jorge J. Rocca

Copyright by Lydia A. Rush 2023

All Rights Reserved

## ABSTRACT

### EXTREME ULTRAVIOLET LASER IONIZATION MASS SPECTROMETRY: PROBING MATERIALS AT THE MICRO AND NANO SCALES

The focus of this dissertation is the use of 50 to 10 nanometer wavelength extreme ultraviolet (EUV) laser light as a next generation probe for mass spectrometry analyses at the micro (>100 nanometers) and nano ( $\leq 100$  nanometer) spatial scales. While the unique properties of EUV light have revolutionized the semiconductor industry through nanoscale lithography fabrication, the use of EUV lasers with analytical instruments, like mass spectrometers, for high spatial resolution chemical analyses is a relatively untapped area. This unexplored territory is owed partly to only recently bringing EUV lasers to an accessible “bench-top” scale.

Herein I show how EUV laser ionization can be used with different types of mass spectrometers as a new route for interrogating nuclear and geologic materials with micro and nano scale lateral spatial resolution. I focus on the application of a compact capillary discharge EUV laser operating at a wavelength of 46.9 nanometers connected to a time-of-flight (TOF) mass spectrometer, called the EUV TOF. I also show for the first time how the 46.9 nm EUV laser ionization source can be connected to a commercial magnetic sector mass spectrometer, called the EUV magnetic sector.

Specifically, I demonstrate that the EUV TOF instrument can measure the  $^{235}\text{U}/^{238}\text{U}$  isotope ratio in 100 nm sized pixels in a heterogeneous uranium fuel pellet that was made by blending different feedstocks together. The results show that the EUV TOF maps similar micrometer sized areas of  $^{235}\text{U}/^{238}\text{U}$  heterogeneity as nanoscale secondary ionization mass spectrometry (NanoSIMS), indicating that EUV laser ionization can be used to accurately probe complex nuclear materials within the scope of the study. I also show that the EUV TOF can be used to measure  $^{206}\text{Pb}/^{238}\text{U}$  and  $^{232}\text{Th}/^{238}\text{U}$  isotope ratios at the 8  $\mu\text{m}$  scale

in select geologic matrices of silicates, zircons, monazites, and iron manganese within error ( $\pm 2\sigma$ ) using a single non-matrix matched calibration standard. However, the precision on the ratio measurements was low for useful geologic applications, ranging between 1-10% at elemental concentrations exceeding hundreds of ppm because of the limitations of using a TOF for isotope ratio measurements.

To this end, I show the current development of the new EUV magnetic sector instrument that uses the EUV laser ionization source with a commercial double-focusing sector-field multi-collector mass spectrometer with the aim of achieving more precise ( $<1\%$ ) and sensitive ( $\leq\text{ppm}$ ) isotope ratio measurements at high spatial scales ( $<10\ \mu\text{m}$  down to the nanoscale). The EUV magnetic sector is being developed to probe more complex isotopic systems in nuclear and geologic materials that was not possible with the TOF mass spectrometer. The work here shows that the 46.9 nm wavelength EUV laser ionization source can be interfaced with Thermo Fisher's commercial sector-field multi-collector mass spectrometer called the Neptune by removing its inductively coupled plasma (ICP) region. The Neptune's ion optics, electric sector, and magnetic sector were modified for acceptance of the pulsed EUV-generated ions. These modifications resulted in ions from  $\leq 2\ \mu\text{m}$  diameter craters created by EUV laser ablation and ionization being successfully focused, separated by mass, and detected using the Neptune's electron multipliers. However, further system upgrades to the Neptune's detectors are needed for accurate isotope ratio measurements at high spatial scales because the 10 to 30 nanosecond wide EUV-generated ion pulses are on the order of the electron multipliers' dead time. With proper detectors, the EUV magnetic sector's accuracy, precision, sensitivity, efficiency, and spatial resolution can be measured in future experiments. The demonstration of the EUV magnetic sector instrument here represents the first time that an EUV laser ionization source has been used with a sector-field mass spectrometer, paving the way for future high spatial resolution isotope ratio analyses.

## ACKNOWLEDGEMENTS

I thank my advisors, Carmen Menoni and Andrew Duffin, for their support throughout this process. There were many times when I felt unconfident or frustrated during this experience, whether it be from unexpected results, a lack of knowledge, or from accidentally breaking equipment, but my advisors helped me push through these uncertain moments. Andrew always reminded me that “you aren’t working hard if you aren’t breaking something.” The combination of patience and tenacity that my advisors have for research is commendable, and I am glad to have learned from them. I would also like to thank my committee members, Delphine Farmer, Jorge Rocca, and Mario Marconi, for being voices of reason and encouragement throughout this process.

Alongside my graduate school mentors, I am also fortunate to have had the opportunity to be mentored by Matthew Cremeens during my undergraduate education. While never a stellar student in the classroom, I always loved working in the lab, and Dr. C endlessly supported this desire. Despite my doubts about getting a PhD in Electrical Engineering because of my undergraduate degree in Biochemistry, he encouraged me to embrace the non-linearity of life. I also offer many thanks to April Carman and Greg Eiden for mentoring me at PNNL and helping me navigate my next steps prior to graduate school. I am further grateful for the steadfast support of a former CSU student, Ilya Kuznetsov, who showed me how to conduct good research in graduate school and, more importantly, how to advocate for myself in the process.

Without the help of undergraduate students, this work would have been less fun and much more difficult to achieve. Hugh Currah was especially instrumental to the success of this project through his unmatched work ethic and inventiveness in mechanical design. I am also very thankful to have had the help of Scott Richards, Karl Spoerl, Jackie Clark, and Merlin Hart in developing various mechanical, optical, and software components. Additionally, a few senior researchers at PNNL were always willing to lend me advice, a hand, or their high voltage power supplies to complete this project. Thank you, Martin Liezers, Kellen Springer, and Norbert Gajos, for your help.

Throughout this process my family, friends, and lab mates reminded me to have fun and to look beyond what I do or don't accomplish in the lab as a metric of career or personal success. My partner Wade has been especially foundational to me throughout (and beyond) graduate school. While this experience was difficult and didn't always bring out the best of me, he without fail supported me and made me laugh. No matter how incremental my research progress, Wade celebrated my successes in the lab as if all were monumental, helping me view the mundane parts of the scientific process as exciting breaks.

Lastly, without my parents' unyielding support, many opportunities that led me to this point would have remained unrealized. I am grateful to my mother, Tina, and to my father, Robert, who in their own ways have shown me how to be bold, creative, and compassionate in all aspects of life.

**Funding:** This work was made possible by the funding support from the Department of Homeland Security through the Nuclear Forensics Graduate Student Fellowship under the Work Force Development Program. The fellowship provided me with invaluable experiences to conduct experiments and attend conferences as well as carry out part of my research at Pacific Northwest National Laboratory. I am particularly appreciative of DHS's Sandra Gogol for her support throughout the duration of the fellowship.

TABLE OF CONTENTS

ABSTRACT..... ii

ACKNOWLEDGEMENTS ..... iv

1. Introduction..... 1

    1.a Background and motivation ..... 1

    1.b Current sources for probing materials with mass spectrometry ..... 3

    1.c Extreme ultraviolet lasers as a new probe for mass spectrometry ..... 9

    1.d Scope of this dissertation ..... 14

2. EUV TOF Fundamentals..... 17

    2.a Background on time-of-flight mass spectrometers ..... 17

    2.b Extreme ultraviolet laser ionization time-of-flight (EUV TOF) ..... 23

    2.c Desktop EUV capillary discharge laser ..... 24

    2.d Sample preparation for EUV TOF ..... 26

    2.e Data collection and analysis for EUV TOF ..... 28

3. Paper #1 on EUV TOF..... 34

    3.a Paper #1 title page..... 34

        3.a.i Overview..... 34

    3.b Introduction..... 35

    3.c Experimental section..... 37

        3.c.i Sample preparation ..... 37

        3.c.ii EUV TOF..... 38

3.c.i	NanoSIMS.....	42
3.d	Results and discussion.....	43
3.d.i	EUV TOF elemental analysis.....	43
3.d.ii	EUV TOF analysis of a homogenous NU CRM.....	45
3.d.iii	EUV TOF and NanoSIMS analyses of LEU sample.....	48
3.d.iv	EUV TOF and NanoSIMS comparison.....	54
3.e	Conclusions.....	55
4.	Paper #2 on EUV TOF.....	58
4.a	Paper #2 title page.....	58
4.a.i	Overview.....	58
4.b	Introduction.....	59
4.c	Experimental section.....	63
4.c.i	Sample preparation.....	63
4.c.ii	EUV TOF.....	65
4.d	Results and discussion.....	69
4.d.i	EUV TOF analysis of NIST 610 CRM.....	69
4.d.ii	EUV TOF $^{206}\text{Pb}/^{238}\text{U}$ measurements.....	72
4.d.iii	EUV TOF $^{232}\text{Th}/^{238}\text{U}$ measurements.....	77
4.e	Conclusions.....	81
5.	EUV Magnetic Sector Development.....	83
5.a	Overview.....	83

5.b	Background on sector-field multi-collector mass spectrometers .....	83
5.c	Neptune sector-field multi-collector mass spectrometer.....	93
5.c.i	Neptune overview .....	93
5.c.ii	ICP module .....	94
5.c.iii	ESA module – Transfer lens system .....	94
5.c.iv	ESA module – Slit lens system .....	97
5.c.v	ESA module – Electrostatic analyzer.....	99
5.c.vi	Multi-collector module – Magnetic sector .....	102
5.c.vii	Multi-collector module – Zoom lenses .....	103
5.c.viii	Multi-collector module – Detector array.....	103
5.d	Extreme ultraviolet laser ionization magnetic sector .....	104
5.d.i	EUV magnetic sector overview .....	104
5.d.ii	EUV magnetic sector design challenges .....	107
5.d.iii	Tabletop EUV capillary discharge laser .....	109
5.d.iv	EUV laser to Neptune interface .....	110
5.d.v	Optical high vacuum chamber – Planar mirrors.....	112
5.d.vi	Optical high vacuum chamber – Gold photodetector.....	115
5.d.vii	Sample high vacuum chamber – Zone plate .....	115
5.d.viii	Sample high vacuum chamber – Ion deflector.....	119
5.d.ix	Sample high vacuum chamber – Coupling lens.....	120

5.d.x	Other features of EUV laser interface .....	121
5.d.xi	Connecting EUV laser interface to Neptune .....	122
5.d.xii	EUV magnetic sector vacuum system.....	126
5.e	Testing the EUV magnetic sector mass spectrometer .....	128
5.e.i	Neptune ion optics' cross overs .....	128
5.e.ii	Tuning the EUV ions' energy - Experiment .....	129
5.e.iii	Transmitting EUV ions through cross-over #1 - Experiment .....	139
5.e.iv	Transmitting EUV ions through cross-over #2 - Experiment .....	147
5.e.v	Transmitting EUV ions through cross-over #3 - Calculation.....	150
5.e.vi	Transmitting EUV ions through cross-over #3 – Experiment #1.....	157
5.e.vii	Transmitting EUV ions through cross-over #3 – Experiment #2.....	163
5.e.viii	Transmitting EUV ions through cross-over #4 - Calculations .....	165
5.e.ix	Transmitting EUV ions through cross-over #4 - Experiment .....	173
5.e.x	Next steps.....	177
6.	Conclusions and outlook.....	180
	REFERENCES .....	184
	APPENDIX.....	190
A.1	EUV TOF components.....	190
A.2	Supplementary Information (SI) for Chapter 4: Paper #2 on EUV TOF .....	192
A.3	EUV magnetic sector components .....	201

A.4	EUUV magnetic sector – Mirror alignment.....	204
A.5	EUUV magnetic sector vacuum schematic.....	205
A.6	EUUV Magnetic Sector Custom Connection Vacuum Flange .....	208

# 1. INTRODUCTION

## 1.a Background and motivation

Mass spectrometry is an analytical tool used to measure the chemical, elemental, molecular and/or isotopic content of a sample. In its most basic form, mass spectrometry separates ionized analyte structures, molecules, or atoms to detect and/or quantify analytes by atomic weight. There is tremendous range in instruments, ionization sources, mass separation methods, and detectors all specialized for various sample forms and desired information return. The expansive field of mass spectrometry is considerably narrowed when only considering instruments or methods that return spatially resolved elemental and isotopic information from a solid sample. In this case, the material needs to be probed at the required lateral and depth spatial scales to enable the mapping of chemical content in one-, two-, or three-dimensions. As depicted in Figure 1.1, to spatially resolve chemical information with mass spectrometry, the following steps are mandatory: (1) remove material from the solid sample with a probe, (2) ionize the removed material, (3) send the ions into a mass spectrometer, and (4) map the intensity and distribution of the detected ions at every sample location that is probed. A mass spectrum is collected at each probed location. The collection of spectra is then analyzed and salient features in the spectrum are used to construct a chemical map. The map is made up of individual pixels that are associated with the probed sample region and contains the number of ions obtained from a designated peak in the mass spectrum, thereby revealing the analyte content at the scale of the probe. The most common and competitive instruments for mass spectral mapping use either an energetic beam of ions or laser light to probe the sample followed by mass analysis using a field-free flight tube or by using a magnetic field, with the latter providing more sensitive and precise mass measurements as will be discussed below and in later chapters. Consequently, ion and laser beams coupled to time-of-flight and magnetic sector mass spectrometers will be the focus of this dissertation.

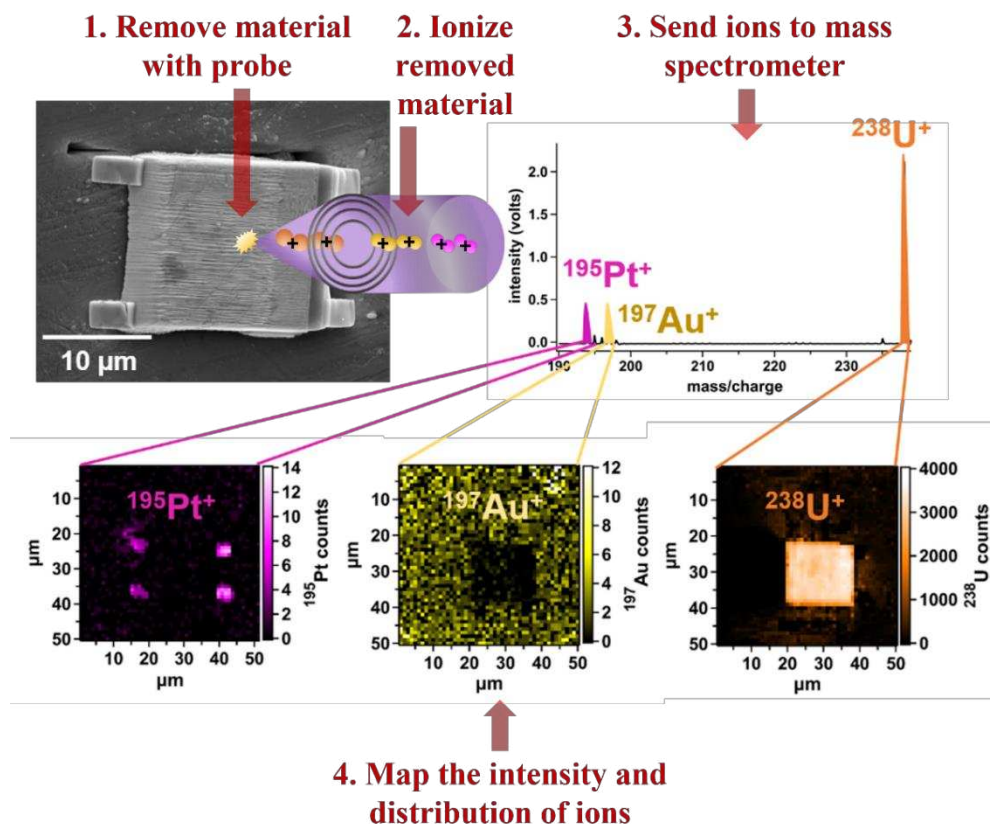


**Figure 1.1** Graphical representation of the main steps involved in mass spectral mapping. In this graphic, the probe is a laser being focused onto a sample made of uranium for material removal via ablation, and the laser light is also acting as the ionization source. The implied mass spectrometer is a time-of-flight that separates ions in time according to mass and charge. [Figure adapted from L. Rush, et al.<sup>1</sup>]

Mass spectral mapping has found applications in biology<sup>2</sup>, geology,<sup>3</sup> nuclear forensics,<sup>4</sup> and more. For example, in biology, understanding how a cell, organ, or organism functions often relies on the ability to follow the spatial distribution of atoms and molecules within the cell. Similarly, the analysis of geologic or nuclear materials can require spatially resolving specific elements or isotopes at trace levels (i.e.,  $\leq$  part per billions (ppb)) to accurately identify the origin or age of the material. Regardless of the application, it is essential in mass spectral mapping that the probe being used to remove the sample material matches the scale of the region of interest. If the probe removes a volume from the sample that is larger than the region of interest, then the latter will not be distinguishable from the surrounding background matrix.

Probing regions of interest at the nanoscale, defined as the spatial scale of 100 nanometers (nm) or less, with mass spectrometry can be especially important for understanding processes that only exist at this spatial scale in biological,<sup>5</sup> geological,<sup>6</sup> and nuclear<sup>7</sup> materials but also semiconductor,<sup>8</sup> metallurgical,<sup>9</sup> and interstellar<sup>10</sup> materials, amongst others. However, mass spectral mapping of these materials at the nanoscale are challenging due to the reduced number of atoms/molecules that are removed from the sample when probing such small volumes. Compared to the micro- and macro- scales, far fewer ions are created and available for mass analysis when probing a material at a spatial scale of 100 nm or less, increasing the error of the mass measurements. That is, the uncertainty in the measurements increases as the number of ions decreases. Alongside the challenge of counting statistics, an additional challenge when trying to map chemical information at the nanoscale is that there are far fewer probes that can achieve a spatial resolution of  $\leq 100$  nm. Those probes that can achieve such a feat can sometimes have severe drawbacks that limit them to very specific and/or time-consuming analyses. Therefore, there is a need to develop new, robust technologies for mass spectrometry that can probe the nanoscale and overcome current limitations to further advance our understanding of materials. The successful development of such a versatile probe would broadly impact and bring new opportunities to nuclear forensics, geology, the semiconductor industry, chemistry, biology, and any number of fields that require chemical information to be probed with high spatial resolution.

## **1.b Current sources for probing materials with mass spectrometry**

Probing materials at the nanoscale with mass spectrometry is most commonly performed through bombarding the material with an energetic and focused beam of ions. The ion beam sputters the surface of the material, resulting in the ejection of atoms and molecules, of which a small portion are also ionized. These secondary ions that have been created by the primary ion beam bombarding the sample are directed into a mass spectrometer for analysis. This technique is therefore referred to as secondary

ionization mass spectrometry (SIMS).<sup>11</sup> Furthermore, there is a special variant of SIMS, called nanoscale SIMS or NanoSIMS, that employs colinear primary and secondary ion beams allowing the focus of the primary ion beam to be less than 100 nm.<sup>12</sup> NanoSIMS is currently the dominant tool for probing elemental and isotopic information at the nanoscale because it is highly sensitive, being able to reach ppm detection limits for most elements, while also being able to probe materials with a lateral spatial resolution of  $\leq 100$  nm.<sup>13</sup> SIMS is also widely used for analyzing the surface of materials because it can achieve a depth resolution on the single digit nanometer scale.<sup>14</sup>

However, SIMS does have limitations that can make analyses challenging, especially at the nanoscale. Due to its use of a charged particle beam as the ionization source, the spatial resolution of SIMS is highly dependent on the element to be measured. If an element has a high ionization yield in a particular sample matrix, then one might be able to measure that specific element with nanoscale spatial resolution, whereas another element might have a lower ionization yield, requiring  $>100$  nm spatial resolution for sufficient ion generation.<sup>15</sup> The spatial resolution of SIMS is also highly dependent on the physical and chemical characteristics of the sample under investigation. Physical effects like sample charging, surface flatness, and even where the sample is positioned relative to the holder all play a role in ion generation and thereby the minimal achievable spatial resolution of SIMS.<sup>16,17</sup> The chemistry of the sample also greatly effects the ion yield for a single element from matrix to matrix.<sup>18,19</sup> These strong matrix effects that SIMS experiences ultimately limits its quantitative capabilities if the effects cannot be calibrated properly using either internal or external calibration procedures. Therefore, the minimal spatial resolution of SIMS instruments is not a universal value that can be achieved for every analysis and must be placed in context of the sample and element under measurement (which is true for the parameter of any analytical technique).

Owing to SIMS maturity there are now well-established procedures for dealing with these limitations. There are, for example, multiple choices of primary ion beams that can be used depending on the element of interest. If the element has a higher positive ion yield (like sodium) then a negative oxygen

primary ion beam is typically used to sputter the sample. If the element has a higher negative ion yield (like chlorine) then a positive cesium primary ion beam can be used. There are also other types of primary ion beams available, including cluster ion beams (e.g.,  $C_{60}^+$ ).<sup>20</sup> However, the choice of primary ion beam will also affect the spatial resolution because they do not always produce the same beam diameter. Oxygen primary ion beams, for example, cannot typically achieve the same sub-100 nm spatial resolution as cesium beams.<sup>13</sup> However, a recently developed oxygen beam (generated from an RF source instead of a duoplasmatron) can reach <50 nm spatial resolution, making positive secondary ion generation more available at the nanoscale.<sup>21</sup> However, the use of a primary ion beam as the ionization source in SIMS can present a different set of challenges beyond spatial resolution because the primary ions can react with the intact and sputtered sample material, making it a reactive technique. Sometimes, the implantation of ions into the sample during the SIMS sputtering process is desired to increase the ionization efficiency of the sample but unwanted molecular ions can also be produced. These molecular ions can make their way into the mass spectrometer, and if not sufficiently resolved, can obstruct the signal of interest.<sup>22</sup>

Together, the challenges experienced with SIMS can limit it to being a qualitative or semi-quantitative technique. However, the advantages of SIMS do not go unnoticed. Its ability to analyze materials at the nanoscale as well as its ability to profile depths at the nanometer level make it a premier option for sub-micron analyses. Additionally, the ability to finely control how much material is sputtered via regulation of the primary ion beam intensity (i.e., the beam's current) makes SIMS especially advantageous for depth profiling at trace levels.

Another mass spectrometry technique used to analyze the nanoscale is atom probe tomography mass spectrometry (APT MS).<sup>23,24</sup> APT MS is the only mass spectrometer technique that can measure a sample's chemical profile at the atomic scale and provide three-dimensional reconstructions of its composition. However, APT MS requires a rigorous type of sample preparation that involves ion milling the sample onto a fine tip or needle, which can take up to ~9 hours to complete. Not all materials can be made into a needle and some sample chemistries result in high failure rates for needles. The sample needle

is then exposed to laser or voltage pulses at kilohertz (kHz) level repetition rates, causing the atoms in the sample to be desorbed and ionized, preferably at the needle apex. The electric fields created by the needle and the extraction lenses magnify the image of the ions at the source onto the detector and the time of flight from the laser or electrical pulse to the detector provides mass resolution. APT MS can sometimes provide relatively good quantitative results (depending on the element measured), but it is selective about its sample compatibility. For example, APT is unable to analyze some glasses due to lower laser absorption.<sup>15</sup> Overall, APT MS is a specialized technique that is typically only used in extreme cases when the elemental distribution of a sample needs to be measured at the three-dimensional scale, and so is only briefly overviewed here.

Laser ablation or laser ionization are also commonly used probes for mass spectral mapping. Lasers are used in an assortment of ways to remove and ionize sample atoms for subsequent mass spectrometry. One of the more common set-ups uses a laser to ablate the sample. The ablated material is removed as a plasma, and the plasma condenses into a particulate aerosol. This aerosol is sent to an external ionization source, like an inductively coupled plasma (ICP), and the ICP atomizes and ionizes the sample for extraction into the mass analyzer.<sup>25</sup> Lasers can also be used directly as the ionization source, similar to the role of the primary ion beam in SIMS. In this case, ions are extracted directly from the plasma formed after laser ablation, precluding the need for a separate, external ionization source.<sup>26</sup> Lasers can also be used at a lower fluence, but with a special matrix surrounding the sample that promotes desorption and ionization of the sample directly with the laser.<sup>27</sup>

The lasers that are typically used in these mass spectrometer set-ups operate at wavelengths in the ultraviolet (UV,  $\lambda = \sim 200 \text{ nm} - 380 \text{ nm}$ ), visible (Vis,  $\lambda = 380 \text{ nm} - 700 \text{ nm}$ ), and infrared (IR,  $\lambda = 700 \text{ nm} - 1 \text{ mm}$ ) ranges (see Figure 1.2) with pulse durations ranging from nanoseconds (ns) to femtoseconds (fs) at repetition rates up to kHz levels. The main advantages of using lasers with mass spectrometry, in general, is the relatively fast analysis times, little to no sample preparation (especially compared to SIMS sample preparation), and high sensitivity (can reach sup-ppm levels but depends on the

mass spectrometer used and amount of material sampled). Additionally, ultra-fast UV/Vis/IR laser pulses operating in the fs regime offer other advantages over ns pulsed lasers like better coupling of the laser light into the solid material that results in mass measurements that are less dependent on the sample composition (i.e., reduced matrix effects).<sup>28–30</sup>

However, the biggest drawback of using any form of UV/Vis/IR laser for mass spectral mapping is that when light in this wavelength range is focused, the theoretical diffraction limit ( $\sim\lambda/2$ ) precludes it from being focused down to spot sizes below the microscale. In fact, typical spot sizes (i.e., lateral spatial resolution) of UV/Vis/IR lasers is a few micrometers and  $\sim 1\ \mu\text{m}$  at best.<sup>31,32</sup> Shorter wavelength light below the UV regime is therefore attractive for mass spectrometry applications at high spatial scales because as the wavelength of the laser light decreases so too does the diffraction angle when the light is focused. As an example, vacuum UV (VUV,  $\lambda = \sim 50\ \text{nm} - 200\ \text{nm}$ ) laser light (at  $\lambda = 125.3\ \text{nm}$ ) was used with mass spectrometry to achieve a  $\sim 500\ \text{nm}$  lateral spatial resolution for mapping the molecular ions in single HeLa cells.<sup>33</sup>

Therefore, reaching past the VUV wavelength regime into the extreme UV (EUV,  $\lambda = \sim 5\ \text{nm} - 50\ \text{nm}$ ) and X-ray ( $\lambda < 5\ \text{nm}$ ) ranges presents an opportunity to use lasers for probing the nanoscale with mass spectrometry. However, generating light at these short wavelengths is not trivial. For example, synchrotron facilities, with electron storage rings nearly a kilometer in circumference, produce high quality short wavelength light, but their low pulse energy precludes sufficient material ablation and ionization of solids for mass spectrometry analysis.

In 1994, at Colorado State University, J. J. Rocca et al. showed the first demonstration of a capillary discharge EUV laser operating at a wavelength of  $46.9\ \text{nm}$  with a  $1.5\ \text{ns}$  pulse duration and  $10\ \mu\text{J}$  of energy per pulse, opening the door for EUV laser light to be realized in a compact form and, perhaps more importantly, in university-level labs.<sup>34,35</sup> This compact EUV laser works by depositing high voltage pulses at a rate of up to  $10\ \text{Hz}$  onto a long, thin alumina capillary tube filled with argon gas. The argon gas is ionized eight times into a neon-like state (i.e.,  $\text{Ar}^{8+}$ ), and a dense plasma forms along the length of the

capillary tube causing the excitation of the neon-like ions. After enough neon-like ions have been excited (i.e., population inversion has been reached) a discharge, like a lightning bolt, occurs and 46.9 nm wavelength light is amplified. Shortly after its inception, G. Vaschenko et al. used this capillary discharge EUV laser to ablate an area 82 nm wide and 7 nm deep on a piece of photoresist, showing that the 46.9 nm light was capable of probing materials at the nanoscale.<sup>36</sup>

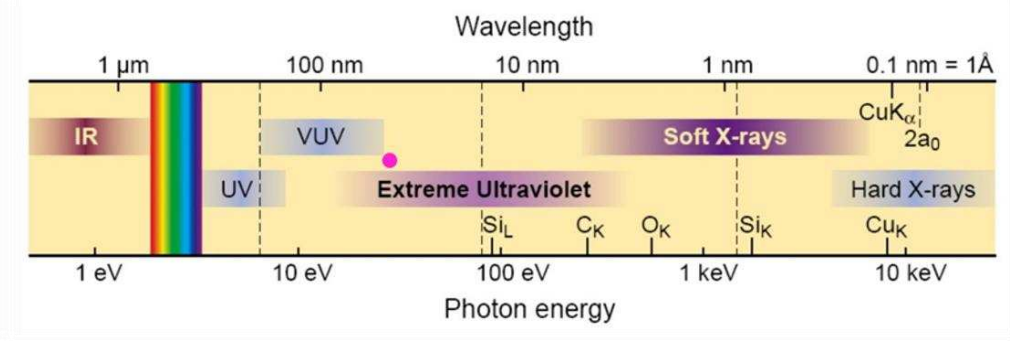


**Figure 1.2** Electromagnetic spectrum with the 46.9 nm wavelength of the EUV capillary discharge laser shown as a pink dot within the EUV range. [Figure adapted from D. Attwood<sup>37</sup>]

Alongside being able to be focused down to the nanoscale, the laser-material interactions with the 46.9 nm EUV laser light are distinct from those of UV/Vis/IR radiation that dominate current laser-based mass spectrometry methods. While the mechanisms of ionization with UV/Vis/IR wavelength lasers are dependent on the pulse duration (i.e., femtosecond vs nanosecond pulses), this is not the case for EUV laser pulses because the EUV laser-created plasma is transparent to the incoming EUV photons.<sup>38-40</sup> The EUV photons with energies ( $h\nu$ ) of 26.4 eV are thereby absorbed by the sample throughout the duration of the 1.5 ns pulse rather than being absorbed by the electrons in the plasma due to inverse Bremsstrahlung as is the case of ablation by nanosecond UV/Vis/IR laser pulses.<sup>41</sup> This is because the critical electron density ( $n_e$ ) for  $\lambda = 46.9$  nm is  $n_e = 5 \times 10^{23} \text{ cm}^{-3}$ , which is greater than solid density.<sup>42</sup> Additionally, the EUV photons realize efficient single photon ionization of atoms and molecules.<sup>43</sup> In this process, energetic photoelectrons are created which can further ionize atoms and molecules in the solid.<sup>41</sup> Single photon ionization processes that dominate ionization with the EUV laser is in contrast with the multiple photons that are needed for ionization when using UV/Vis/IR laser light. These unique characteristics of the compact

EUV laser enable high spatial resolution mass spectral mapping because the 46.9 nm light is (1) absorbed within depths of tens of nanometers in most materials, (2) can be focused down to nanoscale sized spots, and (3) efficiently ionizes the ablated material with its high energy photons.

### 1.c Extreme ultraviolet lasers as a new probe for mass spectrometry

In 2015, I. Kuznetsov et al. successfully coupled the 46.9 nm capillary discharge EUV laser as an ion source for mass spectrometry.<sup>44</sup> In their study, the EUV laser was connected to a time-of-flight (TOF) mass analyzer, called the EUV TOF. Figure 1.3 shows a simplified schematic of the EUV TOF, which will be explained further in Chapter 2. In brief, the EUV laser light is focused down to nanoscale sized spots on a solid sample (using a zone plate focusing optic).<sup>33</sup> The focused EUV light ablates and ionizes the removed material with its high energy 26.4 eV photons. The EUV laser-created ions are then accelerated into a TOF mass spectrometer that separates ions in time according to their mass and charge before being collected by the detector.

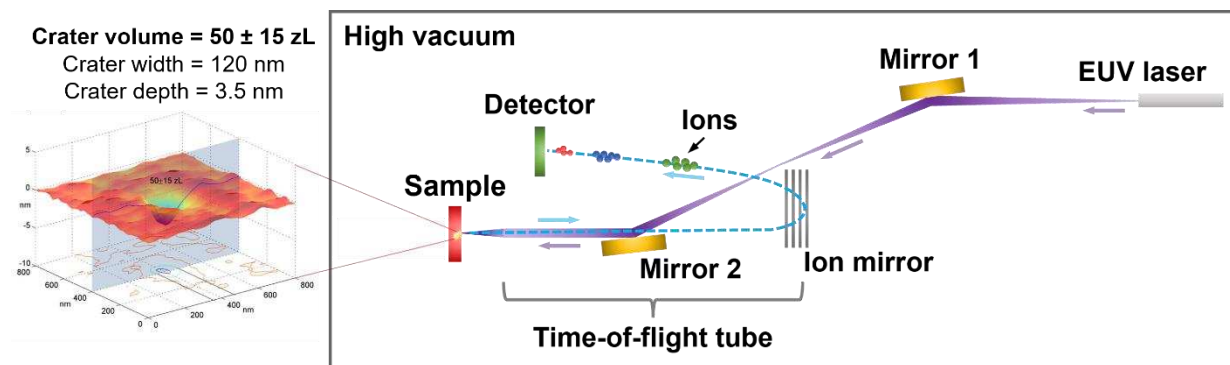


**Figure 1.3** Simplified schematic of the extreme ultraviolet laser ionization time-of-flight mass spectrometer (EUV TOF) built and developed by I. Kuznetsov et al. at Colorado State University. The capillary discharge EUV laser beam is guided and collimated by two mirrors. The EUV light is focused onto a solid sample, where the material is ablated and ionized within a single EUV laser pulse. A 50 zeptoliter (zL) crater ablated on photoresist with the EUV laser is shown as an example of the small craters that can be ablated. The ions formed from the crater are then accelerated on-axis into a time-of-flight tube that separates the ions in time according to their mass and charge. An ion mirror is placed at one end of the flight tube as an ion energy filter. The ions are finally collected by a detector, where lighter ions reach the detector before heavier ions. [Figure adapted from I. Kuznetsov et al.<sup>44</sup> and L. Rush et al.<sup>1</sup>]

I. Kuznetsov's study was ground-breaking because it showed for the first time that a laser-based mass spectrometry technique could be used to map chemical information at the nanoscale. Specifically, the EUV TOF was able to map the chemical composition of a bacterial cell with simultaneously 75 nm lateral and 20 nm depth resolution with high sensitivity. The EUV TOF's sensitivity, defined here as the amount of material removed versus detected, was 0.01 amol for detecting the main molecular ion from an ablated crater with a volume of only 50 zeptoliters (i.e.,  $10^{-21}$  liters) on a ~120 nm thick layer of alanine (see Figure 1.3). For reference, a comparable mass spectrometer set-up using a UV laser, with larger spot sizes, did not show any molecular peaks even after multiple laser shots were fired onto the alanine sample. The EUV laser light, on the other hand, is more strongly absorbed by organic species, allowing molecular peaks to be detected with just a single laser shot. Additionally, when compared to surface analysis performed by SIMS TOF at monolayer depths (~2 nm) on the same sample, the EUV TOF showed a 40x higher sensitivity with a similar amount of molecular fragmentation. Figure 1.4 shows the resulting mass spectra collected from each of the three set-ups. These first results collected on the EUV TOF showed that it could contribute to the challenges associated with nanoscale analyses using mass spectrometry by (1) three-dimensionally mapping molecular information at the nanoscale and (2) doing so with high sensitivity. Prior to these results, laser-based mass spectrometry was limited to analyses at the microscale, and more typically, to  $\geq 10 \mu\text{m}$  scales.

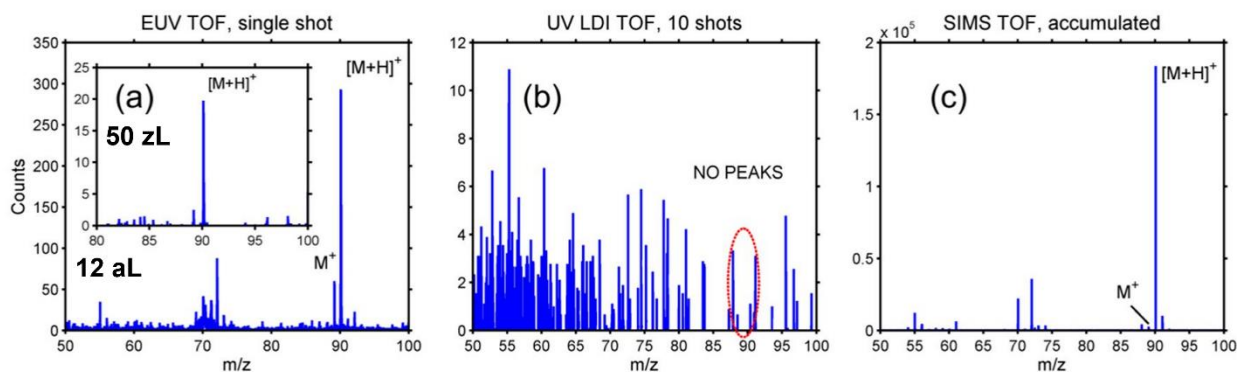


**Figure 1.4** Mass spectra of a ~120 nm thick layer of alanine using (A) EUV TOF, (B) UV laser desorption ionization (LDI) TOF, and (C) SIMS TOF. The mass spectra acquired with the EUV TOF are from single laser shots ablating 12 attoliter (aL) and (inset plot) 50 zeptoliter (zL) volumes (see Figure 1.3 for the corresponding 50 zL crater profile). The UV LDI TOF spectra were acquired using 10 laser shots at a single spot with no additional sample matrix added.

The SIMS TOF mass spectra was measured by scanning an area sized  $150\ \mu\text{m} \times 150\ \mu\text{m}$  with a  $5\ \mu\text{m}$  diameter  $\text{Bi}_3^+$  primary ion beam. The main molecular ion peaks are labeled in the spectra. [Figure adapted from I. Kuznetsov et al.<sup>44</sup>]

After showing that the EUV TOF could be successfully used to map molecular information at the nanoscale, T. Green and I. Kuznetsov et al. extended its application to inorganic materials.<sup>45</sup> Instead of measuring molecular ions, their study focused on understanding how the EUV TOF could be used to measure elemental and isotopic ions in nuclear-relevant material at the nanoscale. The EUV TOF was able to map certified reference materials (CRMs) in the form of micrometer-sized uranium particles with known amounts of the fissile  $^{235}\text{U}$  isotope and the non-fissile  $^{238}\text{U}$  isotope at an  $80\ \text{nm}$  lateral spatial resolution, within  $5\ \text{nm}$  of that achieved for organic materials. Figure 1.5 shows the resulting uranium isotope maps collected on the particles with low ( $500\ \text{nm}$  sized pixels) and high ( $50\ \text{nm}$  sized pixels) spatial resolutions. More pertinently, the resulting  $^{235}\text{U}/^{238}\text{U}$  isotope ratio (used to measure the amount of uranium enrichment in a material) calculated from the average of the EUV TOF's nanoscale map was  $0.248 \pm 0.006$  ( $2\sigma$ ), which is within error of the expected ratio of  $0.2513 \pm 0.0003$ . This result highlighted that alongside organic materials, the EUV TOF could map isotopic information in inorganic materials at the nanoscale with high sensitivity.

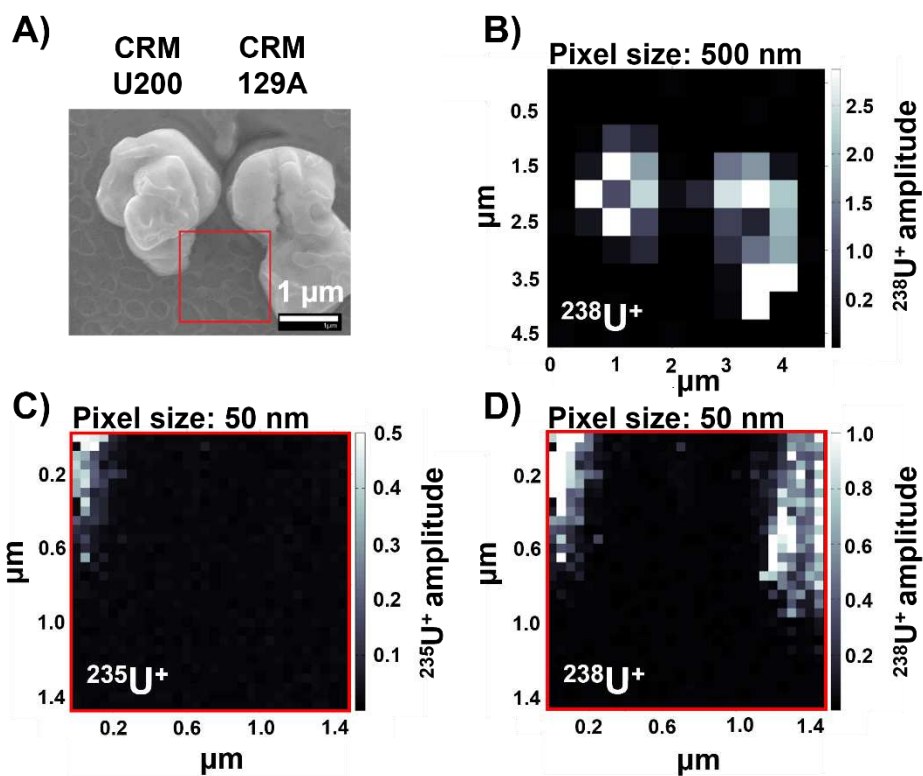


**Figure 1.5** (A) Secondary electron microscope (SEM) image of the two particles mapped with the EUV TOF. The left particle (CRM U200) had a 20%  $^{235}\text{U}$  enrichment, while the right particle (CRM 129A) had a 0.725%  $^{235}\text{U}$  natural abundance. (B-D) Resulting isotope maps collected with the EUV TOF using (B) 500 nm pixels and (C-D) 50 nm pixels, where the pixel size is ~30 nm smaller than the lateral spatial resolution. The 50 nm pixel maps shown in (C) and (D) were collected over the smaller area outlined in red on the particles in (A). In (C), the  $^{235}\text{U}$  signal was too low in the naturally abundant CRM 129A particle to be visible at the spatial scale of analysis. The average  $^{235}\text{U}/^{238}\text{U}$  isotope ratio measured on the CRM U200 particle from the 50 nm pixel map using the EUV TOF was  $0.0248 \pm 0.006$ ; the expected ratio was  $0.2513 \pm 0.0003$ . [Figure adapted from T. Green, et al.<sup>45</sup>]

An additional part of T. Green and I. Kuznetsov's study was showing the differences between the ionization mechanisms between the EUV laser probe and the SIMS ion probe.<sup>45</sup> To do this, both instruments analyzed microscale sized areas of a CRM made by the National Institute of Standards and Technology (NIST), called NIST 610. This CRM is a glass material with a range of elements incorporated into its matrix, providing a good way of comparing ion species formed at low, middle, and high masses between the EUV TOF and SIMS TOF techniques. Figure 1.6 shows the mass spectra collected from 0 to 280 mass/charge using both techniques. The most apparent difference between these two spectra is that the SIMS TOF spectra shows more peaks, specifically in the low and mid-mass ranges, than the EUV TOF spectra. The "extra" peaks in the SIMS TOF analysis are molecular ions created during the primary

ion beam bombardment process. An additional observation, is that in the mass range of the actinides, the EUV TOF produces higher intensity signals of Th and U. The result in Figure 1.6 highlights the differences between ionizing material with EUV laser light versus with a beam of charged particles. Other studies using longer wavelength lasers have also shown fewer molecular ions and higher elemental signal intensities when laser photoionization is used over ion beam bombardment.<sup>33,46</sup>

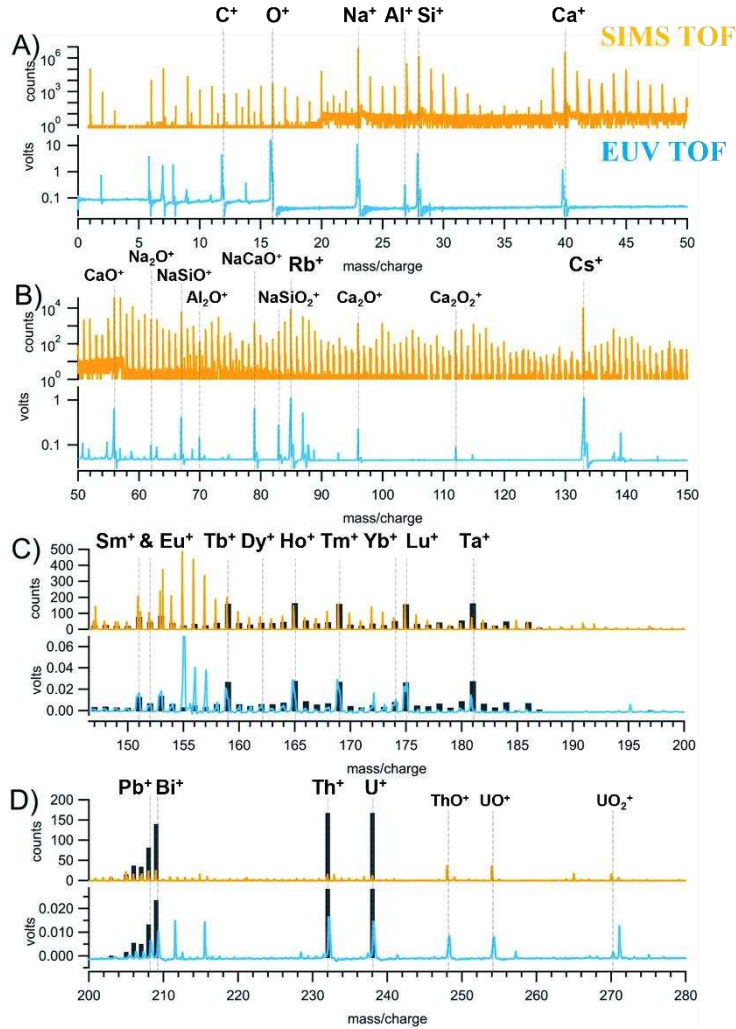


**Figure 1.6** Mass spectra collected from the CRM NIST 610 using (yellow) SIMS TOF and (blue) EUV TOF collected over the mass range from 0 to 280. The main elements and their corresponding oxides are labeled in the spectra. Plots A) and B) are plotted on a logarithmic scale, while plots C) and D) are plotted on linear scales with the gray bars representing nominal elemental content that are scaled to match experimental data. The SIMS TOF mass spectra was measured by scanning an area sized 200  $\mu\text{m}$  x 200  $\mu\text{m}$  with a  $\text{Bi}^+$  primary ion beam. The EUV TOF mass spectra was collected by ablating smaller overlapping craters creating one large “super crater” sized 10  $\mu\text{m}$  x 10  $\mu\text{m}$ . [Figure adapted from T. Green, et al.<sup>45</sup>]

## 1.d Scope of this dissertation

Expanding on I. Kuznetsov's and T. Green's prior work, this dissertation will describe advances in the EUV TOF system for assessing isotopic content at high spatial scales in samples made from uranium fuel pellets and from geologic material. After the EUV TOF system is introduced in Chapter 2, the first study, found in Chapter 3, details how the EUV TOF mapped uranium isotopes (i.e.,  $^{235}\text{U}$  and  $^{238}\text{U}$ ) using 100 nm sized pixels in a non-uniform nuclear fuel pellet.<sup>1</sup> The EUV TOF exposed micrometer sized areas of uranium heterogeneity, characterized by the fissile  $^{235}\text{U}$  isotope being in higher (enriched) and lower (depleted) abundance compared to its natural levels. NanoSIMS was also used to analyze the sample using 98 nm pixels and revealed similar sized areas of  $^{235}\text{U}$  enrichment and depletion, confirming the results collected with the EUV TOF. Prior to this EUV TOF study, the uranium sample had only been analyzed at the micro and bulk scales with other mass spectrometry techniques, and the full profile of its heterogeneity had not been revealed.

The second study, found in Chapter 4, uses the EUV TOF system to measure lead, thorium, and uranium inter-element isotope ratios (i.e.,  $^{206}\text{Pb}/^{238}\text{U}$  and  $^{232}\text{Th}/^{238}\text{U}$ ) in geologic materials at the  $\sim 8\ \mu\text{m}$  scale.<sup>47</sup> The geologic materials that were analyzed included different glasses (silicate, basalt, and phosphate), iron manganese, zircons, monazites, uraninites, and a thorite. The EUV TOF measured the inter-element isotope ratios to understand if the high energy EUV photons could directly probe chemically different materials. For most of the samples, excluding the uraninites and thorites, the EUV TOF could measure the inter-element isotope ratios within error ( $\pm 2\sigma$ ) of the known ratio values using a single external calibration standard that did not have a similar matrix to some of the other samples. This initial study showed that the EUV TOF might have fewer matrix effects than other mass spectrometry techniques (like SIMS).

Chapter 5 details the current progress on a new EUV laser mass spectrometer set-up that uses a double focusing sector-field multi-collector mass analyzer instead of a time-of-flight analyzer. This

new EUV laser mass spectrometer, called the EUV magnetic sector, could potentially assess complex isotopic composition with a precision of <1% at sub-micron spatial scales, which is not possible with the TOF set-up. For comparison, the TOF typically achieves precisions from 1-10%, depending on the spatial resolution and isotope ratio measured. The engineering involved in coupling the pulsed (1-10 Hz) EUV laser ionization source to a commercial magnetic sector mass spectrometer that is typically operated with ions from an ICP will be described. The trajectory of the EUV ions through the mass spectrometer's electric and magnetic sectors is assessed both theoretically from calculations and physically from experimental tests. The initial results from the calculations show that it is possible to couple the EUV laser ionization source to the magnetic sector mass spectrometer. Experiments confirm the calculations by showing that low ( $^{28}\text{Si}^+$ ) and high ( $^{197}\text{Au}^+$ ) mass ions can be detected after the electric and magnetic sectors. However, the proof-of-concept experiments also show that the mass spectrometer's native electron multiplier detectors are not adequate for isotope ratio measurements with the EUV laser because the detector's deadtime is on the order of the ~10-30 ns pulse width of the ions generated with the laser. Therefore, further system upgrades, like faster recovery detectors or a collision gas cell, will need to be incorporated before accurate isotope ratios at high spatial scales can be measured with the EUV magnetic instrument. For clarity, Figure 1.7 graphically summarizes the two types of EUV laser mass spectrometers that will be explored in this dissertation.

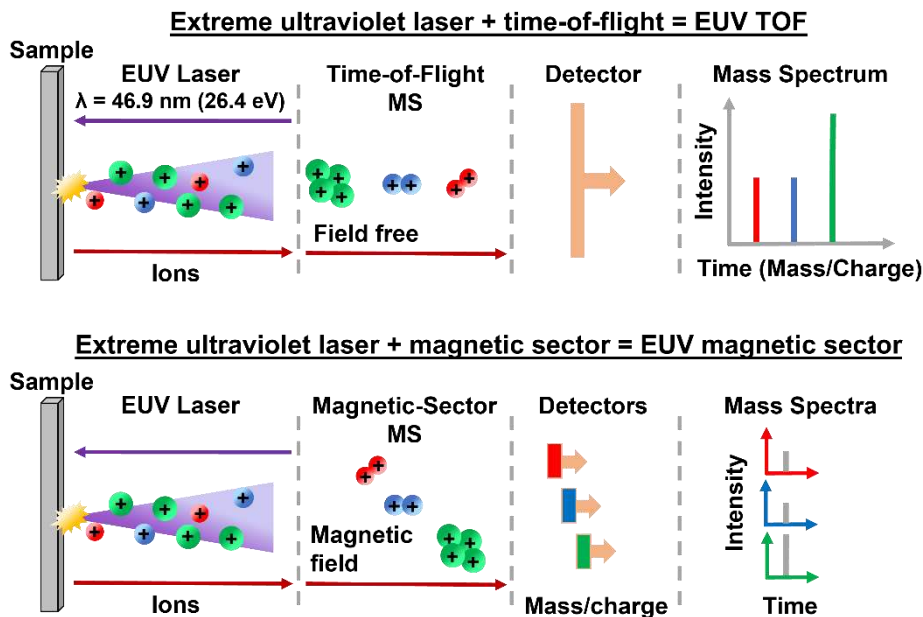


**Figure 1.7** Graphical representation of the two EUV laser mass spectrometer set-ups that will be explored in this dissertation. (Top) The ions created by the EUV laser will be sent into a time-of-flight mass spectrometer, which separates ions in time according to mass and charge. Lighter ions will have a shorter flight time than heavier ions, reaching the detector first. The detector outputs the intensity of the ion packets as a function of their arrival time, which can then be used to calculate their mass/charge. (Bottom) The EUV laser-created ions will be separated in a magnetic field whereby heavier ions have a larger radius of curvature than lighter ions. An array of detectors is placed at the masses of interest that collect the corresponding mass separated ions simultaneously. Each detector outputs a measurement of intensity of each ion at the same time.

Finally, Chapter 6 will provide an outlook on future experiments that can be performed with both EUV TOF and EUV magnetic sector instruments. While EUV lasers are not widely used in the analytical community, they are gaining traction as technology advances and the laser set-ups decrease in size and complexity. As EUV lasers becomes more accessible, it is possible to realize increased applications of this high energy light for offering a unique route for probing materials at high spatial scales for mass spectrometry analyses.

## 2. EUV TOF FUNDAMENTALS

### 2.a Background on time-of-flight mass spectrometers

A time-of-flight mass spectrometer (TOF MS) is a mass analyzer that uses time-dependent mass separation to analyze ions in the absence of electric and magnetic fields. The TOF separates ions in time according to their mass and charge ratio. A TOF MS can detect ions over a wide mass range, making it a prominent tool in biological applications that require the detection of large molecular compounds alongside their corresponding mass fragments. However, TOF mass spectrometers are becoming increasingly popular in other applications due to its versatility and ease of use.

Time-of-flight mass spectrometers made their debut in the late 1940s, with W.E. Stephens proposing its idea followed by A.E. Cameron and D.F. Eggers building the first prototype. However, TOFs did not see their full moment until the late 1980's when ionization probes like lasers and ion beams were becoming more popular in the analytical community, requiring the use of TOF's to properly handle the pulsed ion packets. Ions must be pulsed in a TOF due to the basis of how these mass spectrometers work. An ion, with mass ( $m$ ) and charge ( $q$ ), has potential energy ( $U_P$ ) that turns into kinetic energy ( $U_K$ ) due to the ion, with a velocity ( $v$ ), being accelerated into a field-free TOF tube by a voltage ( $U$ ) using Equations 2.1 and 2.2:

$$U_P = qU \quad 2.1$$

$$U_K = \frac{1}{2}mv^2 \quad 2.2$$

Setting Equation 2.1 equal to Equation 2.2 and substituting the ion's velocity ( $v$ ) in terms of the distance ( $d$ ) the ion travels and the time ( $t$ ) it takes to travel that distance, then Equation 2.3 is obtained:

$$qU = \frac{1}{2}m\left(\frac{d}{t}\right)^2 \quad 2.3$$

Rearranging Equation 2.3 in terms of the ions' flight time ( $t$ ) results in Equation 2.4:

$$t = \frac{d}{2U_K} \sqrt{\frac{m}{q}} \quad 2.4$$

Equation 2.4 is the foundation of how a TOF works, showing that the ions' flight time ( $t$ ) is directly proportional to the ratio of mass and charge. Heavier ions will therefore have a slower flight time than lighter ions over the same distance. The potential energy difference ( $U_K$ ) used to accelerate the ions into the flight tube and the length ( $d$ ) of the tube are typically held constant so that the ions' flight time will strictly change based on their mass to charge ratio.

The total distance that the ions travel in a TOF MS is an important factor in ensuring that ions with different mass and charge have sufficient time to separate in space before reaching the detector. The ability to distinguish between packets of ions with different masses is called mass resolution ( $R$ ) and is expressed in terms of both average arrival time of the ions ( $t$ ) and the ion's mass ( $m$ ) in Equation 2.5:

$$R = \frac{t}{\Delta t} = \frac{m}{\Delta m} \quad 2.5$$

The relationship between the ion's mass and flight time in Equation 2.5 can be derived from Equation 2.4. The denominator  $\Delta t$  and  $\Delta m$  is the distribution of the ion's arrival time and mass, respectively, which can be defined as either (1) the full width at half maximum (FWHM) of a single mass peak ( $m$ ) or (2) the difference between two peaks ( $m_1$  and  $m_2$ ) at 10% of the peaks' intensity. The latter is referred to as the "valley" definition of mass resolution. Herein, we use the former FWHM definition to characterize the EUV TOF's mass resolution. Although subject to opinion, high mass resolution for a TOF is typically  $R > 10,000$  to 20,000 and a moderate mass resolution is  $R > 5,000$ . The EUV TOF's mass resolution is relatively low at  $R = 1,100$ , likely limited by the time it takes to accelerate the ions out of the laser-created plasma on the sample surface.

There are two common ways to increase the mass resolution in a TOF MS: (1) Increasing the length of the flight tube ( $d$ ) (i.e., the flight time) through which the ions travel and/or (2) reducing the spread in energy ( $U$ ) of the ions. A physically longer TOF tube is a straight-forward way to address the former. However, there are more compact ways to achieve an increased flight time. For example, an ion

mirror (commonly known as a reflectron) can be installed at one end of the TOF tube and works through a series of biased grids that turn the ions 180 deg., thereby approximately doubling the length of the ions' flight path without needing to increase the physical length of the TOF tube. Ion mirrors can be installed in different geometries to achieve ever increasing mass resolution. For example, multiple ion mirrors that make the ions travel in a "W" path allows the ions to roughly triple their travel distance as well as other advanced designs.<sup>48</sup>

Alongside increasing the distance traveled by ions, a reflectron also works to reduce the initial energy (or velocity) spread of the ions. Reducing the ions' energy dispersion is accomplished by biasing the reflectron grids such that ions with a higher energy will travel further into the grid compared to lower energy ions. In this way, ions of the same mass and charge, but different starting energies will be able to "catch-up" to each other in the reflectron. Decreasing the energy dispersion of the ions results in an increased mass resolution because the ion peak associated with each mass and charge will be narrower, thereby providing a larger separation of time between successive peaks. Figure 2.8 shows a diagram of a TOF MS with a reflectron, which acts as an energy filter for the ions and approximately doubles the distance that the ions travel through the flight tube.

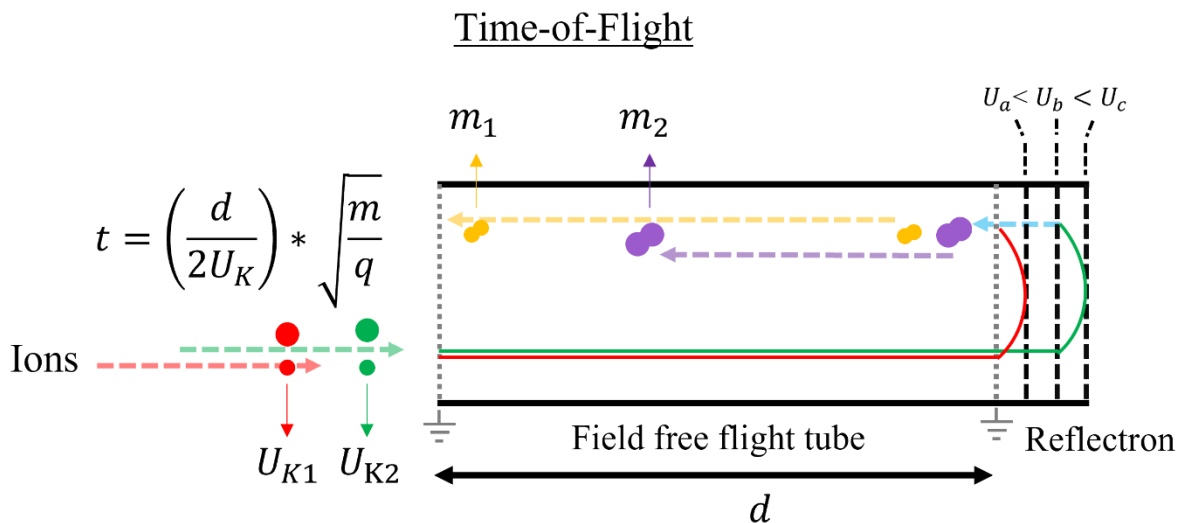


**Figure 2.8** A simplified diagram of a time-of-flight mass spectrometer. The ions travel into a field free flight tube where they separate in time according to their mass and charge. A reflectron (or ion mirror) can be placed at the end of the flight tube to focus the ions with respect to their energy using a series of biased grids.  $U_K$  = ion energy (eV),  $d$  = distance (m),  $m$  = ion mass (kg),  $q$  = ion charge (C),  $U_{a-c}$  = bias applied to reflectron grids (V), and  $t$  = ion flight time (s).

Another way to increase mass resolution using a TOF MS is to extract the ions perpendicular (or orthogonal) to their source. In Figure 2.8 and as will be seen for the EUV TOF set-up, the ions are extracted parallel (or axial) to the source. However, extracting and accelerating ions orthogonal to the source allows for more control of the ions' velocity and position than parallel ion injection, permitting the former set-up to achieve a higher mass resolution. Orthogonal acceleration is also the most common route to couple a continuous ionization source with a TOF MS. While orthogonal TOF MS set-ups are widely used, they do have the disadvantage of a low duty cycle, which is defined as the ratio between the time needed to fill the acceleration region with the ions with the largest mass/charge and the flight time of those largest mass/charge ions. Typically, orthogonal extraction TOF MS set-ups only have duty cycles of ~1-30%, with lighter masses having smaller duty cycles than heavier masses. This means that only ~1-30% of ions that make it to the flight tube are analyzed, while the rest are lost in the acceleration process. Due to the geometry in axial ion acceleration, duty cycle is less of an issue but at the cost of a typically lower mass resolution. Ultimately, the design of a specific TOF set-up will depend on many user-defined factors

such as the type of analysis being performed, the amount of physical space available, and the type of probe being coupled to the TOF, amongst other considerations.

Commonly used pulsed probes with TOF MS include lasers and ion beams, which both allow chemical information in the sample to be spatially resolved. Lasers used with TOF's encompass a variety of configurations. Perhaps the most widely recognized is matrix assisted laser desorption ionization (MALDI) mass spectrometry, which uses a laser (typically at UV/Vis/IR wavelengths) in conjunction with a special matrix surrounding an organic sample that absorbs the laser light, resulting in sample desorption and ionization. MALDI MS is a soft ionization technique that gently ionizes the sample, retaining the molecular compound as well as its mass fragments for mass analysis. MALDI is therefore often used in biological applications where mapping molecular information at the  $\geq 1 \mu\text{m}$  scale is required.<sup>32</sup>

Lasers are also used with TOF's in atom probe tomography (APT) set-ups as well as when lasers are used to directly ablate and ionize the sample, the latter commonly known as laser ionization mass spectrometry (LIMS) or laser microprobe mass analysis (LAMMA).<sup>26</sup> The EUV TOF technique falls into the LIMS/LAMMA category. Compared to MALDI MS, the EUV TOF is a hard ionization technique due to the high EUV photon energy being able to break any molecular bond. Molecular analyses is still possible with the EUV TOF, achieving similar fragmentation as ion beams, but produces more fragmentation than MALDI techniques as well as longer wavelength light.<sup>33,44</sup> However, the EUV TOF achieves a much higher spatial resolution than MALDI, reaching down to 75 nm (see Figure 1.4 and Figure 1.5).<sup>44,45</sup>

Alongside lasers, ion beams are also used in conjunction with TOF analyzers to spatially resolve chemical information in secondary ionization time-of-flight secondary mass spectrometers (SIMS TOF or also called TOF SIMS). In SIMS TOF, a pulsed primary ion beam is focused onto the surface of a sample using a series of ion lenses, creating secondary ions from the top monolayers that are then sent into the TOF for mass analysis. Due to SIMS TOF's high depth resolution, it is often used to measure thin film quality used in semiconductors but is also commonly employed in biological analyses. However, SIMS TOF is not ideal for high lateral spatial resolution measurements; NanoSIMS is used for this because of the

different ion focusing lenses that are required. SIMS TOF is a harder ionization technique compared to MALDI but results in very little changes induced in the sample surface due to the low dose (or flux) of pulsed ions (i.e., the secondary ion yield can be as small as  $1 \times 10^{-3}$  to  $1 \times 10^{-8}$  atoms/cm<sup>3</sup>). Therefore, SIMS TOF is often referred to as “static SIMS”, whereas the term “dynamic SIMS” refers to a high dose of primary ions that sputters the surface of the sample continuously, resulting in a much higher secondary ion yield and apparent surface modifications.

Ion beams and lasers are also used together with TOF MS in a technique known as resonance ionization mass spectrometry (RIMS). RIMS exploits the fact that most atoms created by ion beam bombardment or by vaporization from laser ablation are neutrals. Therefore, additional lasers are focused onto the plume of neutrals ejected from the sample either by a primary ion beam or by a laser. The additional lasers are tuned to precise transition energies to excite a specific atom of interest until the atom’s ionization energy is surpassed. RIMS is essentially a post-ionization strategy for TOF SIMS and/or LIMS that provides a highly selectable ionization route for mass analysis. Additionally, continuous ionization sources are also routinely used with TOFs such as electrospray, electron impact, and chemical ionization as well as ICP ionization. Ions are extracted from these continuous ionization sources by pulsing the optics used for extraction so that the ions can be properly analyzed with the TOF.

Overall, the TOF MS is a flexible mass analyzer that can be used with a range of ionization sources and, in general, is easy to modify based on the application. In fact, TOFs can also be miniaturized, finding their way into space instruments like rovers and other field-deployable set-ups. The TOF also provides information over a large mass range using just a single pulse of ions. While the TOF does have limitations in its quantitative capabilities that will be addressed in later sections, the TOF’s flexibility, ease of use, and typically low-price tag made it an excellent choice for initially benchmarking the EUV laser’s proficiencies as a probe for mass analysis at high spatial scales.

## 2.b Extreme ultraviolet laser ionization time-of-flight (EUV TOF)

The extreme ultraviolet laser ionization time-of-flight mass spectrometer (EUV TOF MS), located at Colorado State University (CSU), was built by prior graduate students, and an in-depth overview of its design and operation can be found in I. Kuznetsov's 2018 PhD Dissertation.<sup>49</sup> For this reason, the EUV TOF system will only be briefly outlined here. The EUV TOF was built by connecting a desktop sized capillary discharge EUV laser to a TOF mass analyzer. Figure 2.9 provides a graphical overview of the main external and internal components of the EUV TOF. The output of the EUV laser, operating at a 46.9 nm wavelength with a ~1.5 ns pulse duration, is collimated and guided into a sample chamber using two gold-coated toroidal mirrors. The EUV beam is focused onto the sample using a zone plate lens with a 0.12 numerical aperture. The sample is ablated, and the removed material is subsequently ionized by the EUV photons. The ions are then accelerated into a ~1-meter-long field-free TOF tube, operated with a reflectron for a total flight distance of ~2-meters, before being collected by a microchannel plate (MCP) detector.

The EUV TOF has been used in the past to analyze inorganic and organic materials down to the nanoscale. For analyzing inorganic materials, the EUV TOF can reach a lateral resolution down to 80 nm and an efficiency of ~0.015%, measured for Th and U, and a sensitivity of ~50 ppm for the measurement of Th and U in a large 20  $\mu\text{m}^2$  area on a NIST 610 certified reference material. Here, efficiency, also commonly known as sample utilization efficiency (SUE), is defined as the amount of material removed divided by the number of ions detected. For organic materials, the EUV TOF has a lateral resolution down to 75 nm and depth resolution of 20 nm and an efficiency of ~0.007% measured for the detection of alanine. Table 2.1 lists the main EUV TOF parameters that have been measured since the instrument's inception. It should be noted that different elements/molecules will have different efficiencies. For example, cesium (Cs) has been shown to have a 100x higher signal intensity than Th and U at similar concentrations when analyzing the same sample (see Figure 1.6). This could be due to the lower ionization energy of Cs or other chemical differences. It would be worthwhile to perform a large-scale investigation of the different "response factors" for each element in different samples using the EUV TOF in the future.

**Table 2.1** EUV TOF parameters for the analysis of inorganic and organic materials.

EUV TOF Parameters		
Parameter	Inorganic materials [T. Green et al. <sup>45</sup> ]	Organic materials [I. Kuznetsov et al. <sup>44</sup> ]
Mass resolution ( $R$ )	1,100	
Lateral resolution	80 nm	75 nm
Depth resolution	N/A	20 nm
Efficiency (i.e., SUE)	0.017% for Th and 0.014% for U measured in NIST 610 glass	0.0073% for alanine
Detection limit	~50 ppm (measured for Th and U over 20 $\mu\text{m}^2$ )	~ ppm (measured for alanine over ~5 $\mu\text{m}^2$ )

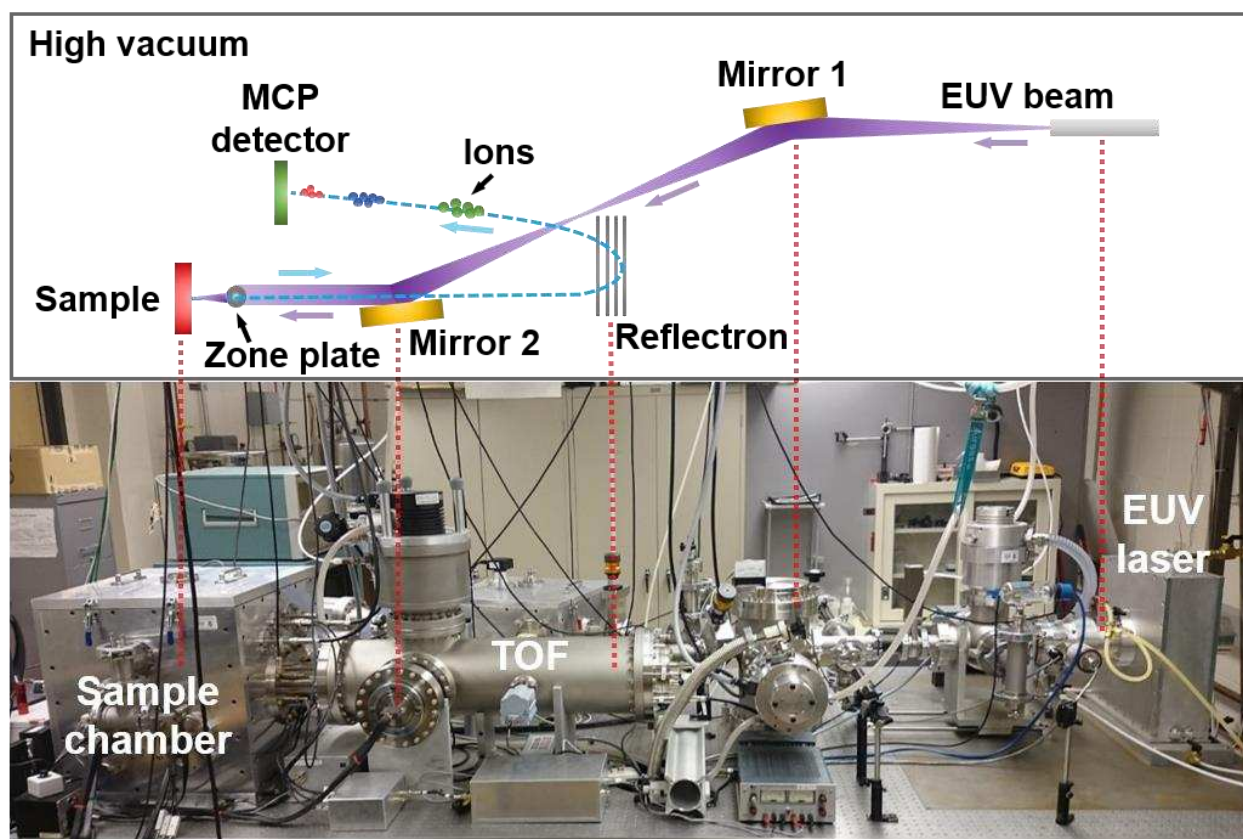


**Figure 2.9** (Bottom) Photograph and (top) schematic of the extreme ultraviolet laser time-of-flight mass spectrometer (EUV TOF MS) at Colorado State University. The EUV laser beam (purple line) is collimated and guided by two gold-coated toroidal mirrors and focused onto the sample using a zone plate lens. The focused EUV beam ablates and ionizes the sample, and the ions (blue line) are accelerated into the TOF tube, operated with a reflectron, before being collected by an MCP detector. [Figure adapted from L. Rush et al.<sup>1</sup>]

## 2.c Desktop EUV capillary discharge laser

The desktop sized EUV capillary discharge laser used in the EUV TOF system operates by delivering high voltage pulses onto an alumina capillary tube that is filled with argon gas that acts as the gain medium. Approximately 300 mTorr of argon gas fills the 21 cm long capillary with a diameter of 3 mm, forming a channel for the pinched plasma. A DC pre-ionization pulse followed by a pre-pulse is delivered to the high voltage electrode situated at one end of the capillary, while a ground electrode is situated on the other end. The pulses result in ionization of the argon gas inside the capillary into a neon-like state (i.e., Ar<sup>8+</sup>). This is followed by a main high voltage pulse of 90 kV and 22 kA that excites the Ar<sup>8+</sup> ions from the 3p <sup>1</sup>S<sub>0</sub> level to 3s <sup>1</sup>P<sub>1</sub> level, creating the necessary population inversion for 46.9 nm light amplification. The resulting EUV light beam from the capillary has a divergence of 5 mrad and has a doughnut-shaped beam profile due to the refractive index gradient of the plasma column formed in the capillary that deflects the amplified light rays sideways. Due to the EUV beam's divergence, two toroidal mirrors are used in the EUV TOF to collimate the beam so that its diameter remains at ~3 mm as it travels ~2.5 m to the sample. Of that 3 mm beam, only the most intense 0.5 mm x 0.5 mm area is focused by the zone plate onto the sample for ablation and ionization.

The desktop version of the EUV capillary discharge laser outputs a pulse 1.5 ns in duration with an absolute energy of approximately 10 μJ per pulse at a repetition rate of 1 Hz. However, when used with the steering and focusing optics in the EUV TOF, only a small fraction of the beam's total energy reaches the sample. The two toroidal mirrors have a total transmission of ~50% and the zone plate has a transmission of ~10% when operated in the first order (and ~1% when operated in the third order). Therefore, the EUV energy is on the order of a few nJ at the sample location. Different focusing optics can be used with the EUV light, but special optics like a zone plate are required for focusing the EUV light down to nanoscale sized spots.

A considerable amount of maintenance is required on the desktop sized version of the EUV laser to keep it operating at optimal conditions, including regular maintenance of the capillary as well as the high voltage triggers delivering the pulses. The capillary must be regularly replaced with a new capillary

because the high voltage pulses ablate the inner walls of the alumina, causing damage to the capillary and decreasing the output energy of the EUV beam. The capillary typically needs to be replaced every 10,000 to 20,000 shots. Additionally, the highly pressurized (up to ~80 psi) spark gaps that act as the voltage triggers must also be thoroughly cleaned every 6 months (depending on frequency of laser use) for proper delivery of the high voltage pulses. As will be seen in the next chapter, a newer version of the EUV capillary discharge laser offers significantly less maintenance due to a more efficient design for generating the 46.9 nm light.

For additional specifics on the EUV laser as well as photodetectors, vacuum pumps, electronics, and all other details of the EUV TOF, the reader is directed to I. Kuznetsov's Dissertation.<sup>49</sup> The reader is also directed to the Appendix where a list of the main components used in the EUV TOF is compiled in Table A.1.1.

## **2.d Sample preparation for EUV TOF**

Sample preparation for the EUV TOF can be performed for both organic and inorganic sample analyses so long as the sample is sufficiently conductive to reduce surface charging.<sup>50</sup> Typically, the sample is loaded onto a glass slide with a 15-30 nm conductive indium tin oxide (ITO) layer. The slide is sized 25 mm x 25 mm x 1.1 mm with a resistance between 30 to 60  $\Omega$  (Delta Technologies, 8SG0115, USA). If the sample is initially in a liquid form, it can be deposited onto the slide by spin-coating the solution onto the slide at the desired thickness (typically between ~60 to 350 nm) and drying.<sup>44</sup> If the sample is a solid it can be directly attached to the ITO glass slide using conductive copper tape. When loading solid samples, a conductive film of gold, aluminum, or carbon is deposited onto the sample surface using magnetron sputtering deposition or thermal evaporation. The choice of coating should consider the mass(es) of interest to be measured within the sample to avoid mass interference from the coating. The experiments

discussed in Chapters 3 and 4 use magnetron sputtering (Denton Vacuum, Desk II, USA) to deposit a gold coating between 30 and 100 nm thick on the analyzed samples.

Prior to coating samples with a conductive film, the sample may need to be polished to reduce surface roughness. For instance, some of the geologic samples analyzed with the EUV TOF in Chapter 4 came as bulk mineral samples. To prepare these samples for analyses, the bulk sample was set in epoxy, cut into disks using a diamond saw to expose the mineral face, and then polished. The polishing procedure consisted of polishing with super fine (grit size = 600) and ultrafine (grit size = 800) sandpaper followed by a final polish with a polishing pad (Pace Technologies, ATLANTIS Polishing Pad, USA) with 3  $\mu\text{m}$  and 1  $\mu\text{m}$  diamond solutions. This procedure followed typical SIMS sample preparation steps that requires samples to have a surface roughness of  $<1 \mu\text{m}$ . However, the EUV TOF only requires a surface roughness of  $<3 \mu\text{m}$ , which is the depth of focus of the zone plate used to focus the EUV laser light onto the sample. As an example, one of the geologic samples analyzed in Chapter 4 had an apparent surface roughness  $>1 \mu\text{m}$  in some areas (Figure 4.1C), and the EUV TOF was still able to measure the isotope ratios with relatively good precision. T. Green et al.'s study also showed that isotope ratios could be measured in micrometer sized uranium particles with a relatively complex sample surface using the EUV TOF (Figure 1.5).

After the sample has been properly prepared and loaded onto the ITO coated glass slide, the slide is screwed into a stainless-steel sample holder and placed into the EUV TOF's sample vacuum chamber. The holder is directly biased by a conductive wire to (+)6000 V to accelerate the ions through the (+)1000 V zone plate and through a ground grid into the TOF tube. Figure 2.10 shows a picture of one of the geologic samples from Chapter 4 loaded onto the EUV TOF sample holder. The sample's size should not exceed an area of 26 mm (W) x 26 mm (H), which is the maximum travel range of the piezo electric stages (Physik Instrumente, Q-Motion Precision Linear Stage Q-545.240, Germany) to which the sample is attached for horizontal and vertical movement. The sample's thickness should also not exceed 26 mm,

which is the maximum travel distance of the actuator used to move the zone plate into its focal position relative to the sample surface.

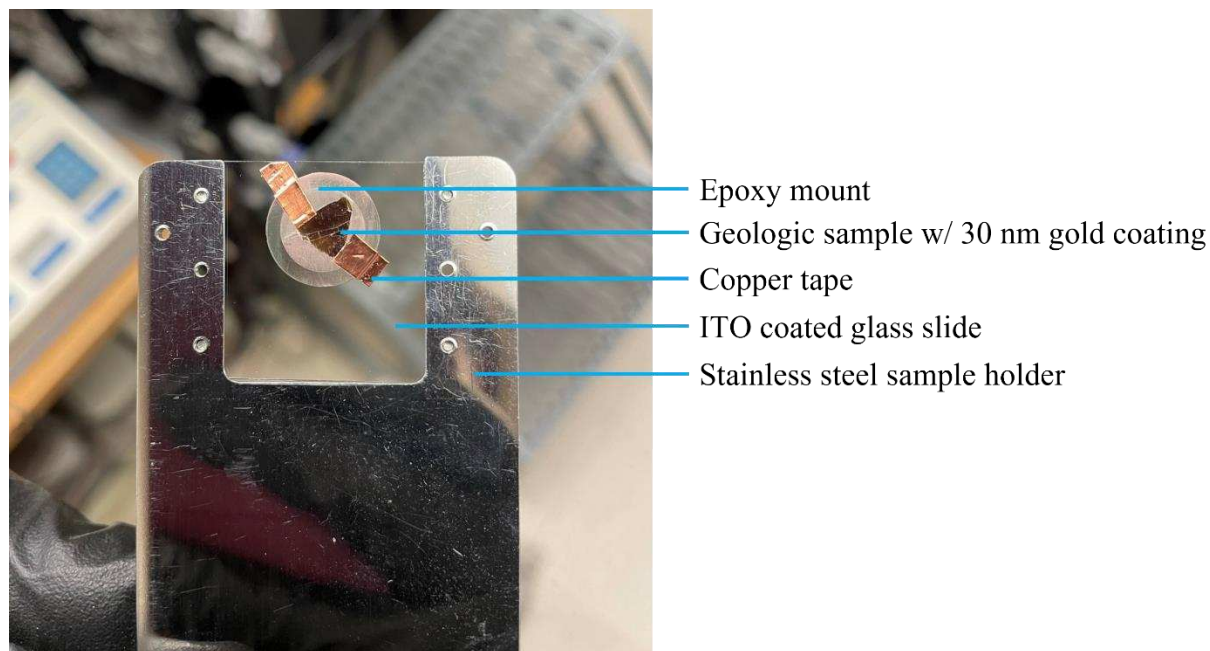


**Figure 2.10** Geologic sample prepared for EUV TOF analysis. The sample has been mounted in epoxy, cut into disks, polished, and coated with  $\sim 30$  nm of gold using magnetron sputtering deposition prior to its loading onto the main sample holder.

## 2.e Data collection and analysis for EUV TOF

To collect data using the EUV TOF, the EUV laser and TOF mass spectrometer are first tuned to the desired parameters. The EUV laser's energy is optimized to the desired energy level using an argon gas cell located immediately after the capillary output. When the cell is operated at its base pressure, the EUV laser operates at its maximum energy of  $\sim 10$   $\mu\text{J}$ . Additional argon gas can be leaked into the cell to reduce the laser energy until the desired spatial resolution is achieved on the sample or the desired mass signal intensity is measured. The zone plate's position is then adjusted relative to the sample such that the zone plate is placed 2.13 mm away from the sample at its first order focal length. The zone plate can also be operated at its third order focal length of 0.7 mm to reduce the amount of material ablated and thereby increase the spatial resolution at the cost of an order of magnitude worse efficiency, decreasing from 10%

to 1%. The zone plate position is tuned by monitoring the mass signal output by the EUV TOF. If one is ablating a pure gold sample, for example, then the zone plate position with respect to the sample is optimized when the  $^{197}\text{Au}^+$  peak intensity is maximized and the peaks associated with surface contamination, like  $^{12}\text{C}^+$  and  $^{16}\text{O}^+$ , are minimized. The zone plate is attached to linear stages with motorized actuators that can move in steps down to 500 nm. The sample is attached to piezo electric stages that move it in the horizontal and vertical directions by a total of 26 mm x 26 mm for sample placement relative to the zone plate. All other settings on the TOF typically do not need to be tuned at the start of the run. The exception to this is that occasionally the TOF deflection plates and reflectron potentials need to be slightly adjusted if the peak width is >20 ns, indicating that the ions are not being properly focused through the TOF tube.

After the EUV laser and TOF MS settings have been tuned, the ion signal produced at every laser pulse is monitored by the MCP detector in the TOF tube. The current signal from the MCP is digitized by a 1 channel, 12 bit, 1 GS/s analog-digital-converter (ADC) (DynamicSignals (now Vitrek), EON CompuScope CS121G1, USA) and a spectrum of the intensity of the detected ions as a function of their arrival time is recorded. The ADC is triggered by the laser pulse via the Rogowski coil that measures the pulse current. For automated data collection, a home built Labview program is used to save each spectrum output by the ADC at every user-defined x, y, and z coordinate over a certain sample area. According to the specified array size, the piezo electric stages to which the sample is attached moves in the desired horizontal (x) and vertical (y) directions across the sample separated by a step size between each location that is also specified by the user. The minimum step size that can be taken with the piezo electric stages is 6 nm. The number of EUV laser shots taken at each spot (z) is also specified by the user in the automated data collection program. After all spectra have been collected, the arrival time of the ions is correlated to their mass by performing a calibration of time to two known masses (typically encompassing the low and high mass range) for further analysis. Figure 2.11 shows a simplified graphic of the EUV TOF

data collection process on a piece of pure silver, where the mass spectra collected at every EUV laser shot can be used to measure the sample's isotopic composition.

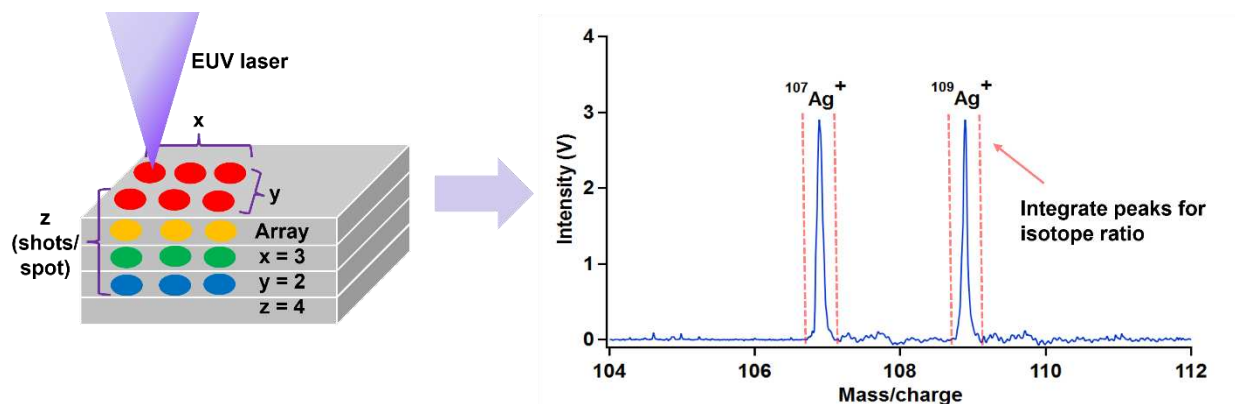


**Figure 2.11** Graphical depiction of the EUV TOF data collection process on a pure silver sample. (Left image) The EUV laser is focused onto a sample and ablates a series of craters following a user specified array size in the horizontal (x) and vertical (y) directions as well as the number of shots at each spot (z). (Right image) At every laser shot, a mass spectrum is recorded at the MCP detector and digitized by an analog-to-digital convertor. The area of each peak of interest in the spectrum can be integrated to calculate the isotope ratio between different masses.

The data analysis procedure explained here will focus specifically on isotope ratio measurements with the EUV TOF. The isotope peaks of interest in each collected mass spectrum are integrated to calculate the isotope ratio. The individual spectrum acquired at each sample location, or the average spectrum collected over the entire array can be used to calculate the isotope ratio. When the isotope signal is low, the average spectrum is more useful to calculate the isotope ratio because the background noise is averaged out (see top plot in Figure 4.2). When the isotope signal is sufficiently high above the background (like the bottom plot in Figure 4.2 and in Figure 2.11), isotope ratios can be calculated using individual spectrum. An IgorPro program was developed to automate the data analysis process for both cases. The selected files are automatically imported into the program, mass calibrated, background subtracted, averaged (if applicable), and the specified peak areas are integrated spectrum by spectrum or using the average spectrum. The area of the peaks, which are output in units of V\*s are converted to ion counts using the gain of the MCP detector, which is determined for every experiment because the operational gain will decrease over time (see Experimental Sections of Chapters 3 and 4). Other features were also added to the program for specific analyses, like a threshold function that deletes spectrum if the

isotope of interest is below a specified voltage (or count) threshold (see Experimental Section of Chapter 3). Occasionally, the laser's current signal measured with the Rogowski coil that is used to trigger the ADC is subject to a timing jitter that results in peak shifts, which must be appropriately corrected prior to peak integration.

To show resulting isotope ratio measurements collected with the EUV TOF using a straightforward example, the graphical analysis in Figure 2.11 using a silver sample will be expanded. The EUV TOF analyzed a  $\geq 99\%$  pure silver foil (GoodFellow, AG000467, UK) with a natural abundance of its major isotopes (i.e.,  $\sim 52\%$   $^{107}\text{Ag}$  and  $\sim 48\%$   $^{109}\text{Ag}$ ).<sup>51</sup> Individual mass spectra were collected over an area sized  $500\ \mu\text{m} \times 500\ \mu\text{m}$  with  $50\ \mu\text{m}$  steps between each ablation spot and six laser shots at every spot using a laser energy of  $\sim 5\ \mu\text{J}$ . The  $^{107}\text{Ag}/^{109}\text{Ag}$  isotope ratio was calculated from each background-subtracted peak area in the mass spectrum using the IgorPro program described above. Figure 2.12A shows the resulting two isotope ratio plot from single shot spectra. The average ratio from the single shot EUV TOF spectra is measured using the slope of the linear best fit line through the data points in Figure 2.12A, which is  $^{107}\text{Ag}/^{109}\text{Ag} = 1.11 \pm 0.03$  ( $2\sigma$ ). The measured  $^{107}\text{Ag}/^{109}\text{Ag}$  isotope ratio agrees within error of the certified value of 1.08. Because the measured isotope ratio agrees within error of the expected ratio, a calibration factor is not applied to the measured ratio to account for instrumental biases that result in low or high deviations from the expected value. Calibration factors (internal or external) are applied to analytical measurements when measuring a standard alongside an “unknown” sample.

Figure 2.12B provides a more statistical view of the data by plotting the ratio of each point as a function of ion counts in the form of a tree plot, where the expected  $\pm 2\sigma$  and  $\pm 3\sigma$  uncertainty envelopes are plotted at the respective counting statistics uncertainty. The counting statistics uncertainty provides a measure of the instruments' variability based on the number of atoms detected. Variations in measured ion intensities are likely from a combination of shot-to-shot laser energy fluctuations, slight variations in the sample (e.g., topography, geometry, and conductivity), and the probability of detecting infrequent ion events. The Ag analysis shows that EUV TOF can determine the isotope ratio in a single laser shot in the

case in which the isotopes of interest have a similar abundance and when the ion count rate is sufficient (i.e., individual  $^{107}\text{Ag}/^{109}\text{Ag}$  ratios measured at  $\sim 100$  ion counts all show good agreement with the certified value in Figure 2.12B). As will be seen in the more complex isotope ratio measurements performed in Chapters 3 and 4 using similar procedures as the one shown here, multiple spectra were needed at each location to reduce the uncertainty in the measurement because of low ion counts for some isotope signals.

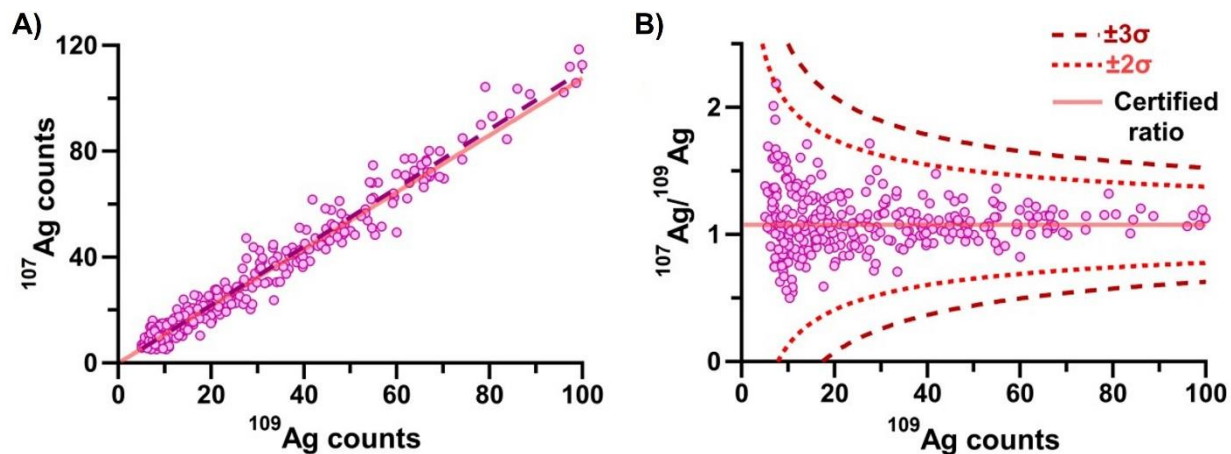


**Figure 2.12** Silver (A) two-isotope and (B) ratio plots of the EUV TOF data collected on the silver sample. Each data point is from a single laser shot. (A)  $^{107}\text{Ag}$  counts plotted as a function of  $^{109}\text{Ag}$  counts. The dotted line represents the linear best fit line (average ratio) of the EUV TOF data (intercept of line is not fixed at zero), whose slope is  $1.11 \pm 0.03$  ( $2\sigma$ ). The certified  $^{107}\text{Ag}/^{109}\text{Ag}$  ratio, shown as a red solid line in (A,B), is 1.076. (B) Corresponding  $^{107}\text{Ag}/^{109}\text{Ag}$  ratios plotted as a function of  $^{109}\text{Ag}$  counts. The red dotted lines represent the  $\pm 2\sigma$  and  $\pm 3\sigma$  error from the certified ratio based on counting statistics.

Although the analysis of silver shown here does not represent a mapping study that the EUV TOF can perform, it is straightforward to translate the data plotted in Figure 2.12 into pixels that would result in a corresponding isotope map. The pixel size of the map would correspond to the sample step size taken between each location, and the horizontal (x) and vertical (y) dimensions of the array would determine the size of the map. It should be noted that for the pixel size to be representative of the spatial resolution, the EUV laser's spot size on the sample needs to be adjusted accordingly through the adjustment of the laser energy via the argon gas cell or by adjustment of the zone plate's position.<sup>44,45</sup>

It should be noted that although it is recognized that the procedure described here to calculate the isotope ratio from EUV TOF measurements and translate it into a spatially resolved map has

been automated to a certain extent, it could certainly be improved. For example, it would be ideal to automate the analysis procedure to analyze the data in real time as it is being collected with the Labview program. It would also be good to move the data analysis to an open-source software platform like Python in the future to make it more accessible and user-friendly.

### 3. PAPER #1 ON EUV TOF

#### 3.a Paper #1 title page

This chapter describes the following peer-reviewed published work that shows the use of the EUV TOF MS for imaging the uranium composition in 100 nanometer sized pixels in a heterogenous uranium fuel pellet.\*

##### 3.a.i Overview

We use extreme ultraviolet laser ablation and ionization time-of-flight mass spectrometry (EUV TOF) to map uranium isotopic heterogeneity at the nanoscale ( $\leq 100$  nm). Using low-enriched uranium fuel pellets that were made by blending two isotopically distinct feedstocks, we show that EUV TOF can map the  $^{235}\text{U}/^{238}\text{U}$  content in 100 nm-sized pixels. The two-dimensional (2D) isotope maps reveal U ratio variations in sub-microscale to  $\geq 1$   $\mu\text{m}$  areas of the pellet that had not been fully exposed by microscale or bulk mass spectrometry analyses. Compared to the ratio distribution measured in a homogeneous U reference material, the ratios in the enriched pellet follow a  $\sim 3\times$  wider distribution. These results indicate U heterogeneity in the fuel pellet from incomplete blending of the different source materials. EUV TOF results agree well with those obtained on the same enriched pellets by nanoscale secondary ionization mass spectrometry (NanoSIMS), which reveals a comparable U isotope ratio distribution at the same spatial scale. EUV TOF's ability to assess and map isotopic heterogeneity at the nanoscale makes it a promising tool in fields such as nuclear forensics, geochemistry, and biology that could benefit from uncovering sub-microscale sources of chemical modifications.

---

\*Lydia A. Rush, John B. Cliff, Dallas D. Reilly, Andrew M. Duffin, and Carmen S. Menoni, **Isotopic Heterogeneity Imaged in a Uranium Fuel Pellet with Extreme Ultraviolet Laser Ablation and Ionization Time-of-Flight Mass Spectrometry**, *Analytical Chemistry*, **2021**, 93(2), 1016-1024.<sup>1</sup> An accompanied peer-reviewed conference proceeding to this work is also referenced in this chapter: **Imaging isotopic content at the nanoscale using extreme ultraviolet laser ablation and ionization mass spectrometry** by Lydia A. Rush, John B. Cliff, Dallas D. Reilly, Andrew M. Duffin, and Carmen S. Menoni, *International Conference on X-Ray Lasers 2020*, **2021**, 118860Z, 1-8.<sup>51</sup>

### 3.b Introduction

Material heterogeneity can provide information about a sample's composition, quality, or origin. The means for probing a material's heterogeneity depends on the analytical goal coupled with the limitations of the instrument or method being used for analysis. Measuring/mapping elemental and isotopic heterogeneity in, for example, geologic or nuclear materials often relies on mass separated atom counting (mass spectrometry), a destructive but highly sensitive technique.<sup>7,52-55</sup> When elemental or isotopic heterogeneity exists at the nanoscale ( $\leq 100$  nm), accurately mapping the material's heterogeneity with mass spectrometry is challenging because of the limited number of atoms for detection.

Current mass spectrometry techniques used for mapping elemental and isotopic content at the nanoscale include nanoscale secondary ionization mass spectrometry (NanoSIMS) using ion beam sputtering,<sup>56,57</sup> atomic probe tomography (APT) using field ion microscopy,<sup>7,58</sup> and the more recent tip-enhanced ablation-ionization mass spectrometry (TEAI-MS) using near-field effects.<sup>59,60</sup> All achieve nanoscale mapping but can struggle from limited ionization capabilities (TEAI-MS)<sup>60</sup> or complex sample preparation (APT).<sup>58</sup> SIMS is the standard for spatially resolved elemental and isotopic analysis, with NanoSIMS reaching lateral spatial resolutions (primary ion beam diameter) below 100 nm.<sup>21,61</sup> Although, more commonly, the lateral resolution is limited to a few hundred nanometers using a standard setup for positive secondary ion generation, that is, the duoplasmatron primary O<sup>-</sup> source.<sup>13</sup> Additionally, SIMS can suffer from isobaric interferences and matrix effects.<sup>16,45,62,63</sup> Another popular technique used for mapping elemental and isotopic composition is laser ablation inductively coupled plasma mass spectrometry (LA ICP-MS), which benefits from high sensitivity and fast analysis times but is limited from nanoscale mapping because of the typical  $\mu\text{m}$  sized laser spot.<sup>52,54,64</sup>

The use of a focused extreme ultraviolet laser coupled to a time-of-flight mass spectrometer (EUV TOF) offers a new path for isotopic mapping with three-dimensional (3D) nanoscale spatial resolution, as we have demonstrated in organic and inorganic solids.<sup>44,45</sup> This is achieved using a 46.9 nm

wavelength laser that can be focused down to <100 nm diameter spots (lateral spatial resolution).<sup>36</sup> The absorption depth at this wavelength is tens of nanometers in most materials, and a high ionization efficiency is produced in the relatively low temperature EUV laser-created plasmas.<sup>41,42,65</sup> Therefore, while conceptually similar to standard laser ablation mass spectrometry, EUV TOF has the advantage of ablating nanoscale-sized spots while simultaneously realizing efficient ionization (without the need of a secondary ionization source like an ICP).<sup>66,67</sup> In this sense, EUV TOF is more like NanoSIMS and is the logical choice of technique to benchmark the developing EUV TOF results for isotopic mapping at the nanoscale. In previous work, EUV TOF has shown less spectral interferences than TOF-SIMS for the analysis of NIST 611.<sup>45</sup> This work also showed that EUV TOF can accurately map  $^{235}\text{U}/^{238}\text{U}$ , isotopes relevant to uranium enrichment in nuclear materials, with ~80 nm lateral resolution in a homogeneous U particle standard (NBL, CRM U200).<sup>45</sup>

Recent studies in nuclear fuel cycle materials highlight the need for mass spectrometry techniques with high spatial resolution, such as EUV TOF, for mapping sub-microscale uranium isotopic heterogeneities to accurately identify the source of the materials.<sup>56,57,64,68</sup> In one study, Kips, et al. used NanoSIMS to investigate low enriched uranium (LEU) oxide ( $\text{UO}_2$ ) fuel particles from the 4th Collaborative Materials Exercise (CMX-4).<sup>56,69</sup> Their analyses revealed microscale distributions of  $^{235}\text{U}/^{238}\text{U}$  that were not identified by bulk analysis techniques, such as ICP-MS. Fallon, et al. and Varga, et al. revealed similar findings in CMX-5 samples using NanoSIMS and LA ICP-MS, respectively, but the latter was limited by its 5  $\mu\text{m}$  spot size.<sup>57,64</sup> Similarly, Reilly, et al. also used NanoSIMS and LA ICP-MS, amongst other MS methods, to investigate a LEU oxide fuel pellet made from one of the same sources (ES-2) in the CMX-4 studies but was prepared with a focused ion beam/scanning electron microscope (FIB/SEM) technique.<sup>68,69</sup> NanoSIMS revealed  $^{235}\text{U}/^{238}\text{U}$  heterogeneity in 1  $\mu\text{m}$  regions of interest. LA ICP-MS showed overlapping  $^{235}\text{U}/^{238}\text{U}$  variations but was limited by its 3  $\mu\text{m}$  spot size.

Expanding on these previous studies, this research aims to demonstrate the utility of EUV TOF for isotopic analyses at the nanoscale by further characterizing the  $^{235}\text{U}/^{238}\text{U}$  distribution in a

heterogeneous LEU oxide fuel pellet, made and previously investigated in Reilly et al.<sup>68</sup> Using 100 nm-sized pixels, EUV TOF maps the  $^{235}\text{U}/^{238}\text{U}$  ratio in the fuel pellets, which were made by blending two isotopically distinct feedstocks. EUV TOF results reveal a large ratio distribution in sub-micrometer- to  $\sim 1\text{--}2\ \mu\text{m}$ -sized patches across the fuel pellet. The LEU's ratio distribution measured in the 100 nm pixels is  $\sim 3\times$  larger than that measured in a homogeneous natural uranium (NU) certified reference material (CRM) and  $\sim 2\times$  larger than prior microscale and whole pellet studies had revealed. For comparison, NanoSIMS maps a similar  $^{235}\text{U}/^{238}\text{U}$  distribution across  $\sim 100\ \text{nm}$ -sized pixels. These results indicate U heterogeneity in the LEU fuel pellet from incomplete blending of the feedstock, where a more complete picture of the heterogeneity is captured with nanoscale mapping as opposed to microscale or whole pellet analyses. These results also show that an EUV laser ablation and ionization method with TOF mass spectral mapping is a promising tool for nuclear forensic studies by accurately assessing isotopic variations at the nanoscale, where sector field instruments, such as NanoSIMS, usually dominate.

### **3.c Experimental section**

#### **3.c.i Sample preparation**

The heterogeneous LEU  $\text{UO}_2$  samples mapped with EUV TOF and NanoSIMS were prepared at Pacific Northwest National Laboratory (PNNL) and are described in detail in D. D. Reilly et al.<sup>68</sup> In brief, a LEU  $\text{UO}_2$  fuel pellet nominally enriched to  $\sim 2.19\%$   $^{235}\text{U}$  was mounted in epoxy, polished, and extracted using a dual focused ion beam secondary electron microscope (FIB-SEM, FEU Helios NanoLab 660).<sup>70</sup> A FIB-SEM uses a focused beam of ions for milling sample surfaces down to the nanometer level in conjunction with an intersecting electron beam to achieve simultaneous imaging of the sample. The resulting samples were  $\sim 20\ \mu\text{m} \times 20\ \mu\text{m} \times 3.5\ \mu\text{m}$ , containing 5–10 ng of elemental U and mounted on Al planchets using Pt/C deposition. The same FIB-SEM technique was also used to prepare similarly sized samples from the certified reference material (CRM) 112-A. The CRM 112-A samples have

a natural uranium (NU) content of 0.725%  $^{235}\text{U}$  and were used as the standard in a standard-sample bracketing method for EUV TOF analysis (while NanoSIMS used a CRM U010 sample).<sup>71</sup>

Figure 3.1 shows SEM images of the LEU  $\text{UO}_2$  and CRM 112-A samples made with the FIB-SEM technique. Although outside of the scope here, the reasoning behind using a FIB-SEM for the preparation of these uranium samples was (1) to create a sample that allows bulk techniques, like TIMS and solution-based quadrupole-ICP-MS, to have some sort of spatial resolution, which is dictated by the size of the sample, and (2) to create uranium samples that are small enough and non-dispersible to allow entry into non-radiological or ultra-trace facilities.

The LEU and NU samples analyzed with the EUV TOF had been previously analyzed with large geometry (LG) SIMS, whose results are reported elsewhere.<sup>68</sup> For EUV TOF analyses, all samples were re-coated with  $\sim 100$  nm of 99.99% Au by magnetron sputtering deposition (Denton Vacuum, Desk II) to reduce charge buildup at the sample. Similarly, a 20 nm Au coating was deposited on samples investigated by NanoSIMS. SEM images were taken before and after EUV TOF and NanoSIMS analysis.

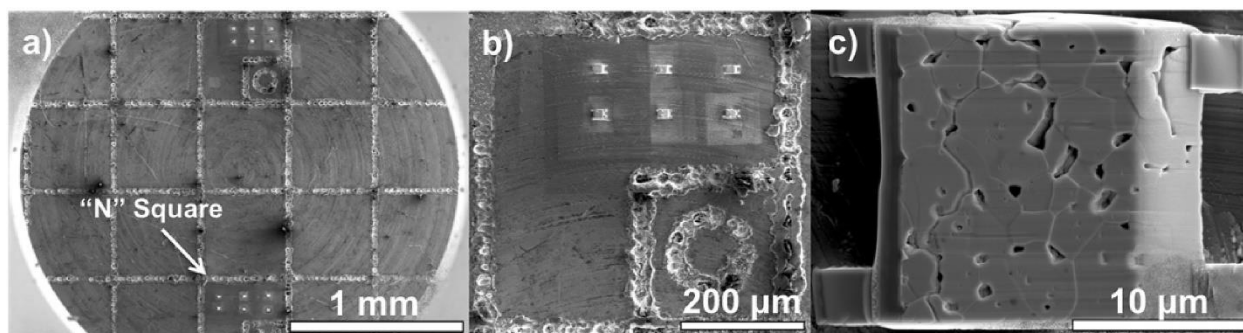


**Figure 3.1** SEM images of the mounted FIB-SEM samples. (A) Heterogenous LEU  $\text{UO}_2$  samples are in “square O” and homogenous NU CRM 112-A samples are in square “N.” (B) All six LEU samples in “square O” and (C) zoomed in image of one of the LEU samples. (Figure taken from D. D. Reilly et al.<sup>68</sup>)

### 3.c.ii EUV TOF

The EUV TOF system, built and developed at Colorado State University, is described in detail elsewhere, and a simplified diagram is shown in Figure 2.9.<sup>44,45,49</sup> In short, the system uses a compact EUV laser for ablation and ionization coupled to a TOF mass spectrometer for ion detection and analysis.

The EUV laser works through amplification of Ne-like Ar ions ( $\text{Ar}^{8+}$ ) in a highly ionized capillary discharge column, resulting in an operating wavelength of 46.9 nm (26.4 eV photon energy).<sup>34,35</sup> The laser output consists of a train of pulses with each pulse reaching an energy of up to 10  $\mu\text{J}$  and a duration of  $\sim 1.5$  ns at a repetition rate of up to 10 Hz. The laser pulse energy is controlled through a variable argon gas pressure cell. The EUV laser output is steered and collimated by two Au-coated toroidal mirrors and focused onto the sample using a zone plate lens with an outer diameter of 500  $\mu\text{m}$ , numerical aperture of 0.12, and 10% efficiency when operated in the first order.<sup>72</sup> At the zone plate location, the EUV laser beam is doughnut-shaped with a 3 mm diameter.<sup>35</sup> The zone plate is aligned on the most intense and uniform region of the beam. For mapping, the sample is moved by piezoelectric stages (Physik Instrumente, Q-Motion Precision Linear Stage Q-545.240, Germany) that can move in step sizes down to 6 nm, where the step size of the sample positioning determines the pixel size of the acquired ion map. Positive ions are extracted from the EUV laser-created plasma through the zone plate's 50  $\mu\text{m}$  central opening and accelerated into a 1 m-long TOF tube (Jordan TOF Products). The ions are subsequently detected by their time-of-arrival to a 40 mm chevron-type microchannel plate (MCP) detector (Jordan TOF Products). The analogue signal from the MCP detector is processed by a 1 channel, 12 bit, 1 GS/s digitizer (DynamicSignals (now Vitrek), EON CompuScope CS121G1).

The results described in this study were obtained using similar EUV TOF parameters described in Green, et al. for mapping micrometer-sized uranium particles with 80 nm spatial resolution.<sup>45</sup> The EUV laser was operated at 1 Hz repetition rate. The laser pulse energy was measured before and after every experiment using an Al photodiode and measured throughout the experiment using a photoionization detector, both built in-house.<sup>34,49</sup> A potential gradient between the sample, zone plate, and ground grid was used to accelerate the ions to 6 keV into the TOF tube, operated in reflectron mode for a total ion travel distance of  $\sim 2$  m. The TOF tube was kept at a pressure of  $\leq 10^{-7}$  Torr and the mass resolving power, determined previously for a similar mass range used here, was  $m/\Delta m = 1100$ .<sup>45</sup> The MCP detector was operated with a  $\sim 20$   $\mu\text{s}$  delay to exclude large signals from low mass/charge ( $m/q$ ) ions that cause detector

saturation. Single-shot mass spectra were collected by the digitizer connected to the MCP's output. The digitizer was operated with its maximum vertical offset to extend the vertical range for  $^{235}\text{U, UO}$  ( $\leq 2\%$  abundance) and  $^{238}\text{U, UO}$  ( $\geq 98\%$ ) ion collection. For optimum focusing of the 2.13 mm focal length zone plate, the U signal intensities were maximized prior to data collection. Mass calibration of the spectra was also done before every experiment using a quadratic least squares fit of known isotopes, such as Au from sample coating and U.<sup>49</sup>

The EUV TOF was used to map the  $^{235}\text{U}$  and  $^{238}\text{U}$  isotopic content in the LEU and NU samples by initially collecting 1  $\mu\text{m}$  pixels (step size) over the sample and surrounding matrix using two different fluences,  $\sim 5 \text{ J/cm}^2$  and  $\sim 1 \text{ J/cm}^2$ , with mapping field sizes of  $50 \mu\text{m} \times 50 \mu\text{m}$  and  $30 \mu\text{m} \times 30 \mu\text{m}$ , respectively. Because the ablated crater volume is dependent on the EUV laser fluence, the isotope maps collected on the LEU sample with 100 nm pixels over a  $\sim 20 \mu\text{m} \times 1 \mu\text{m}$  area were acquired using a fluence of  $< 1 \text{ J/cm}^2$ .<sup>44</sup> These are laser conditions previously used to produce craters in resist with a full width at half maximum diameter of  $\leq 400 \text{ nm}$  and a depth  $\leq 40 \text{ nm}$  with the zone plate in the first order.<sup>44</sup> For inorganic materials with a higher ablation threshold than resist, the ablated spots can have a significantly smaller diameter and depth. This makes it possible to displace the sample in steps smaller than the beam diameter to obtain a distinct mass spectrum at each step/pixel.<sup>45</sup> Because the lateral resolution was not independently measured here (for either the EUV TOF or NanoSIMS), spot size and pixel size are not used interchangeably in this study. Nonetheless, isotopic information collected with 100 nm pixels could be resolved pixel by pixel. For all maps, three EUV laser shots were taken at each pixel location. The integrated number of counts for the  $^{235,238}\text{U}$  and  $^{235,238}\text{U}^{16}\text{O}$  isotopes collected at each location were summed to a single pixel (indicated hereafter as “summed U”).<sup>45,73</sup> The pixels of the resulting EUV TOF ion maps were not smoothed to show the isotopic information in each pixel. Mass bias corrections were not made to the EUV TOF data because the measured ratios from the NU CRM followed the expected ratio within analytical error. Table 3.1 lists the main EUV TOF conditions for the mapping analyses of the LEU  $\text{UO}_2$  and NU samples.

**Table 3.1** EUV TOF experimental parameters used for collecting the low and high spatial resolution isotope maps on the LEU UO<sub>2</sub> and NU CRM samples.

<b>EUV TOF Parameters</b>	<b>Low Spatial Resolution Map</b>	<b>High Spatial Resolution Map</b>
<b>Repetition rate</b>	1 Hz	1 Hz
<b>Fluence</b>	~5 to 1 J/cm <sup>2</sup>	<1 J/cm <sup>2</sup>
<b>Shots/spot</b>	3	3
<b>Step size (i.e., pixel size on map)</b>	1 μm	100 nm
<b>Mapping field size</b>	30 μm x 30 μm / 50 μm x 50 μm	19 μm x 1 μm
<b>Total number of shots</b>	2,700 / 7,500	5,700
<b>Time/map</b>	~45 min. / ~2 hrs	~1.5 to 2 hrs.
<b>Isotopes used in ratio</b>	<sup>235</sup> U, <sup>238</sup> U, <sup>235</sup> U <sup>16</sup> O, <sup>238</sup> U <sup>16</sup> O	
<b>Detector type</b>	Chevron-type microchannel plate	
<b>Vertical scale of digitizer</b>	+10 V (+5V offset applied for increased dynamic range)	

For EUV TOF <sup>235</sup>U/<sup>238</sup>U ratio analysis, all mass spectra were subjected to an automated threshold test using scripts written in Igor Pro that were used to identify and remove data with insufficient or saturated U signals. The low threshold was chosen for the <sup>238</sup>U and <sup>238</sup>U<sup>16</sup>O ion amplitudes such that it is statistically likely to observe ≥1 ion of <sup>235</sup>U and <sup>235</sup>U<sup>16</sup>O based on the average isotope concentration. The high threshold is set slightly below the digitizer's upper dynamic range. Both the elemental (U) and oxide (U<sup>16</sup>O) peaks in each spectrum must pass the threshold to be included in the ratio analysis, and the background subtracted area of each peak is subsequently calculated. Random and infrequent fluctuations in the background can produce negative integrated areas for <sup>235</sup>U and <sup>235</sup>U<sup>16</sup>O signals after background subtraction. Here, this resulted in negative U ratios, which were kept in all subsequent isotope plots so that the resulting ratio would not be unintentionally biased. The integrated analog signal (in units of V × s) is then converted to ion counts using the MCP's gain, resulting in continuous data (unlike the discrete data produced by pulse counting detectors used in NanoSIMS). The gain of the EUV TOF MCP detector was calculated by plotting and fitting the resulting Gaussian distribution of U and U<sup>16</sup>O signals that correspond to zero- and single-ion events, as previously shown.<sup>44,45,49</sup> In this study, a single-ion count correlates to ~4 mV on the MCP, resulting in a gain of approximately 5 × 10<sup>5</sup> electrons/ion.

### 3.c.iii NanoSIMS

NanoSIMS U isotopic mapping was performed using a CAMECA 50L ion microprobe located at the Environmental Molecular Sciences Laboratory at Pacific Northwest National Laboratory. Conditions for NanoSIMS isotopic mapping of the LEU sample has been previously described in detail by D. D. Reilly, et al.<sup>68</sup> In brief, prior to mapping analyses, the LEU sample was pre-sputtered with  $\sim 2 \times 10^{16}$  ion/cm<sup>2</sup> using a 16 keV O<sup>-</sup> primary beam. For mapping, a 2–4 pA O<sup>-</sup> primary beam with a diameter of  $\sim 300$  nm scanned over a  $30 \mu\text{m} \times 30 \mu\text{m}$  sample area using 98 nm-sized pixels (256  $\times$  256 pixel array). That is, the primary ion beam spot size was larger than the pixel size. The resulting positively charged secondary ions were accelerated to 8 keV, and the isotopes of interest were accessed through magnetic peak switching and detected using electron multipliers. <sup>235</sup>U and <sup>235</sup>U<sup>16</sup>O were acquired in one cycle, and <sup>238</sup>U and <sup>238</sup>U<sup>16</sup>O were acquired in the next cycle using two separate detectors at each magnetic field. Each cycle was repeated eight times, for a total of eight stacked map frames. Maps were processed using the Fiji distribution of the ImageJ plugin OpenMIMS [<https://nano.bwh.harvard.edu/openmims>]. The ion counts detected in each layer were dead time-corrected pixel by pixel, and individual map frames were aligned and summed together to a single map consisting of 98 nm pixels. Like EUV TOF, the pixels in the NanoSIMS ion maps were not smoothed. For ratio analyses, all U signals were subjected to a threshold like that applied for EUV TOF data. Zero U ion counts were kept in NanoSIMS' ratio analysis for the same reason negative U signals were included in the EUV TOF analysis. Table 3.2 lists the main NanoSIMS conditions for the mapping analyses of the LEU UO<sub>2</sub> sample.

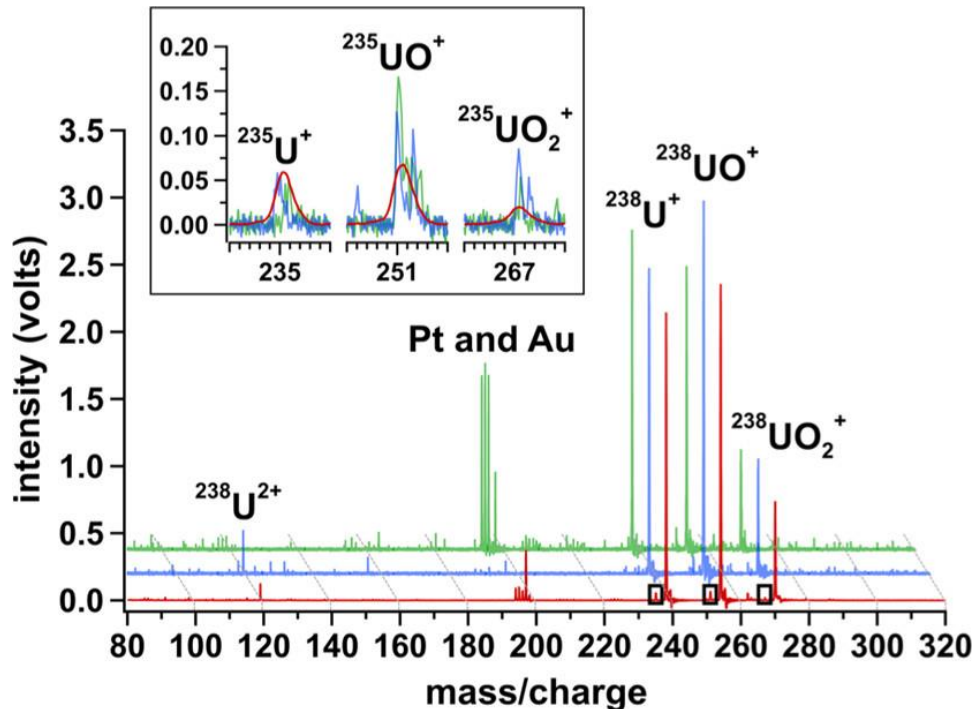
**Table 3.2** NanoSIMS experimental parameters used for collecting the high spatial resolution isotope maps on the LEU UO<sub>2</sub> sample.

NanoSIMS Parameters	High Spatial Resolution Map
Primary ion beam	O <sup>-</sup>
Beam current	2-4 pA
Beam diameter	$\sim 300$ nm
Pixel size	98 nm
Mapping field size	$\sim 30 \mu\text{m} \times 30 \mu\text{m}$
# Cycles	8
Total number of pixels/cycle	65,536
Time/map	N/A
Isotopes used in ratio	<sup>235</sup> U, <sup>238</sup> U, <sup>235</sup> U <sup>16</sup> O, <sup>238</sup> U <sup>16</sup> O
Detector type	Electron multipliers

### 3.d Results and discussion

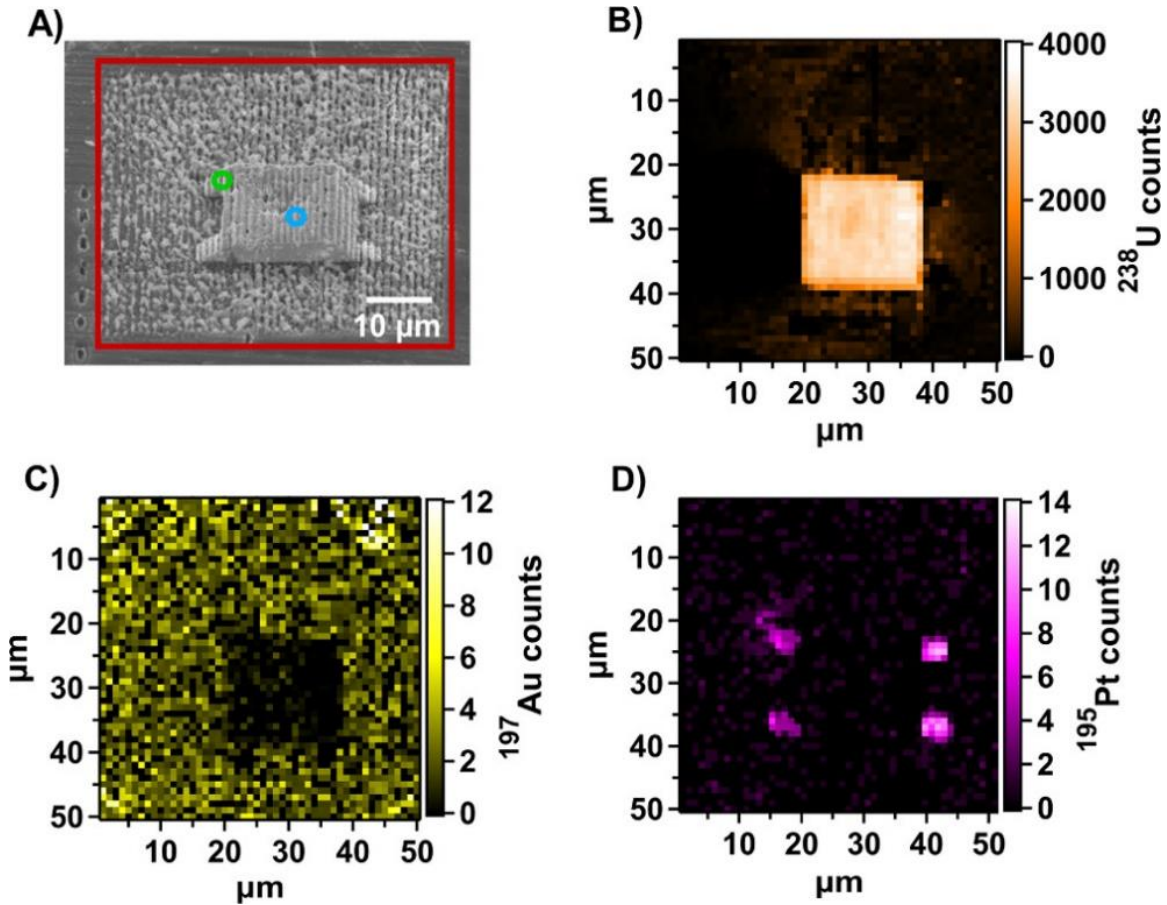
#### 3.d.i EUV TOF elemental analysis

Figure 3.2 shows an EUV TOF mass spectrum averaged from hundreds of EUV laser shots on the LEU sample and surrounding area alongside two single-shot spectra collected at different LEU sample locations. Alongside the expected  $^{235}\text{U}^+$  and  $^{238}\text{U}^+$  elemental signals, the single and double oxide species ( $\text{U}^{16}\text{O}^+$  and  $\text{U}^{16}\text{O}_2^+$ ) for both isotopes are also present. The U and UO species are produced in approximately equal amounts, while the  $\text{UO}_2$  species is much less prevalent.<sup>45</sup> For this reason, the double oxide species were excluded from subsequent U isotopic analyses. Additionally,  $^{238}\text{U}^{2+}$  is also detected alongside the major isotopes for Au ( $^{197}\text{Au}^+$ ) (conductive coating) and Pt ( $^{194}\text{Pt}^+$ ,  $^{195}\text{Pt}^+$ ,  $^{196}\text{Pt}^+$ , and  $^{198}\text{Pt}^+$ ) (FIB attachment tabs) from magnetron sputtering and sample mounting depositions, respectively.



**Figure 3.2** Waterfall plot comparison of average (red) and single shot (blue and green) EUV TOF mass spectra (intensity in volts plotted as a function of mass/charge). The red spectrum shows the average across the LEU sample and surrounding area. The single-shot spectra are extracted from a position on the Pt mounting tab (green) and in the center of the LEU pellet (blue). The relative sample location for each spectrum is identified in Figure 3.3. The inset plot shows overlapping signals of the  $^{235}\text{U}$  species with the spectral position identified by black boxes.

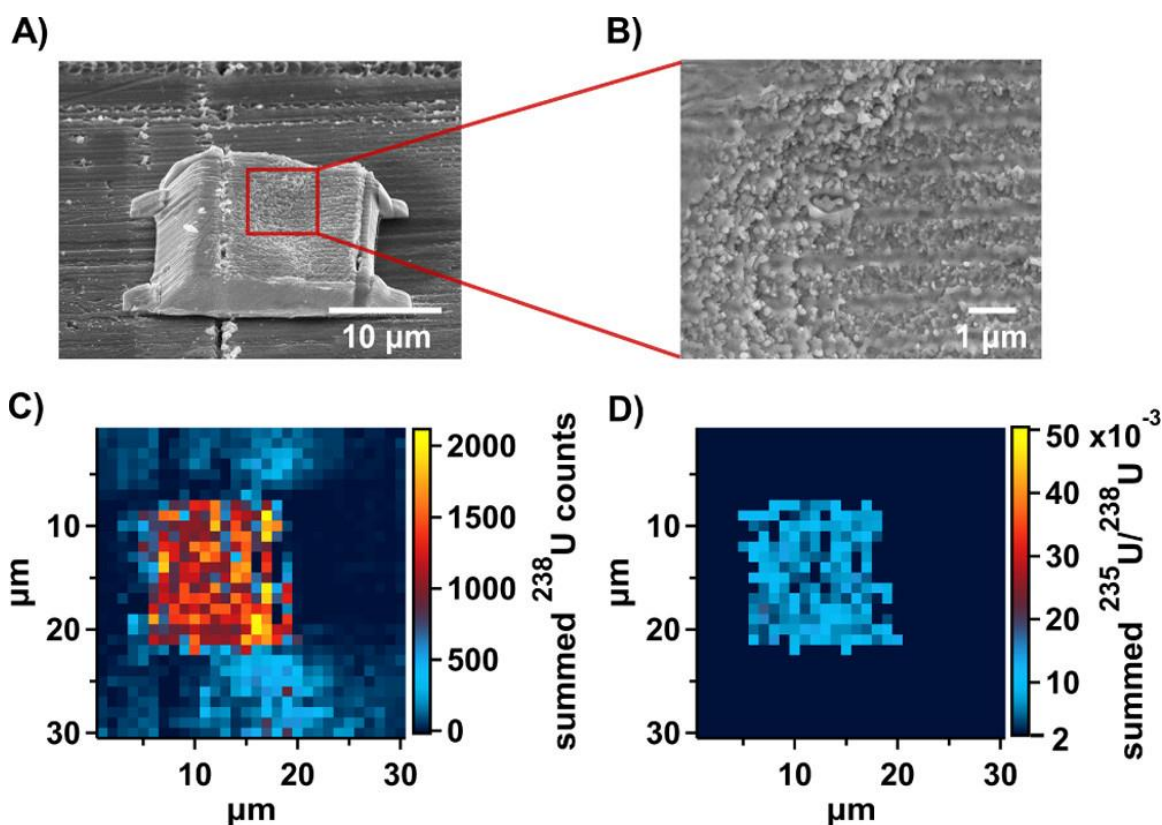
The full mass spectra collected at each laser shot with the EUV TOF system allow for the creation of isotope maps. Figure 3.3A shows an SEM image of the LEU UO<sub>2</sub> sample after EUV ablation at a laser fluence of  $\sim 5 \text{ J/cm}^2$ . Figure 3.3B–D shows corresponding  $50 \text{ }\mu\text{m} \times 50 \text{ }\mu\text{m}$  isotope maps, where the ion intensities are converted from volts to counts using the process described in the sections above. The maps in Figure 3.3B–D show the distribution of <sup>238</sup>U, <sup>197</sup>Au, and <sup>195</sup>Pt in the FIB sample vicinity with concentrations localized in the LEU pellet, Au coating, and Pt tabs, respectively. There is also a faint U signal surrounding three sides of the pellet plotted in Figure 3.3B. This peripheral signal is likely indicative of redeposition associated with the prior LG-SIMS sputtering analysis. The Pt map in Figure 3.3D shows potential artifacts of redeposition as well. Figure 3.3C shows Au most concentrated around the LEU sample, regardless of the entire sample having been Au-coated. This pattern in the Au map can be explained by considering the different vertical positions of the background and FIB sample and the effect this has on the EUV beam's spot size. The FIB sample is vertically raised  $\sim 3 \text{ }\mu\text{m}$  from the background, and the EUV beam can be slightly defocused when the zone plate is not within  $\pm 3 \text{ }\mu\text{m}$  of its focal length.<sup>49</sup> This results in a focused EUV beam on the sample and a less focused beam on the background. The less focused beam maintains enough energy for ablation but removes more gold per shot on the background from the larger spot size. Overall, Figure 3.3 illustrates the advantage of using EUV laser ablation and ionization with TOF mass spectral mapping by showing that EUV TOF can map the distribution of multiple elements/isotopes over a wide mass range at each laser shot.



**Figure 3.3** (A) SEM image at 45° of a LEU sample after high-energy EUV laser ablation over a 50  $\mu\text{m} \times 50 \mu\text{m}$  area with 1  $\mu\text{m}$  steps between each ablation spot. (B–D) Corresponding EUV TOF 50  $\mu\text{m} \times 50 \mu\text{m}$  isotope maps of (B)  $^{238}\text{U}$ , (C)  $^{197}\text{Au}$ , and (D)  $^{195}\text{Pt}$  plotted as ion counts. The pixel size (i.e., step size) for (B–D) is 1  $\mu\text{m}$ . The red square in (A) represents the hundreds of laser shots used for the red averaged mass spectrum in Figure 3.2. Similarly, the green and blue circles represent the relative locations of the correspondingly colored single-shot spectra in Figure 3.2. The pixels in the elemental maps are not smoothed or interpolated.

### 3.d.ii EUV TOF analysis of a homogenous NU CRM

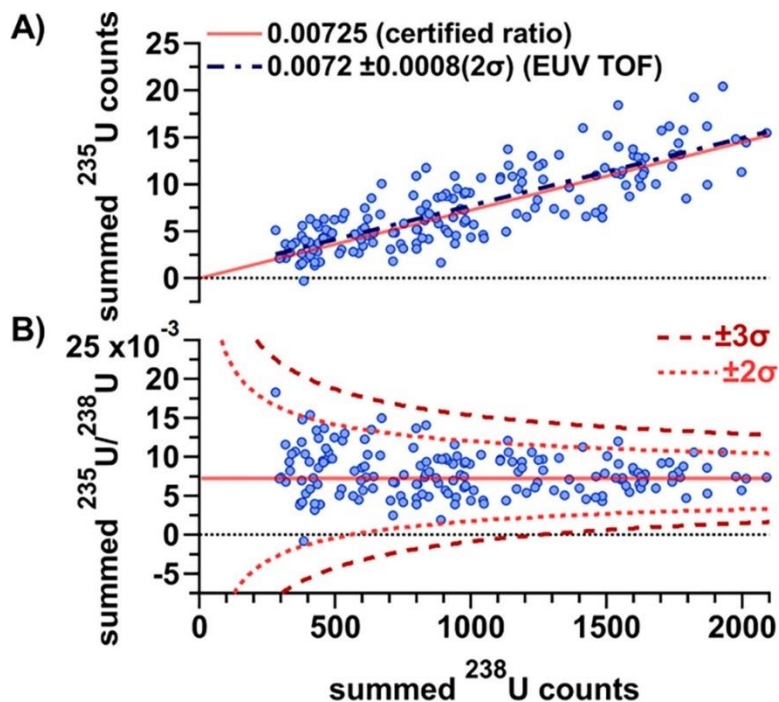
The homogeneous NU CRM was analyzed alongside the heterogeneous LEU  $\text{UO}_2$  fuel pellet to measure EUV TOF's instrumental response for assessing isotopic heterogeneity. Figure 3.4A,B shows SEM images of the NU sample, made using the same FIB/SEM technique as the LEU sample, post-EUV low-energy ablation using a fluence of  $\sim 1 \text{ J/cm}^2$ . Figure 3.4C,D shows corresponding 30  $\mu\text{m} \times 30 \mu\text{m}$  summed (i.e., U + UO)  $^{238}\text{U}$  isotope and  $^{235}\text{U}/^{238}\text{U}$  ratio maps with 1  $\mu\text{m}$  pixels. All U and UO signals were included in the isotope map in Figure 3.4C but prior to summation for ratio analyses, these ions were subjected to a minimum and maximum threshold described in earlier sections.



**Figure 3.4** (A,B) SEM images of the NU CRM after low-energy EUV ablation of a  $30\ \mu\text{m} \times 30\ \mu\text{m}$  area with  $1\ \mu\text{m}$  steps. The image in (A), taken at  $45^\circ$ , shows the entire ablated region (larger ablation spots in and around the sample are from a separate high-fluence laser scan) and (B), taken at  $18,000\times$  magnification, further highlights each crater in the ablated rows. (C,D) Corresponding EUV TOF  $30\ \mu\text{m} \times 30\ \mu\text{m}$  (C)  $^{238}\text{U}$  isotope and (D)  $^{235}\text{U}/^{238}\text{U}$  ratio maps of the ablated NU CRM and surrounding area. The pixel/step size for (C,D) is  $1\ \mu\text{m}$ . The pixels in the isotope and ratio maps are not smoothed or interpolated.

Unlike the more qualitative isotope maps in Figure 3.3, the maps in Figure 3.4 were collected using a lower laser fluence so that (1) both  $^{235}\text{U, UO}$  and  $^{238}\text{U, UO}$  isotopes were within the instrument's dynamic range for accurate isotope ratio calculations and (2) to keep the ablated spot size diameter to about  $1\ \mu\text{m}$ , the pixel size.<sup>44,45</sup> Although, as can be seen in Figure 3.4B, the ablated craters appear to have spot sizes  $<1\ \mu\text{m}$  in diameter. Keeping the isotopic signal within the instrument's dynamic range is especially challenging for the analysis of NU because of the low  $^{235}\text{U, UO}$  content ( $\sim 0.7\%$ ) and high  $^{238}\text{U, UO}$  content ( $\sim 99\%$ ). Nevertheless, the isotope ratio map of the NU CRM in Figure 3.4D shows a relatively uniform  $^{235}\text{U}/^{238}\text{U}$  distribution across the sample area, as expected. Figure 3.5 shows the same ratio data used to generate the map in Figure 3.4D as a two-isotope plot and a ratio plot against ion intensity. Based on the slope of the linear best fit line through the two-isotope plot in Figure 3.5A, the average

$^{235}\text{U}/^{238}\text{U}$  ratio is  $0.0072 \pm 0.0008$  ( $2\sigma$ ). The expected U ratio of the NU CRM is  $0.00725$ .<sup>71</sup> Because the measured ratio agrees with the certified ratio within analytical error, no mass bias corrections were made to the EUV TOF measurements.



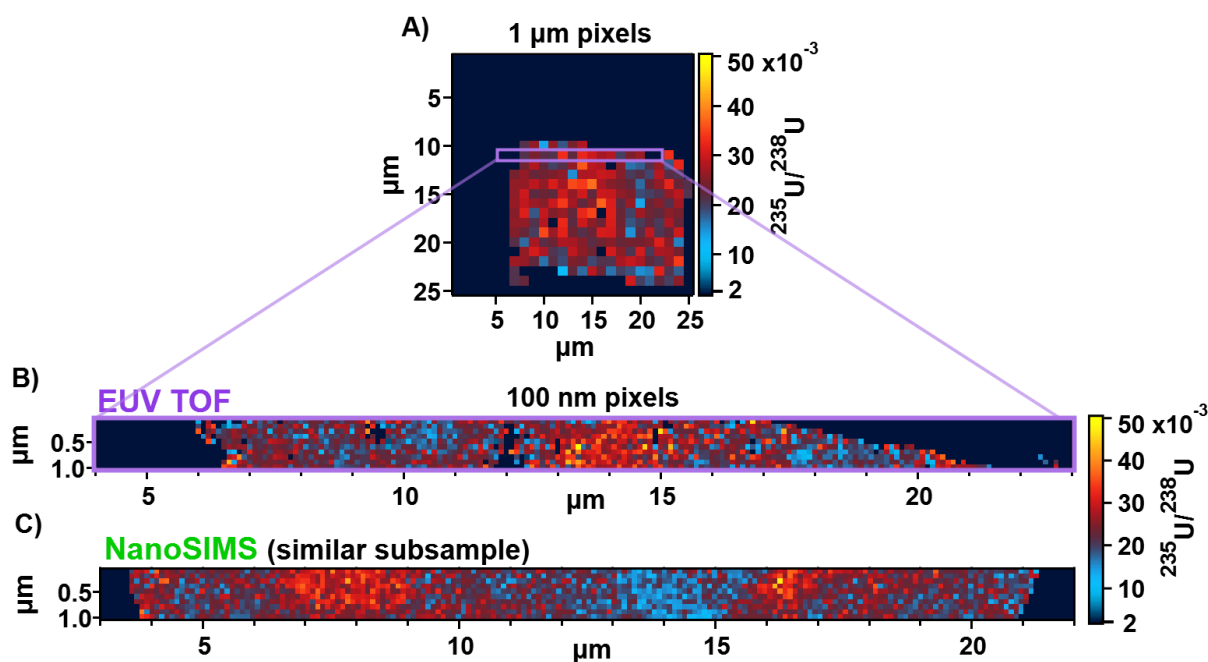
**Figure 3.5** Uranium (A) two-isotope and (B) ratio plots using the NU CRM data from the EUV TOF maps in Figure 3.4. (A)  $^{235}\text{U}$  counts plotted as a function of  $^{238}\text{U}$  counts with the dark blue dotted line representing the best-fit line (average  $^{235}\text{U}/^{238}\text{U}$  ratio) through the data, whose value is given in the legend. (B)  $^{235}\text{U}/^{238}\text{U}$  ratio plotted as a function of  $^{238}\text{U}$  counts, where the red dotted lines represent the theoretical  $\pm 2\sigma$  and  $\pm 3\sigma$  uncertainty derived from the ion intensities. The red solid line in both plots is the certified  $^{235}\text{U}/^{238}\text{U}$  ratio of the NU CRM, whose value is also given in the legend.

Figure 3.5B plots the isotope ratio along with the expected ratio's  $\pm 2\sigma$  and  $\pm 3\sigma$  uncertainty at the corresponding  $^{238}\text{U}$  ion counts (counting statistics uncertainty). Figure 3.5B shows that most points fall within  $\pm 2\sigma$  of the expected uncertainty and all points are within  $\pm 3\sigma$ , demonstrating that the measured variability does not exceed what is expected based on the number of atoms detected. This provides high confidence that data points outside of the counting statistics uncertainty envelope would arise from isotopic heterogeneity rather than instrumental uncertainty. Error bars are not shown on the individual points in Figure 3.5B for clarity but would be the width of the  $\pm 2\sigma$  or  $\pm 3\sigma$  brackets at the respective  $^{238}\text{U}$  counts. The accuracy of both the average and individual NU ratios by the EUV TOF is significant for a TOF instrument,

especially considering the relatively low number of counts and overall points used in the analysis.<sup>74</sup> The low number of counts is because of the minimal crater volume that is being probed, which is on the order of a few tens of attoliters using a EUV laser fluence of  $\sim 1 \text{ J/cm}^2$ .<sup>44</sup>

### **3.d.iii EUV TOF and NanoSIMS analyses of LEU sample**

The EUV TOF initially mapped the LEU  $\text{UO}_2$  sample over a  $25 \mu\text{m} \times 25 \mu\text{m}$  area using  $1 \mu\text{m}$  pixels.<sup>51</sup> This was followed by mapping a smaller  $19 \mu\text{m} \times 1 \mu\text{m}$  sub-section of the same sample using  $100 \text{ nm}$  pixels at a fluence of  $< 1 \text{ J/cm}^2$  to identify potential sub-microscale and microscale sized  $^{235}\text{U}/^{238}\text{U}$  heterogeneities from isotopic mixing processes that were not fully identifiable at the  $1 \mu\text{m}$  scale.<sup>68,69</sup> NanoSIMS mapped the entire area of another LEU  $\text{UO}_2$  sub-sample made from the same batch as the one analyzed with the EUV TOF with  $98 \text{ nm}$  sized pixels. A randomly selected  $19 \mu\text{m} \times 1 \mu\text{m}$  area was selected from the area mapped with NanoSIMS to match the size of the nanoscale map collected with the EUV TOF for comparison. Figure 3.6 shows the resulting isotope ratio maps collected on the LEU  $\text{UO}_2$  sample with the EUV TOF using  $1 \mu\text{m}$  and  $100 \text{ nm}$  sized pixels; the NanoSIMS map collected with  $98 \text{ nm}$  pixels is also shown. For clarity, all LEU ratio maps are plotted on the same color scale between  $0.002$  and  $0.050$  because most ratios fall within this range (the map in Figure 3.4D of the NU CRM is also plotted on the same scale).



**Figure 3.6** (A-B) EUV TOF  $^{235}\text{U}/^{238}\text{U}$  ratio maps of the LEU  $\text{UO}_2$  sample mapped with (A) 1  $\mu\text{m}$  and (B) 100 nm sized pixels. The 100 nm pixel map was collected over a small 19  $\mu\text{m}$  x 1  $\mu\text{m}$  section of the same sample mapped with 1  $\mu\text{m}$  pixels (highlighted with a purple rectangle in A). (D) NanoSIMS  $^{235}\text{U}/^{238}\text{U}$  ratio map of a different 19  $\mu\text{m}$  x 1  $\mu\text{m}$  section of an LEU  $\text{UO}_2$  sample mapped with 98 nm pixels. All  $^{235}\text{U}/^{238}\text{U}$  ratios are “summed  $^{235}\text{U}/^{238}\text{U}$ ” (i.e., U + UO). The pixels in all ratio maps are not smoothed or interpolated. (Figure adapted from L. Rush, et al.<sup>1,51</sup>)

While the EUV TOF and NanoSIMS mapped different locations on the LEU pellets, Figure 3.6B-C shows that both techniques mapped comparable sized areas of  $^{235}\text{U}/^{238}\text{U}$  heterogeneity that range from  $<1$   $\mu\text{m}$  to a few micrometers, with the most pronounced heterogeneity found in  $\sim 1$ – $2$   $\mu\text{m}$ -sized areas. This implies that on a 100 nm spatial scale, the isotopic mixing of the starting materials, likely micrometer-sized oxide powders, was mostly successful, but that sections remain that are representative of the individual feedstock material.<sup>56</sup> On the 1  $\mu\text{m}$  map collected with the EUV TOF, heterogeneous areas are also detected but with much less resolution than the map collected at the nanoscale. These findings are in line with prior microscale mapping studies on the same FIB samples using NanoSIMS and LA ICP-MS as well as on similar samples from the same source also using NanoSIMS.<sup>56,68</sup> The maps in Figure 3.6, however, represent the first analysis performed on these types of samples at the nanoscale using the EUV TOF technique, and reveal additional sub-micrometer features not previously observed.

While the isotope maps in Figure 3.6 give some indication that the unmixed (feedstock) components might be resolvable at the 100 nm scale, statistical analysis of the data reveals a single isotope ratio distribution. Figure 3.7 plots the distribution of the LEU UO<sub>2</sub> ratio data measured with EUV TOF and NanoSIMS using 100 nm pixels as two-isotope and ratio plots against ion intensity. The expected <sup>235</sup>U/<sup>238</sup>U ratio used in Figure 3.7,  $0.0226 \pm 0.0006$  ( $2\sigma$ ), is the aggregated ratio from NanoSIMS, LG-SIMS, LA ICP-MS, quadrupole-ICP-MS, and TIMS analyses on multiple LEU UO<sub>2</sub> sample pellets.<sup>68</sup> The elemental (U), oxide (UO), and summed (U + UO) species are each plotted separately for comparison. There are more NanoSIMS data in these plots because results from the entire sample area were used, while EUV TOF data were generated from the smaller sample area mapped in Figure 3.6A. The analysis in Figure 3.7 demonstrates that when the mapped data are plotted together, the <sup>235</sup>U/<sup>238</sup>U isotope ratios in the micron-sized mixed areas statistically dominate the smaller unmixed domains. The ratios in the unmixed domains therefore cannot be separated/resolved, and a single isotope ratio distribution prevails. However, this distribution is indicative of U heterogeneity as it is much more varied than what can be expected (and measured) for a homogeneous sample, such as the NU CRM.

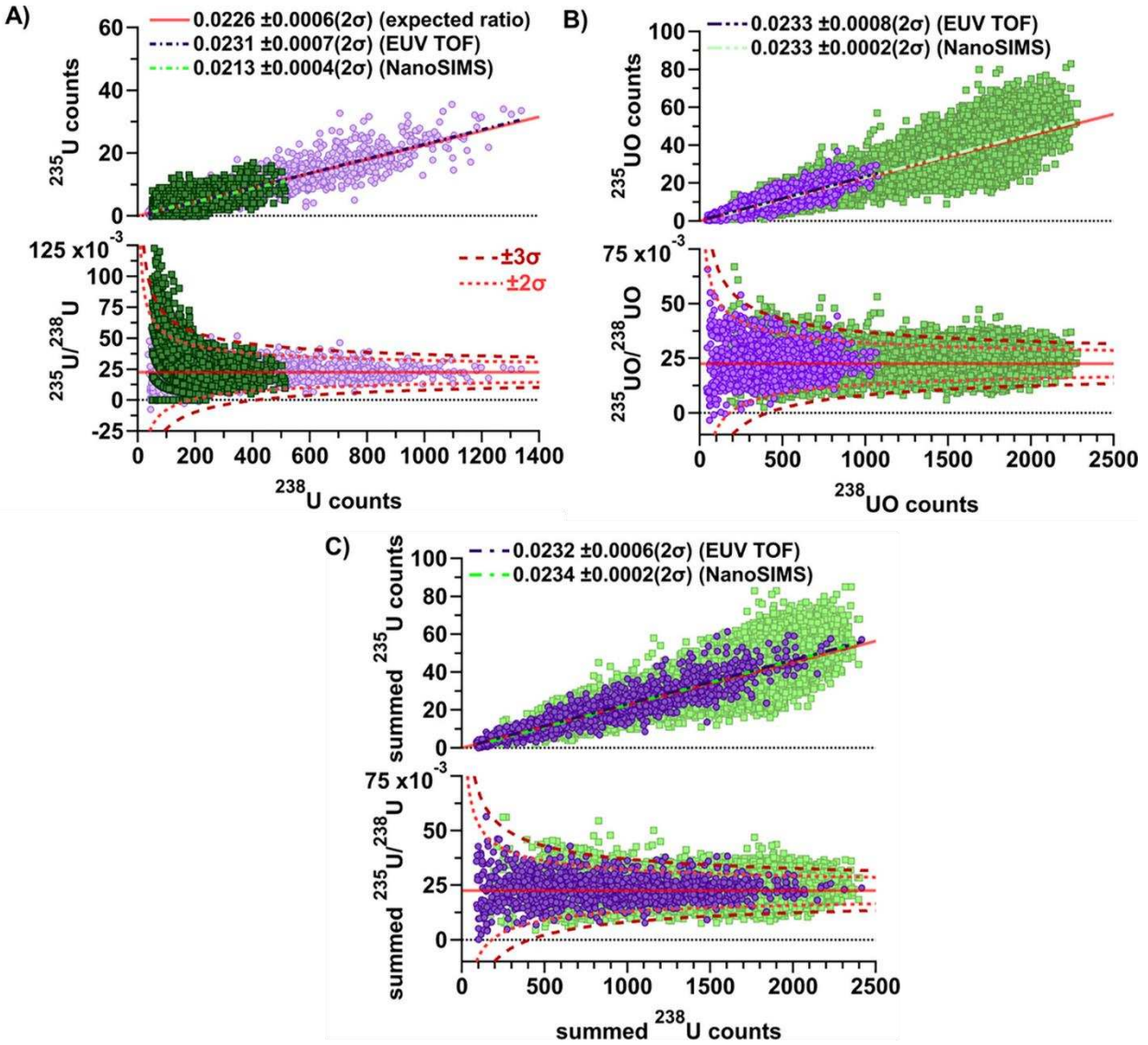


**Figure 3.7** (A–C) Uranium two-isotope and ratio plots for (A) U, (B) UO, and (C) U + UO ion species using the LEU data collected with 100 nm pixels by the EUV TOF (purple) and NanoSIMS (green). The top plots in A–C are  $^{235}\text{U}$  ion counts plotted as a function of  $^{238}\text{U}$  counts for each U species. The dotted purple and green lines represent the best-fit line (average ratio) through the EUV TOF and NanoSIMS data, respectively. The bottom plots in A–C are the  $^{235}\text{U}/^{238}\text{U}$  ratio plotted as a function of  $^{238}\text{U}$  ion counts for each species. The red dotted lines represent the  $\pm 2\sigma$  and  $\pm 3\sigma$  uncertainty from the expected (aggregate) ratio represented by the red solid line in all plots.

In contrast to the analysis in Figure 3.5 that shows all NU ratios in the CRM to agree within  $\pm 3\sigma$  of the expected value, Figure 3.7 shows a wider distribution of  $^{235}\text{U}/^{238}\text{U}$  content measured on the LEU sample with EUV TOF and NanoSIMS that deviate outside of the LEU sample’s expected uncertainty. This indicates that statistically significant heterogeneity was seemingly detected by both techniques. However, further analyses would have to be performed to resolve those statistically significant points due to the width

of the error bars overlapping the  $\pm 3\sigma$  uncertainty envelope. Nonetheless, it is promising that these outlying points were detected at high ion counts and that the EUV TOF and NanoSIMS points overlap with one another. Because the NanoSIMS data were taken over the whole sample area, more instances of heterogeneity are detected, that is, more points fall outside  $\pm 3\sigma$  of the expected value. The two isotope plots in Figure 3.7 also indicate multiple slopes (isotope ratios) in the data produced by the points diverging from the origin (0,0) as the U intensity increases. A homogeneous material would be expected to show the opposite trend in a two-isotope plot, that is, a decrease in the spread of data points around a single isotope ratio with increasing ion counts. The trend in Figure 3.7, indicating at least two isotope ratios in the data, further confirms that the LEU sample has U heterogeneity.

Reilly, et al. showed that for similarly prepared sections of LEU  $\text{UO}_2$  samples, whole pellet and microscale analyses provide a limited picture of U heterogeneity.<sup>68</sup> For whole pellet analyses, the LEU  $\text{UO}_2$  samples provided indications of  $^{235}\text{U}/^{238}\text{U}$  heterogeneity even when the whole pellet was consumed with bulk MS methods (i.e., TIMS and solution ICP-MS). However, the spatial distribution of the heterogeneity was limited by the size of the pellet. Similarly, when the  $^{235}\text{U}/^{238}\text{U}$  ratios across all 100 nm pixels from EUV TOF and NanoSIMS analyses are averaged to replicate “whole pellet” analysis, the variations of the ratios and their spatial distribution are lost. The average EUV TOF and NanoSIMS summed  $^{235}\text{U}/^{238}\text{U}$  ratios are  $0.0232 \pm 0.0006$  ( $2\sigma$ ) and  $0.0234 \pm 0.0002$  ( $2\sigma$ ), respectively (Figure 3.7C). This shows that when the LEU pellet’s isotopic content is analyzed using larger pixels or on the whole pellet scale, important features of the heterogeneity are averaged out, which is also shown in Figure 3.6C. It is worth noting that the average  $^{235}\text{U}/^{238}\text{U}$  ratio measured by EUV TOF from the small subsection of the LEU  $\text{UO}_2$  sample unexpectedly agrees with the aggregate ratio of  $0.0226 \pm 0.0006$  ( $2\sigma$ ). This indicates that the subsection of the LEU pellet sampled by the EUV TOF using 100 nm pixels contained heterogeneity representative of the larger sample and that the isotopic domains remaining after incomplete mixing are likely evenly dispersed across the pellet. The average  $^{235}\text{U}/^{238}\text{U}$  ratio measured with NanoSIMS also agrees with the aggregate value, which is to be expected because data were taken over the entire sample area.

When the EUV TOF used 1  $\mu\text{m}$ -sized pixels to map the entire LEU pellet (Figure 3.6A), the resulting isotope ratio distribution was  $\sim 2\times$  smaller than that obtained with 100 nm pixels. Figure 3.8 plots the LEU ratio distributions mapped with 100 nm and 1  $\mu\text{m}$  pixels alongside the NU CRM ratio distribution as histograms, fitted with a Gaussian. The histograms show that the EUV TOF's 1  $\mu\text{m}$  pixel analysis of the LEU sample has a larger ratio distribution than the NU CRM, indicating some heterogeneity in the LEU pellet, where the width of the fitted NU and LEU ratio distributions are 0.018 and 0.025, respectively. EUV TOF and NanoSIMS' 100 nm pixel analyses, however, reveal even more heterogeneity in the LEU sample with a ratio distribution  $>0.05$  for both techniques. Table 3.3 lists other microscale analyses that were performed in different studies on the same LEU source material using NanoSIMS and fs-LA-ICP-MS.<sup>56,68</sup> These microscale analyses show a  $\sim 0.01$  to  $\sim 0.03$  wide isotope ratio distribution that is similar to EUV TOF's 1  $\mu\text{m}$  pixel analysis. These results further demonstrate that a beam or pixel size on the order of a micron or more can average over  $\mu\text{m}$  and sub-micrometer-sized domains of heterogeneity. EUV TOF and NanoSIMS 100 nm analyses, therefore, indicate that the LEU sample contains microscale and sub-microscale U heterogeneity that requires high spatial mapping for identification. Separately, it is also significant that EUV TOF shows similar mapping capabilities with NanoSIMS, making it a viable option for other isotopic investigations that require high spatial mapping mass spectrometry.

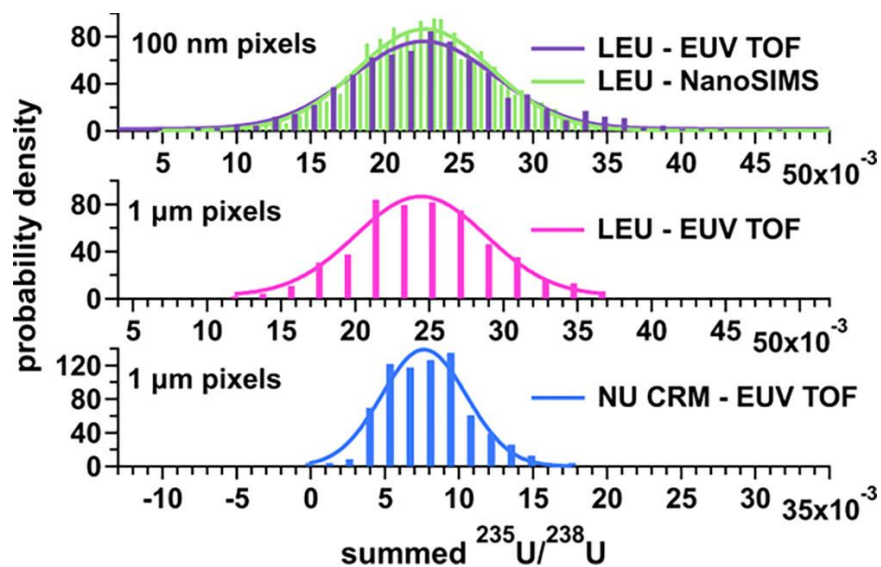


**Figure 3.8** Probability density (normalized) plotted as a function of the  $^{235}\text{U}/^{238}\text{U}$  ratio for EUV TOF and NanoSIMS. The data were obtained from the analysis of the 100 nm (top) and 1  $\mu\text{m}$  (middle) pixel LEU sample maps. Similar analysis for the NU CRM, 1  $\mu\text{m}$  pixel maps is shown at the bottom. The LEU data from the 100 nm pixel maps are the same data plotted in Figure 3.7, while the NU data are taken from Figure 3.5. The histograms were made according to the Freedman–Diaconis rule, where the number and width of bins directly corresponds to the amount of data and are fitted with a Gaussian distribution.

**Table 3.3** Compilation of different mapping analyses performed on the ES-2 sample (i.e., the LEU  $\text{UO}_2$  sample) from the 4<sup>th</sup> Collaborative Materials Exercise (CMX-4).

LEU $\text{UO}_2$ Sample (ES-2, CMX-4)				
Technique	Sample Preparation	Pixel size	$^{235}\text{U}/^{238}\text{U}$ distribution	Width of $^{235}\text{U}/^{238}\text{U}$ distribution
EUV TOF <sup>1</sup>	FIB	100 nm	~0.002 – 0.050	0.055
NanoSIMS <sup>1</sup>	FIB	100 nm	~0.005 – 0.050	0.051
NanoSIMS <sup>56</sup>	Solid fragments in epoxy	N/A (700 nm beam diameter)	0.008 – 0.035	0.027
EUV TOF <sup>1</sup>	FIB	1 $\mu\text{m}$	0.012 – 0.037	0.025
NanoSIMS <sup>68</sup>	FIB	1 $\mu\text{m}$ (ROIs)	0.013 – 0.033	0.020
fs-LA-ICP-MS <sup>68</sup>	FIB	3 $\mu\text{m}$	0.014 – 0.024	0.010
NanoSIMS <sup>68</sup>	FIB	2-5 $\mu\text{m}$ (ROIs)	0.018 – 0.027	0.009

### 3.d.iv EUV TOF and NanoSIMS comparison

Alongside identifying similar isotopic distributions in the LEU sample at the nanoscale, EUV TOF and NanoSIMS also detected similar total counts of U isotopes from the respective ablation and sputtering processes. Although we did not measure the sample utilization efficiency using the samples investigated here, prior studies have measured EUV TOF's efficiency to be 0.014% for  $^{238}\text{U}$ .<sup>45</sup> Small geometry SIMS achieves  $\sim 2 \times 10^{-6} \%$  efficiency,<sup>75</sup> while LG SIMS achieves  $>1\%$  efficiency<sup>76</sup> for U using an  $\text{O}^-$  primary ion beam. We expect NanoSIMS to have an efficiency that is around the LG-SIMS value because of the similar transmission of both instruments.<sup>77</sup> It should also be noted that the total material removed for either method was not measured, just that EUV TOF data were collected using three laser shots per pixel and NanoSIMS used eight passes per pixel. Figure 3.7C shows that the summed (U + UO) species measured by both methods is approximately equal. On the other hand, when the U and UO species are plotted separately in Figure 3.7A-B, differences between EUV TOF and NanoSIMS become apparent. EUV TOF produces about twice as many U ions as NanoSIMS and an almost equal amount of UO as U. The average U and UO ratios measured with EUV TOF are similar, where  $^{235}\text{U}/^{238}\text{U} = 0.0231 \pm 0.0007 (2\sigma)$  and  $^{235}\text{U}^{16}\text{O}/^{238}\text{U}^{16}\text{O} = 0.0233 \pm 0.0008 (2\sigma)$ . For NanoSIMS, average U and UO ratios measured are different, where  $^{235}\text{U}/^{238}\text{U} = 0.0213 \pm 0.0004 (2\sigma)$  and  $^{235}\text{U}^{16}\text{O}/^{238}\text{U}^{16}\text{O} = 0.0233 \pm 0.0002 (2\sigma)$ .<sup>73,78</sup> This could be from the low overall U ion counts from NanoSIMS preferentially producing UO species from uranium oxides because of the lower ionization potential of the  $\text{O}^-$  adducts compared to the atomic ions, that is, 5.7 eV for  $\text{UO}^+$  (41) versus 6.2 eV for  $\text{U}^+$ . (42) All EUV TOF and NanoSIMS U ratios are generated from the two-isotope plots in Figure 3.7. The ability of EUV TOF to accurately assess both U and UO content at low ion intensities shows the versatility of EUV ablation and ionization for isotope ratio analyses. In general, it is significant that EUV TOF measures similar isotope ratio values, albeit with less precision, as NanoSIMS, considering the magnetic sector multi-collector system employed in the latter is generally superior for determining isotope ratios.

### 3.e Conclusions

We have described EUV TOF's ability to map  $^{235}\text{U}/^{238}\text{U}$  isotopic heterogeneity at the nanoscale in a LEU fuel pellet. The heterogeneity was likely feedstock material that was not completely mixed during manufacturing, resulting in sub-micrometer- to  $\geq 1\ \mu\text{m}$ -sized nonuniform uranium enrichment sites that had not been fully identified with microscale or bulk analyses. This type of mapping of  $^{235}\text{U}/^{238}\text{U}$  heterogeneity at the nanoscale could improve the accuracy of nuclear forensics and safeguards applications to determine provenance and in nuclear fuel development to help determine how heterogeneity can impact fuel performance. We also showed that EUV TOF has similar nanoscale isotopic mapping capabilities to NanoSIMS (within the scope of this study). This demonstrates that the EUV laser ablation and ionization source expands the capabilities of the straightforward and relatively inexpensive TOF mass spectrometer for isotopic analyses at the nanoscale, as opposed to the more complex and expensive sector-field instruments. However, the use of the TOF MS limits high precision isotope ratio measurements that are achieved with sector-fields. Direct comparisons between the spatial resolution, accuracy, and precision of EUV TOF and NanoSIMS should be investigated in future studies. Another advantage of the TOF mass spectrometer coupled to the EUV laser is the TOF's ability to detect a wide range of masses in a single laser shot, as we showed that the EUV TOF could map multiple elements in the LEU sample in each laser pulse. The EUV TOF could therefore be advantageous for measuring multiple elements/isotopes in a particle, where the amount of sample for analysis is limited, or in forensic studies where simultaneous acquisition of elemental signatures could provide additional insights into provenance or history.

Beyond mapping  $^{235}\text{U}/^{238}\text{U}$  heterogeneity in U materials, more evidence about the enrichment of the feedstock from analysis of the minor U isotopes (i.e.,  $^{234}\text{U}$  and  $^{236}\text{U}$ ) would be beneficial for nuclear forensic investigations. These isotopes are currently below the EUV TOF's detection limits when probing sample volumes of a few attoliters, that is, craters with  $\leq 400\ \text{nm}$  diameter and  $\leq 40\ \text{nm}$  depth. Other materials such as geological or astronomical samples could also be investigated to continue assessing the EUV TOF's proficiencies. Extending the capabilities of EUV mass spectrometry could propel it toward

becoming a standard for elemental analyses or isotope ratio measurements in a wide range of materials that require high spatial mapping.

## 4. PAPER #2 ON EUV TOF

### 4.a Paper #2 title page

This chapter describes the following peer-reviewed published work that shows the use of the EUV TOF MS for measuring inter-element isotope ratios of Pb, Th, and U in various geologic matrices in 8  $\mu\text{m}$  sized areas.\*\*

#### 4.a.i Overview

Extreme ultraviolet laser ablation and ionization time-of-flight mass spectrometry (EUV TOF), using a laser that operates at a wavelength of 46.9 nm (26.4 eV photon energy), is a relatively new analytical technique with many unexplored performance characteristics. In this work, we use the EUV TOF to directly measure the  $^{206}\text{Pb}/^{238}\text{U}$  and  $^{232}\text{Th}/^{238}\text{U}$  isotope ratios in different geological materials to investigate if the EUV laser is a good candidate for reducing matrix effects in geological analyses. We use the EUV TOF to analyze synthetic glasses of silicate, basalt, and phosphate as well as mineral samples ranging from iron manganese to zircons and monazites to uraninites and a thorite at a spatial scale of approximately 8  $\mu\text{m}$  and at depths  $\leq 500$  nm. The results show that the EUV TOF measures  $^{206}\text{Pb}/^{238}\text{U}$  ratios that have a systematically low bias in glass, iron manganese, zircon, and monazite matrices. This bias can be calibrated using NIST 610 as a non-matrix matched external calibration sample, resulting in  $^{206}\text{Pb}/^{238}\text{U}$  ratios that are within analytical uncertainty ( $\pm 2\sigma$ ) of the expected values. Unlike  $^{206}\text{Pb}/^{238}\text{U}$ , the  $^{232}\text{Th}/^{238}\text{U}$  ratios measured in the glass, zircon, and monazite matrices do not show a systematic bias and are within  $\pm 2\sigma$  of the expected values from direct measurements. The  $^{206}\text{Pb}/^{238}\text{U}$  and  $^{232}\text{Th}/^{238}\text{U}$  ratios measured in the uraninite and thorite samples are not within analytical uncertainty of the expected values. The uncertainty in the uraninite and thorite measurements are likely a result of the high amounts of Pb, Th, and U in these samples relative to the other analyzed samples and their effect on the instrument's performance. Overall,

---

\*\* Lydia A. Rush, Andrew M. Duffin, and Carmen S. Menoni, **Measuring Pb, Th, and U Inter-element Ratios in Geological Materials using Extreme Ultraviolet Laser Ablation and Ionization Mass Spectrometry**, *Journal of Analytical Atomic Spectrometry*, **2022**, 37, 1902-1914.<sup>47</sup>

this study shows that the EUV ionization mechanisms for Pb, Th, and U are similar in glass, iron manganese, zircon, and monazite matrices, resulting in inter-element ratios that are within analytical uncertainty. EUV laser ablation and ionization is therefore a good candidate for directly measuring the isotopic content in select geological materials at spatial scales of <10  $\mu\text{m}$ .

## 4.b Introduction

Measuring or spatially mapping the elemental or isotopic information in geological materials, like Pb–Th–U ratios, with mass spectrometry is a powerful diagnostics tool that can provide information about material formation and origin.<sup>79</sup> However, geological materials are challenging to probe with mass spectrometry because of their chemical complexity. Specifically, in direct analysis, the large range of compositions making up geological materials can result in measured isotope ratios that differ from true ratios. These matrix effects occur when responses of the analytes of interest are either under- or over-represented due to the sample chemistry. Measuring Pb–Th–U isotope ratios is a particularly important isotopic dating method to the geological community because of the large timescales that these ratios can track.<sup>80</sup> However, the chemical differences between Pb, Th, and U, alongside the requirement of appropriate matrix-matched reference standards and the challenges of measuring these analytes at low concentration, make Pb–Th–U ratio measurements with mass spectrometry difficult; especially at micron-length spatial scales.

Two techniques routinely employed in geological analyses are laser ablation inductively coupled plasma mass spectrometry (LA ICP-MS) and secondary ionization mass spectrometry (SIMS).<sup>3,54,81</sup> Both LA ICP-MS and SIMS, operated with sector-field mass spectrometers, offer precise and accurate measurements with high sensitivity that is necessary for measuring and mapping elemental/isotopic information in geological materials at the microscale.<sup>12,68,82,83</sup> In LA ICP-MS and SIMS analyses of geological materials, matrix effects play an important role in the accuracy and precision of isotope ratio

measurements. LA ICP-MS measurements suffer from laser or plasma induced fractionation.<sup>84,85</sup> For example, laser parameters such as wavelength, pulse length, spot size, fluence, irradiance, repetition rate, ablation mode (i.e., raster vs. single spot), and the gas environment all play a role in correctly measuring the isotope ratio.<sup>86-89</sup> Additionally, the ICP parameters (RF-power, plasma potential, gas flows, etc.) also play a role alongside the sample properties (absorbance, morphology, homogeneity, etc.).<sup>86,87</sup> SIMS isotope ratio measurements are highly dependent on the sample characteristics (i.e., flatness or conductivity of the sample, binding energy of surface atoms, mass ratio of isotopes, work function of the surface, emission angle, ionization potential, and even the positioning of the sample relative to the holder) as well as the energy of the primary and/or secondary ion beams.<sup>16,17</sup> Quantitative analyses in SIMS are difficult because the secondary ion yield is highly dependent on the mentioned parameters and more importantly, on sample chemistry.<sup>18,19</sup> Another mass spectrometry technique that is employed in geological analyses is isotope dilution thermal ionization mass spectrometry (ID-TIMS) for bulk measurements. ID-TIMS offers high accuracy due to the removal of the matrix via chemical separations. ID-TIMS is often used to establish accepted/literature ratio values for unknown materials, but it requires rigorous sample preparation steps and has limited or no spatial resolution or mapping capability.<sup>79</sup>

Laser ablation and laser ionization mass spectrometry (usually called either LAMS or LIMS) is another mass spectral mapping technique that uses a laser to ablate/remove the sample area and concomitantly form a plasma from which ions can be extracted.<sup>1,26,30,33,44-46,67,90,91</sup> LAMS/LIMS instruments are typically operated with time-of-flight (TOF) mass analyzers, which lack the accuracy and precision of sector-field configurations but are easy to use with pulsed laser sources and offer a wide mass range. Depending on the laser wavelength and focusing optics used, LAMS/LIMS can achieve a lateral resolution of tens of microns down to the nanoscale, making it a suitable candidate for geological mapping analyses.<sup>1,30,44,45,90</sup> Like LA ICP-MS and SIMS, LAMS/LIMS is not free of matrix effects. LAMS/LIMS ratio measurements also vary with sample chemistry. In this case, the distribution of polyatomic and atomic species stems from laser-material interactions and the properties of the laser-created plasma.<sup>30,67</sup> However,

these matrix effects in LAMS/LIMS systems have not been widely investigated, especially in regard to geological materials.

Reducing the effects of sample chemistry in laser-based mass spectrometry methods has been achieved by optimizing the laser's pulse duration and wavelength (amongst other system modifications).<sup>9,92,93</sup> For example, using ultraviolet/visible/infrared (UV/Vis/IR) wavelength lasers with pulse durations of femtoseconds (fs) over typical nanosecond (ns) pulses has resulted in the reduction of thermal effects from ablation.<sup>28-30,94,95</sup> Reducing thermal effects from laser ablation is especially advantageous for measuring Pb/U ratios in different matrices because Pb is more sensitive to heating than U (and Th) due to chemical differences.<sup>29,30</sup> In LAMS/LIMS, use of fs lasers has also resulted in more efficient ionization in the bulk/solid phase rather than in the gas phase that is characteristic of longer ns pulses.<sup>30</sup> Additionally, the use of UV over visible and IR wavelength lasers have resulted in ratio measurements that are less susceptible to variations in the sample chemistry because the higher energy photons are more absorbed by the sample material, resulting in more efficient ablation and ionization.<sup>96,97</sup> Extreme ultraviolet (EUV) and soft X-ray lasers producing trains of pulses with ns down to picosecond (ps) durations bring new capabilities to mass spectrometry in that these lasers can ablate solids at the nanoscale ( $\leq 100$  nm) while efficiently ionizing the ablated species in the solid phase. EUV and soft X-ray lasers therefore show promise to reduce the effects of the sample chemistry in laser-based mass spectrometry.<sup>36,40,98</sup>

Our group at Colorado State University has developed an EUV laser ablation and ionization time-of-flight mass spectrometer (EUV TOF), a LAMS/LIMS technique that uses a capillary discharge laser producing pulses at a wavelength of 46.9 nm (26.4 eV photon energy) with a duration of  $\sim 1.5$  ns.<sup>1,44,45</sup> The EUV laser light can be focused down to spots less than 100 nm in diameter where it is absorbed within depths of tens of nanometers in most materials, allowing for ablation of nanoscale ( $\leq 100$  nm) sized craters.<sup>36,65</sup> The EUV laser-material interactions are distinct from those of UV/Vis/IR radiation that dominate current laser-based mass spectrometry methods. While the mechanisms of ionization with

UV/Vis/IR wavelength lasers are dependent on pulse duration (i.e., fs vs. ns), this is not the case for EUV laser pulses because the EUV laser-created plasma is transparent to the incoming EUV photons.<sup>38–40</sup> The EUV photons are thereby absorbed by the sample throughout the duration of the  $\sim 1.5$  ns pulse rather than being absorbed by the electrons in the plasma due to inverse Bremsstrahlung as is the case of ablation by ns UV/Vis/IR laser pulses.<sup>41</sup> This is because the critical electron density ( $n_e$ ) for  $\lambda = 46.9$  nm is  $n_e = 5 \times 10^{23}$  cm<sup>-3</sup>, which is greater than solid density.<sup>42</sup> Additionally, the EUV photons realize efficient single photon ionization of atoms and molecules.<sup>43</sup> In this process, energetic photoelectrons are created which can further ionize atoms and molecules in the solid.<sup>41</sup> Our previous studies with the EUV TOF have highlighted its capabilities for 3D nanoscale chemical and isotopic mappings in organic and inorganic materials.<sup>1,44,45</sup> In this study, we investigate the application of the EUV TOF for the direct measurement of Pb–Th–U ratios in geological samples.

The EUV TOF system was evaluated here by directly measuring the inter-element ratios of  $^{206}\text{Pb}/^{238}\text{U}$  and  $^{232}\text{Th}/^{238}\text{U}$  in different geological materials. We analyze synthetic glasses with major compositions of silicate, basalt, and phosphate alongside mineral samples that include an iron manganese powder, zircons, monazites, uraninites, and a thorite. We analyze areas on each sample sized  $8 \mu\text{m} \times 8 \mu\text{m}$  with depths  $\leq 500$  nm, comparable to a single spot analysis by traditional UV/Vis/IR laser-based methods. The EUV TOF results show that  $^{206}\text{Pb}/^{238}\text{U}$  ratios measured in the glass, iron manganese, zircon, and monazite matrices have a systematically low bias. We show that this bias can be calibrated using NIST 610 as an external standard, resulting in  $^{206}\text{Pb}/^{238}\text{U}$  ratios that are within  $\pm 2\sigma$  of the expected value for glass, iron manganese, and monazite matrices (and just outside  $\pm 3\sigma$  for zircon). Unlike the  $^{206}\text{Pb}/^{238}\text{U}$  ratios, the  $^{232}\text{Th}/^{238}\text{U}$  ratios measured with the EUV TOF do not have an apparent bias, where direct ratio measurements in the glasses, zircons, and monazites agree within  $\pm 2\sigma$  of the expected values (and within  $\pm 3\sigma$  for the iron manganese material). Most  $^{206}\text{Pb}/^{238}\text{U}$  and  $^{232}\text{Th}/^{238}\text{U}$  ratios measured in the uraninite and thorite materials are not within analytical error, indicating possible matrix effects or other instrumental limitations, like decreased detector performance at high Pb, Th, and U signal intensities characteristic of

uraninite and thorite materials. These results show that the EUV TOF might be a good candidate for directly measuring Pb–Th–U inter-element ratios in select glass, iron manganese, zircon, and monazite matrices at spatial scales of <10 μm. The EUV laser could therefore offer the geological community a new way to directly probe elemental and isotopic content in complex geological materials.

## 4.c Experimental section

### 4.c.i Sample preparation

The samples investigated in this study include a suite of different synthetic glasses and minerals. Glass sample matrices include NIST 610 (National Institute of Standards and Technology),<sup>99</sup> USGS GSE-1G (basalt, United States Geological Survey),<sup>100</sup> and STDP5 (phosphate, Klemme et al.).<sup>101,102</sup> Mineral sample matrices include FeMnOx-1 (iron manganese oxide, Jochum et al.),<sup>103</sup> SR1 and EA (zircons, provided by the USGS), 14971 (monazite, provided by the USGS), Bananeira (monazite, Goncalves et al.),<sup>104</sup> Diamantina-1 (monazite, Goncalves et al.),<sup>105</sup> SL-B, Mogok 2A, and Mogok 2C (uraninites, provided by the USGS), and Mogok 1 (thorite, provided by the USGS). Table 4.1 lists the <sup>206</sup>Pb/<sup>238</sup>U and <sup>232</sup>Th/<sup>238</sup>U certified or expected ratios in each sample. Select ratio values were calculated from the measured mass fraction (i.e., mass per mass) values (Table A.2.1), while others are from direct isotope ratio measurements. When multiple measurement methods are listed in Table 4.1, ID-TIMS ratio values are used as the accepted literature value for comparison to the EUV TOF data because of the high accuracy yielded in ID-TIMS measurements. The <sup>232</sup>Th/<sup>238</sup>U ratio for the Diamantina monazite is not listed in Table 4.1 because of the high degree of Th heterogeneity found between sample fragments.<sup>105</sup>

**Table 4.1** Samples analyzed with the EUV TOF in this study and the method(s) used to determine the certified or expected isotope ratio values for <sup>206</sup>Pb/<sup>238</sup>U and <sup>232</sup>Th/<sup>238</sup>U. The error for each ratio is given as ±2σ in parenthesis.

Sample	Type	Material	Method	<sup>206</sup> Pb/ <sup>238</sup> U (±2σ)	<sup>232</sup> Th/ <sup>238</sup> U (±2σ)
NIST 610 <sup>99</sup>	Synthetic glass	Silicate	LA (SF)-ICP-MS, (SF)-ICP-MS, ID (SF)-TIMS, etc.	0.2230 (0.0007)	0.993 (0.004)

<b>USGS GSE-1G</b> <sup>100</sup>	Synthetic glass	Basalt	LA (SF)-ICP-MS, (SF)-ICP-MS, ID (SF)-TIMS, EPMA	0.22 (0.04)	0.91 (0.04)
<b>STDP5</b> <sup>29,101</sup>	Synthetic glass	Phosphate	LA (SF)-ICP-MS, (SF)-ICP-MS	0.25 (0.02)	0.9 (0.2)
<b>FeMnOx-1</b> <sup>103</sup>	Mineral	Iron-manganese	LA (SF)-ICP-MS, (SF)-ICP-MS, XRF	0.72 (0.08)	0.98 (0.04)
<b>SR1</b> <sup>†</sup>	Mineral	Zircon	LA (SF)-ICP-MS	0.0886 (0.0002)	0.0754 (0.0003)
<b>EA</b> <sup>†</sup>	Mineral	Zircon	LA (SF)-ICP-MS	0.0888 (0.0005)	0.363 (0.002)
<b>14971</b> <sup>†</sup>	Mineral	Monazite	LA (SF)-ICP-MS ID (SF)-ICP-MS	N/A 0.1515 (0.0005)	33 (1) 27 (2)
<b>Bananeira</b> <sup>104</sup>	Mineral	Monazite	LA (Q)-ICP-MS LA (SF)-ICP-MS ID (SF)-TIMS	0.081 (0.001) 0.081 (0.002) 0.0829 (0.0004)	N/A N/A 27.8 (1.4)
<b>Diamantina-1</b> <sup>105</sup>	Mineral	Monazite	ID (SF)-TIMS	0.07986 (0.00009)	N/A
<b>SL-B</b> <sup>†</sup>	Mineral	Uraninite	LA (SF)-ICP-MS	0.108 (0.001)	1.96 (0.02)
<b>Mogok 2A</b> <sup>†</sup>	Mineral	Uraninite	LA (SF)-ICP-MS	0.0109 (0.0001)	1.55 (0.01)
<b>Mogok 2C</b> <sup>†</sup>	Mineral	Uraninite	LA (SF)-ICP-MS	0.0105 (0.0002)	0.931 (0.009)
<b>Mogok 1</b> <sup>†</sup>	Mineral	Thorite	LA (SF)-ICP-MS	0.00389 (0.00004)	0.084 (0.003)

\*SF = sector field (with multi-collection); Q = quadrupole; ID = isotope dilution; EPMA = electron probe microanalyzer; XRF = x-ray fluorescence

<sup>†</sup>Ratio values provided directly by USGS (raw data is available upon request)

All samples were prepared similarly by mounting them in epoxy and polishing with super fine (grit size = 600) and ultrafine (grit size = 800) sandpaper followed by a final polish with a polishing pad (Pace Technologies, ATLANTIS Polishing Pad) with 3  $\mu\text{m}$  and 1  $\mu\text{m}$  diamond solutions. NIST 610 was directly provided by the vendor as a polished, glass wafer. The FeMnOx-1 sample came as a powder and was mounted in epoxy and polished like all other samples. The typical hydraulic pressing technique to form a pressed pellet from the powder was not used to prepare the FeMnOx-1 material for EUV TOF analysis because the samples are directly analyzed by the EUV laser in vacuum.<sup>103</sup> For this reason,

individual particles of the powder, each with sizes of roughly a few tens of microns, were analyzed. All samples were coated with approximately 30 nm of gold using magnetron sputtering deposition (Denton Vacuum, Desk II) to eliminate surface charging.

#### **4.c.ii EUV TOF**

The EUV TOF system is described thoroughly elsewhere.<sup>1,44,45</sup> Briefly, a capillary discharge EUV laser, operating at a wavelength of 46.9 nm and producing a train of 1.5 ns pulses up to a repetition rate of 10 Hz, is used for ablation and ionization of the sample. A TOF MS is used for subsequent mass analysis of the ions created in the EUV laser-produced plasma. The EUV laser operates via amplification of Ne-like Ar ions ( $\text{Ar}^{8+}$ ) in a capillary discharge column.<sup>34,35</sup> The entire EUV TOF system is differentially pumped from a pressure of 300 mTorr in the laser capillary (from Ar gas) to  $\leq 10^{-7}$  Torr in the TOF tube.

Each of the campaigns carried out with the EUV TOF on the geological samples were systematically performed under similar conditions. The EUV laser beam was collimated and guided into the sample chamber by two gold-coated toroidal mirrors set at grazing incidence. A zone plate, with a 0.12 numerical aperture and depth of focus of 3  $\mu\text{m}$ , was used to focus the EUV laser beam onto the sample surface to spots of approximately 500 nm in diameter.<sup>72</sup> The zone plate was positioned around its focal length of 2.13 mm to maximize the elemental signal of interest. For all sample ablation (excluding NIST 610, explained further below) the EUV laser pulse energy was maximized between 7–10  $\mu\text{J}$ , corresponding to a fluence of  $\sim 1 \text{ J cm}^{-2}$ . These conditions, in most cases, maximize the elemental signals over the oxide signals as well as decrease the signals from surface contaminants on the sample.<sup>45</sup>

Atoms and molecules ablated from the sample are ionized in the EUV laser-created plasma, producing ions that are accelerated by a 6 kV potential between the sample, zone plate, and ground grid into a 1-meter long TOF mass spectrometer (Jordan TOF). The TOF is operated in reflectron mode for a total travel length of  $\sim 2$  meters. After the desired number of laser shots at each spot, the sample can be

moved in lateral steps down to 6 nm via piezoelectric stages (Physik Instrumente, Q-Motion Precision Linear Stage Q-545.240, Germany).

In the field-free TOF tube, the ions are separated in time according to their mass-to-charge ratio ( $m/q$ ). The TOF's mass resolving power is  $m/\Delta m = 1100$ , determined previously using a similar mass range as in this study.<sup>45</sup> The ions are detected by a 40 mm chevron-type microchannel plate (MCP) detector (Jordan TOF), which is biased to (-)2200 V to start acquisition 13 to 23  $\mu\text{s}$  after the laser is fired. This delay is put on the detector to eliminate low  $m/q$  peaks with a large intensity (like  $^{12}\text{C}$  and  $^{16}\text{O}$ ) and background noise caused by scattered photons from the incoherent emission of the EUV laser plasma discharge. The resulting analog signal is digitized by an analog-to-digital converter (Dynamic Signals, EON CompuScope CS121G1, 1GS/s, 12 bit). Mass calibration is performed on the acquired mass spectra using a quadratic least squares fit of known isotopes at low and high masses that encompass the signals of interest.<sup>49</sup> The mass spectra's intensity in volts is converted to ion counts using the MCP gain, which is measured through a process that is described elsewhere.<sup>44,45,49</sup> Here, 1 ion detected by the MCP is equal to  $\sim 2.5$  mV, corresponding to a detector gain of approximately  $3 \times 10^5$  electron per ion.

The Pb, Th, and U content in each sample was measured with the EUV TOF by ablating an array of partially overlapping craters using single laser shots to create what we call a “super crater.”<sup>45</sup> EUV TOF super craters consist of single laser shots arranged in a  $15 \times 15 \times 3$  (length  $\times$  width  $\times$  depth) matrix for a total of 675 shots in one super crater. The lateral step size between each consecutive ablation spot is 500 nm. The total size of the super crater is  $\sim 8 \mu\text{m}$  wide  $\times 8 \mu\text{m}$  long  $\times \leq 500$  nm deep.

Figure 4.1A-B shows two optical microscope images of the  $8 \mu\text{m} \times 8 \mu\text{m}$  square EUV laser super craters ablated from 675 individual shots on the 14971 and Diamantina monazites. On the 14971 monazite, typical  $\sim 10$ – $15 \mu\text{m}$  sized LA ICP-MS craters from 155 shots per spot (Ar-F excimer laser,  $\lambda = 193$  nm with pulse duration = 15 ns operated at 5 Hz and  $\sim 2 \text{ J cm}^{-2}$ ) are also shown for size comparison. The LA ICP-MS spots have a depth of  $\sim 10 \mu\text{m}$  ( $\sim 70$ – $75$  nm per pulse). Figure 4.1C shows a 3D laser scanning confocal microscope (Keyence, VK-X series) image of different sized EUV super craters ablated

on the USGS GSE-1G sample. The confocal microscope image provides information on the crater depths, confirming that the depth of the EUV laser-ablated super craters are  $\leq 500$  nm. The confocal microscope laser image also shows the complexity of the USGS GSE-1G surface, with asymmetric peaks and valleys in the sample topography exposed throughout the area of the EUV TOF analysis.

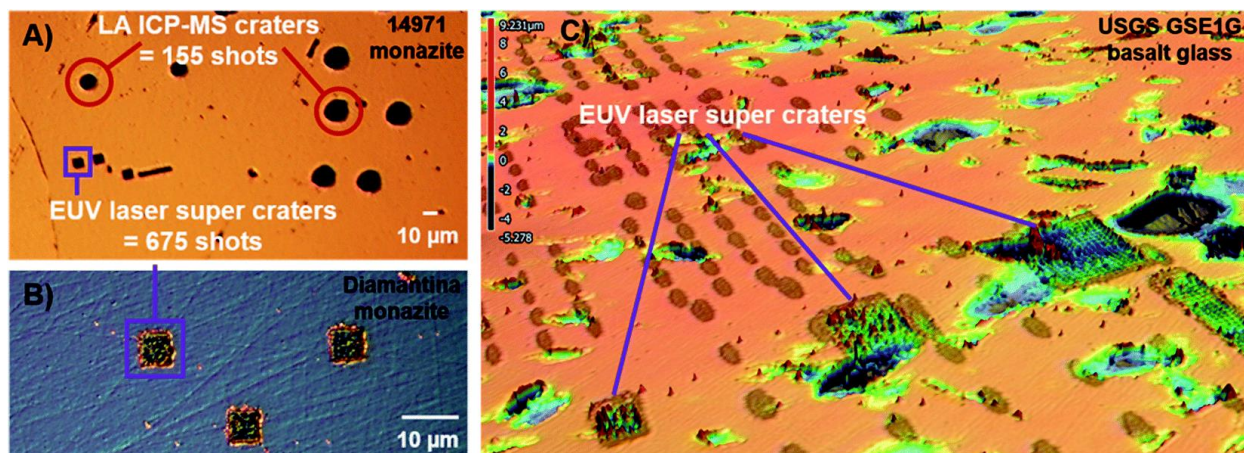


**Figure 4.1** EUV laser-ablated super craters outlined in purple on the (A) 14971 monazite and (B) Diamantina monazite. Each EUV super crater consists of 675 overlapping laser shots ablated from an array sized  $15 \times 15$  with a 500 nm step size between each laser shot to ensure spot-to-spot overlap and 3 shots at every spot. In (A), LA ICP-MS craters from 155 shots per spot on the 14971 monazite are shown surrounding the EUV laser super craters. (C) Confocal laser microscope image of different sized EUV laser super craters ablated on the USGS GSE-1G basalt glass. The large beam imprints surrounding the super craters are from a separate scan and are not part of the analysis.

Figure 4.2 shows the EUV TOF mass spectra from a single EUV laser shot in a super crater alongside the average mass spectra from all 675 shots in the super crater collected from a particle of FeMnOx-1 and from the SL-B uraninite. The spectra from the FeMnOx-1 material highlights the need of the super crater analysis for increasing the signal to noise when the amount of Pb, Th, and U is in the hundreds of  $\mu\text{g/g}$  because the single shot spectrum shows a low signal to noise ratio from the limited number of atoms removed for each shot. Additionally, a prior study using the super crater analysis on the suite of NIST 61X glasses showed that the EUV TOF's detection limits were roughly  $50 \mu\text{g/g}$  for Pb, Th, and U.<sup>23</sup> In the SL-B uraninite, where the abundance of Pb is  $\sim 100\times$  higher and the abundance of Th and U is  $\sim 1000\times$  higher relative to FeMnOx-1, the super crater analysis is not necessary because signals in the single shot spectra are sufficiently intense to be above the detector's background and the instrument's  $50 \mu\text{g/g}$

detection limits. Nonetheless, all samples were analyzed using super craters for consistency between analyses.

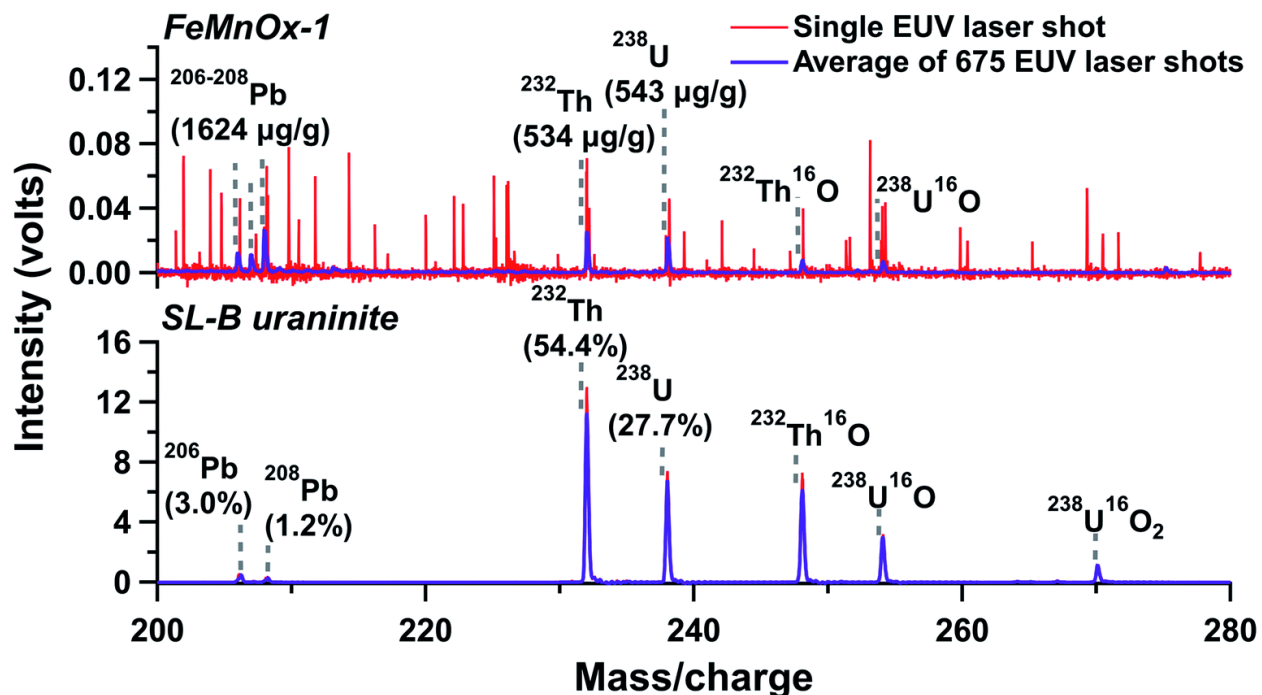


**Figure 4.2** EUV TOF mass spectrum from a single EUV laser shot (red) alongside an averaged spectrum from ~675 laser shots (purple), i.e., a super crater, collected from (top) FeMnOx-1 particle and (bottom) SL-B uraninite. The mass peaks of the isotopes of interest and their expected abundance are identified with dotted lines. The amount of  $^{207}\text{Pb}$  in the SL-B uraninite is  $<0.1\%$  and is not visible at the vertical scale shown here.

Using the average mass spectrum collected from each super crater, the Pb, Th, and U peaks are background subtracted and integrated using the Igor Pro software. More specifically, the areas of the  $^{206}\text{Pb}$ ,  $^{232}\text{Th}$ ,  $^{238}\text{U}$ ,  $^{232}\text{Th}^{16}\text{O}$ , and  $^{238}\text{U}^{16}\text{O}$  peaks are calculated as well as the peak areas of  $^{232}\text{Th}^{16}\text{O}_2$  and  $^{238}\text{U}^{16}\text{O}_2$  when the dioxide species are detected and/or formed. Unlike  $^{232}\text{Th}$  and  $^{238}\text{U}$ , an oxide species of  $^{206}\text{Pb}$  is not observed. All Th and all U species are summed to give the total Th and total U counts used for the isotope ratio measurements (i.e.,  $^{232}\text{Th} + ^{232}\text{Th}^{16}\text{O} + ^{232}\text{Th}^{16}\text{O}_2$  and  $^{238}\text{U} + ^{238}\text{U}^{16}\text{O} + ^{238}\text{U}^{16}\text{O}_2$ ). Hereafter, “ $^{206}\text{Pb}/^{238}\text{U}$ ” and “ $^{232}\text{Th}/^{238}\text{U}$ ” implies that all elemental and oxide species of Th and U are being incorporated into the ratio measurement. The  $^{238}\text{U}^{16}\text{O}_2$  species was detected in all samples except FeMnOx-1 and the Diamantina monazite, while  $^{232}\text{Th}^{16}\text{O}_2$  was only detected in the 14971 and Bananeira monazites as well as the uraninites (Table A.2.2). Typically, every sample showed the largest intensity of elemental

Th and U, followed by the oxide species and then the dioxide species, except in the case of zircon and thorite where the  $^{238}\text{U}^{16}\text{O}$  species dominates over its elemental form (Figure A.2.1).

At least three super craters were ablated on each sample using laser pulse energies in the 7–10  $\mu\text{J}$  range at a repetition rate of 1 Hz at different locations spaced  $\geq 10 \mu\text{m}$  apart. All samples were assumed to be homogenous down to the microscale, so sampling sites were randomly selected with the exception that obvious cracks and fractures were avoided. Table 4.2 lists the main EUV TOF parameters used to collect data from the different geologic samples. The weighted average for each isotope ratio measured on these samples was calculated using the equations in Table A.2.3 (i.e., ratios measured with more ion counts are weighted more heavily in the average than ratios measured with less ions). The NIST 610 certified reference material (CRM) was analyzed to track any system changes during the  $\sim 30$  day campaign, with a total of 19 super craters ablated on the CRM at the beginning, middle, and end of the experiment. The EUV laser energy was decreased down to  $\sim 3 \mu\text{J}$  for some isotope ratio measurements on the NIST 610 glass to see how the number of ions affected the isotope ratio measurement, which is further discussed in the next section. The raw EUV TOF data collected on each sample can be found in Table A.2.2.

**Table 4.2** EUV TOF parameters used to analyze the geologic samples.

<b>EUV TOF Parameters</b>	<b>Super Crater Analysis</b>
<b>Repetition rate</b>	1 Hz
<b>Fluence</b>	$\sim 5 \text{ J/cm}^2$
<b>Shots/spot</b>	3
<b>Step size</b>	500 nm
<b>Ablated area</b>	$8 \mu\text{m} \times 8 \mu\text{m}$
<b>Total number of shots/ super crater</b>	675
<b>Time/super crater</b>	$\sim 10$ to 15 min.
<b>Isotopes used in ratio</b>	$^{206}\text{Pb}$ , $^{232}\text{Th}$ , $^{238}\text{U}$ , $^{232}\text{Th}^{16}\text{O}$ , $^{238}\text{U}^{16}\text{O}$ , $^{232}\text{Th}^{16}\text{O}_2$ , $^{238}\text{U}^{16}\text{O}_2$
<b>Vertical scale of digitizer</b>	Variable (adjusted on a sample-by-sample basis)

#### 4.d Results and discussion

#### 4.d.i EUV TOF analysis of NIST 610 CRM

Figure 4.3 shows the  $^{206}\text{Pb}/^{238}\text{U}$  and  $^{232}\text{Th}/^{238}\text{U}$  ratio measurements from the EUV TOF analysis of the NIST 610 CRM. The data is plotted as a “tree plot” where the ratio is plotted as a function of  $^{238}\text{U}$  counts as well as a “two-isotope plot” where the counts of  $^{206}\text{Pb}$  and  $^{232}\text{Th}$  are plotted as a function of  $^{238}\text{U}$  counts. Each plotted data point corresponds to the number of counts from an  $8\ \mu\text{m} \times 8\ \mu\text{m}$  super crater. The NIST certified (i.e., expected)  $^{206}\text{Pb}/^{238}\text{U}$  and  $^{232}\text{Th}/^{238}\text{U}$  ratios is shown in the plot alongside its corresponding  $\pm 2\sigma$  uncertainty based on counting statistics. The ratios were collected at  $^{206}\text{Pb}$ ,  $^{232}\text{Th}$ , and  $^{238}\text{U}$  counts ranging from  $\sim 40$  to 1600 by varying the EUV laser energy where there is a linear dependence on ion signal intensity as a function of laser energy.<sup>45</sup> Varying the ion counts aids in determining the number of ions required for precise isotope ratio measurements at the  $8\ \mu\text{m}$  spatial scale of analysis.<sup>80</sup>

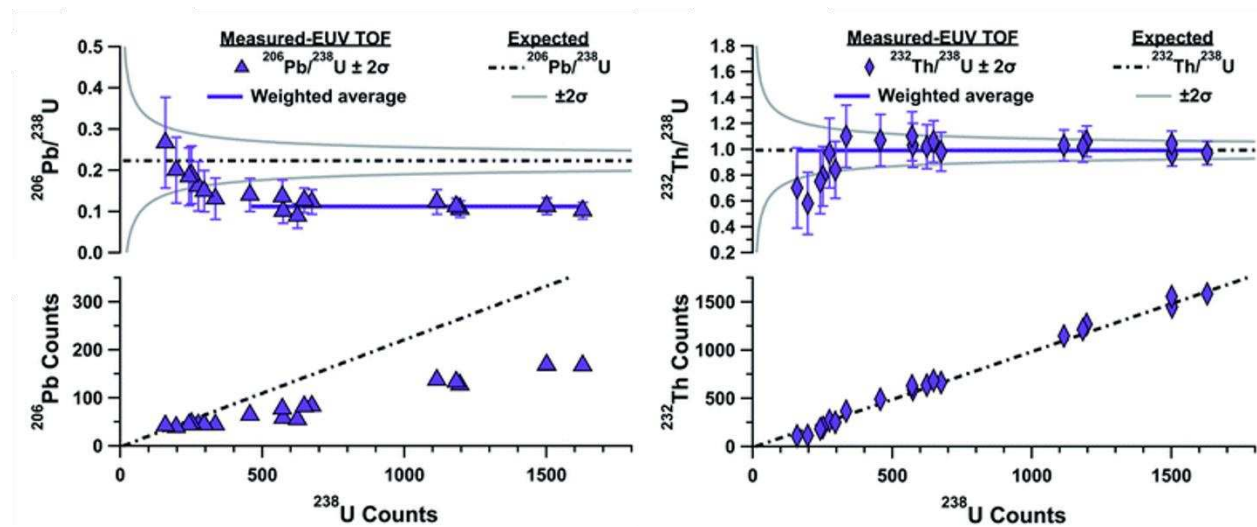


**Figure 4.3** EUV TOF (left)  $^{206}\text{Pb}/^{238}\text{U}$  and (right)  $^{232}\text{Th}/^{238}\text{U}$  ratio measurements in the NIST 610 certified reference glass. (Top left)  $^{206}\text{Pb}/^{238}\text{U}$  and (top right)  $^{232}\text{Th}/^{238}\text{U}$  ratios, shown with  $\pm 2\sigma$  error bars, both plotted as a function of  $^{238}\text{U}$  counts. The purple solid lines representing the weighted average of  $^{206}\text{Pb}/^{238}\text{U} = 0.112 \pm 0.007$  ( $2\sigma$ ) and  $^{232}\text{Th}/^{238}\text{U} = 0.99 \pm 0.03$  ( $2\sigma$ ). For the measured  $^{206}\text{Pb}/^{238}\text{U}$  weighted average, only  $^{238}\text{U}$  counts  $>400$  is included, while for the  $^{232}\text{Th}/^{238}\text{U}$  weighted average, all points are included. The solid gray lines represent the  $\pm 2\sigma$  uncertainty of the expected ratio based on the number of detected ions. (Bottom left)  $^{206}\text{Pb}$  counts and (bottom right)  $^{232}\text{Th}$  counts plotted as a function of counts of  $^{238}\text{U}$ . All plotted data points represent the ratio/counts measured in a super crater. The black dotted lines in both plots represent the NIST certified/expected ratio, where  $^{206}\text{Pb}/^{238}\text{U} = 0.2230$  and  $^{232}\text{Th}/^{238}\text{U} = 0.993$ . (Figure adapted from L. Rush et al.<sup>47</sup>)

Figure 4.3 highlights the differences between the response of  $^{206}\text{Pb}$ ,  $^{232}\text{Th}$ , and  $^{238}\text{U}$  to the EUV laser. The  $^{206}\text{Pb}/^{238}\text{U}$  ratios measured with the EUV TOF are relatively precise ( $\sim 7\%$ ), at  $^{238}\text{U}$  counts  $>400$ , but not accurate.<sup>74</sup> The inaccuracy in the  $^{206}\text{Pb}/^{238}\text{U}$  ratios is from a systematic bias, specifically at

$^{238}\text{U}$  counts >400. Below  $^{238}\text{U}$  counts of 400 the measured ratio starts biasing exponentially high. The systematically low bias in the ratios at the highest counts indicates that less  $^{206}\text{Pb}$  (or more  $^{238}\text{U}$ ) is being formed than expected. The reason for this systematic bias could be because Pb and U are chemically different, and therefore U is being selectively ablated and/or ionized at the conditions used for data collection. Alternatively, there might be more neutral or negative ions of Pb being formed relative to U. In the latter case, since the EUV TOF is only analyzing positive ions for this analysis, the negative ions of Pb would not be detected. It is also possible that  $^{206}\text{Pb}^{2+}$  could be forming at higher laser energies, but the double ionized species were not found in the NIST mass spectra. Further investigation is required to understand the specific cause of the systematic bias (i.e., chemical vs. instrumental bias) in the measurement of the  $^{206}\text{Pb}/^{238}\text{U}$  ratio. As will be seen in the next section, this systematic bias also appears in the other samples that are analyzed.

As the number of U counts decreases below 400 from decreasing the laser energy, the  $^{206}\text{Pb}/^{238}\text{U}$  ratio starts biasing exponentially high relative to those ratios measured at higher counts. This high bias could be from polyatomic interferences at Pb that are selectively formed at lower laser energies. For example, in a previous study, low EUV laser energies have been shown to support the formation of oxide species over their elemental counterpart.<sup>45</sup> As such, the interference could be an oxide species that is not formed at high laser energies. Taking this into consideration, the resulting  $^{206}\text{Pb}/^{238}\text{U}$  weighted average is calculated only using ratios measured at U counts >400. The measured  $^{206}\text{Pb}/^{238}\text{U}$  weighted average is  $0.112 \pm 0.007$  ( $2\sigma$ ), whereas the NIST certified ratio is 0.2230. The analysis of NIST 610 shows the need to collect  $^{206}\text{Pb}/^{238}\text{U}$  ratios in the other samples at the highest EUV laser energies, ensuring a sufficient number of ions are detected for precise ratio measurements in the  $8\ \mu\text{m} \times 8\ \mu\text{m}$  super craters.

In comparison to  $^{206}\text{Pb}/^{238}\text{U}$ , the  $^{232}\text{Th}/^{238}\text{U}$  ratios measured in NIST 610 are both precise ( $\sim 3\%$ ) and accurate. Unlike the  $^{206}\text{Pb}/^{238}\text{U}$  ratios, the  $^{232}\text{Th}/^{238}\text{U}$  ratios show a less apparent systematic bias and all ratios agree with the expected value within  $\pm 2\sigma$ , including those ratios collected at the lowest ion counts. This indicates that the  $^{232}\text{Th}/^{238}\text{U}$  ratios are less sensitive to low laser energies. The  $^{232}\text{Th}/^{238}\text{U}$

weighted average measured in NIST 610, using all ratio measurements, with the EUV TOF is  $0.99 \pm 0.03$  ( $2\sigma$ ). For reference, the NIST  $^{232}\text{Th}/^{238}\text{U}$  value is 0.993. The fact that the measured  $^{232}\text{Th}/^{238}\text{U}$  ratio agrees with the expected value indicates that the  $^{232}\text{Th}/^{238}\text{U}$  ratio can be directly measured while the  $^{206}\text{Pb}/^{238}\text{U}$  ratio requires a calibration factor to account for the systematic bias.

It should be emphasized that each data point in Figure 4.3 represents the approximate number of ions detected in a single super crater (i.e., from  $\sim 675$  EUV laser shots), originating from much less material than traditional UV/Vis/IR laser-based mass spectrometry analyses. Increased precision and accuracy in the isotope ratio measurement would certainly be expected if a larger sample volume and thereby more ions were collected. However, the ratios in Figure 4.3 are relatively precise ( $<10\%$ ) for a TOF MS at the highest ion counts/highest laser energy in the  $8\ \mu\text{m} \times 8\ \mu\text{m}$  super craters.<sup>74</sup> Future studies with the EUV TOF could focus on developing analyses for ultra-high precision ( $\ll 1\%$ ) isotope ratio measurements that would be more useful to the geochronological community for mineral aging.<sup>80</sup>

#### **4.d.ii EUV TOF $^{206}\text{Pb}/^{238}\text{U}$ measurements**

Figure 4.4 shows the  $^{206}\text{Pb}/^{238}\text{U}$  ratios measured with the EUV TOF, which are normalized to 1 using the expected values from Table 4.1, in the glass and mineral samples. Normalization of the ratios is done by dividing the measured ratio by the expected ratio.<sup>92</sup> The error bars on each point in Figure 4.4 are  $\pm 2\sigma$ , which incorporates the weighted uncertainty of the average (Table A.2.3). Figure 4.4 also shows gray shaded bars that corresponds to the  $\pm 2\sigma$  uncertainty of the expected values. Table 4.3 lists the corresponding unnormalized  $^{206}\text{Pb}/^{238}\text{U}$  ratios plotted in Figure 4.4 alongside the percent error from the expected value. The  $^{206}\text{Pb}/^{238}\text{U}$  ratio could not be accurately measured on the EA zircon because the  $^{206}\text{Pb}$  signal was not clearly observed due to its low concentration of  $70\ \mu\text{g/g}$  in the sample, which is around the EUV TOF's  $50\ \mu\text{g/g}$  detection limits.<sup>45</sup>

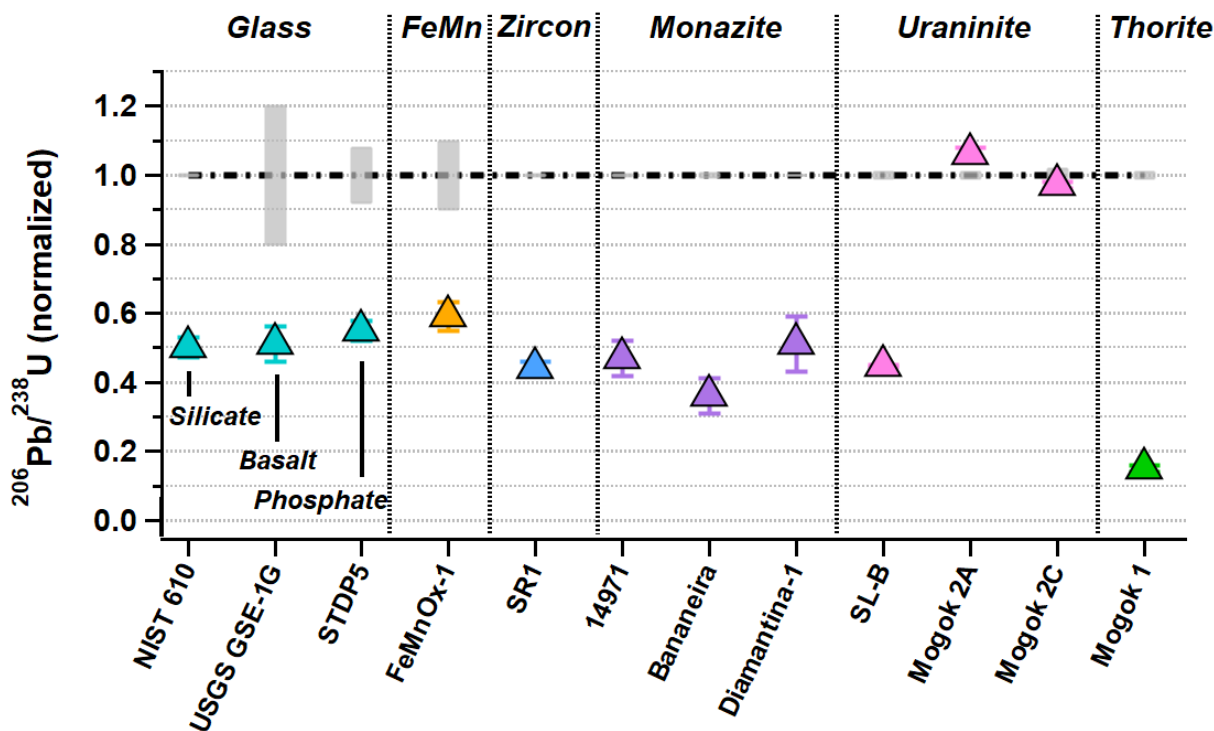


**Figure 4.4** Normalized  $^{206}\text{Pb}/^{238}\text{U}$  ratios measured with the EUV TOF in different matrices. Each point represents the weighted average from at least three super craters. The error bars are  $\pm 2\sigma$ , which incorporates the weighted uncertainty of the average. The black dotted line at  $^{206}\text{Pb}/^{238}\text{U} = 1$  represents the expected normalized ratios, and the gray shaded bars are the  $\pm 2\sigma$  errors of the expected values.

**Table 4.3**  $^{206}\text{Pb}/^{238}\text{U}$  ratios measured with the EUV TOF alongside the corresponding  $\pm 2\sigma$  uncertainty and percent error from the expected ratios.

Sample	Expected $^{206}\text{Pb}/^{238}\text{U}$ ( $\pm 2\sigma$ )	Measured $^{206}\text{Pb}/^{238}\text{U}$ ( $\pm 2\sigma$ )	% Error
NIST 610	0.2230 (0.0007)	0.112 (0.007)	(+) 49.9%
USGS GSE-1G	0.22 (0.04)	0.11 (0.01)	(+) 48.9%
STDP5	0.25 (0.02)	0.138 (0.006)	(+) 45.0%
FeMnOx-1	0.72 (0.08)	0.42 (0.02)	(+) 41.4%
SR1	0.0886 (0.0002)	0.039 (0.002)	(+) 55.6%
EA	0.0888 (0.0005)	$^{206}\text{Pb}$ below detection limits	
14971	0.1515 (0.0005)	0.071 (0.007)	(+) 53.2%
Bananeira	0.0829 (0.0004)	0.030 (0.004)	(+) 63.8%
Diamantina-1	0.07986 (0.00009)	0.041 (0.006)	(+) 48.8%
SL-B	0.108 (0.001)	0.0482 (0.0004)	(+) 55.4%
Mogok 2A	0.0109 (0.0001)	0.0116 (0.0002)	(-) 6.1%
Mogok 2C	0.0105 (0.0002)	0.0102 (0.0001)	(+) 2.6%
Mogok 1	0.00389 (0.00004)	0.00058 (0.00004)	(+) 85.1%

Figure 4.4 shows that the  $^{206}\text{Pb}/^{238}\text{U}$  ratios measured with the EUV TOF on the glasses, iron manganese, zircon, 14971 and Diamantina monazites, and SL-B uraninite samples are lower than the

expected ratio by approximately 41 to 56% (Table 4.3), indicating a systematically low bias. The low bias measured in these samples is in line with the bias measured in NIST 610 (Figure 4.3), whose weighted average ratio is also plotted in Figure 4.4. On the other hand, the  $^{206}\text{Pb}/^{238}\text{U}$  ratios measured in the Mogok uraninites do not follow this bias and are closer to their expected values. The ratio measured in Mogok 2A is higher than its expected value by ~6%, while the ratio measured in Mogok 2C is lower than expected by ~3%. The Mogok 1 thorite also deviates from the majority trend with a  $^{206}\text{Pb}/^{238}\text{U}$  ratio that is 85% lower than expected. While not as apparent as the Mogok samples, the  $^{206}\text{Pb}/^{238}\text{U}$  ratio measured in the Bananeira monazite is also lower than expected and is not within  $\pm 2\sigma$  of the ratios measured in the other 14971 and Diamantina monazites as would be expected.

To provide a better picture of the range of ratios being measured in the samples and how this might contribute to the uncertainty in some of the measurements, Figure 4.5 shows the unnormalized  $^{206}\text{Pb}/^{238}\text{U}$  ratios (from Table 4.3) measured with the EUV TOF plotted as a function of the expected ratios. Figure 4.5 shows that the Mogok uraninites and Mogok thorite have the lowest expected  $^{206}\text{Pb}/^{238}\text{U}$  ratios out of all the samples, with values  $\leq 0.01$ . All other samples, with expected  $^{206}\text{Pb}/^{238}\text{U}$  ratios ranging from approximately 0.08 to 0.7, behave similarly as can be seen from the linear best fit line through the measured data (shown as a red dotted line in Figure 4.5). Figure 4.5 indicates that the EUV TOF ratio measurements are dependent on a sample's isotopic abundance, such that the EUV TOF cannot accurately measure  $^{206}\text{Pb}/^{238}\text{U}$  ratio when the difference between  $^{206}\text{Pb}$  and  $^{238}\text{U}$  content is  $\geq 100\times$ .<sup>74</sup> Similarly, the performance of the MCP detector used in the EUV TOF set-up could be degrading at the high U signal intensities characteristic of the uraninites and thorites, both related to the known limitations in the linear dynamic range of MCP detectors.<sup>106,107</sup>

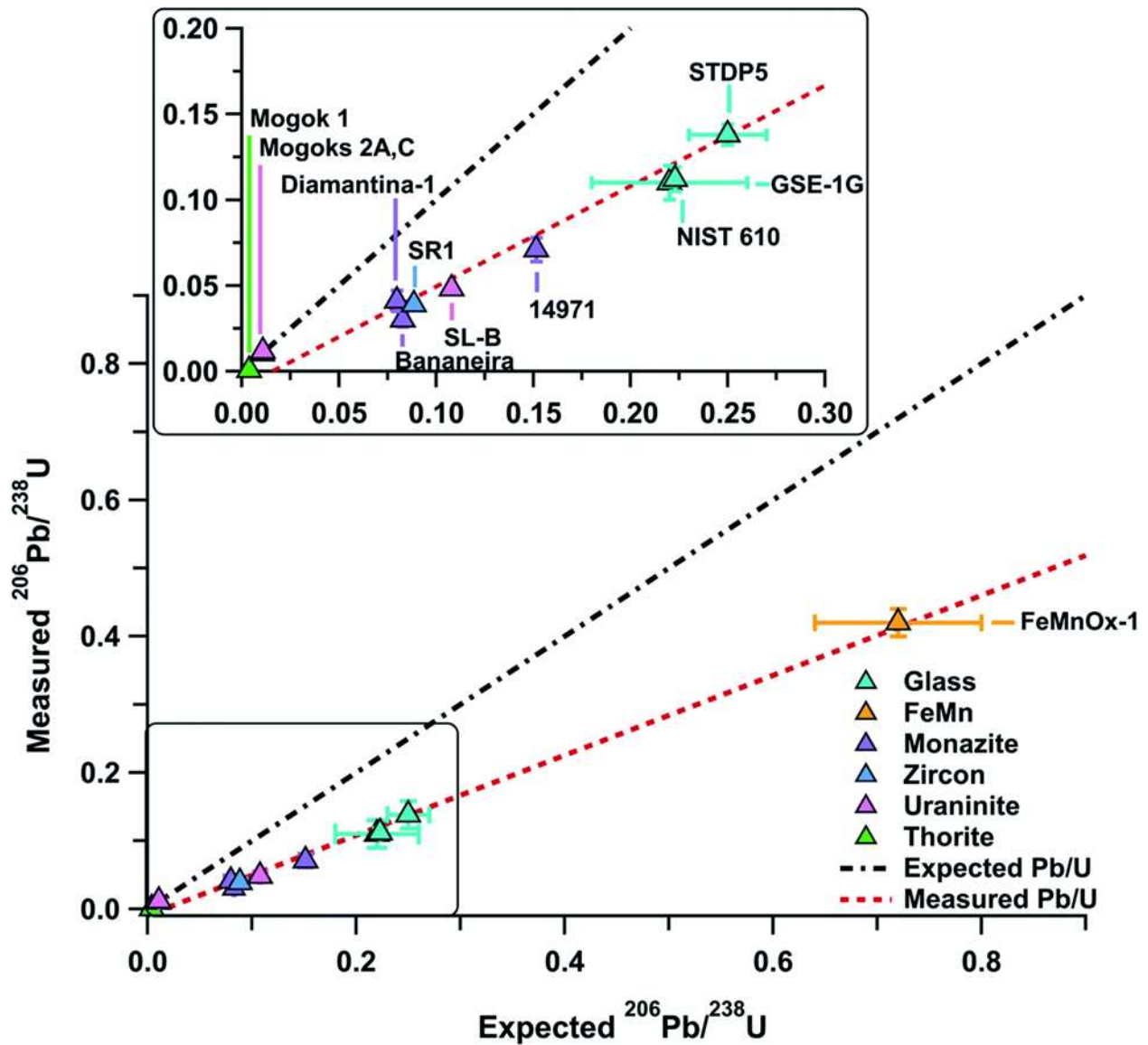


**Figure 4.5** Measured  $^{206}\text{Pb}/^{238}\text{U}$  ratios collected with the EUV TOF plotted as a function of the expected ratios in the different sample matrices. Each measured ratio is the raw unnormalized ratio from Figure 4.4. The vertical and horizontal error bars are the  $\pm 2\sigma$  uncertainty of the measured and expected ratios, respectively. The inset plot is zoomed in on the  $^{206}\text{Pb}/^{238}\text{U}$  ratios that are less than 0.3. The expected  $^{206}\text{Pb}/^{238}\text{U}$  ratio line is shown as a black dotted line. In comparison, the red dotted line is the linear best fit line through the measured  $^{206}\text{Pb}/^{238}\text{U}$  ratios collected with the EUV TOF.

Additionally, while double ionized species were not observed in the other samples, the Mogok samples show formation of  $\text{Pb}^{2+}$  and  $\text{U}^{2+}$  (as well as  $\text{Th}^{2+}$ ). However, the double ionized species for the Mogok 2A and 2C uraninites are much lower in magnitude than the elemental and oxide signals, such that their incorporation into the ratio does not result in significant changes. On the other hand, the Mogok 1 thorite forms  $\text{Pb}^{2+}$  in a similar magnitude to  $\text{Pb}^+$ , which could explain the lower-than-expected  $^{206}\text{Pb}/^{238}\text{U}$

ratio (relative to the majority trend) measured by the EUV TOF, which only accounts for  $^{206}\text{Pb}^+$ . Separately, the uraninite and thorite samples could also have variations in Pb and U content throughout the sample, in which case the small  $8\ \mu\text{m} \times 8\ \mu\text{m}$  area analyzed with the EUV TOF could not be expected to match the bulk value. Overall, further investigation is required to specify whether the uncertainty in the ratio measurements on the Mogok samples is from instrumental biases, matrix effects, and/or sample composition.

On the other hand, the uncertainty in the ratio measured in the Bananeira sample could be from sample discordance, which was previously identified by ID-TIMS measurements.<sup>104</sup> Discordance appears in a geological system through differences in the  $^{206}\text{Pb}/^{238}\text{U}$  and  $^{207}\text{Pb}/^{235}\text{U}$  ratios that can be caused by a number of factors, such as the presence of non-radiogenic (“common”) Pb, amongst other mechanisms.<sup>108</sup> The discordant  $^{206}\text{Pb}/^{238}\text{U}$  ratio measured in the Bananeira monazite by ID-TIMS, which is not used in the expected ratio, is 0.06976 as compared to the expected  $^{206}\text{Pb}/^{238}\text{U} = 0.07986$ .<sup>104</sup> The low  $^{206}\text{Pb}/^{238}\text{U}$  ratio measured by the EUV TOF in the Bananeira monazite could therefore be from discordance. However, it is not possible to verify this using the EUV TOF data because, alongside  $^{206}\text{Pb}$  and  $^{238}\text{U}$ , the  $^{207}\text{Pb}$  and  $^{235}\text{U}$  isotopes are needed for verification of discordance, and these isotopes are below the EUV TOF's detection limits at the instrumental parameters used for data collection.

While further investigation is required to determine the specific cause of the uncertainties in the  $^{206}\text{Pb}/^{238}\text{U}$  ratios measured with the EUV TOF in the Mogok and Bananeira samples, the ratio measurements in the other samples are promising in terms of matrix effect reduction. Figure 4.4 and Figure 4.5 show that while direct measurements of the  $^{206}\text{Pb}/^{238}\text{U}$  ratios by the EUV TOF in the glasses, iron manganese, zircon, monazite (14971 and Diamantina), and SL-B uraninite samples are biased low, it also shows that the bias is systematic and can be calibrated using a non-matrix matched standard. Specifically, the results show that the NIST 610 silicate reference material can be used as a suitable external calibration sample to account for the low bias by applying a factor of 2.0 to the measured ratios. This would result in  $^{206}\text{Pb}/^{238}\text{U}$  ratios measured in the USGS GSE-1G basalt glass, STDP5 phosphate glass, FeMnOx-1 powder,

14971 monazite, and Diamantina monazite to be within  $\pm 2\sigma$  of their expected values, while the SR1 zircon and SL-B uraninite ratios would deviate from their expected values by  $\sim 11\%$ , putting them just outside of  $\pm 3\sigma$  (Figure A.2.2). While the accuracy and precision of these measurements are limited by the TOF MS, these results indicate that the EUV laser ablates and ionizes  $^{206}\text{Pb}$  and  $^{238}\text{U}$  (i.e.,  $^{238}\text{U} + ^{238}\text{U}^{16}\text{O} + ^{238}\text{U}^{16}\text{O}_2$ ) similarly between different glass, iron manganese, zircon, and monazite matrices.

It should be noted that all the uranium oxide species formed during EUV laser ablation and ionization must be included in the  $^{206}\text{Pb}/^{238}\text{U}$  ratio calculation for accurate and precise results between matrices, indicating that  $\text{U}/\text{UO}$  and  $\text{U}/\text{UO}_2$  is matrix dependent in the EUV TOF (Figure A.2.2). The inclusion of the oxide species into the ratio measurements is relatively straightforward with the TOF set-up because of its large mass range, detecting all elemental and oxide species of uranium in a single laser shot. On the other hand, this type of analysis would be more tedious on a sector-field multi- (or single) collector mass spectrometer, the preferred mass analyzer for geological analyses, where multiple passes with different detector positions would be required to detect all the elemental and oxide species of uranium. In future experiments, it would be valuable to investigate the relationship between the formation of the uranium oxide species and the  $^{206}\text{Pb}/^{238}\text{U}$  ratio within each matrix using the EUV laser source and how it compares to the sources used in LA ICP-MS and SIMS.<sup>18,109–111</sup>

#### **4.d.iii EUV TOF $^{232}\text{Th}/^{238}\text{U}$ measurements**

The  $^{232}\text{Th}/^{238}\text{U}$  ratios were also measured with the EUV TOF in the different sample matrices. Figure 4.6 shows the normalized  $^{232}\text{Th}/^{238}\text{U}$  ratios, with  $\pm 2\sigma$  errors, measured in the glass and mineral samples. Table 4.4 lists the unnormalized  $^{232}\text{Th}/^{238}\text{U}$  ratios measured with the EUV TOF. It should be noted that for the SR1 and EA zircon samples, only the  $^{232}\text{Th}^{16}\text{O}$  and  $^{238}\text{U}^{16}\text{O}$  species were used in the calculation of the isotope ratio because of interferences at the elemental signals. The main interference is on  $^{232}\text{Th}$  from  $^{92}\text{Zr}_2^{16}\text{O}_3$  at  $m/q = 232$ , which has an abundance of  $\sim 20\%$ . There is also an interference on  $^{238}\text{U}$  from the known zircon isotopologue  $^{94}\text{Zr}^{96}\text{Zr}^{16}\text{O}_3$  at  $m/q = 238$  with an abundance of  $\sim 1\%$ . However, this interference accounts for  $< 0.5\%$  of the total U signal (i.e.,  $\text{U} + \text{UO} + \text{UO}_2$ ) measured in the SR1 zircon.

On the other hand, the  $^{94}\text{Zr}^{96}\text{Zr}^{16}\text{O}_3$  interference cannot be neglected in the EA zircon because it accounts for >15% of the total U signal due to the  $\sim 3\times$  lower abundance of  $^{238}\text{U}$  in EA compared to SR1. There were no detectable  $\text{Zr}_2\text{O}_4$  species interfering with the  $^{232}\text{Th}^{16}\text{O}$  or  $^{238}\text{U}^{16}\text{O}$  signals in either zircon.

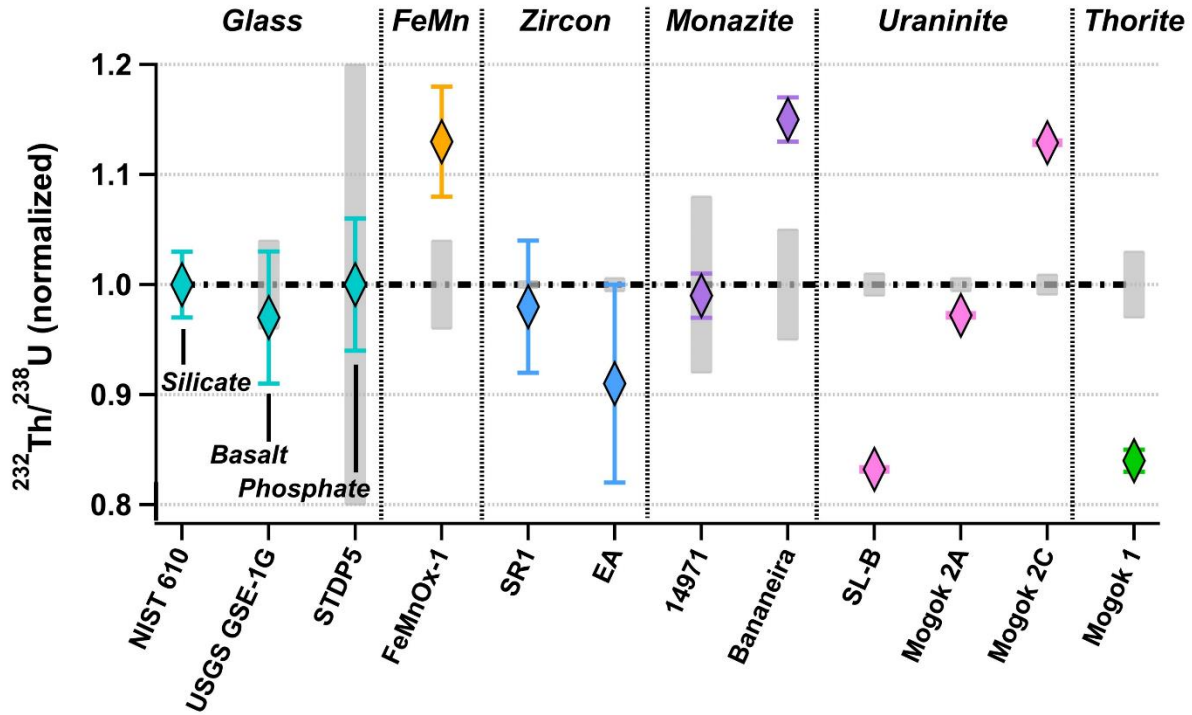


**Figure 4.6** Normalized  $^{232}\text{Th}/^{238}\text{U}$  ratios measured with the EUV TOF in the different matrices. Each point represents the weighted average from at least three super craters. The error bars are  $\pm 2\sigma$ , which incorporates the weighted uncertainty of the average. The black dotted line at  $^{232}\text{Th}/^{238}\text{U} = 1$  represents the expected normalized ratios, and the gray shaded bars are the  $\pm 2\sigma$  errors of the expected values.

**Table 4.4**  $^{232}\text{Th}/^{238}\text{U}$  ratios measured with the EUV TOF alongside the corresponding  $\pm 2\sigma$  uncertainty and percent error from the expected ratios.

Sample	Expected $^{232}\text{Th}/^{238}\text{U}$ ( $\pm 2\sigma$ )	Measured $^{232}\text{Th}/^{238}\text{U}$ ( $\pm 2\sigma$ )	% Error
<b>NIST 610</b>	0.993 (0.004)	0.99 (0.03)	(+) 0.4%
<b>USGS GSE-1G</b>	0.91 (0.04)	0.88 (0.04)	(+) 3.3%
<b>STDP5</b>	0.9(4) (0.2)	0.94 (0.04)	(+) 0.0%
<b>FeMnOx-1</b>	0.98 (0.04)	1.10 (0.05)	(-) 12.6%
<b>SR1</b>	0.0754 (0.0003)	0.074 (0.004)	(+) 1.7%
<b>EA</b>	0.363 (0.002)	0.33 (0.03)	(+) 9.5%
<b>14971</b>	27 (2)	26.8 (0.5)	(+) 0.7%
<b>Bananeira</b>	27.8 (1.4)	32.0 (0.7)	(-) 15.0%
<b>Diamantina-1</b>	Non-uniform Th composition		
<b>SL-B</b>	1.96 (0.02)	1.633 (0.003)	(+) 16.8%
<b>Mogok 2A</b>	1.55 (0.01)	1.503 (0.003)	(+) 2.8%
<b>Mogok 2C</b>	0.931 (0.009)	1.051 (0.002)	(-) 12.9%

<b>Mogok 1</b>	0.084 (0.003)	0.0698 (0.0006)	(+) 16.4%
----------------	---------------	-----------------	-----------

Figure 4.6 shows that direct measurements of the  $^{232}\text{Th}/^{238}\text{U}$  ratios with the EUV TOF are within  $\pm 2\sigma$  of the expected values for select glasses, zircons, and monazites. The  $^{232}\text{Th}/^{238}\text{U}$  ratio measured in the Mogok 2A uraninite is within 3% of the expected value but is outside of analytical uncertainty. The  $^{232}\text{Th}/^{238}\text{U}$  ratios measured in the FeMnOx-1 iron manganese, Mogok 2C uraninite, SL-B uraninite, and Mogok 1 thorite samples show the largest deviation of ( $\pm$ )13 to 17% from their expected values. However, the ratio measured in the FeMnOx-1 sample is within  $\pm 3\sigma$  of its expected value.

Figure 4.7 shows the unnormalized  $^{232}\text{Th}/^{238}\text{U}$  ratios measured with the EUV TOF plotted as a function of the expected ratio using the values from Table 4.4. Figure 4.7 shows that there is no clear correlation between the values of the  $^{232}\text{Th}/^{238}\text{U}$  ratio and their uncertainty, unlike the  $^{206}\text{Pb}/^{238}\text{U}$  ratios in Figure 4.5. However, the fact that both the  $^{206}\text{Pb}/^{238}\text{U}$  and  $^{232}\text{Th}/^{238}\text{U}$  ratios measured in the uraninites and thorite generally have the largest uncertainty in the EUV TOF measurements likely confirms that either (1) the detector's performance is compromised at high signal intensities and/or (2) the accuracy of the ratio measurements is influenced by the isotopic abundance, especially considering these samples have the highest amounts of Pb, Th, and U. The uraninite and thorite matrices could also have more matrix effects relative to the other samples, including the formation of double (and triple) ionized species.<sup>112</sup> It would be intriguing to further understand how/if the EUV ablation and ionization mechanisms are contributing to the uncertainty in the measurements in the uraninite and thorite matrices in future studies.

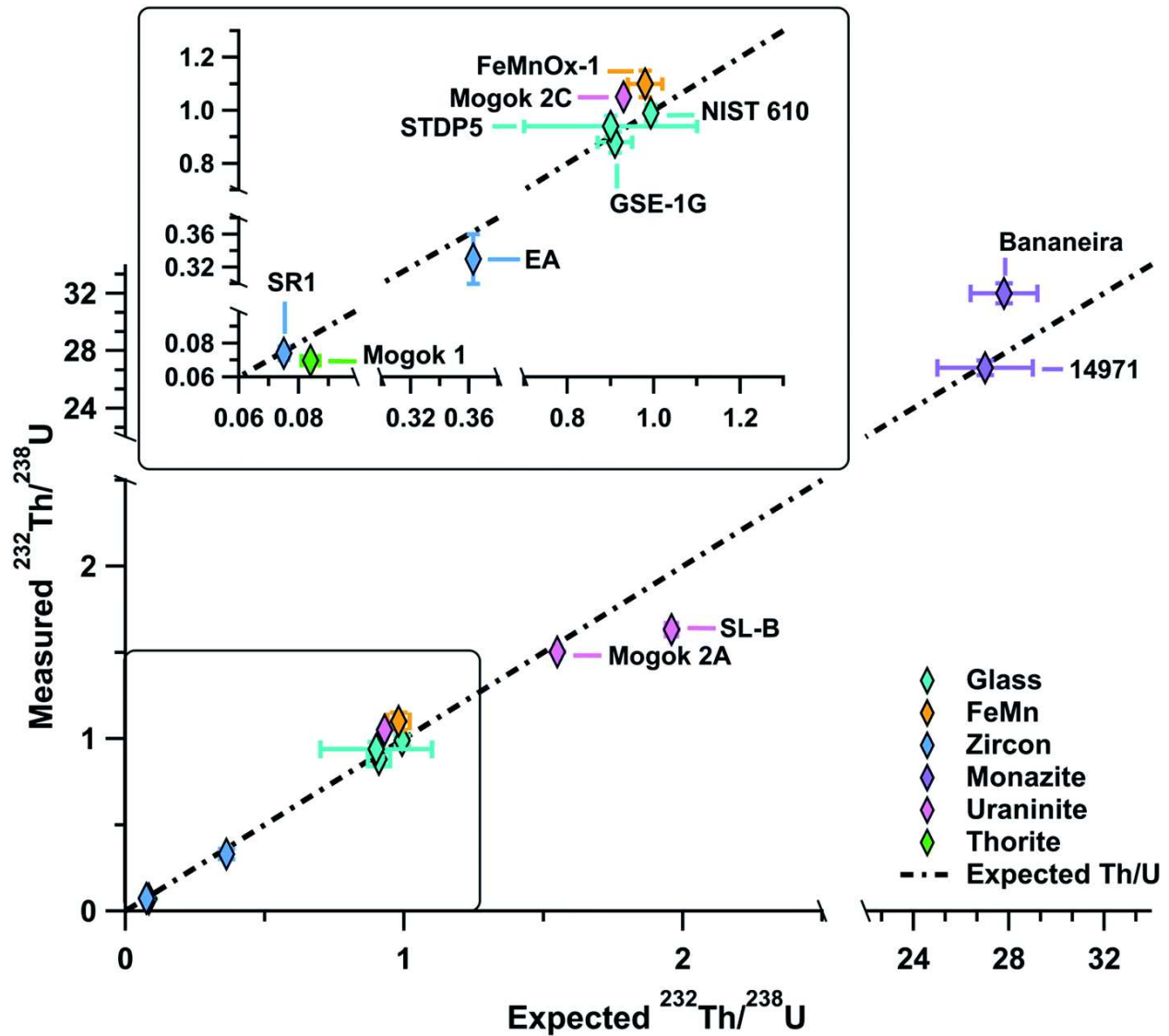


**Figure 4.7** Measured  $^{232}\text{Th}/^{238}\text{U}$  ratios collected with the EUV TOF plotted as a function of the expected ratios in the different sample matrices. Each measured ratio is the raw unnormalized ratio from Figure 4.6. The vertical and horizontal error bars are the  $\pm 2\sigma$  uncertainty of the measured and expected ratios, respectively. The inset plot is zoomed in on the  $^{232}\text{Th}/^{238}\text{U}$  ratios that have values less than 1.3.

Additionally, the  $^{232}\text{Th}/^{238}\text{U}$  ratio measured in the Bananeira monazite is not within analytical uncertainty of the expected value, and it is biased higher than would be expected based on the ratio measured in the other monazite (14971). That is, the  $^{232}\text{Th}/^{238}\text{U}$  ratio measured in the Bananeira monazite does not overlap the ratio measured in 14971 within  $\pm 2\sigma$ . As stated earlier, ID-TIMS measurements detected discordance in the Bananeira samples. The discordant  $^{232}\text{Th}/^{238}\text{U}$  ratio measured in the Bananeira monazite with ID-TIMS is 29.9 as compared to the expected  $^{232}\text{Th}/^{238}\text{U} = 27.8$ .<sup>104</sup> The

$^{232}\text{Th}/^{238}\text{U}$  ratio measured on the Bananeira sample with the EUV TOF is  $32.0 \pm 0.7$ , which is relatively close to the discordant ratio measured by ID-TIMS. Like the  $^{206}\text{Pb}/^{238}\text{U}$  ratio, the high  $^{232}\text{Th}/^{238}\text{U}$  ratio measured by the EUV TOF in the Bananeira monazite is likely from discordance.

The  $^{232}\text{Th}/^{238}\text{U}$  ratio measured in the FeMnOx-1 sample is also biased higher than expected, agreeing within  $\pm 3\sigma$  of the expected value. Prior studies on FeMnOx-1 using LA ICP-MS shows a variation of  $\sim 15\%$  in the Th composition when analyzing the material using 40 to 100  $\mu\text{m}$  laser spot sizes.<sup>103</sup> Therefore, at the 8  $\mu\text{m}$  spatial scale of the EUV TOF analysis further variation in the isotopic composition could be present.

#### 4.e Conclusions

The results from this study show that the EUV TOF can measure  $^{206}\text{Pb}/^{238}\text{U}$  and  $^{232}\text{Th}/^{238}\text{U}$  isotope ratios in select glasses, iron manganese, zircons, and monazites within  $\pm 2\sigma$  of the expected value at the 8  $\mu\text{m}$  lateral and 500 nm depth scales. While  $^{232}\text{Th}/^{238}\text{U}$  isotope ratios can be measured directly from each sample without an external calibration standard, the  $^{206}\text{Pb}/^{238}\text{U}$  ratios possess a systematically low bias that we show can be accounted for using NIST 610 as a non-matrix matched external calibration standard. This indicates that the EUV laser ablates and ionizes these specific materials in such a way that Pb, Th, and U have similar responses from matrix-to-matrix. The  $^{206}\text{Pb}/^{238}\text{U}$  and  $^{232}\text{Th}/^{238}\text{U}$  ratios were also measured in uraninite and thorite samples but showed more uncertainty. Further studies are required to understand the uncertainty in the  $^{206}\text{Pb}/^{238}\text{U}$  and  $^{232}\text{Th}/^{238}\text{U}$  isotope ratios measured in these samples as well as other select samples like the Bananeira monazite, which could be from sample discordance or heterogeneity or from instrumental limitations of the EUV TOF, like the detector performance at high signal intensities.

A broader investigation of the relative sensitivity factors (i.e., RSFs) of other elements and isotopes of interest in different geological materials using the EUV TOF would also be a beneficial metric to further assess its matrix effects. Additionally, increasing the EUV TOF's sensitivity by upgrading the

detector and/or electronics would aid in improving the accuracy of the isotope ratio measurements, especially at low ion counts. These results also contribute to the growing body of research that show the potential of the TOF MS for elemental and isotope ratio measurements, offering ease-of-use and a flexible mass range.<sup>45,51,74,90,106,113–115</sup> However, the EUV TOF MS is limited in highly precise and accurate isotope ratio measurements that are typically required for geochronology, specifically at the 8  $\mu\text{m}$  spatial scale that is used for the analysis here. Expanding the capability of the EUV laser ablation and ionization source by coupling it to other types of mass spectrometers, like the sector-field multi-collector mass analyzers, could overcome the limitations of the TOF and provide the precision and accuracy needed for dating minerals at the microscale. Furthermore, examining the fundamental EUV laser-material interactions with the different materials investigated here would also contribute to further insight into the EUV laser ablation and ionization processes at the laser-sample interface. Directly comparing the EUV laser-material interactions on geologic materials with other techniques, like LA ICP-MS or SIMS, would help further expand the EUV laser's analytical capabilities as a next generation probe for mass spectrometry applications at the microscale and below.

## **5. EUV MAGNETIC SECTOR DEVELOPMENT**

### **5.a Overview**

In Chapters 2-4, the reader was shown how an EUV laser can be used with a TOF mass spectrometer to measure the isotopic composition in different materials, namely nuclear and geologic materials, at spatial scales ranging from ~10  $\mu\text{m}$  down to 100 nm. The strengths of using the EUV laser with a TOF mass spectrometer is the wide mass range that can be detected in a single laser ablation event as well as the TOF's ease of use, both in terms of its operation and its high compatibility with a pulsed ionization source like the EUV laser. However, a TOF is limited in its ability to offer precise (<1%) isotope ratio measurements that are often needed to appropriately identify, trace, or date nuclear or geologic materials. The aim of the work presented in Chapter 5 is to expand the use of the EUV laser for high precision isotope ratio measurements at high spatial scales by connecting the laser to a magnetic sector multi-collector mass spectrometer. Unlike TOFs, sector-field multi-collector mass spectrometers particularly excel in measuring complex isotope ratios with high precision (<1%) and high sensitivity (<ppm), depending on the analyte concentration and sampled volume. These types of mass spectrometers are therefore the choice systems in geologic and nuclear applications where isotope ratio variations on the order of 1% or less need to be measured at trace levels and/or with high spatial resolution to pinpoint the origin, age, or intended use of the material.

### **5.b Background on sector-field multi-collector mass spectrometers**

A sector field multi-collector mass spectrometer is a specific type of mass analyzer that, in its simplest form, uses a magnetic field for mass separation followed by multiple detectors (i.e., multi-collectors) for measuring ions of different mass/charge simultaneously. The use of multiple detectors specifically permits high precision (<1%, 2SD) isotope ratio data to be obtained with a high dynamic range

(from single ion counts to  $10^7$  counts per second) because different isotopes are detected by multiple detectors with variable gains. However, to explain how these types of mass spectrometers work, the terms “sector-field” and “multi-collector” can be split into two separate categories being as not all sector-field mass spectrometers are multi-collectors.

Despite being relatively complex, sector-field mass spectrometers were the first type of mass analyzers to be developed in the early 20<sup>th</sup> century for the discovery of isotopes by physicists J. J. Thompson and Frances Aston and further developed by Alfred Nier, amongst others. Sector-field mass spectrometers are so named because they are composed of sectors made up of electromagnetic fields for mass separation. The Lorentz force law is consequently the fundamental equation for understanding how ions behave in a sector-field instrument because it describes the force ( $\mathbf{F}$ ) that the ions, with a charge ( $q$ ) and velocity ( $\mathbf{v}$ ), experience in either an electric ( $\mathbf{E}$ ) or magnetic ( $\mathbf{B}$ ) field, as shown in Equation 5.1 (where  $\times$  is the vector cross product and all boldface quantities are vectors):

$$\mathbf{F} = q (\mathbf{E} + \mathbf{v} \times \mathbf{B}) \quad 5.1$$

Therefore, ions in a uniform electric field and where  $\mathbf{B} = 0$  experience an electric force ( $\mathbf{F}_E$ ) according to Equation 5.2:

$$\mathbf{F}_E = q\mathbf{E} \quad 5.2$$

Positive ions experience a force in the direction of the electric field, while negative ions experience a force opposite of the direction of the electric field. Ions in a uniform magnetic field and where  $\mathbf{E} = 0$  experience a magnetic force ( $\mathbf{F}_B$ ) according to Equation 5.3:

$$\mathbf{F}_B = q\mathbf{v} \times \mathbf{B} \quad 5.3$$

The magnetic force experienced by an ion is perpendicular to the ion’s velocity and causes an ion to move in a circular motion, whose direction of motion will depend on its charge with respect to the direction of the magnetic field. Equation 5.3 shows that the force an ion experiences in a magnetic field depends on the

ion's velocity as well as the ion's charge and the magnetic field strength, while Equation 5.2 shows that the force in an electric field only depends on the ion's charge and the strength of the electric field.

In a sector-field mass spectrometer, the ions travel through the electric and magnetic sectors in a path that follows the radius ( $r$ ) of the electric and magnetic sectors. In the electric sector, ions are filtered according to their energy using a static electric field ( $\mathbf{E}$ ), so the total energy of the positive ions is conserved. That is, the ions enter the electric sector with kinetic energy ( $U_K$ ) (recall Equation 2.2 from Chapter 2). Once in the electric sector, the kinetic energy transforms to potential energy ( $U_{P,E}$ ), which for simplicity is written in Equation 5.4 for a parallel plate capacitor:

$$U_{P,E} = qE(r - r_0) \quad 5.4$$

Therefore, in the electrostatic sector, the positive ions move in a constant radius ( $r$ ) to maintain a constant potential energy. Positive ions with a larger initial kinetic energy will have a larger radius of travel than ions of the same mass and charge in the electric sector, as shown in Equation 5.5:

$$r = \frac{U_K}{qE} \quad 5.5$$

In the magnetic sector, the ions experience both the magnetic force ( $\mathbf{F}_B$ ) alongside an equal and opposite centrifugal force ( $\mathbf{F}_c$ ) with a radius of travel ( $r$ ), shown in Equation 5.6:

$$\mathbf{F}_c = \frac{mv^2}{r} \hat{r} \quad 5.6$$

Unlike electric sectors, magnetic sectors possess a mass/charge dependence that results in mass separation, assuming a group of ions have a uniform velocity (or energy) when entering the magnetic field. In the magnetic sector, the ions will experience a centrifugal force equal and opposite to the magnetic force, shown in Equation 5.7:

$$\frac{mv^2}{r} = qvB \quad 5.7$$

Equation 5.7 can be rewritten in terms of the ion's velocity ( $v$ ) and simplified to Equation 5.8:

$$v = \frac{rqB}{m} \quad 5.8$$

Considering the ion's kinetic ( $U_K$ ) and potential ( $U_P$ ) energy from Equations 2.2 and 2.3 in Chapter 2, Equation 5.8 can then be substituted into the velocity term of Equation 5.7 to obtain Equation 5.9:

$$r = \sqrt{\frac{m2U_K}{qB^2}} \quad 5.9$$

Or rewritten in terms of the ions mass ( $m$ ) and charge ( $q$ ), one obtains Equation 5.10:

$$\frac{m}{q} = \frac{B^2r^2}{2U_K} \quad 5.10$$

Equations 5.9 and 5.10 highlight the mass dependence on the radius of the ions trajectory as they travel through a magnetic sector. Assuming a constant magnetic field and energy, then from Equation 5.10, we see that heavier ions will have a larger radius ( $r$ ) of travel than lighter ions. In this way, a magnetic sector is used as an effective mass analyzer for separating ions with different mass/charge.

As stated previously, it is important that the ions entering the magnetic sector possess a near-uniform velocity ( $v$ ) (or similar energies) due to the velocity dependence in the Lorentz force of the magnetic field ( $F_B$ ). If ions of the same mass/charge enter the magnetic sector with very different velocities, then they will experience different forces and thereby travel different radial paths ( $r$ ) due to their velocity rather than solely due to their mass/charge. This difference, or spread, in the velocity of the ions will affect the mass resolution of the instrument or the ability to distinguish between ions of different mass/charge.

To limit the velocity dispersion of the ions, which is directly correlated to their difference in energies ( $U$ ) as explained previously, you will often find electric sectors preceding magnetic sectors in what is called a "forward geometry" configuration of sector-field mass spectrometers. Figure 5.1 shows a simplified diagram of a sector-field mass spectrometer in the forward geometry. In this type of configuration, the electric sector filters the ions with respect to their energy so that when the ions travel into

the magnetic sector their difference in energies is minimized, resulting in an increased mass resolution. A smaller spread in the ions' energies will directly correlate to a higher mass resolution. In this discussion, one might notice similarities between the electric sector in the sector-field mass spectrometer and the reflectron in the TOF. Both the electric sector and reflectron possess similar jobs of using an electric field to filter ions with respect to their energy, helping to increase the mass resolution of the system.

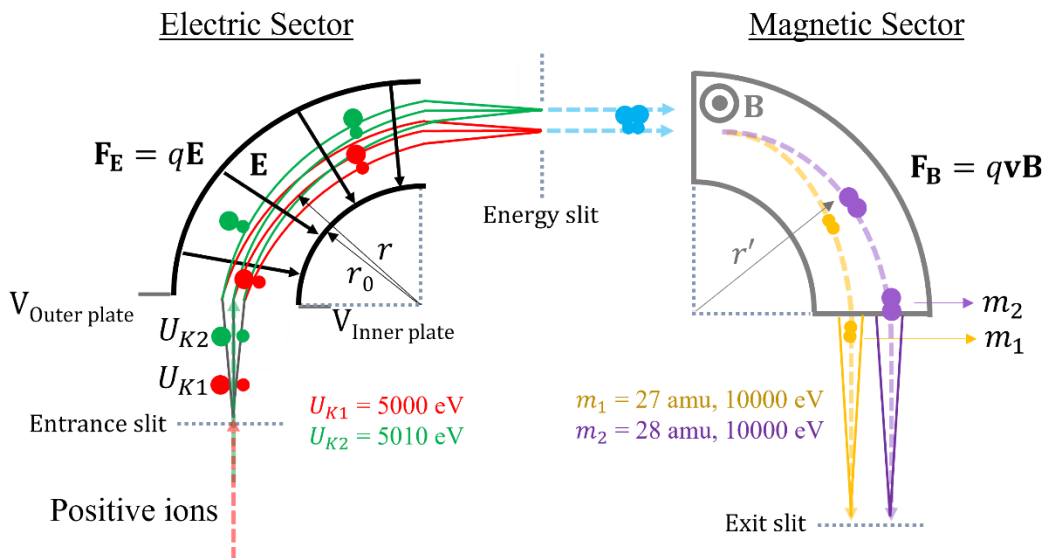


**Figure 5.1** A simplified diagram of a dual sector-field mass spectrometer in the forward geometry with the electric sector preceding the magnetic sector. The positive ions travel over a radius ( $r$ ) through the electric sector where they are filtered with respect to their energy via an electrostatic force ( $\mathbf{F}_E$ ) before traveling into the magnetic sector where they are separated according to their mass/charge using a magnetic force ( $\mathbf{F}_B$ ). Variables in bold are vectors.

Additionally, sector-field instruments typically use ion optics that ensure the energy dispersion in the electric and magnetic sectors are equal in magnitude but opposite in sign. This results in the energy dispersion of both sectors being cancelled out in the image plane of the mass analyzer (i.e., where the ions are detected). Ion optics in sector-field instruments will also correct for differences in the angular distributions of incoming ions (which is not depicted in Figure 5.1). Therefore, ions of the same mass/charge but with different ion energies and different angular distributions are focused onto the same mass in the focal plane of the mass analyzer, ensuring proper mass analysis. When a sector-field mass spectrometer focuses ions with respect to their energy and angular distribution it is called double focusing, a common designation of modern-day sector-field instruments.

Of course, not all sector-field mass spectrometers are constructed in the forward geometry. “Reverse geometry” configurations also exist with the electric sector preceding the magnetic sector. Sector-field mass spectrometers made in the reverse geometry are used for mass analyses that require increased mass resolution and transmission than the forward geometry can offer. In reverse geometry instruments, the ions are filtered by their mass before being filtered and focused by their energy. Through this route, only an ion beam made up of a single mass/charge is transmitted through the mass spectrometer, reducing the effects of neighboring interfering ions via their elimination early in the instrument’s magnetic sector and with relatively good transmission of the ion beam of interest. Therefore, reverse geometry configurations are desired when the isotopes of interest exist at trace levels with close interferences, such as the case of measuring U-Pb in minerals using ion beam sputtering (i.e., SIMS) for geologic dating.

There also exists other types of sector-field configurations that use more than two sectors for benefits towards specific applications. There are also single-sector mass spectrometers that only possess a magnetic sector. The latter is commonly seen in applications that use a thermal filament as the ionization source because the energy spread can be minimal (i.e., <1 eV) in these sources (compared to ion beam sputtering and ICP ionization routes, for example), precluding the need for an energy filter. Overall, sector-field configurations widely vary and factors such as ionization source, type of analyses, etc. should be considered when determining the optimal set-up. This dissertation will focus on the use of a dual sector-field mass spectrometer with an electric and magnetic sector configured in the forward geometry.

Now that the fundamentals of how a sector-field mass spectrometer filters ions according to energy and/or mass, the detector (or “multi-collector”) section can be added into the discussion to complete the instrument’s function. In the forward geometry of a dual sector-field mass spectrometer the ions that are separated according to mass/charge in the magnetic sector travel downstream to an array of detectors that are placed at the focal plane of the mass analyzer. The detectors are positioned at the mass of interest. Incoming ions that correspond to the mass that the detector is placed at will travel into the corresponding detector. Ions of different mass/charge will therefore travel into different detectors. The

detector array is typically made up of Faraday cups and ion counting electron multipliers for lower (typically  $\geq 1000$  cps) and higher (hundreds to single ion counts) gain isotope measurements, respectively. The use of multiple detectors provides increased ion sensitivity for isotope ratio measurements as well as an independence from fluctuations in the ionization source because of simultaneous isotope measurements on multiple detectors. This capability provides a range of isotope systems to be accurately and precisely measured. However, the mass range of sector-field multi-collector systems are limited, especially compared to TOF mass analyzers. Most sector-field mass spectrometers are typically limited to simultaneous measurements of masses in an  $\sim 40$  amu range (but this ultimately depends on the multi-collector configuration). If a wider mass range needs to be measured, separate analyses will need to be performed at each mass range. It should be noted that dual sector-field mass spectrometers operated in the reverse geometry are “single-collectors” because an ion beam of only a single mass is transmitted through to the detector. This explains why not all sector-field mass spectrometers are “multi-collectors”.

The most common ionization sources used with sector-field mass spectrometers are inductively coupled plasmas (ICPs), ion beam bombardment (SIMS/NanoSIMS), and thermal ionization (TIMS). All are continuous, hard ionization sources that provide a constant stream of ions into the sector-field mass spectrometer. Because sector-field mass spectrometers are specifically designed for elemental and isotopic measurements, hard ionization sources are used with these types of analyzers. Each ionization source excels in different areas. In general, TIMS typically provides the most precise isotope ratio measurements but can have complex sample preparation and can only perform bulk analyses. Laser ablation ICP-MS has fast analysis times and does not require extensive sample preparation but can only spatially resolve elemental and isotopic information down to a few microns. SIMS/NanoSIMS has the best spatial resolution being able to reach  $\leq 50$  nm lateral resolution but is limited in its quantitative capabilities because of the high dependence on the ion sputtering process with the chemical and physical composition of the sample being analyzed. There is not a “one size fits all” when it comes to the different ionization sources

used with sector-field mass spectrometers. Often, different techniques will be used to analyze the same sample, each providing their own angle to the overall analysis.

The goal of the work in this fifth chapter is to demonstrate that a pulsed 46.9 nm wavelength EUV laser ionization source can be coupled to a sector-field multi-collector mass spectrometer with the eventual aim of spatially resolve isotopic information. Specifically, EUV laser light could offer improvements in spatial resolution over typical UV/Vis/IR lasers because the shorter 46.9 nm wavelength light can be focused down to spot sizes of 80 nm. Additionally, as was previously shown, EUV laser ionization generates fewer molecular ions than ion beam sputtering. It is therefore interesting to understand if EUV laser ionization can be used with a sector-field multi-collector mass spectrometer to perform isotope ratio measurements with sensitivity at or below ppm levels with precisions of  $\leq 1\%$  at high spatial scales ranging from the micro down to nano scales.

The following sections will describe how the EUV capillary discharge laser is interfaced with a modified commercial sector-field multi-collector mass spectrometer called the Neptune made by Thermo Fisher. First, the components of the Neptune will be described in detail. This will be followed by the design of the EUV laser interface system that attaches to the entrance of the Neptune by removing the Neptune's ICP ionization source. The steering and focusing optics used to transmit the ions created by EUV laser ionization from the interface region into the Neptune will be described. A discussion of the modifications made to the electric and magnetic sectors for proper mass separation and subsequent detection of the EUV-generated ions using the Neptune's electron multipliers will be described. Future experiments to fully enable multi-collection and accurate isotope ratio measurements using the newly built EUV magnetic sector instrument will also be outlined.

## **5.c Neptune sector-field multi-collector mass spectrometer**

### **5.c.i Neptune overview**

The Neptune is a double-focusing sector-field multi-collector mass spectrometer that was made by Thermo Fisher Scientific (the Neptune has recently been replaced with a newer predecessor called the Neoma). The Neptune is designed in the forward geometry with the electric sector preceding the magnetic sector followed by an array of multiple detectors (i.e., multi-collectors) for simultaneous mass/charge measurements. Following the terminology of the Neptune Hardware Manual for simplicity, the Neptune can be split into three different modules: (1) the “ICP Module”, (2) the “ESA Module”, and (3) the “Multi-collector Module”. Figure 5.2 provides a graphical depiction of each of the modules.

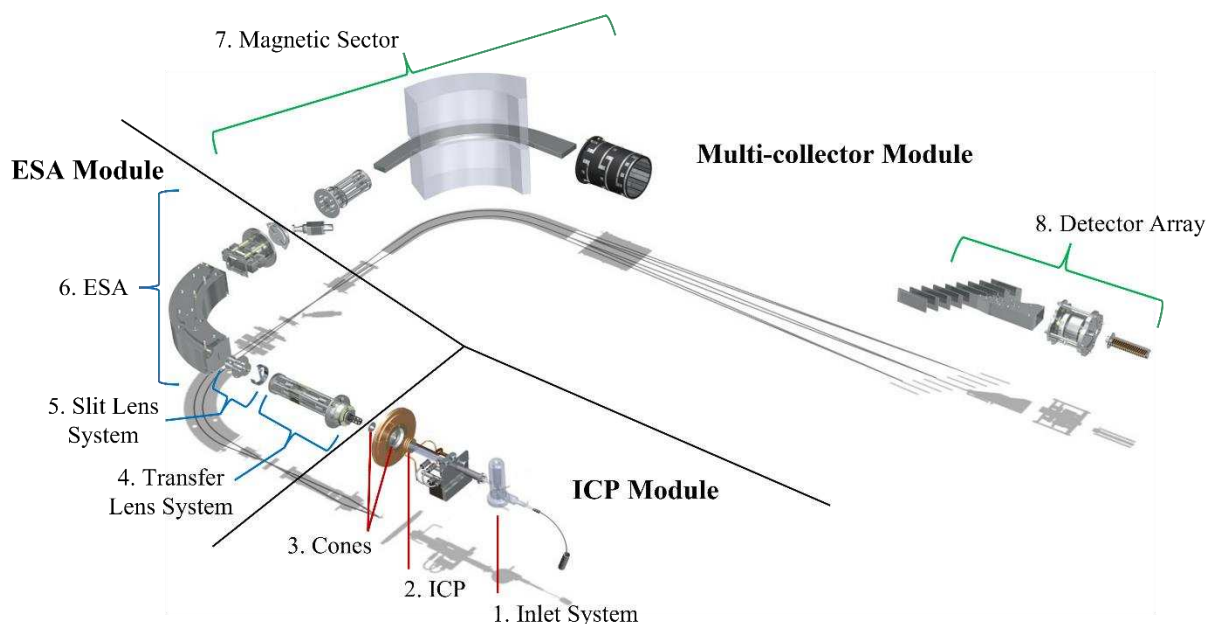


**Figure 5.2** A diagram of the different modules of the Neptune. The ions are created in the ICP Module and subsequently focused, steered, and accelerated in the ESA Module before being separated according to the ions’ mass and charge and detected in the Multi-collector Module. The components in each module are further expanded in Table 5.1 and Table 5.2. [Image adapted from Thermo’s Neptune Hardware Manual]

Each module consists of different components that ultimately work together to optimize the incoming positive ions generated from an ICP ionization source for mass analysis. Table 5.1 outlines the different components in each module of the Neptune shown in Figure 5.2. Table 5.2 lists the corresponding potentials typically applied to each ion optic component used for transferring and focusing the ions into the detector region. Each of these listed components will be detailed further in the upcoming sections.

**Table 5.1** The components of the ICP, ESA, and Multi-collector Modules in the Neptune.

<b>ICP Module</b>	<b>ESA Module</b>	<b>Multi-collector Module</b>
1. Inlet System 1.a Nebulizer 1.b Spray Chamber 1.c Laser Ablation System	4. Transfer Lens System 4.a Extraction Lens 4.b Focus Lens 4.c X/Y Deflection 4.d Lens 4 4.e Lens 5 4.f Shape Quadrupole 4.g Turbo Pump A 4.h Turbo Pump C	7. Magnetic Sector 7.a Gate Valve 7.b Zoom Lens #1 7.c Magnet 7.d Zoom Lens #2 7.e Ion Getter Pumps (x2)
2. ICP 2.a Torch	5. Slit Lens System 5.a Low, Medium, and High Mass Resolution Slits 5.b Rotation Quadrupole #1 5.c Focus Quadrupole #1 5.d. Turbo Pump B	8. Multi-collectors 8.a Electron Multipliers (x5) 8.b Faraday Cups (x10)
3. Cones 3.a Sample Cone 3.b Skimmer Cone 3.c Skimmer Cone Gate Valve 3.d Interface Vacuum Pump	6. ESA 6.a Herzog Plates (x2) 6.b ESA Outer Plate 6.c Matsuda 6.d ESA Inner Plate 6.e Acceleration Lens 6.f Intermediate Slit 6.g Rotation Quadrupole #2 6.h Turbo Pump D	

**Table 5.2** Typical nominal potentials applied to each component in the Neptune listed in Table 5.1. The components are listed in order of appearance in the ions' path. Values in parenthesis represent the potential range that can be adjusted by the user in the Neptune software from its typical operating potentials if necessary. The potential listed for the magnet is the field probe value (in volts) and the values in brackets are the corresponding magnetic field strengths (in Tesla).

<b>Neptune</b>	<b>Nominal (V)</b>
(2.a) ICP	Ground
(4.a) Extraction Lens	-2000
(4.b) Focus Lens	-450 to -650
(4.c) Y(+/-) Deflection	-1830 ( $\pm 50$ )
(4.c) X(+/-) Deflection	-1860 ( $\pm 50$ )
(4.d) Lens 4	-2000
(4.e) Lens 5	-5000
(4.f) Shape Quadrupole	-4800 (+200)
(5.b) Rotation Quadrupole #1	-5000 ( $\pm 20$ )
(5.c) Focus Quadrupole #1	-5000 ( $\pm 20$ )
(6.a) Herzog Plates	-5000

(6.b) ESA Outer	-4600
(6.c) Matsuda Plate	-5000 ( $\pm 20$ )
(6.d) ESA Inner	-5400
Vertical Deflection	-5000
(6.e) Acceleration Lenses	-10000
(6.g) Rotation Quadrupole #2	-10000 ( $\pm 20$ )
(7.b) Zoom Lens #1	OFF
(7.c) Magnet Field Probe	0.05 [0.15 Tesla] to 11.08 [1.20 Tesla] *(1.90 V = 28 amu; 7.68 V = 197 amu)
(7.d) Zoom Lens #2	OFF
(8.a) Electron Multipliers	-2000 to -2300
(8.b) Faraday Cups	N/A
HV Control	-10000 ( $\pm 50$ )

Briefly, in its commercial form, the Neptune is designed with an ICP as the ionization source, whereby liquid, gas, or solid samples that have been aerosolized are sent into the ICP. Using differential pumping and a series of negatively biased lenses, positive ions are extracted from the grounded ICP module and subsequently focused and accelerated to a nominal energy of (-)5000 eV into an electrostatic sector (also known as the electrostatic analyzer or ESA). The ESA filters the ions with respect to their energy and the transmitted ions are focused through a narrow slit that defines a ~5-10 eV energy window. After exiting the ESA, the ions are further focused and accelerated to a nominal energy of (-)10000 eV via acceleration lenses before entering the magnetic sector that separates the ions according to their mass/charge using a magnetic field. The magnetic field can be adjusted via a magnetic field probe up to 1.2 Tesla to span a mass range from approximately 1 amu to 310 amu at a nominal ion energy of (-)10000 eV. Each mass separated ion beam travels into their own separate detector that is placed at the corresponding mass of interest in the multi-collector module. A combination of ten Faraday cups and five ion-counting electron multipliers are used to detect ions signals on the order of  $10^7$  counts per second (cps) down to single ion counts, respectively. Eight of the Faraday cups and one of the electron multipliers can be physically moved via motor-driven platforms. The use of multiple and moveable detectors gives the Neptune wide-ranging utility in measuring a variety of isotopic systems with high precision (<1%, 2SD) and sensitivity ( $\leq 1$  ppm), depending on the sampled volume.<sup>116</sup> In the following sections, each component listed in Table 5.1 and Table 5.2 will be further detailed.

### **5.c.ii ICP module**

The ICP module is only briefly outlined here because it will be removed from the Neptune for attachment of the EUV laser ionization source. The ICP module consists of the inlet system for sample introduction, the ICP for sample ionization, and the cones for separating the ions from the gas stream created in the ICP. The inlet system is where liquid or gas samples are introduced into the ICP via a nebulizer that aerosolizes the sample. The aerosol is then sent into a spray chamber that refines the aerosol mixture by removing larger droplets before being sent into the ICP for ionization. In Figure 5.2, the inlet system shown consists of a nebulizer attached to a spray chamber. Alternatively, solid samples can be analyzed with the Neptune by replacing the nebulizer and spray chamber with a UV/Vis/IR laser system that ablates and aerosolizes an area of the solid sample before being sent into the ICP.

After the liquid, gas, or solid sample is aerosolized and then ionized by the ICP, the ions travel into the vacuum region of the mass spectrometer through two small (<1 mm in diameter) orifices called cones. The first cone is called the sample cone while the proceeding cone is called the skimmer cone. The region between the two cones is evacuated by an interface pump. Behind the skimmer cone, marking the end of the ICP module, the remainder of the system is under high vacuum (<10<sup>-4</sup> Torr) using turbo and ion getter pumps. The pressure differential created in the interface region between the cones and after the skimmer cone draws the ions from the atmospheric pressure ICP into the lower pressure mass spectrometer region, removing the excess gas stream that travels with the ions from the ICP. The ions created in the ICP start near ground potential.

### **5.c.iii ESA module – Transfer lens system**

After the ions created in the ICP travel through the sample and skimmer cones, positive ions are extracted from the cone region, focused, and accelerated by the transfer lens system, marking the beginning of the ESA module. Figure 5.3 shows a picture and diagram of the different ion optics making up the transfer lens system alongside the applied voltages.

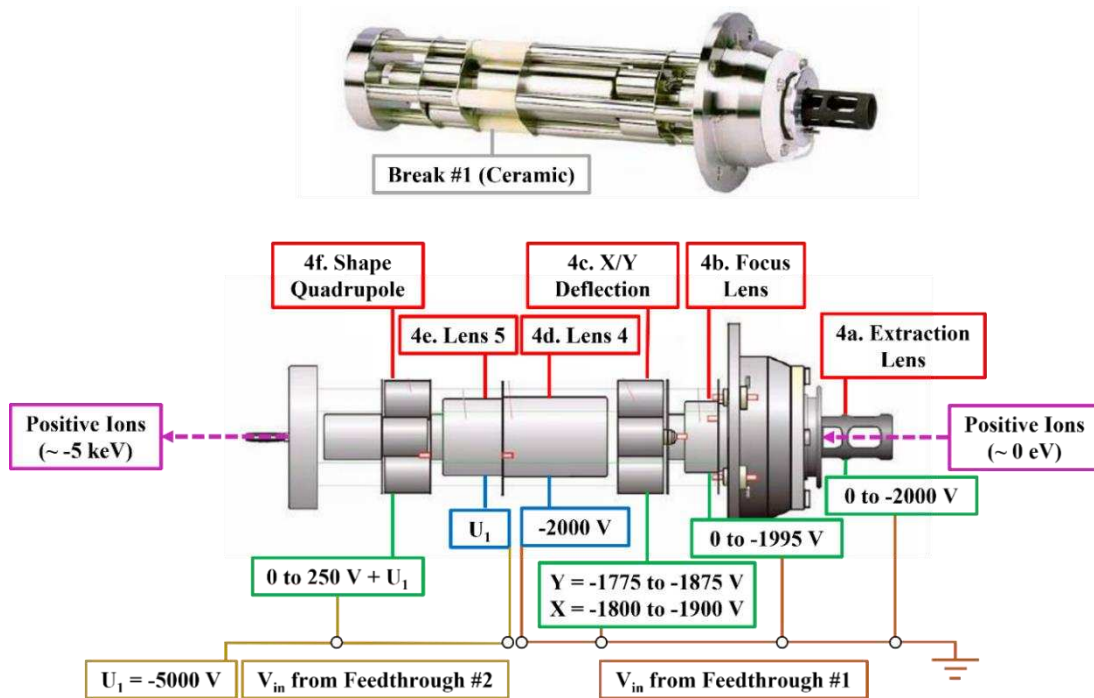


**Figure 5.3** Picture (top) and diagram (bottom) of the transfer lens system at the start of the ESA module in the Neptune. Positive ions are drawn into the mass spectrometer using a negatively biased extraction lens (4a). The ions are subsequently focused (4b), steered (4c), accelerated (4d, e), and shaped (4f) by a series of biased lenses for transport into the proceeding slit lens system. The corresponding voltage applied to each element in the transfer lens system is shown in the picture. Voltages highlighted by a green box can be adjusted within the listed range in the Neptune’s software interface, while voltages in blue boxes are fixed and cannot be adjusted in the software. Lenses 4a-d have a base potential at instrument ground and are biased via conductor pins on “Feedthrough #1”, while lenses 4e-f have a base potential at a nominal value of  $U_1 = (-)5000$  V and are biased from conductor pins on “Feedthrough #2.” A ceramic break (“Break #1” is placed between Lens 4 and 5 due to the change in base potential (“Break #1”). All base potentials are referenced to +10 V. [Image taken from Thermo’s Neptune Hardware Manual]

The extraction lens is the first component in the transfer lens system. It is made of pure graphite and is biased negatively to extract the positive ions from the cone region. The extraction lens is typically operated at a nominal bias of (-)2000 V but can be varied down to 0 V via the Neptune’s software. The extracted positive ions travel down the length of the extraction lens and through a small ~5 mm sized aperture at the end of the lens (not shown in Figure 5.3). At this point, the positive ion beam is divergent and needs to be focused with the lens that immediately follows the extraction lens so that the ion beam can travel through the downstream mass resolution slit in the slit lens system. The focus lens squeezes the ion beam into a narrow vertical line for transmission through the downstream slit lens system. The potential on the focus lens can be changed from 0 to (-)1995 V on the instrument software but is typically operated with a bias between (-)450 to (-)650 V.

The X and Y deflections plates follow the focus lens for horizontal and vertical ion beam positioning, respectively. Both X/Y deflection plates can be changed by ( $\pm$ )50 V from their base potentials. The positive ions are then accelerated to approximately (-)5000 eV using lens 4 and lens 5. Lens 4 is biased to approximately (-)2000 V and lens 5 is biased to approximately (-)5000 V to accelerate the ions. The potentials on lenses 4 and 5 are fixed and cannot be changed in the Neptune software. The (-)5000 eV ions then travel through the last optic in the transfer lens system, the shape quadrupole. The shape quadrupole is responsible for further shaping the beam so that it can fit through the upcoming vertical slits. The potential on the shape quadrupole can be changed by up to (+)250 V from its base potential. Lens 5 and the shape quadrupole are biased higher than the upstream lenses, and so they are electrically isolated via ceramic breaks because of this potential difference, as can be seen in Figure 5.3.

It is important to note that not all potentials on the Neptune instrument software consider the base potentials applied to each component. For example, in the software, the X/Y deflection potential range is shown as (+)50 V to (-)50 V. This potential range correlates to nominal potentials of (-)1780 to (-)1880 V for Y deflection and (-)1810 to (-)1910 V for X deflection (see Table 5.2). Additionally, the ion optics throughout the Neptune have varying base potentials depending on their location in the instrument. The base potential for the extraction, focus, and X/Y deflection lenses as well as lens 4 have base potentials at instrument ground (at +10 V reference). All lenses with a base potential at ground are biased via external connector pins on “Feedthrough #1” located on the outside of the transfer lens system chamber. The base potential for lens 5 and the shape quadrupole have a nominal base potential of (-)5000 V (at +10 V reference), which is hereby referred to as  $U_1$  in the text and figures. The remaining lenses in the ESA module from lens 5 up to the acceleration lens after the ESA plates have a base potential at  $U_1$ . At the acceleration lens, the nominal base potential for all remaining optics is (-)10000 V (at +10 V reference), hereby called  $U_2$ . All lenses with a base potential at  $U_1$  and  $U_2$  are biased via “Feedthrough #2” on the outside of the ESA chamber. For clarity, all figures, tables, and text in this dissertation account for the base potentials.

#### **5.c.iv ESA module - Slit lens system**

After the positive ions have been properly extracted, focused, steered, accelerated to approximately (-)5000 eV, and shaped in the transfer lens system, the ions are ready to travel through the slit lens system. Figure 5.4 shows a picture of the slit lens system, which is composed of the mass resolution entrance slits, rotation quadrupole #1, and focus quadrupole #1. The three modes of operation for the mass resolution entrance slits are low, medium, and high resolution. The low resolution slit has the largest width while the high resolution slit has the smallest width. The slit width determines the mass resolution by defining the ion beam's peak width at the detectors. For example, a mass interference can be physically "cut out" by decreasing the width that the ion beam travels through (if the mass interference is on one side of the peak of interest). While increasing mass resolution is a benefit to certain analyses, it must be performed with care because increasing the mass resolution will result in decreasing the intensity of the ion signal from fewer ions will travel through the narrower slit. The low-resolution mode on the Neptune is typically  $>400 \text{ m}/\Delta\text{m}$  while high resolution mode achieves  $>8000 \text{ m}/\Delta\text{m}$ .

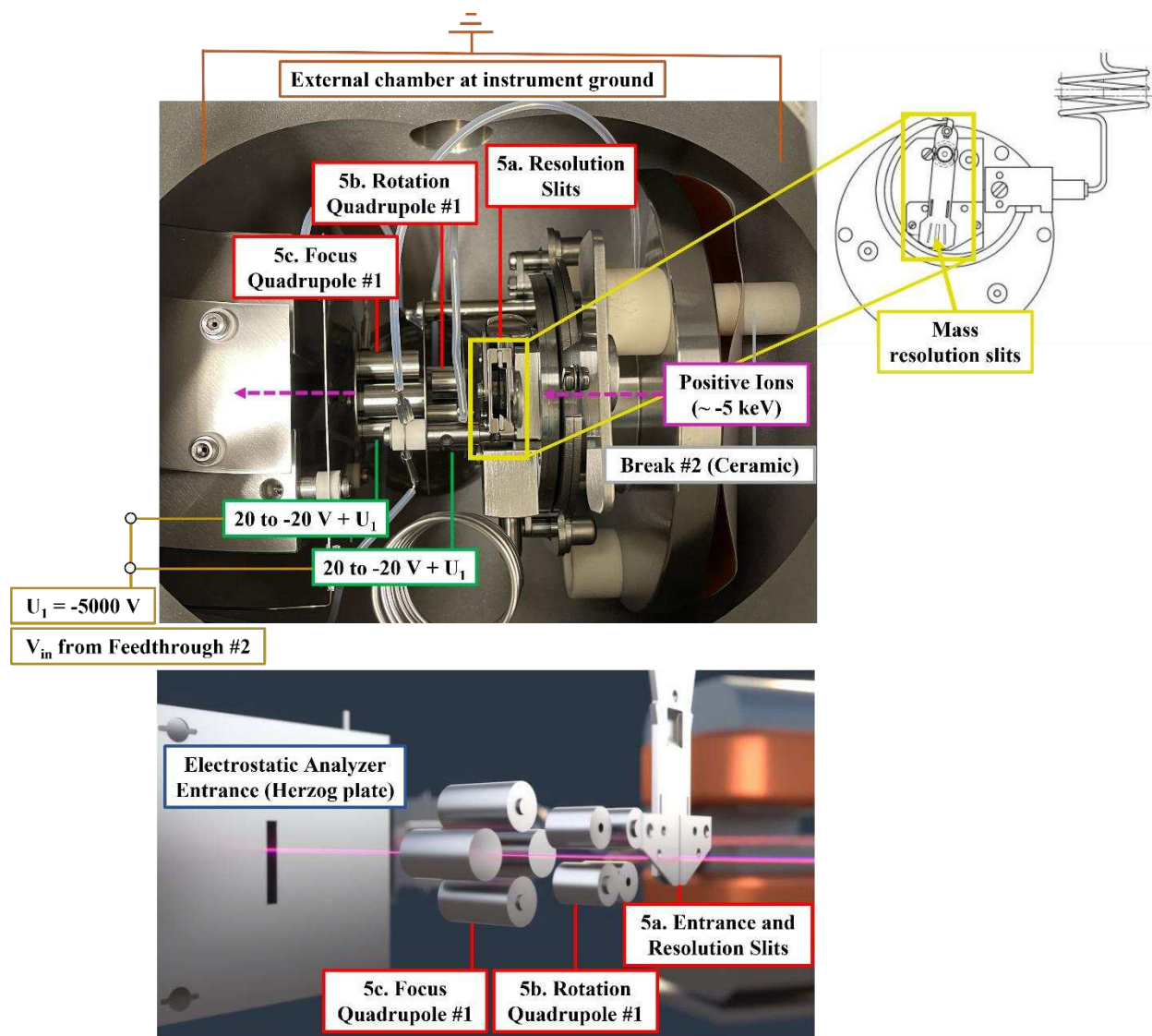


**Figure 5.4** (Top) Picture and (bottom) simulation of the slit lens system in the Neptune. The positive ion beam that has been focused and accelerated by the transfer lens system travels through narrow mass resolution slits (5a) that determine the ion peak width. A pair of proceeding quadrupoles help to further rotate (5b) and focus (5c) the ion beam after passing through the resolution slit if necessary for entrance into the electrostatic analyzer region. The corresponding voltage applied to each element in the slit lens stack is also shown in the picture, which can be adjusted within the specified range in the instrument software. All elements in the slit lens system have a base potential at  $U_1 = (-)5000\text{ V}$  and are biased using conductor pins from “Feedthrough #2.” The slit lens system is electrically isolated from the surrounding external chamber held at instrument ground using a ceramic break (“Break #2”). All base potentials are referenced to +10 V. [Part of Image Taken from Thermo’s Hardware Manual. The simulation graphic is adapted from Thermo’s “Ion Path Video Simulation” of the Neoma MC-ICP-MS.]

After traveling through the resolution entrance slits, the ions are then rotated and focused onto the image plane of the ESA using the two last quadrupoles. Rotation quadrupole #1 and focus quadrupole #1 can both be varied by  $(\pm)20\text{ V}$  from their base potentials ( $U_1$ ). However, these quadrupoles are typically only adjusted during medium and high mass resolution modes. As depicted in Figure 5.4, the

resolution slit system has a nominal base potential at (-)5000 V ( $U_1$ ). The potential of the surrounding chamber that holds the slit system has a base potential at instrument ground. Therefore, there is an internal ceramic break that isolates the slit lens system from its surrounding chamber.

### **5.c.v ESA module - Electrostatic analyzer**

After the positive ions travel through the slit lens system, they enter the electrostatic analyzer (ESA) that deflects the ions approximately  $90^\circ$  and filters the ions with respect to their energy. Energy filtering is followed by acceleration to the ions' final energy of (-)10000 eV prior to entering the magnetic sector. Figure 5.5 and Figure 5.6 shows pictures of the ESA and surrounding ion optics making up the remainder of the ESA module. The ESA is made of two curved plates called the inner and outer plates. The inner plate is biased more negatively than the outer plate so that the positive ions are attracted to the inner plate and repelled by the outer plate. The potential difference between the two plates is approximately (-)785 V, which has been optimized according to the ions' (-)5000 eV energy upon entering the ESA. Ions traveling into the ESA with a higher energy will have a larger radius of travel than lower energy ions. To reduce fringe field effects, two Herzog plates are placed at the entrance and exit of the ESA and biased to (-)5000 V, which defines the center voltage of the ESA.

After leaving the ESA, the ions, with diverging angles, are focused into a cross over at the intermediate slit (or image) that is located between the ESA and magnetic sector and is shown in the simulation graphic in Figure 5.6. Ions with different ion energies are focused onto slightly different spots along the intermediate slit. Depending on the mass resolution slit used, the energy bandpass of the ESA ranges from a few to 10 eV, ensuring that the ions' energy dispersion is reduced for proper mass analysis in the magnetic sector. Unlike other mass spectrometer set-ups, the width of the intermediate slit after the ESA cannot be changed. The potentials on the ESA and Herzog plates are also fixed and cannot be adjusted by the user in the Neptune software. The ESA also has a plate on its top and bottom called the Matsuda plate, which can be changed by ( $\pm$ )20 V in the Neptune software. The Matsuda plate is typically operated

at its base potential of (-)5000 V. The Matsuda plate is typically not adjusted from its base potential but can be used to improve the ion peak shape when operating in high resolution mode.

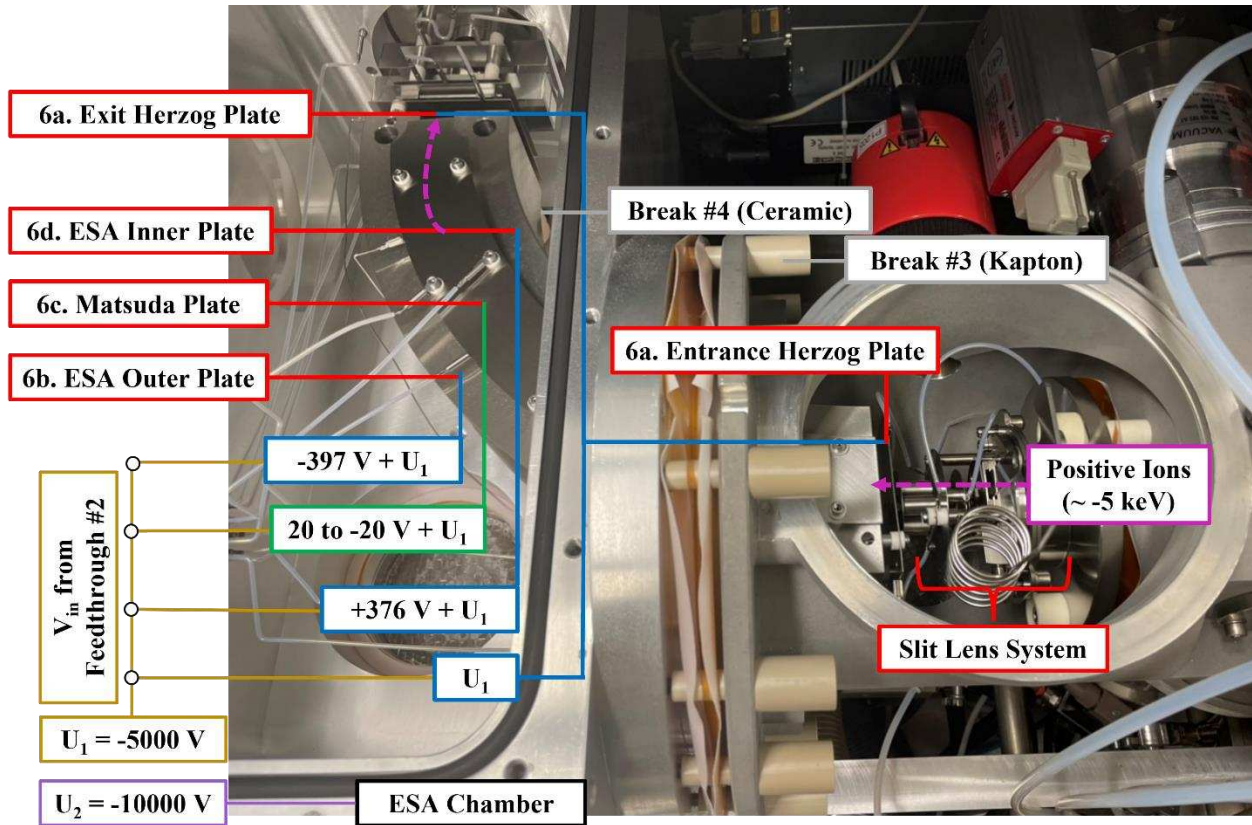


**Figure 5.5** Picture of the ESA section of the Neptune. After the ions travel through the slit lens stack, they proceed to the entrance of the ESA through a Herzog plate (6a). After entering the ESA, the ions are filtered and deflected approximately 90° through the Herzog plate at the exit of the ESA. The ESA consists of the ESA outer (6b) and inner (6d) plates that repel and attract the ion beam, respectively. The ESA also has Matsuda plates (6c) on its top and bottom for extra focusing if needed. The corresponding voltage applied to each element in the ESA is also shown in the picture. Besides the Matsuda plate, all voltages are fixed on the ESA. All elements in the ESA labeled here have a base potential at  $U_1 = (-)5000 \text{ V}$  and are biased using conductor pins from “Feedthrough #2.” The ESA chamber, however, is held at  $U_2 = (-)10000 \text{ V}$ . For this reason, the ESA chamber is isolated from the preceding grounded chamber and from the ESA using an external Kapton break (“Break #3”) and internal ceramic break (“Break #4”), respectively. All base potentials are referenced to (+)10 V.

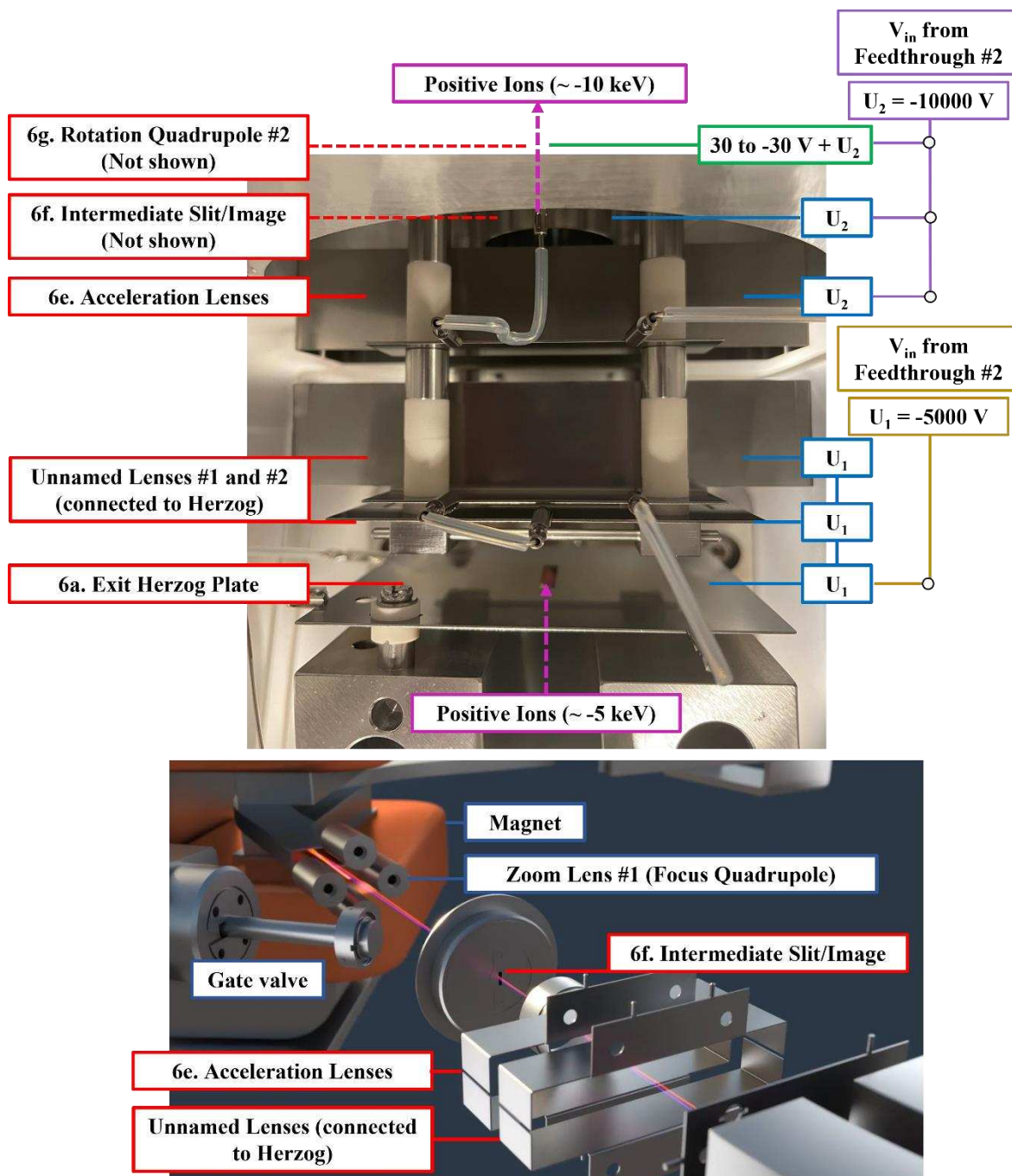


**Figure 5.6** (Top) Picture and (bottom) simulation of the ions exit the ESA through the Herzog plate (6a) with approximately (-)5 keV of energy before being accelerated to their final energy of approximately (-)10 keV by the downstream acceleration lens (6e). The intermediate slit (6f) following the acceleration lens defines the image plane where the ions focused by the ESA reach a crossover point. Only ions within an approximately 5-10 eV window will make it through the intermediate slit for mass analysis in the multi-collector module. A second rotation quadrupole (6g) is located behind the intermediate slit to aid in further alignment of the ion beam if needed. The corresponding voltage applied to each element is shown in the diagram. Besides rotation quadrupole #2, all voltages are fixed. The Herzog plate and the following two unnamed lenses connected to the Herzog plate have a base potential at  $U_1 = (-)5000$  V. The remaining downstream lenses have a base potential at  $U_2 = (-)10000$  V. All lenses are biased via conductor pins from “Feedthrough #2.” All base potentials are referenced to (+)10 V. [The simulation graphic is adapted from Thermo’s “Ion Path Video Simulation” of the Neoma MC-ICP-MS.]

Prior to passing through the intermediate slit, the ions are further focused and accelerated after leaving the ESA through a series of additional ion optics, shown in Figure 5.6. After exiting the ESA, the ions travel through two lenses, which are unnamed, but are electrically connected to the Herzog plates. These plates likely offer some focusing effects and aid in transmitting the ions from the ESA to the acceleration lens. The acceleration lens immediately follows the unnamed slits and accelerates the ions to their final energy of approximately (-)10000 eV. After being accelerated, the ions reach a crossover point at the intermediate slit. After passing through the intermediate slit, the ions travel through rotation quadrupole #2, which can be changed by ( $\pm$ )30 V in the Neptune software. The second rotation quadrupole offers additional alignment capabilities that can be needed when working in high mass resolution mode.

#### **5.c.vi Multi-collector module - Magnetic sector**

Upon exiting the ESA module, the positive ions have been accelerated to their final energy of approximately (-)10000 eV and have been sufficiently focused with respect to their energy. The ions are now ready for mass separation in the magnetic sector portion of the Neptune's multi-collector module. The ions are separated and focused into different positions along the focal plane of the mass analyzer according to their mass and charge as they travel through a magnetic field. The magnetic field separates ions with the same energy according to their mass and charge. Heavier ions will have a larger radius of curvature than lighter ions in the magnetic field.

The magnetic sector is made up of a large, curved magnet with a radius of 23 cm and deflection angle of 90°. The shape of the magnet is in an “extended geometry”, named so because the pole pieces are asymmetric. This type of geometry allows for an equivalent mass dispersion to be achieved as a magnet in the “standard geometry” with a radius of 81 cm, thereby providing a more compact design and ample room for the array of downstream detectors. The magnetic field can be adjusted to a maximum of 1.2 Tesla (12000 Gauss) by adjusting the potential on a magnetic field probe that is located in the air gap of the magnet. At an ion energy of approximately (-)10000 eV, the magnetic field range can be changed over a corresponding mass range of 1 to 310 amu.

### 5.c.vii Multi-collector module – Zoom lenses

At both the entrance and exit of the magnetic sector, there are two quadrupoles called zoom lenses that aid in changing the ions' mass dispersion. Unless special measurements are being performed, the zoom lenses are typically not used during analyses, and so only a brief description of them is given here. Changing mass dispersion comes into play when, for example, the isotopes in a single element need to be subsequently measured at a fixed position without moving the positions of the detectors. The Neptune manual uses the example of measuring  $^{86}\text{Sr}$ ,  $^{87}\text{Sr}$ , and  $^{88}\text{Sr}$ . If one wishes to measure  $^{87}\text{Sr}$  and  $^{88}\text{Sr}$  on the same detectors as  $^{86}\text{Sr}$  and  $^{87}\text{Sr}$ , then the latter requires a slightly wider spacing at the detectors than the former masses. The zoom optics can compensate for the dispersion change that is needed to achieve perfect peak overlap for both isotope pairs being measured in the same detectors without the need to physically adjust the position of the detectors. The zoom lenses can change mass dispersion within a range of approximately  $\pm 5\%$  within a timeframe of milliseconds.

### 5.c.viii Multi-collector module – Detector array

The Neptune's detector array consists of ten Faraday cups and five ion-counting electron multipliers. Eight of the Faraday cups have  $10^{12} \Omega$  resistors for gain amplification and are used to detect ion signal intensities on the order of tens of picoamps ( $\sim 10 \text{ V}$  or  $\sim 10^7 \text{ cps}$ ) down to hundreds of attoamps ( $\sim 0.1 \text{ mV}$  or  $\sim 1000 \text{ cps}$ ). Two of the Faraday cups have  $10^{13} \Omega$  resistors which allows detection of ion signal intensities down to and below tens of attoamps ( $\leq 0.01 \text{ mV}$  or  $\leq 100 \text{ cps}$ ). The electron multipliers are used to detect the lowest intensity ion signals on the order of single ion counts (but can go up to  $\sim 10^5 \text{ cps}$ ).

The main advantages of using multiple Faraday cups for isotope ratio measurements is a wide dynamic range that can cover more than six orders of magnitude (desirable for measuring  $^{234}\text{U}/^{238}\text{U}$  and  $^{235}\text{U}/^{238}\text{U}$  ratios), high gain stability, stable dark current, and long lifetime. The major drawbacks of Faraday cups, however, are the slow response time to changing ion currents, which can induce systematic errors in isotope ratio measurements when ion signals are rapidly fluctuating or are transient in nature (like

that from laser ablation sample introduction). Additionally, Faraday cups with a current amplifier can have high dark current equivalent up to hundreds of cps from the signal amplification's feedback resistor. Therefore, while Faraday cups' stability are ideal for the highest precision isotope ratio measurements, they are not ideal for measuring the smallest ion signals on the order of tens to single ion counts like that of ion counting electron multipliers. However, electron multipliers have their own drawbacks. For instance, care must be given to time-dependent changes in the gain of ion counting detectors that can be a major contribution to analytical errors in isotope ratio measurements. Overall, the expectation is that the ion counting electron multipliers in the Neptune will be more suitable for measuring ions created from the EUV laser ionization source because of the small craters probed on the sample that are  $\leq 2 \mu\text{m}$  in diameter. The Faraday cups with  $10^{13} \Omega$  resistors might be sensitive enough depending on the ion yield of the EUV laser.

## **5.d Extreme ultraviolet laser ionization magnetic sector**

### **5.d.i EUV magnetic sector overview**

The extreme ultraviolet laser ionization magnetic sector mass spectrometer built at Pacific Northwest National Laboratory (PNNL) is designed using the newest tabletop version of the EUV capillary discharge laser operating at a wavelength of 46.9 nm made by XUV Lasers and a modified commercial Neptune sector-field multi-collector mass spectrometer made by Thermo Scientific. Figure 5.7 shows a simplified diagram of the main components of the EUV magnetic sector system. The EUV laser is interfaced with the Neptune mass spectrometer via two customized high vacuum chambers, called the optical and sample vacuum chambers, that aid in steering and focusing both the EUV laser beam and the resulting ion beam. Specifically, the optical vacuum chamber contains two gold-coated planar mirrors that steer the EUV beam onto the zone plate, located in the proceeding sample vacuum chamber. The zone plate, which is the same as the one used in the EUV TOF, has a numerical aperture of 0.12 and focuses the EUV light onto the sample, resulting in material ablation and ionization. The resulting positive ions are

accelerated back through the zone plate's 50  $\mu\text{m}$  central opening and enter an electrostatic quadrupole deflector that turns the ions 90° using oppositely biased metal rods. A coupling lens made up of X, Y, and Z deflection plates and an Einzel focusing lens is placed right before the entrance of the Neptune mass spectrometer to aid in transmission of the EUV generated ions from the sample vacuum chamber. Upon entering the Neptune, the ions are filtered with respect to their energy using the electrostatic analyzer, followed by mass separation in the magnetic sector. Ions of different mass/charge will travel into their own detector at the multi-collector array for mass analysis. Table 5.3 lists the corresponding potentials typically applied to each component used for transferring and focusing the ions in the EUV laser interface vacuum chambers and Neptune, which will be further explained in later sections.

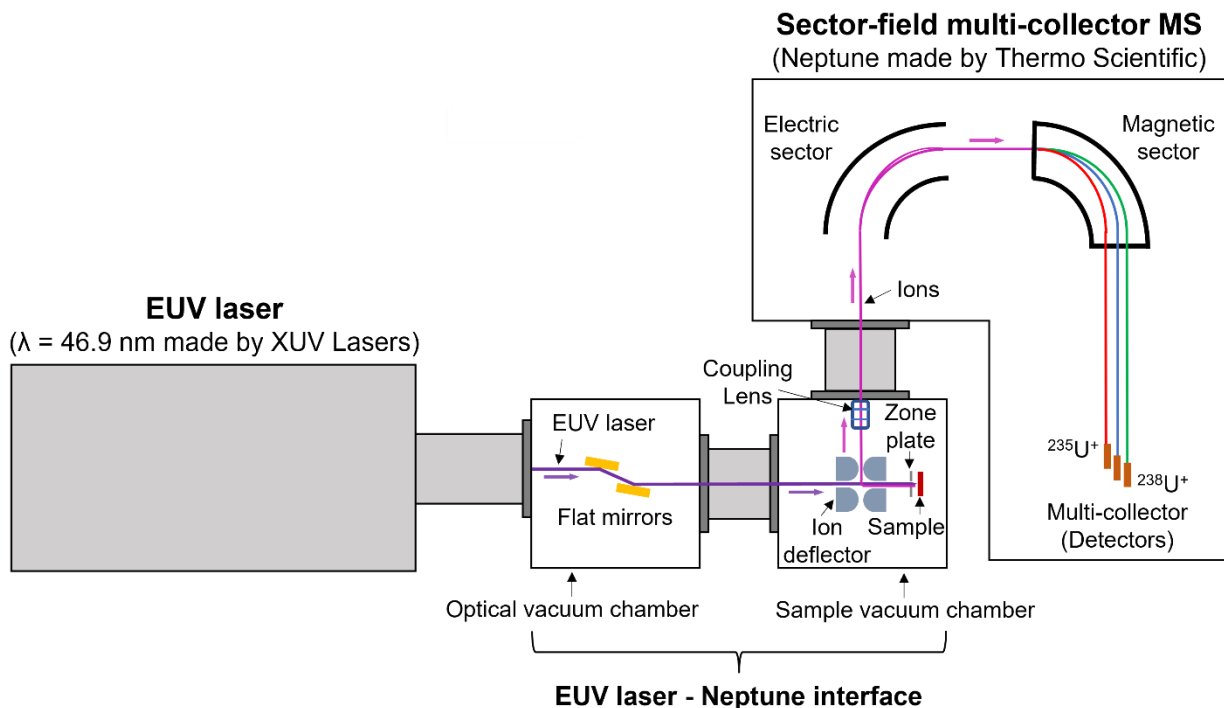


**Figure 5.7** Schematic of the EUV laser magnetic sector mass spectrometer. The 46.9 nm wavelength EUV laser beam (purple line) is guided by two gold-coated flat mirrors in the optical vacuum chamber onto a zone plate in the sample vacuum chamber that focuses the light onto the sample. The EUV laser ablates and ionizes an area of the sample. The ions (pink line) are accelerated from the sample through the zone plate's central opening and turned 90° by an ion beam deflector into the Neptune sector-field multi-collector mass spectrometer. The ions travel through an electric sector followed by a magnetic sector for energy filtering and mass separation, respectively. Ions of different mass/charge are measured in separate detectors in the multi-collector array.

**Table 5.3** Typical potentials applied to each component of the EUV magnetic sector mass spectrometer. Values in parenthesis represent the potential range that may need to be fine-tuned prior to each run. The Neptune potentials

highlighted in red are components that need to be adjusted from their typical operating potentials with the ICP (Table 5.2) to properly transmit the EUV generated ions. \*Equivalent magnetic field probe values to detect ions generated from EUV laser ionization with starting energies of (+)1300 eV at masses 28 amu (<sup>28</sup>Si) and 197 amu (<sup>197</sup>Au).

<b>EUV Magnetic Sector – Sample Chamber</b>	<b>Nominal (V)</b>
Sample	+1300 V
Zone Plate	Ground
Ion Deflector, Circular Electrodes (x4)	±2000 (±100)
Ion Deflector, Shim Electrodes (x8)	±1000 (±50)
Ion Deflector, Einzel Slits (x8)	Ground
Coupling Lens, X/Y/Z Deflection	Ground
Coupling Lens, Einzel Lens	+720 (±30)
<b>EUV Magnetic Sector – Neptune</b>	<b>Nominal (V)</b>
Extraction Lens	-2000
<b>Focus Lens</b>	<b>-700 (±50)</b>
<b>Y(+/-) Deflection</b>	<b>-1820 (±10)</b>
<b>X(+/-) Deflection</b>	<b>-1850 (±10)</b>
Lens 4	-2000
Lens 5	-5000
Shape Quadrupole	-4600
Rotation Quadrupole #1	-5000
Focus Quadrupole #1	-4990
Herzog Plates	-5000
<b>ESA Outer</b>	<b>-5389</b>
Matsuda Plate	-5000
<b>ESA Inner</b>	<b>-4401</b>
Vertical Deflection	-5000
Acceleration Lenses	-10000
Rotation Quadrupole #2	-10000
Zoom Lens #1	OFF
Magnet Field Probe	0.05 [0.15 Tesla] to 11.08 [1.20 Tesla] <b>*(2.115 V = 28 amu; 8.287 V = 197 amu)</b>
Zoom Lens #2	OFF
Electron Multipliers	-2000 to -2300
Faraday Cups	N/A
HV Control	-10000
Source Offset	+10

Briefly, positive ions created from EUV ablation and ionization are accelerated from the sample using a (+)1300 V bias between the sample plate and zone plate. The (+)1300 eV ions are turned 90 degrees by an ion beam deflector, which consists of four main circular electrodes that are equally and oppositely biased to approximately (±)2000 V to turn the ion beam in the desired direction. The deflector also has eight smaller shim electrodes, two on each side of the circular electrodes, that are equally and

oppositely biased to ( $\pm$ )1000 V to further aid in turning and focusing the ion beam. The Einzel slits surrounding the entrance and exit of the deflector are all grounded. After the ions created by the EUV laser have been turned 90 degrees by the beam deflector, they are aligned in the X, Y, and Z directions and focused using a series of ion lenses called the coupling lens. The coupling lens is from Thermo's commercial Triton TIMS instrument to extract, steer, and focus ions from a thermal ionization filament prior to entering a magnetic sector mass analyzer. The coupling lens is adapted into the EUV magnetic sector system by using its steering and focusing optics to increase the transmission of EUV generated ions at the crossover point from the sample vacuum chamber into the Neptune. Because the ions from EUV laser ionization start at (+)1300 eV, the ion optics in the Neptune, which are set according to the ICP generated ions starting at ground, must be adjusted accordingly. Specifically, the potentials of the focus lens, X/Y deflection plates, and ESA plates are changed for proper transmission of the higher energy EUV ions, whose values are highlighted in red in Table 5.3. The magnetic field of the magnetic sector must also be recalibrated to the higher energy ions. After these adjustments to the Neptune are made, the ions generated from EUV laser ionization can be successfully detected using the Neptune's electron multipliers. The challenges associated with optimizing the conditions of the Neptune to properly transmit the ions created by the EUV laser are outlined in the next section.

#### **5.d.ii EUV magnetic sector design challenges**

Unlike TOF mass spectrometers, sector-field instruments like the Neptune are not typically operated with pulsed ionization sources like the EUV laser, which operates between 1 to 10 laser pulses per second. As stated previously, UV/Vis/IR lasers are often coupled to sector-field instruments in LA ICP-MS configurations, but they are typically operated with repetition rates in the kHz range and the ICP, not the laser, generates the ions. In the past, pulsed MALDI sources using UV/Vis/IR lasers operating with up to 20 pulses per second have been used with magnetic sectors and have faced the challenge of trying to detect ions using a magnetic sector that is designed to scan over a time that is orders of magnitudes longer than the ns laser pulse.<sup>117</sup> For example, typically the magnetic field strength of the magnetic sector is scanned

through a set of mass values as a continuous source of ions is transmitted into the mass spectrometer. Scanning the magnetic field allows a specific mass/charge to be calibrated to a specific magnetic field value at a set of instrumental conditions in a process called mass calibration. If the pulse of ions occurs with less frequency than the change in the magnetic field strength, then the desired mass signal may be missed during the calibration. This results in time consuming calibration and increased sample consumption. Using the EUV laser with the Neptune will present the same set of challenges as the laser ionization source used with MALDI magnetic sector instruments.

Additional challenges that arise from using the EUV laser ionization source with the Neptune is adjusting the multiple ion optics in the mass spectrometer that are finely tuned in accordance with ions emitted from the ICP. Such components that effect ion transmission include the steering and focusing ion lenses found throughout the ions' path as well as the fields produced in the electric and magnetic sectors (see Chapter 5.c). The Faraday cups and electron multipliers used in the multi-collector region also present their own set of challenges because their dead times are on the order of the ns pulses of ions that the EUV laser produces, resulting in inaccurate measurements. A collision gas cell that acts to spread out the ion signal in time would mitigate the detector challenges, but the Neptune is not currently equipped with this technology.<sup>118</sup> Another challenge is that because the EUV laser is removing material at the single digit micrometer scale down to the nanoscale, there is a limited number of ions that are produced for mass analysis.

In the proceeding sections, the strategies to realize the design of the EUV magnetic sector system will be explained in detail. First, the design of the EUV laser interface region will be explained, which is made up of the newest tabletop EUV laser that is attached to the optical and sample vacuum chambers. The sample chamber attaches directly to the Neptune and holds the ion optics that were designed to transmit the ions generated from the EUV laser into the Neptune mass spectrometer. The modifications made to the ion optics and sector-fields of the Neptune to transmit and focus the ions generated from EUV laser ionization will then be discussed. Finally, future experiments that will further aid in the development

of the EUV magnetic sector instrument will be proposed. For a complete list of components comprising the EUV magnetic sector system, see Table A.3.2 in the Appendix.

### **5.d.iii Tabletop EUV capillary discharge laser**

The tabletop sized EUV capillary discharge laser used in the EUV magnetic sector system operates using the same physical principle for achieving 46.9 nm wavelength lasing as the desktop version used on the EUV TOF instrument. However, the EUV laser on the EUV magnetic sector system is the newest, commercialized form of the capillary discharge laser made by XUV Lasers and has a more efficient design than its older counterpart used with the EUV TOF. Specifically, the newest EUV laser ionizes the argon gas in the capillary tube through a process that damages the capillary less for a 100-fold increase in capillary lifetime (from 10,000 shots to up to 1,000,000 shots per capillary), provides 5x more energy per pulse (from 10  $\mu$ J to 50  $\mu$ J), and a 10x greater repetition rate (from 1 Hz to 10 Hz) compared to the older desktop version of the EUV laser.

Unlike the older version of the EUV laser that solely uses high voltage pulses to accomplish the necessary population inversion for lasing, the newest tabletop model uses a combination of RF heating followed by high voltage pulses. In the new EUV laser, RF plasma ignition of the argon gas in the capillary is the first step in the ionization process towards creating an Ar<sup>8+</sup> plasma. To realize RF plasma ignition, one end of the argon-filled capillary tube is surrounded by an inductive RF coil. The 60 MHz RF power ignites the argon in the capillary through an impedance matching network for plasma ignition. Due to the highly accurate “dose” of RF power deposited into the capillary, the capillary walls degrade at a much slower rate than the older version of the laser.

Approximately 2 to 4  $\mu$ s after the initial argon plasma is created in the capillary tube by the RF supply, an 8 kV pulse, called the pre-ionization pulse, is discharged through the plasma in the capillary. The pre-ionization pulse ionizes the plasma further but does not excite the Ar<sup>8+</sup> electrons required for lasing (i.e., population inversion is not achieved at this point). About 6 to 12  $\mu$ s after the pre-ionization

pulse, the main high voltage pulse of approximately 42 kV is discharged through the capillary, exciting the  $\text{Ar}^{8+}$  ions for the necessary population inversion that leads to 46.9 nm amplification.

Alongside using a novel ionization strategy for plasma ignition, another key difference between the older desktop EUV laser used with the TOF set-up and the newer tabletop version used with the sector-field MS is the route through which the high voltage pulses are delivered to the capillary. As explained in Chapter 2, the older version of the laser uses spark gap switches to deliver the high voltage pulses to the capillary. While spark gaps are effective and fast high voltage switches, they require routine maintenance to properly deliver high voltage pulses. In the desktop EUV laser, the spark gaps are prone to getting dirty and wear out easily because they are highly pressurized (up to ~80 psi). On the other hand, the new EUV laser uses high voltage power supplies that do not require spark gap switches. The main 42 kV high voltage pulse is delivered via a thyratron trigger, which requires little to no maintenance throughout its lifetime. The new EUV laser therefore has minimal maintenance over the course of a capillary's 1,000,000 shot lifetime.

#### **5.d.iv EUV laser to Neptune interface**

The EUV laser – Neptune interface consists of two high vacuum chambers that hold the components for steering and focusing the EUV laser onto the sample as well as the ion optics for steering and focusing the ions into the Neptune mass spectrometer. Figure 5.8 shows a picture of the external view of the two chambers connected to the desktop EUV laser as well as a detailed SolidWorks model of the chambers' internal components. Each of the listed components will be explained in detail in the following sections. Briefly, the first chamber is the optical high vacuum chamber that guides and aligns the EUV laser light using two planar mirrors onto a zone plate focusing lens in the proceeding sample vacuum chamber. The zone plate focuses the EUV light onto the sample for ablation and ionization. The EUV generated positive ions are accelerated from the sample through the zone plate's 50  $\mu\text{m}$  central opening, where they are subsequently turned 90 degrees by an ion beam deflector towards the Neptune's entrance. After exiting

the deflector, the positive ions travel through the coupling lens where they are aligned and focused into the Neptune's entrance.

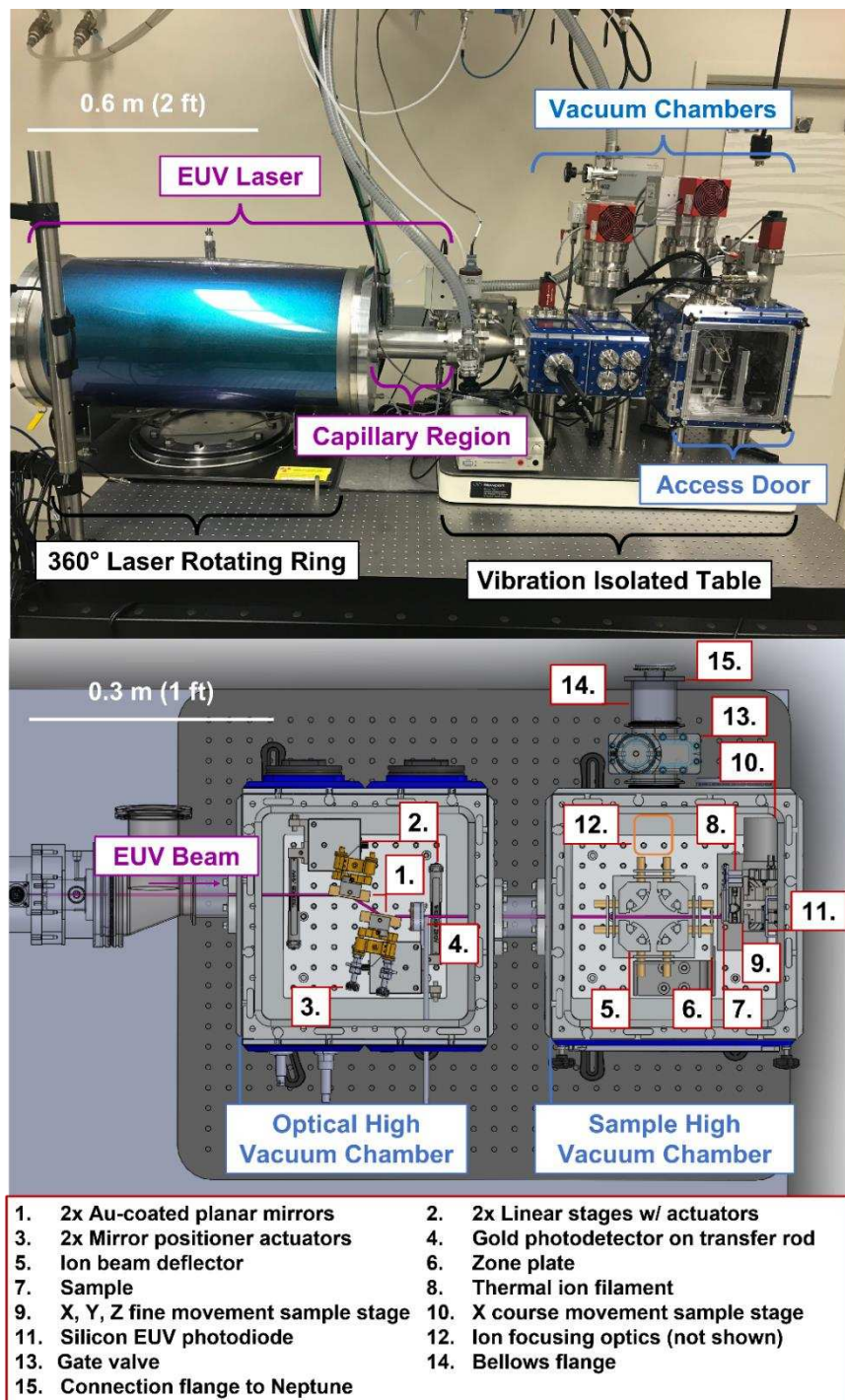


**Figure 5.8** Photograph (top) and SolidWorks model (bottom) of the EUV laser connected to the high vacuum chambers that are used to interface the laser with the Neptune mass spectrometer. The photograph shows an external view of the main components in the set-up as well as additional features that includes the rotating ring that allows the EUV laser to be rotated up to 360° for easy capillary maintenance as well as the vibration isolated table that the

vacuum chambers are placed on to minimize mechanical disturbances. The model shows the corresponding internal components of both vacuum chambers that are used to steer and focus the EUV beam as well as the resulting ion beam. The EUV laser beam is shown in the model as a purple line.

#### **5.d.v Optical high vacuum chamber – Planar mirrors**

The two planar mirrors in the optical high vacuum chambers are used to position the most intense area of the 5 mm diameter EUV beam onto the downstream 0.5 mm diameter zone plate focusing lens. Mirrors are needed to steer the EUV beam because the beam created by the capillary discharge process has a divergence of 5 mrad and has areas of lower and higher intensity because of the varying refractive index from the electron gradient in the capillary. As a result, after the EUV beam has traveled ~1 m from the capillary output to the zone plate, it grows to a final diameter of ~5 mm and is doughnut-shaped. The planar mirrors are used to physically move the EUV beam so that its most intense 0.5 mm x 0.5 mm area is positioned onto the zone plate for optimal sample ablation and ionization.

The planar mirrors, with dimensions of 5.1 cm (2 in) (L) x 2.5 cm (1 in) (H) x 1.3 cm (0.5 in) (W), are made from fused silica slabs (Knight Optical, United Kingdom, MQG2105-C). The mirrors are coated with 100 nm of unprotected gold and are placed in the EUV beam line at approximately grazing incidence (~10°) relative to the incoming beam to maximize the transmission of the highly absorptive EUV light. At a 10° angle of incidence combined with the 100 nm Au coating, each mirror has a reflectivity ( $R$ ) of ~70%. Combined, the mirrors have a transmission ( $T$ ) of ~50%, calculated using Equation 5.11:

$$T = R_1 R_2 \quad 5.11$$

The reflectivity of a mirror with a single layer coating at a specified photon energy can be estimated using The Center for X-Ray Optic “Layered Mirror Reflectivity” Calculator ([https://henke.lbl.gov/optical\\_constants/layer2.html](https://henke.lbl.gov/optical_constants/layer2.html)). Figure 5.9 shows the expected relationship between the reflectivity of an Au-coated mirror as a function of the angle of incidence for 30 eV photons (the minimum allowable photon energy for the calculator). This plot highlights the highly absorptive nature of EUV light because the reflectivity of the light exponentially decreases as the light’s angle of incidence on

the coated mirror increases. It is therefore important to properly align the Au-coated mirrors with the incoming beam to maximize the transmission of the 26.4 eV light.

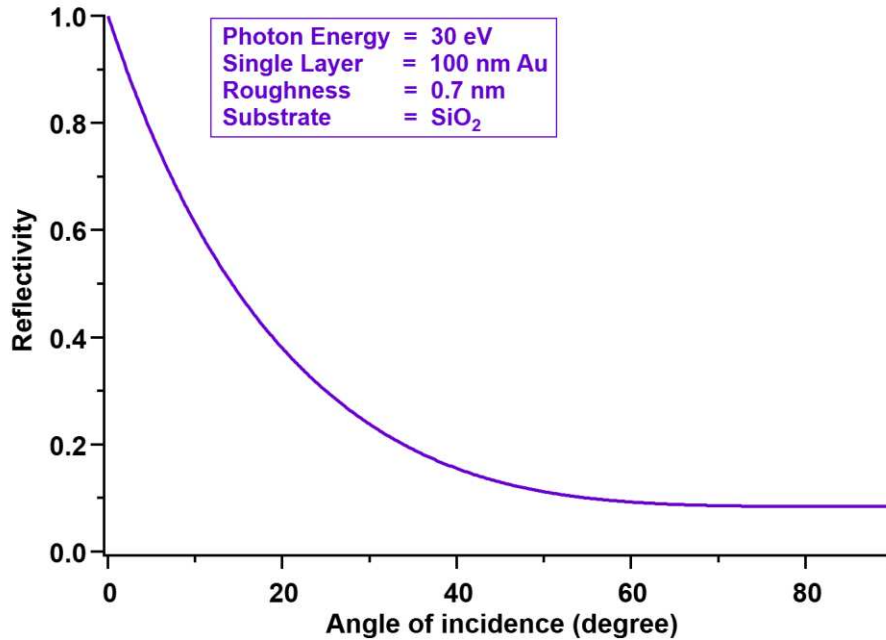


**Figure 5.9** The reflectivity of a silica mirror coated with 100 nm of gold plotted as a function of the angle of incidence of 30 eV photons. (Data collected from [https://henke.lbl.gov/optical\\_constants/layer2.html](https://henke.lbl.gov/optical_constants/layer2.html))

To align the planar mirrors with the EUV laser beam, the mirrors are installed on linear stages (Newport, USA, 9062-COM) with vacuum compatible actuators (Thorlabs, USA, Z812V) so that their linear position can be adjusted in vacuum within a 12 mm range using minimum step sizes of 200 nm (see Figure 5.8). The mirrors are attached to the linear stages by custom-made platforms that are physically angled at 10° to ensure that the mirrors are at approximately grazing incidence relative to the incoming EUV beam. A full description of the alignment procedure for the EUV beam with the mirrors can be found in Figure A.4.1 of the Appendix.

To move the position of the EUV beam across the zone plate, a pair of vacuum compatible actuators (Physik Instrumente, N-470.11V, Germany) are affixed to the second planar mirror's horizontal (x) and vertical (y) angular positioners (see Figure 5.8). Under high vacuum, the EUV beam is moved in approximately 0.5 mm steps across the zone plate by remotely moving the second planar mirror's actuators

in step sizes of 0.03 mm and 0.21 mm in the horizontal and vertical directions, respectively. The actuators' step sizes were calibrated by imaging the size of the EUV beam near the position of the zone plate using a piece of photoresist. The corresponding actuator step sizes required to recreate the beam's shape in 0.5 mm increments was then determined by placing an EUV sensitive silicon photodiode (Opto Diode, USA, SXUV100) after the zone plate to monitor the beam's intensity at every actuator step. After calibration, the EUV beam's most intense 0.5 mm x 0.5 mm area is determined by moving the actuators using the step sizes specified above while monitoring the intensity using the photodiode to collect an intensity map of the EUV beam. After the entire area of the beam is mapped, the actuators are placed at the mirror positions that corresponds to the highest intensity. Figure 5.10 shows the EUV beam imprint on a piece of photoresist as well as the corresponding intensity mapped after the zone plate using the described procedure. The imaged EUV beam shows the expected doughnut-like shape, with areas of lower and higher intensity and is sized ~4 mm x 4 mm, relatively close to the expected 5 mm diameter.

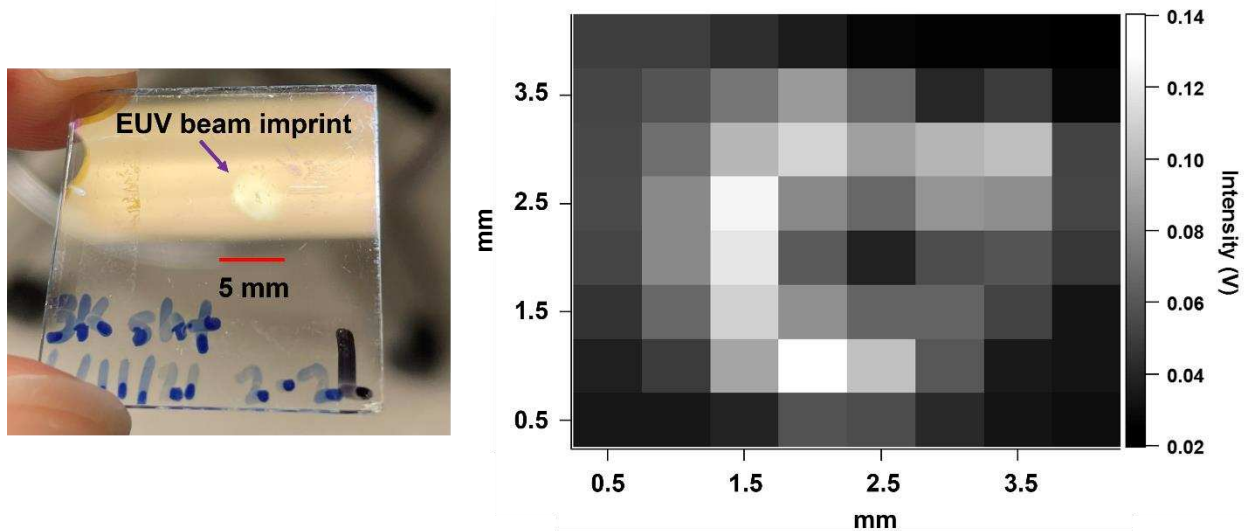


**Figure 5.10** (Left) EUV beam imprint on a piece of photoresist. (Right) Corresponding intensity map of the EUV beam collected after the zone plate using the silicon photodiode. The intensity of each pixel is calculated using the average maximum collected for 5 laser shots per pixel measured from the photodiode. Each pixel is approximately 0.5 mm x 0.5 mm, collected by moving the angular position of the second planar mirror by 0.03 mm steps in the horizontal direction and 0.21 mm steps in the vertical direction.

Unlike the toroidal mirrors used to steer and collimate the EUV beam in the EUV TOF system, the planar mirrors used in the EUV magnetic sector system only act to steer the beam. Because the

laser output in the EUV magnetic sector system is only ~1 m from the zone plate, beam collimation from toroidal mirrors is not needed. The planar mirrors have the benefit of being much easier to align than toroidal mirrors because the latter do not have horizontal and vertical axes. Therefore, unlike in the EUV TOF, the planar mirrors in the EUV magnetic sector system allow direct movement of the EUV beam while keeping the zone plate position stationary. The benefit of maintaining a stationary zone plate position in the EUV magnetic sector system is so to simplify the alignment procedure into the Neptune mass spectrometer by keeping the location of the ion source (i.e., the zone plate) constant.

#### **5.d.vi Optical high vacuum chamber – Gold photodetector**

Alongside the silicon photodiode located after the zone plate, the EUV beam's intensity can also be monitored using a gold photodetector located immediately after the second planar mirror in the optical vacuum chamber (see Figure 5.8). The gold photodetector is attached to a linear transfer rod so that it can be pulled in and out of the beam line. The absolute intensity of the EUV beam is monitored using this detector. The gold photodetector is built in house and consists of a grounded gold mesh that the EUV beam hits, resulting in the ejection of electrons that are collected by a (-)1800 V biased gold-coated copper cathode, and the resulting signal is monitored on an oscilloscope.

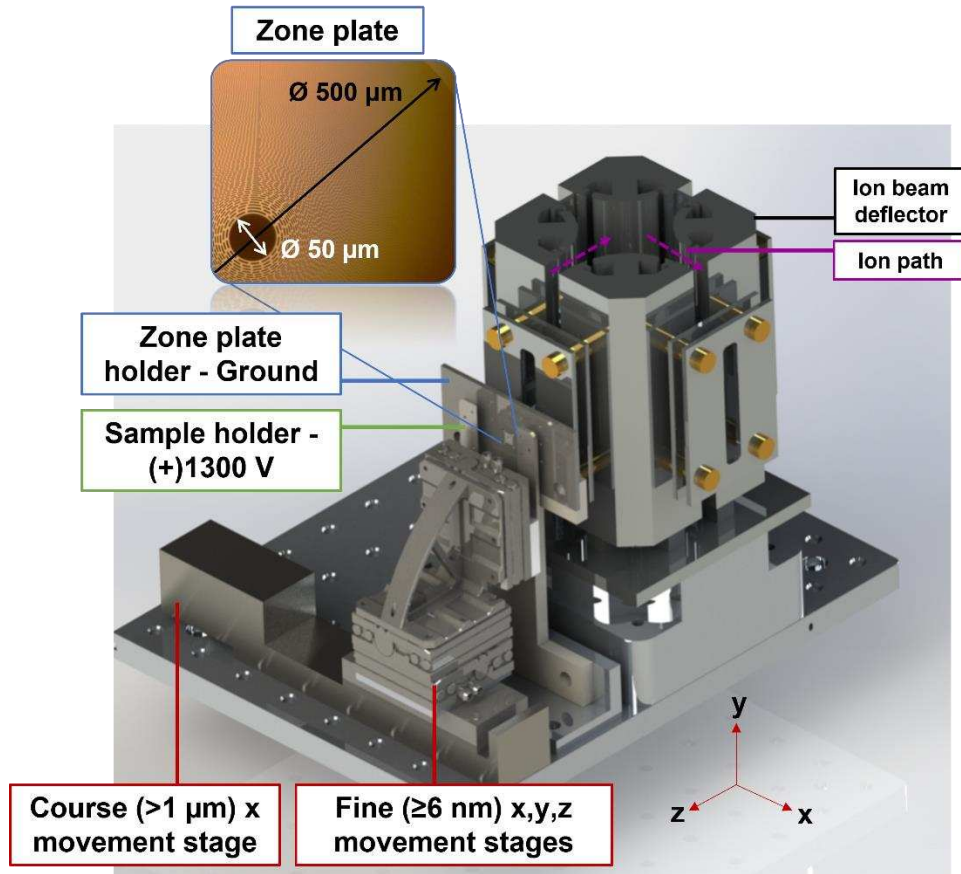
#### **5.d.vii Sample high vacuum chamber – Zone plate**

After exiting the optical vacuum chamber, the EUV beam travels into the sample high vacuum chamber where it proceeds through the ion beam deflector onto the zone plate, which focuses the most intense 0.5 mm x 0.5 mm area of the beam via diffraction. The zone plate is the same free-standing Fresnel zone plate used in the EUV TOF set-up with an overall diameter ( $D$ ) of 0.5 mm, central diameter of 0.05 mm, and outer zone width ( $w$ ) of 200 nm (ZonePlates, United Kingdom). The zone plate is etched into a SiN membrane with a top coating of >2 nm Ni and with a lower coating of ~5 nm Al. Using the zone plate in its first diffraction order ( $n$ ) with the  $\lambda = 46.9$  nm EUV wavelength laser, the focal length ( $f$ ) of the zone plate can be calculated using Equation 5.12:

$$f = \frac{Dw}{n\lambda} = \frac{0.5 \text{ mm} * 2E-3 \text{ mm}}{1 * 4.69E-4 \text{ mm}} = 2.13 \text{ mm} \quad 5.12$$

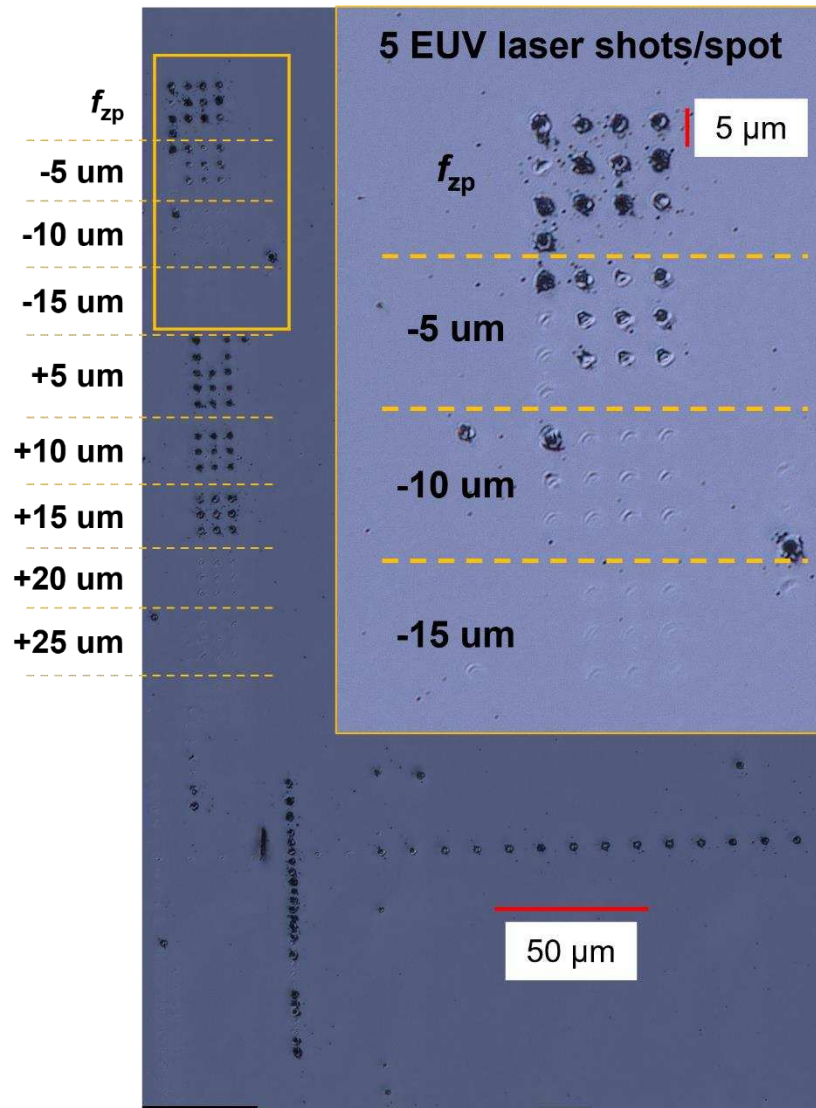
The zone plate's depth of focus is  $\sim 3 \mu\text{m}$ . The 200 nm outer zone width of the zone plate correlates to a focal spot size of approximately 244 nm, calculated as  $1.22 * w$ . However, the focal spot size does not directly correlate to the spatial resolution of the EUV laser. The effective spot size of the laser, defined as the area where material is removed, can be larger or smaller than the focal spot size depending on the ablation threshold of the material and the energy of the laser, thereby affecting the spatial resolution. Additionally, a higher spatial resolution can be achieved by operating the zone plate in its third diffraction order, with a focal position of 1.07 mm, resulting in less material ablation. However, operating the zone plate in its third order comes at the cost of a 10x lower efficiency. In the first order, the zone plate's efficiency is 10%, whereas in the third order the zone plate's efficiency is 1%. For testing the EUV magnetic sector system, the zone plate is operated in its first order to maximize the number of ions being transmitted into the Neptune mass spectrometer.

Figure 5.11 shows how the sample is positioned in the zone plate's 2.13 mm focus using a 3-axis motorized stage (Physik Instrumente, Q-545.140, Germany). The z-axis stage moves the sample closer or further away from the zone plate's focal length. The x-axis and y-axis stages move the sample horizontally and vertically, respectively, so that the EUV laser can ablate different areas of the sample. Each of the 3-axis stages can move a total distance of 13 mm in step sizes down to 6 nm. To horizontally move the sample over a longer distance  $>13 \text{ mm}$ , the sample holder is also attached to a larger linear stage that has a longer travel range of 50 mm but with a larger minimum step size of  $1.25 \mu\text{m}$  (Standa, Lithuania, 8MT30V-50). A longer travel range can be beneficial when switching between two samples during the same run or for sample loading/unloading. The sample can be retrieved via the hinged access door on the sample chamber, which also acts as a large viewing window (see Figure 5.8).



**Figure 5.11** SolidWorks model of the main components used to generate positive ions using the EUV laser beam. The zone plate, located at the center of the zone plate holder, focuses the EUV light onto the sample. The fine movement z-axis stage positions the sample at the zone plate's 2.13 mm focus. The fine and course movement horizontal (x) and vertical (y) stages position the sample at the desired sample location. The positive ions generated from EUV laser ablation and ionization are accelerated from the sample and through the zone plate using a (+)1300 V potential gradient.

Figure 5.12 shows how EUV laser ablation changes on a silicon wafer as the wafer is moved in and out of the zone plate's focal length by moving the z-axis stage in 5 µm steps. When the wafer is placed at the zone plate's 2.13 mm focus, material removal is maximized. As the wafer is moved further away from the focus, material removal decreases. An exception is that at (+)15 µm from the zone plate's focus, material ablation seems to be similar to that at the focus, which could be a result of the EUV beam having an astigmatism. The astigmatism could be from debris on the planar mirrors that affects the focus of the beam, which must be periodically cleaned and recoated. Nonetheless, positive ions are generated from each EUV laser-ablated crater. The positive ions are then accelerated from the sample's surface and through the zone plate's 50 µm central opening by a (+)1300 V gradient between the sample and zone plate.



**Figure 5.12** Arrays of EUV ablation craters on a silicon wafer at varying distances from the zone plate's 2.13 mm focus ( $f_{zp}$ ). The sample was moved in 5  $\mu\text{m}$  steps away from the zone plate's focus in both the positive and negative directions. Each ablated array consists of 5 EUV laser shots at every spot with 5  $\mu\text{m}$  steps taken between each spot in an array. EUV ablation craters around the arrays are from separate runs.

#### 5.d.viii Sample high vacuum chamber – Ion deflector

After the ions are accelerated through the zone plate's central opening, they enter the ion beam deflector. The ion deflector uses a two-dimensional electrostatic quadrupole field to turn the positive ions 90° towards the Neptune mass spectrometer's entrance. The quadrupole field is created using a combination of larger circular electrodes and smaller shim electrodes to produce hyperbolic equipotentials (Beam Imaging Solutions, USA, QID-900). The electrostatic field is created by biasing the electrodes based

on the incoming ions' energies, such that only ions with a certain energy will be properly transmitted through the deflector's electric field. In this way, the deflector is an electrostatic analyzer, as explained in the beginning of this chapter, because the ions' energies dictate their radius of travel through the electric field. As will be seen in later sections, the ions will also travel through an electrostatic analyzer in the Neptune, where they will be filtered according to their energy a second time.

Figure 5.13 shows a diagram of how the electrodes are biased to turn positive ions created by the EUV laser with an energy ( $U$ ). The circular electrodes are typically biased between ~150 to 100% of the ion energy ( $U$ ), while the smaller shim electrodes are biased between 70 and 50% of the potential applied to the circular electrodes. The deflector also has 2 pairs of Einzel slits at each entrance/exit that are used as 2-dimensional focusing optics for the ion beam as it enters and exits the deflector. The Einzel slits are typically grounded but can be operated up to 50% of the circular electrodes (depending on the bias applied to the shim electrodes). To turn the (+)1300 eV positive ions from the sample, the optimal deflector conditions were determined to be ( $\pm$ )2000 V on the circular electrodes and ( $\pm$ )1000 V on the shim electrodes, while the Einzel slits remained grounded. Prior to each run, the circular and shim electrodes may need to be fine-tuned by ( $\pm$ )100 V to optimize the ion signal into the Neptune mass spectrometer.

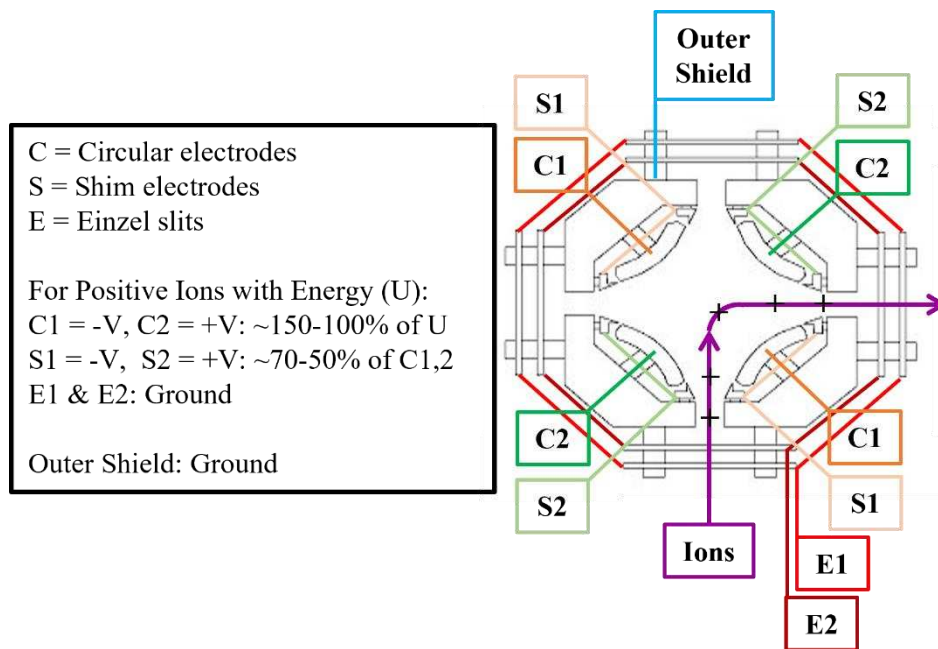


**Figure 5.13** Diagram of the ion beam deflector in the sample vacuum chamber that is used to turn the incoming positive ions 90° towards the mass spectrometer entrance.

#### 5.d.ix Sample high vacuum chamber – Coupling lens

After the ions have been turned 90° by the deflector, they travel through a set of ion optics that steers and focuses them into the Neptune mass spectrometer. The stack of optics used is commercially made by Thermo for their Triton mass spectrometer (i.e., basically the Neptune without the ESA portion) and is typically placed in front of a thermal ionization filament to extract, steer, and focus the thermally created ions into a magnetic sector mass analyzer. Here, the stack of optics is placed immediately after the ions have been deflected 90°. Figure 5.14 shows a picture of the stack of optics and their placement in the sample vacuum chamber. The optics can shift the ion beam in the X, Y, and Z directions prior to entering the Neptune mass spectrometer, aiding with the precise alignment of the ion beam into the mass spectrometer entrance if needed. Typically, the directional optics are left grounded unless there is a need to apply a positional correction to the ion beam, while the Einzel lens is biased to around (+)720 V to focus the (+)1300 eV positive ions generated from the EUV laser. The Einzel lens is specifically designed to focus incoming ions into the shape of a vertical line to match the entrance parameters of the Triton mass spectrometer. Although the Neptune entrance is in the shape of a small, circular aperture (defined by the

~3 mm aperture after the extraction lens), focusing the beam of ions aids in optimizing transmission into the mass spectrometer, which will be experimentally detailed in a later section.

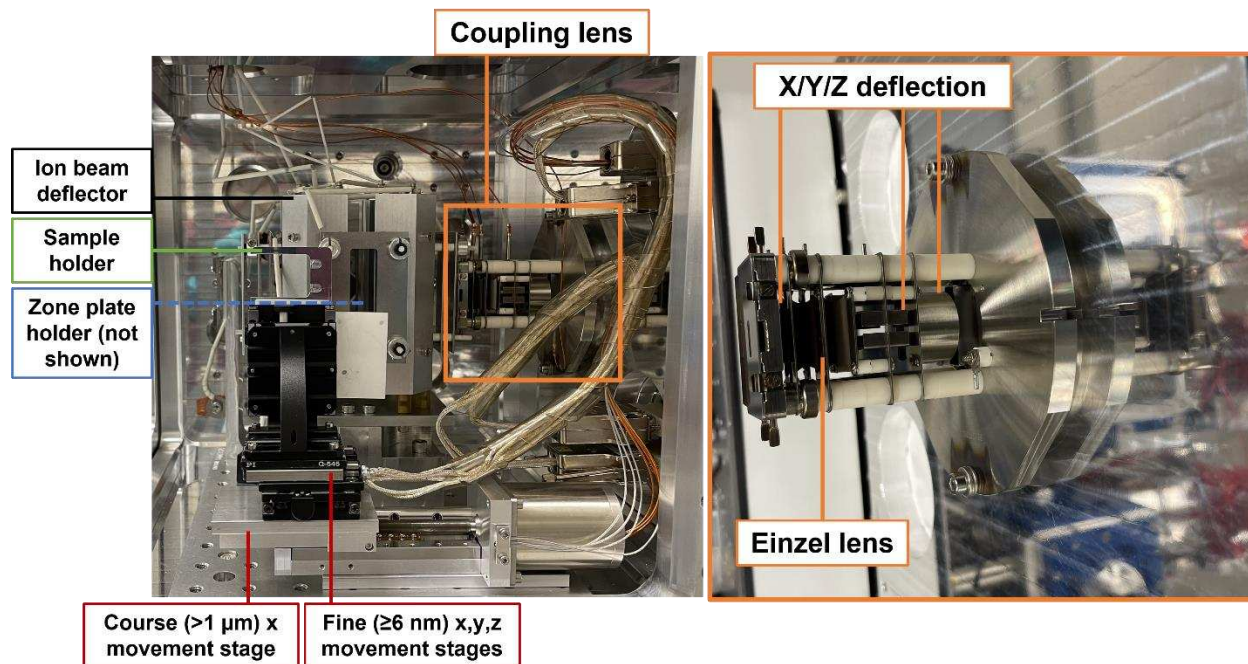


**Figure 5.14** Picture of the lens stack that is typically operated with the Triton mass spectrometer. The lens stack is installed in after the ion beam deflector in the sample vacuum chamber to aid in guiding and focusing the ions into the Neptune mass spectrometer. The lens stack has X/Y/Z steering as well as an Einzel lens for focusing.

#### 5.d.x Other features of EUV laser interface

Additional features of the EUV laser interface include a thermal ionization filament in the sample vacuum chamber that can be used as a continuous ionization source when needed, as opposed to the more complex pulsed EUV laser source. The thermal ionization source can be placed on the sample holder, adjacent to the sample that is ablated and ionized by the EUV laser. The filament is biased through a high voltage supply connected to its current supply. In this way, the filament can be biased so that the ions' energies are similar to the ions created by the EUV laser. However, the thermal filament and EUV laser are different ion sources, thereby producing ions with different emittance characteristics. For example, the ion velocity dispersion of ions created from the thermal filament is very low (i.e., on the order of a few eV), which is why TIMS instruments do not typically need to be built with ESAs for ion energy focusing.

Therefore, the filament was only used intermittently during the build of the EUV magnetic sector system to test certain ion optics where a continuous ion signal was beneficial.

Another feature of the EUV laser interface includes a rotating ring (Kaydon, USA, RK6-16P1Z) at the base of the EUV laser, allowing the laser to be rotated up to 360° when disconnected from the vacuum chambers. The rotating ring was included in the design so that the laser could be rotated to make changing the capillary easier. Changing the capillary on this version of the EUV laser requires that the front ~30.5 cm (12 in) long “nose” region of the laser, where the capillary is contained (see Figure 5.8), is completely removed. To avoid having to physically move the vacuum chambers away from the laser to access the capillary, the EUV laser can be rotated to remove the laser nose when the capillary needs to be changed. Another feature of the EUV laser interface region is the separate vibration isolated table (Newport, USA, BT-2436-OPT) to which the vacuum chambers are attached. This table pneumatically isolates mechanical disturbances that could affect the alignment of the components in the optical and sample high vacuum chambers.

#### **5.d.xi Connecting EUV laser interface to Neptune**

The EUV laser interface is connected to the Neptune by (1) removing the mobile ICP table from the Neptune, (2) moving the mobile EUV laser interface to the Neptune, (3) aligning the EUV laser interface with the Neptune’s entrance, and (4) using special vacuum flanges to connect the EUV laser interface to the entrance of the Neptune. Figure 5.15 shows a model and a photograph of an external view of the EUV magnetic sector system after these steps have been completed.

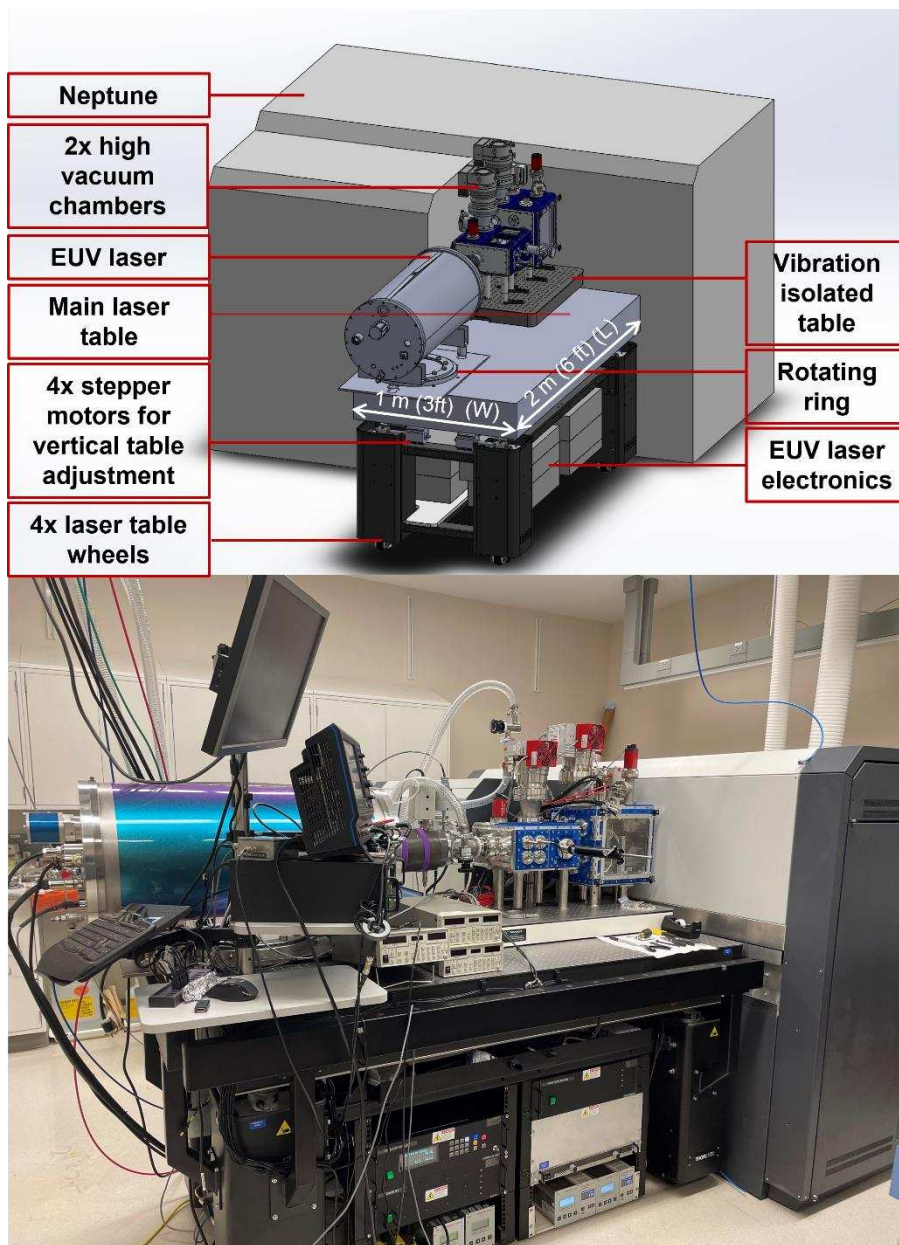


**Figure 5.15** SolidWorks model (top) and photograph (bottom) of the EUV magnetic sector system, located at Pacific Northwest National Laboratory. The EUV laser and its high vacuum chambers are coupled to a modified Neptune sector-field multi-collector mass spectrometer made by Thermo by removing the ICP portion of the Neptune.

The Neptune's ICP is located on a moveable table that can be disconnected from the Neptune's entrance. Moving the ICP table can be easily done by a single person. The EUV laser interface, consisting of the EUV laser, optical vacuum chamber, sample vacuum chamber, and the system electronics, is also located on a moveable table, sized 2 m (6 ft) (L) x 1 m (3 ft) (W) (Thorlabs, USA, TF1020A7 and

T36H). All the electronics controlling the laser, vacuum pumps, and ion optics are placed under or on the laser table, making the entire set-up mobile. Moving the EUV laser system usually requires 2-3 people.

After moving the EUV laser interface close to the Neptune's entrance, the latter is carefully aligned with the Neptune's entrance. To do this, an alignment procedure was developed using a visible wavelength Helium-Neon (HeNe) laser and two external planar mirrors, allowing the alignment procedure to take place out of vacuum. Figure 5.16 diagrams the alignment set-up. The HeNe is first aligned through the center of the beam deflector by aligning the first mirror (i.e., "Alignment mirror #1") with "Alignment plate #1". The center of the beam deflector represents the path that the ions take after being accelerated through the zone plate. Then, using "Alignment mirror #2", the HeNe is aligned through the center of "Alignment plate #2", which represents the entrance of the coupling lens that the ions travel through before entering the mass spectrometer. The first and second mirrors are iteratively adjusted onto the first and second alignment plates, respectively, until the ion beam is traveling through the center of both plates.

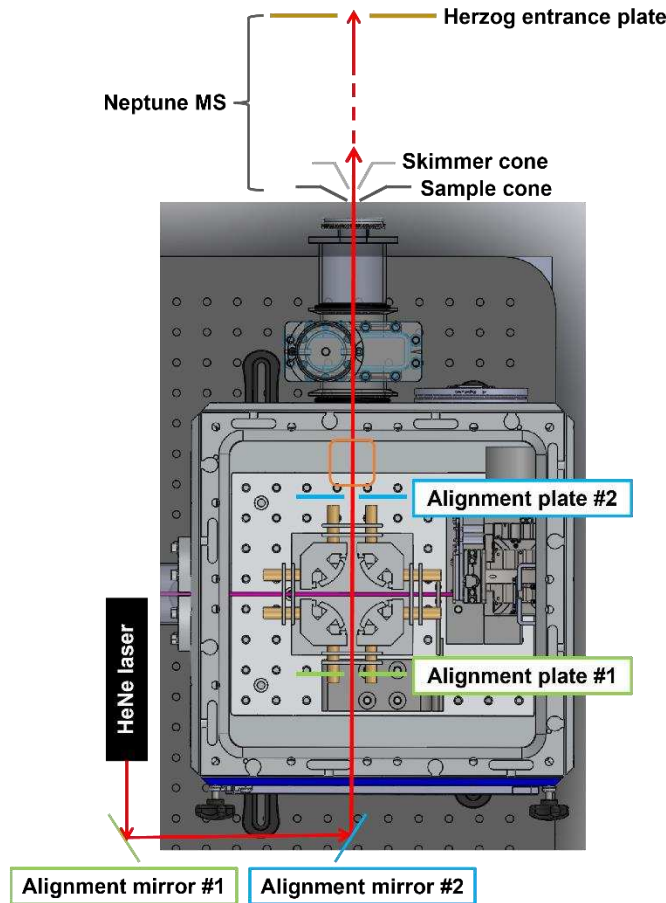


**Figure 5.16** Diagram (not drawn to scale) of the procedure to align the EUV laser system with the Neptune mass spectrometer, ensuring that the ions created in the sample high vacuum chamber have the proper trajectory into and through the entrance of the mass spectrometer.

After the ions' path through the sample vacuum chamber has been mirrored by the HeNe laser, the entire EUV laser system is moved horizontally and vertically so that the HeNe travels through the center of the skimmer and sample cones at the Neptune's entrance and subsequently reaches the center of the Herzog plate at the entrance of the ESA. To make viewing the HeNe beam easier at the Herzog entrance plate, the slit lens system is typically removed from the Neptune for the alignment procedure. To horizontally shift the EUV laser system, the smaller, vibration isolated table that the chambers are attached can be manually moved forwards and backwards. There is a bellows flange between the EUV laser and the optical high vacuum chamber to allow for this horizontal movement. To vertically shift the EUV laser system, the entire tabletop can be moved up and down using Arduino-controlled stepper motors that are

installed under the larger laser table in place of their original supports (Applied Motion Products, USA, STR4/8).

After aligning the EUV laser system with the Neptune's entrance, the EUV laser is connected to the Neptune via the high vacuum sample chamber. The Neptune's sample and skimmer cones are removed to attach the chamber using a custom-built vacuum flange (see Appendix). The sample and skimmer cones are not needed with the EUV laser source because, as opposed to the ICP, the EUV laser system is already under high vacuum. Therefore, the differential pumping that the cones provide when operating with the atmospheric pressure ICP is not needed with the EUV laser.

The process of connecting and aligning the EUV laser system to the Neptune typically takes ~4-8 hrs. However, this timeline could be reduced if the entire EUV laser system were moved via motors, rather than manually. Additionally, if the EUV laser system could be attached to the Neptune at the same position each time, then the horizontal position of the system would not have to be adjusted in reference to the Neptune each time the EUV laser system was connected. Disconnecting the EUV laser system from the Neptune is much easier, typically requiring only ~5 to 10 minutes.

#### **5.d.xii EUV magnetic sector vacuum system**

The EUV magnetic sector's vacuum system consists of a total of eight turbo pumps, two ion getter pumps, two roots pumps, and two rotary vane pumps to achieve a vacuum level of  $10^{-6}$  Torr in the optical vacuum chamber down to  $10^{-8}$  Torr in the multi-collector region. The EUV laser interface region is pumped down to high vacuum by a combination of two roots pumps and four turbo pumps. Figure 5.17 shows a simplified diagram of the EUV laser's vacuum system. One roots pumps is used to directly pump out excess argon gas used in the laser's capillary region, while the second roots pump provides the base pressure for the four turbo pumps. The first turbo pump is connected to a differential pumping region immediately after the laser output and is separated from the laser capillary and optical high vacuum chamber using two apertures, sized 3 mm (a2) and 5 mm (a3) in diameter. Immediately after the capillary output

there is a 1 mm (a1) diameter aperture that also aids in differential pumping. The differential pumping after the laser capillary aids in reducing the flow of excess argon from the capillary to the optical and sample high vacuum chambers. The optical high vacuum chamber has dimensions of 30.5 cm (12 in) (L) x 15 cm (6 in) (H) x 30.5 cm (12 in) (W) (Ideal Vacuum, USA, P109160) and is pumped down to  $\leq 10^{-6}$  Torr using one 300 L/s turbo pump (Pfeiffer, Germany, HiPace 300). The sample high vacuum chamber has dimensions of 30.5 cm (12 in) (L) x 30.5 cm (12 in) (H) x 30.5 cm (12 in) (W) (Ideal Vacuum, USA, P108246) and is pumped down to  $\leq 10^{-7}$  Torr using two turbo pumps with speeds of 300 L/s and 80 L/s (Pfeiffer, Germany, HiPace 300 and 80).

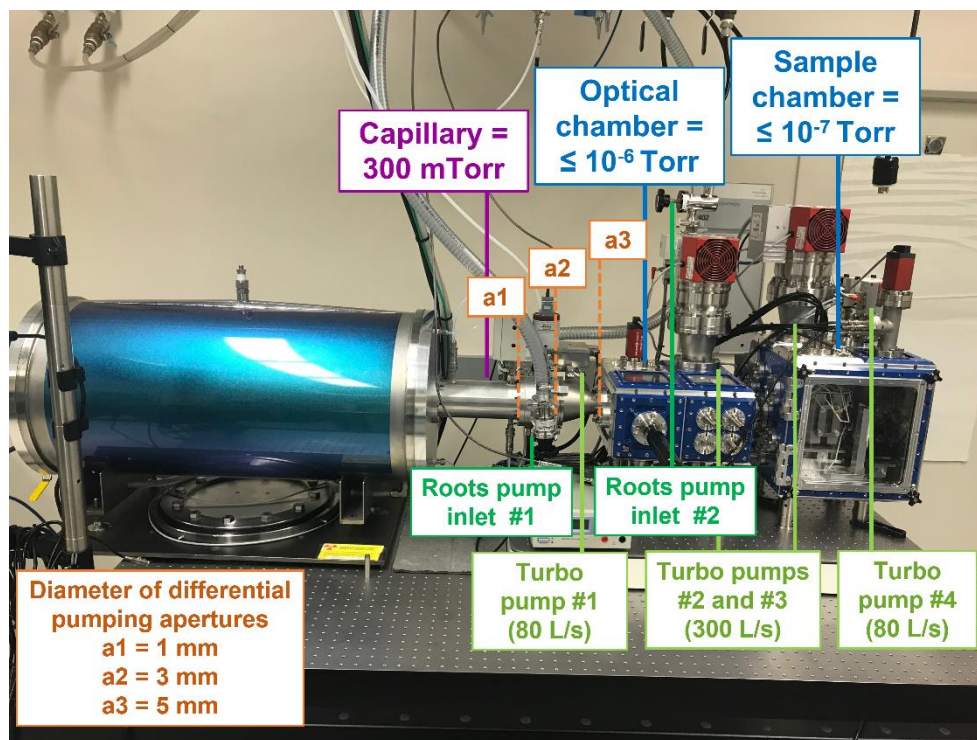


**Figure 5.17** Picture of the EUV laser interface with the main vacuum system components labeled.

The Neptune’s vacuum system consists of one rotary vane pump at the entrance of the mass spectrometer (typically used for pumping down the area between the sample and skimmer cones). A second rotary vane pump is used to establish a base pressure for the four turbo pumps fitted throughout the Neptune’s ESA module to achieve pressures down to  $\leq 10^{-8}$  Torr. Two ion getter pumps in the multi-collector module pump down the back end of the system to  $\leq 10^{-8}$  Torr. The Neptune also uses differential

pumping apertures/slits placed throughout the modules to aid in pumping the different modules. When the EUV laser is attached to the Neptune, all the Neptune's vacuum pumps are used in their typical configuration. A diagram of the entire EUV magnetic sector's vacuum system and further details on each vacuum component can be found in Figure A.5.1 and Table A.5.1 of the Appendix.

## **5.e Testing the EUV magnetic sector mass spectrometer**

### **5.e.i Neptune ion optics' cross overs**

The ion optics in the EUV laser system and Neptune need to be carefully tuned for proper ion transmission from the source to the detectors. Transmitting and focusing the ions created from EUV laser ionization into the Neptune is challenging because the Neptune's ion optics are highly attuned to the emittance characteristics of ions created by the ICP. In particular, the image produced by one ion lens in the system serves as an object for succeeding lenses, meaning that the EUV generated ions must be finely focused with minimal geometrical or chromatic aberrations for proper transmission through the Neptune. These image points are referred to here as "cross-over" points. The cross-over points in the Neptune are physically defined by narrow, vertical slits or small diameter apertures. The four main cross-over points in the Neptune that must be considered are (1) at the extraction lens, (2) at the low mass resolution slit, (3) at the slit after the ESA, and (4) at the detectors' entrance after the magnet. Figure 5.18 identifies where these cross-over points are located throughout the Neptune. It should be noted that regardless of the ion source used (i.e., ICP vs EUV laser), cross-over points 2-4 should be the the same. However, the first cross-over point is different for ions created by the EUV laser versus ions created by the ICP. For the ICP ions, the first cross-over is defined by the skimmer cone entrance, while for the EUV ions it is at the extraction lens aperture because the skimmer cone has been removed for the latter set-up. The following sections will describe theoretical models and experimental tests to determine the necessary modifications to the ion

optics for transmitting ions created by EUV laser ionization through these different cross-over points in the Neptune for ion detection.

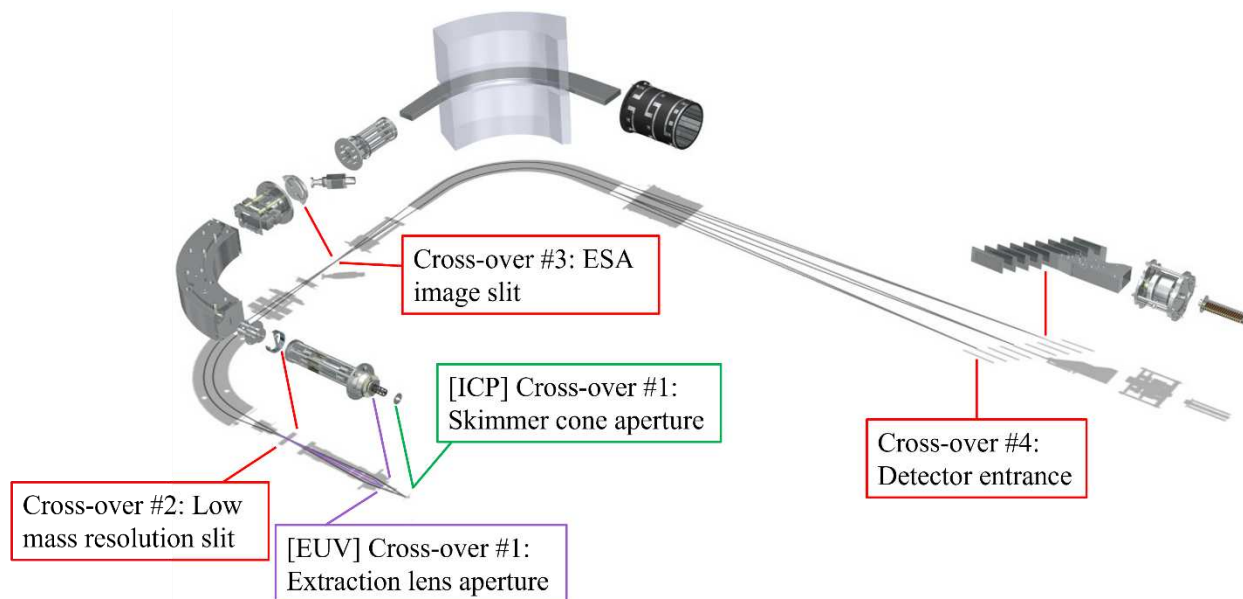


**Figure 5.18** Cross-over/image points that the EUV ions must be focused through for proper transmission through the Neptune. Cross-over #1 for the EUV ions is at the extraction lens aperture (purple), while cross-over #1 for the ICP ions is at the skimmer cone entrance (green). Cross-overs 2-4 are the same for either ion source (red).

### 5.e.ii Tuning the EUV ions' energy - Experiment

As briefly overviewed earlier, the ions created by the EUV laser are accelerated on-axis from the sample through the zone plate via a (+)1300 V potential gradient. After the ions travel through the zone plate, they are turned 90 degrees by an ion beam deflector before entering the coupling lens that provides additional steering and focusing. After traveling through the coupling lens, the ions enter the extraction lens, which marks the entrance into the Neptune. At the end of the extraction lens is a ~5 mm diameter aperture that marks the first cross over point that the EUV ions need to be focused through for proper transmission into the mass spectrometer. A (+)1300 V potential gradient between the sample and zone plate was experimentally determined to provide the most intense ion signal after the ions enter the Neptune through the first cross-over point. The following experiments will detail how this optimal accelerating potential was determined as well as the corresponding conditions for the ion beam deflector and coupling lens.

Ideally, the potential gradient between the sample and zone plate used to accelerate the EUV ions should resemble the gradient used to accelerate the ICP ions to reduce the changes made to the Neptune's ion optics. The ICP ions start at (or near) ground potential and are accelerated to approximately (-)2000 eV by the extraction lens. If the ions created by the EUV laser are accelerated into the Neptune using a positive potential gradient between the sample and zone plate, then the ions will have excess energy that will need to be accounted for in the Neptune's optical components. If the ions are accelerated using a negative potential gradient then the ions will not have excess energy upon entering the Neptune. Therefore, the latter conditions are theoretically ideal for accelerating the EUV-created ions from the source into the Neptune.

To experimentally determine the optimal potential gradient to accelerate the ions created from EUV laser ionization into the Neptune, the ion signal was monitored prior to the ions' entrance into the Neptune using two different microchannel plate (MCP) detectors installed at the exit of the sample chamber. One of the MCP detectors was configured with the typical metal anode located after the MCP plates that outputs a current signal from the incident ions. The other MCP detector was an imaging detector that was configured with a phosphor screen after the MCP plates that fluoresces upon ion detection, providing spatial information of the incident ion beam. Both MCP detectors provide complimentary information regarding the ion beams' intensity and shape, which are important characteristics for properly transmitting the EUV ions through the first cross-over point.

The MCP imaging detector consists of two resistance matched 40 mm diameter plates followed by a similar sized phosphor screen (Beam Imaging Solutions, USA, BOS-40). The MCP plates and phosphor screen are contained in a 4.5"-CF flange with a viewing window that allows the user to observe the phosphor screen fluoresce when ions hit the MCP plate. When the ions hit the front MCP plate, electrons are emitted and multiplied through the plate channels and accelerated to the phosphor screen. For positive ion detection, the front MCP plate was biased up to a maximum potential of (-)2000 V while the back plate was held at ground, and the phosphor screen was biased up to (+)3000 V.

The other MCP detector configured with a metal anode was “miniature” in size, being only 7.1 mm wide and having a total assembly diameter of 27.5 mm, with two resistance matched 14.5 mm diameter plates (Hamamatsu, F14884, Japan). Alongside its size, this mini-MCP detector is also unique from a typical MCP detector because it maintains minimal dark current even at pressures up to  $7 \times 10^{-3}$  Torr. Usually, MCP detectors must be operated at a vacuum level of at least  $1 \times 10^{-6}$  Torr to minimize this dark current caused by ion feedback, which is important for reducing signal-to-noise and avoiding discharge affects. Operating at higher pressures can be advantageous for compact mass spectrometer set-ups. However, for our experiments, the mini-MCP was always operated under high vacuum conditions. For positive ion detection on the mini-MCP, the front plate was biased up to a maximum potential of (-)2000 V while the back plate was biased up to (-)100 V and the anode was held at ground.

Figure 5.19 shows a photograph of the experimental set-up. The mini-MCP detector was secured to a moveable transfer rod, located ~6”(15 cm) from the sample chamber exit, and the MCP imaging detector was attached immediately behind the mini-MCP in its own vacuum flange with a glass window on the back side to view the phosphor screen. A CMOS camera (Thorlabs, CS165MU, USA) was positioned behind the glass window of the MCP imaging detector to collect images of the resulting ion beam, while the mini-MCP detector signal was collected from the anode using an oscilloscope with a  $50\Omega$  input impedance.

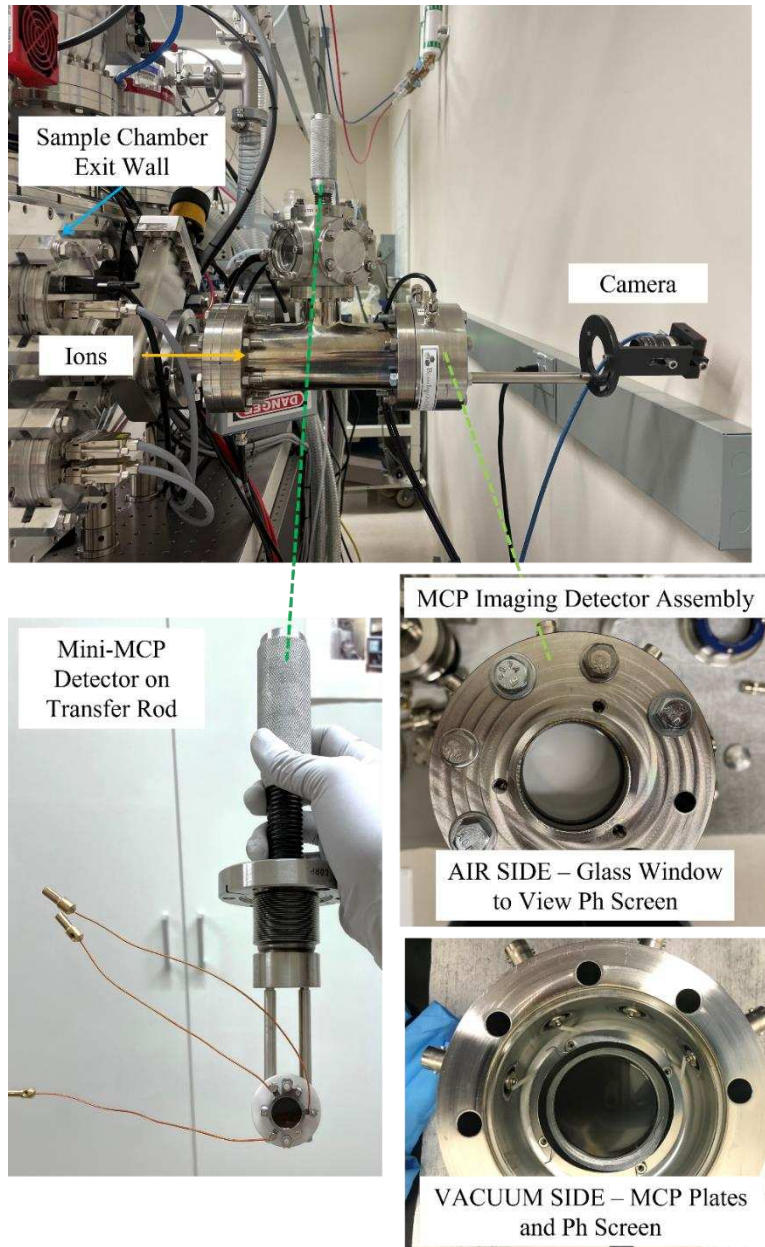


**Figure 5.19** (Top) MCP detectors installed at the exit flange of the sample high vacuum chamber in the EUV laser interface to measure the ion intensity as a function of ion acceleration conditions. (Bottom, left) Mini-MCP detector secured on a bellows-type transfer rod. (Bottom, right) MCP imaging detector installed in a vacuum housing with a viewport window to observe the phosphor screen in real-time.

For ion generation, the EUV laser light was focused onto a 6 mm x 6 mm silicon wafer for ablation and ionization. As stated previously, the zone plate with a numerical aperture of 0.12 and first order focal length of 2.13 mm at 46.9 nm was used. The sample was positioned at the first order focus of the zone plate, ablating craters  $\leq 2$   $\mu\text{m}$  in diameter using an EUV laser intensity of  $\sim 20$  uJ at a 1 Hz repetition

rate. Figure 5.20 shows a digital microscope (Keyence, VHX-7000 series, Japan) image of the EUV laser-ablated craters on the wafer. To avoid sample charging, the silicon wafer was attached to a conductive 25 mm x 25mm x 1.1 mm indium-tin-oxide (ITO) glass slide with a resistance between 30 to 60  $\Omega$  (Delta Technologies, 8SG0115, USA) via copper tape and attached to the biased sample holder. Sample preparation for the EUV magnetic sector is similar to that used for the EUV TOF, which is described in Chapter 2d.



**Figure 5.20** EUV laser ablation craters on a silicon wafer imaged using a digital microscope at a 1500X magnification. The number of EUV laser shots taken at every spot varies from single shots (smallest spots and least material removal) to >100 laser shots (largest spots and most material removal).

To find the optimal accelerating potentials for the EUV created ions, the bias on the sample and zone plate was varied, and the resulting ion signal was measured on the MCP detectors. The ion beam deflector was biased according to the expected ion energy to turn positively created ions 90 degrees into the MCP detector region. In this way, the accelerating potential between the sample and zone plate can be changed until the accelerating conditions produce ions that match that of the deflector. Alternatively, the

ion beam deflector can be changed according to the ion acceleration conditions, but it is easier to change the potentials on the sample and zone plate. Once an ion signal is measured on the MCPs, the deflector potentials can be further adjusted if needed. For initial optimization of the ion accelerating conditions from the sample, all elements in the coupling lens after the deflector were grounded.

Initially, tests were performed by applying a negative bias ranging from (-)10 V down to (-)1000 V to the zone plate and grounding the sample to better replicate the conditions of the ICP ions, as explained earlier. However, no ions were observed using this type of configuration on either MCP detector. It is possible that instead of the ions being accelerated through the zone plate, that they were lost to the surrounding metal zone plate holder that provides the bias to the zone plate. Even with the sample biased positively, no ions were detected when the zone plate was negatively biased. These initial tests indicated that the EUV ions will have to enter the Neptune with excess energy because the zone plate and sample cannot be negatively biased for positive ion extraction.

Further tests were conducted where the zone plate was grounded while the sample was positively biased. Using this configuration, ions were successfully detected at both MCPs, indicating that the ions were being accelerated through the zone plate and turned by the electrostatic ion beam deflector. To optimize the ion acceleration conditions, the mini-MCP detector was used to measure the ion intensity at different acceleration conditions by varying the sample bias. Figure 5.21 shows acquired spectra from single laser shots on the silicon wafer at ion energies ranging from (+)660 eV up to (+)2160 eV. The time scale of the spectra have been shortened because the large peak, likely Si ions, dominated all spectra. Two expected trends in the spectra are apparent: (1) the Si peak intensity increases with ion energy and (2) the ion arrival time decreases with increasing ion energy. Higher energy ions will also have a larger velocity than lower energy ions, thereby having a shorter flight time from the source to the detector. Higher energy ions should also result in a larger ion signal than lower energy ions because the former will have higher transmission and increased peak compression. Interestingly, the Si peak acquired at an ion energy of (+)2160 eV is the most intense but appears to have a non-ideal split peak shape, while the peak acquired at

(+)1300 eV is less intense but has the most ideal peak shape. The ion peak shape is most likely tied into the focusing conditions prior to reaching the detector. For example, the bias of the Einzel lens in the coupling lens, which was turned off for the spectra acquired in Figure 5.21, can be adjusted to improve the shape of the peaks, which will be discussed further below and in later sections.

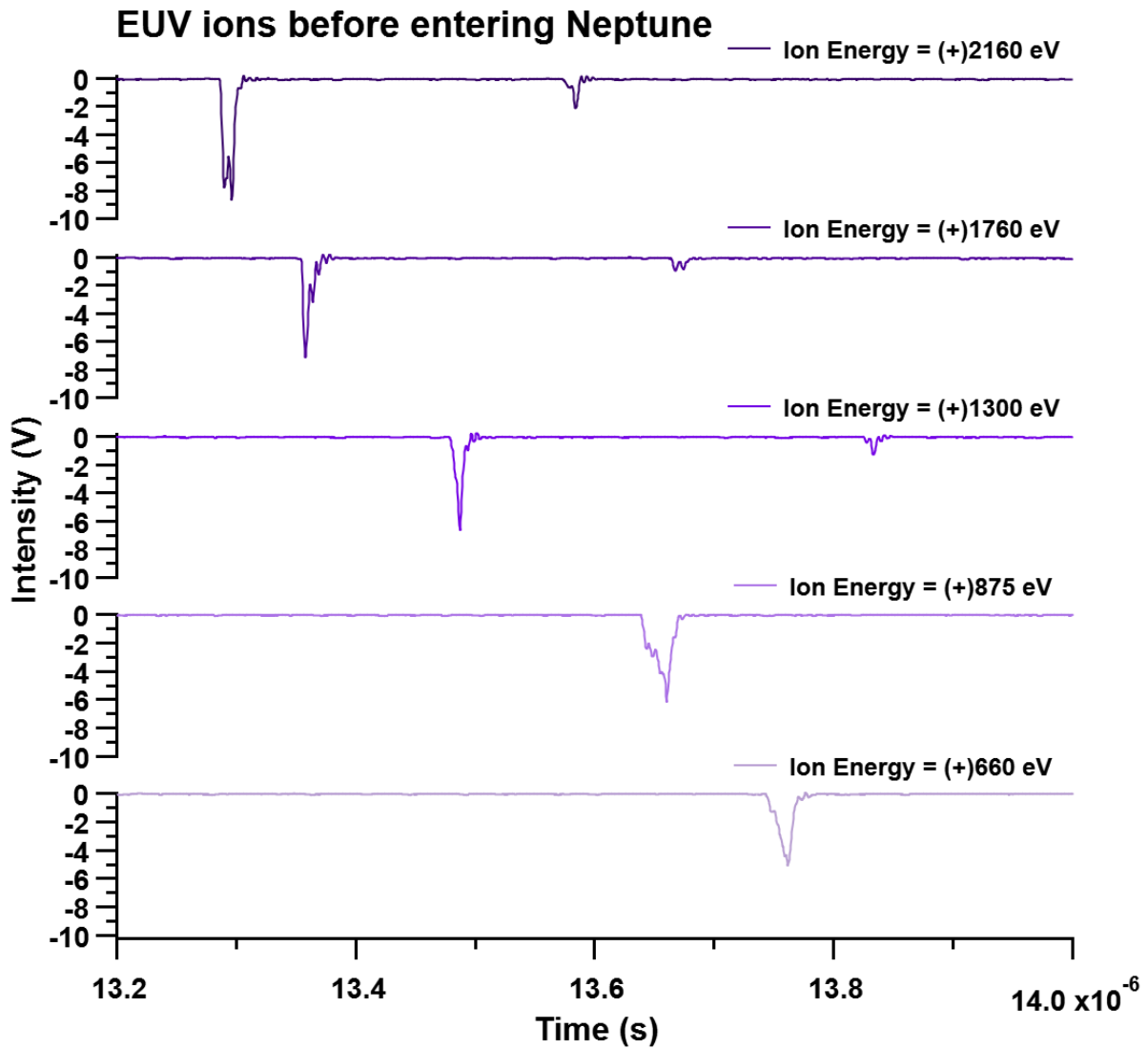


**Figure 5.21** Ion signal intensity measured as a function of arrival time with the mini-MCP detector from EUV laser ablation and ionization of a silicon wafer. The most intense signal is the peak of interest (likely Si), while the other smaller peaks are likely reflected signals due to non-ideal impedance matching from the detector's signal output. Each spectrum was acquired using a single EUV laser shot on a fresh spot on the Si wafer. The detector was placed perpendicular to the ion source at the sample chamber exit so that the ion signal could be measured prior to traveling into the Neptune. The ion energy was changed from (+)2160 eV (top plot) down to (+)660 eV (bottom plot) by changing the potential gradient between the sample and zone plate. The electrodes in the beam deflector were adjusted according to the ion energy.

Figure 5.22 shows a more detailed view of how the shape and width of the ion peaks change as a function of ion energy. The full width of the peak at ion energies  $\geq 1300$  eV is  $\sim 20$  ns, while the width of the corresponding peak at energies  $\leq 875$  eV is  $\sim 30$  ns. As expected, these experimental results suggest that a higher accelerating potential  $\geq 1300$  eV between the sample and zone plate will result in a more intense ion signal through the Neptune mass spectrometer.

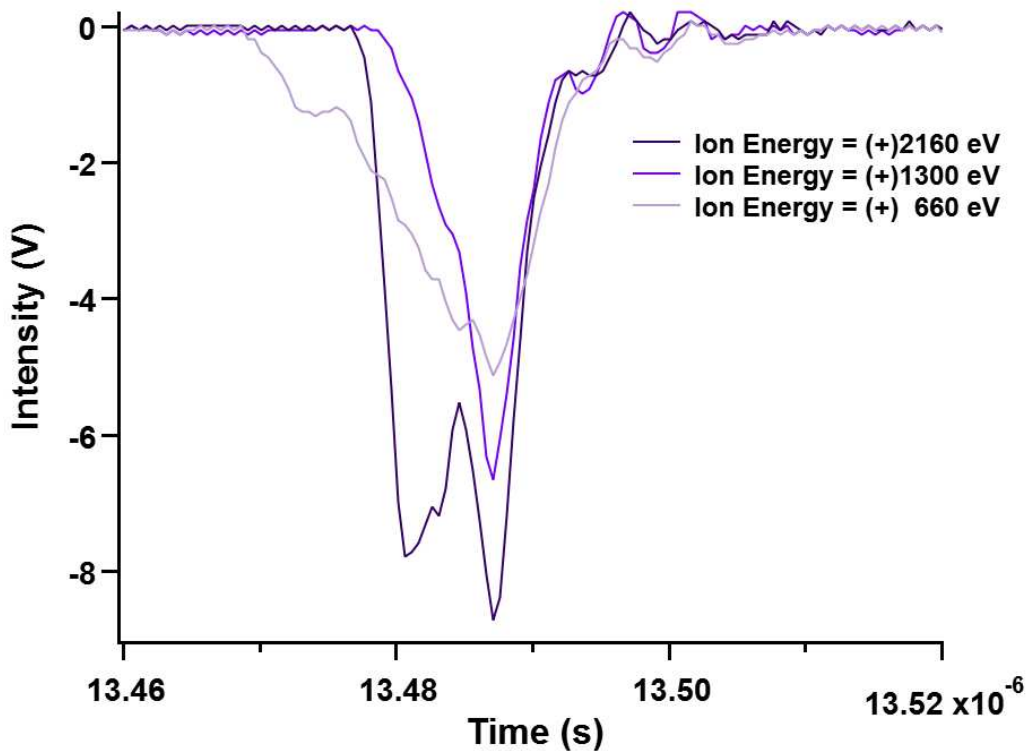


**Figure 5.22** Zoomed in spectra of the Si peaks for ion energies (+)2160 eV, (+)1300 eV, and (+)660 eV from Figure 5.21. The bottom axis on the spectra collected at an ion energy of (+) 2160 eV and (+)660 eV has been offset so that the peak widths can be more directly compared.

The accelerating potential for the EUV generated ions could have been further increased past (+)2160 eV for a more intense signal. However, the limits of the downstream components in the Neptune should be kept in mind. As will be seen in later sections, if the ion energy increases, the potentials between the electrostatic analyzer plates need to increase as well as the magnetic field strength for proper ion focusing and mass separation, respectively. The magnetic sector in particular has strict limits on the field values that it operates at, not to exceed 1.2 Teslas. Because the magnetic field will have to increase

with increasing ion energy for proper mass separation, this needs to be taken into account when optimizing the acceleration potential for the EUV ions, especially with regards to being able to access the high mass isotopes (like  $^{238}\text{U}$ ). Therefore, the EUV ion energy range that will be explored will have an upper limit of (+)2160 eV to stay within the magnetic field working conditions of the Neptune.

After determining that an ion energy of  $\geq 1300$  eV would produce the highest intensity signal, the focus of the ion beam at (+)2160 eV energy was optimized by spatially monitoring the ion beam with the MCP imaging detector as the elements in the coupling lens were changed. To perform these tests, the mini-MCP detector was pulled out of the ion beam pathway using the transfer rod to which it was attached so that the ions could access the MCP imaging detector. The X/Y/Z lenses were slightly adjusted by ( $\pm$ )30 V to center the ion beam on the detector, and the ion beam was focused by adjusting the Einzel lens potential.

Figure 5.23 shows the EUV ion beam profiles with the Einzel lens in the coupling lens turned off and on. When the Einzel lens is turned off, the ion beam shape matches the entrance of the coupling lens, defined by a square-like opening (the image in the figure is slightly rotated because of the positioning of the camera relative to the detector). When the Einzel lens is turned on to an optimal bias of (+)1000 V, the ion beam is focused into the expected vertical line shape. In its original configuration, the coupling lens focuses the ions from a thermal filament into a vertical slit shape for transferring the ion beam into the magnetic sector's entrance slit.

However, while the Einzel lens obviously helps with focusing the EUV generated ions, the shape of the focused ion beam is not necessarily ideal. For comparison, Figure 5.23 also shows a focused beam of rhenium (Re) ions generated from a thermal filament using similar conditions (i.e., ion energy, deflector conditions, and Einzel lens bias are the same). The focus of the ions from the filament results in a more narrow vertical line shape than that of the focused EUV ion beam. The differing beam profiles could be because the coupling lens was specifically designed to focus ions generated from a thermal filament. Additionally, the energy spread of ions created via thermal ionization is more narrow than ions created from

the EUV laser ionization process. While the ion beam deflector does help with energy focusing, it was determined that changing the EUV ions' energy by approximately  $\pm 100$  eV still resulted in a signal at the detector versus the thermal filament ion signal was lost when changing the energy only by  $\pm 10$  eV. The ions generated from the filament therefore have at least a 10X more narrow energy dispersion than the EUV ions, resulting in a more focused beam of filament ions upon arrival at the MCP imaging detector. Note that differences in the ion intensities in the images in Figure 5.23 between the EUV laser and filament source should be ignored because they are producing a different number of ions.

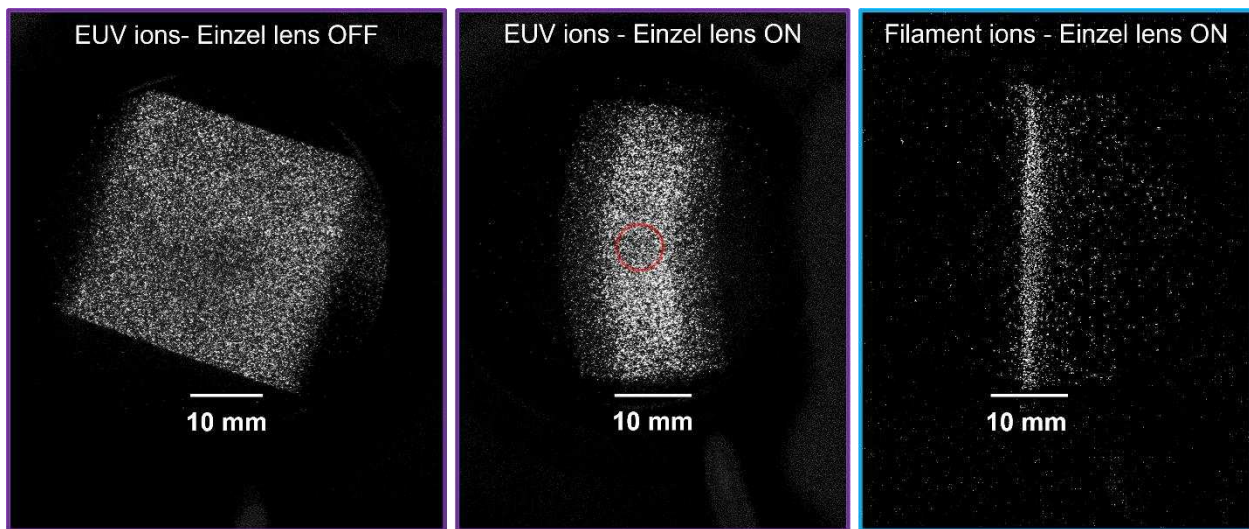


**Figure 5.23** Ion beam profiles collected with the MCP imaging detector prior to the ions' entrance into the Neptune. (Left and middle image) Ions generated from a single EUV laser shot on the silicon wafer were captured without and with potentials applied to the Einzel lens in the coupling ion optics. (Right image) Ions generated from a thermal ionization filament, made of Re, were imaged at similar conditions to the EUV ions with the potentials applied to the Einzel lens. The optimal potential applied to the Einzel lens was (+)1000 V for both ion sources. The red circle in the middle image represents the  $\sim 20$  mm<sup>2</sup> aperture after the extraction lens that represents the first cross-over point into the Neptune.

Another interesting observation of the focused EUV ion beam profile in Figure 5.23 is that the beam shape is slightly bent. This could be a result of one of the deflection plates not being properly tuned. Another cause could be space-charge effects at the MCP detector's active area from the increase flux of ions in the center of the detector when the ions are focused. Looking back, the detector gain or the EUV laser intensity should have been decreased for these acquisitions. Nonetheless, it is promising that the EUV ions can be focused for transmission into the Neptune. However, it should also be noted that the first cross

over into the Neptune is not defined by a vertical slit but rather by a ~5 mm diameter aperture. Therefore, even though focusing the ions with the coupling lens will help aid transmission into the Neptune, ions outside of the ~20 mm<sup>2</sup> area aperture will be lost during this transition. The mismatched shape of the vertical ion beam and circular entrance aperture is graphically depicted in the middle image in Figure 5.23. Better ion optics could surely be designed in the future that would be more suitable for focusing the EUV generated ions into the Neptune.

### **5.e.iii Transmitting EUV ions through cross-over #1 - Experiment**

After confirming suitable acceleration and focusing conditions for transmitting the EUV generated Si ions from the source to the exit of the sample chamber, the ion signal was measured after the ions traveled through the Neptune's first cross-over point and through the entirety of the transfer lens system. Both the mini-MCP and MCP imaging detectors were used again for these measurements by installing them in the Neptune. To make room for the detectors, specifically the larger MCP imaging detector assembly, the slit lens system in the Neptune located between the transfer lens system and ESA was removed.

To install the MCP imaging detector in the Neptune, the MCP plates and phosphor screen were removed from the 4.5"-CF vacuum housing and placed on a mirror mount that fits into the space created by the removal of the slit lens system. Figure 5.24 shows a picture of the MCP imaging detector set-up in the Neptune. A mirror was positioned on the holder behind the phosphor screen at an approximate angle of 45° relative to the screen so that the ion beam image could be viewed perpendicular to the placement of the detector. A viewport window was attached directly above the mirror and the camera was fixed to the viewport so that ion beam images could be captured.

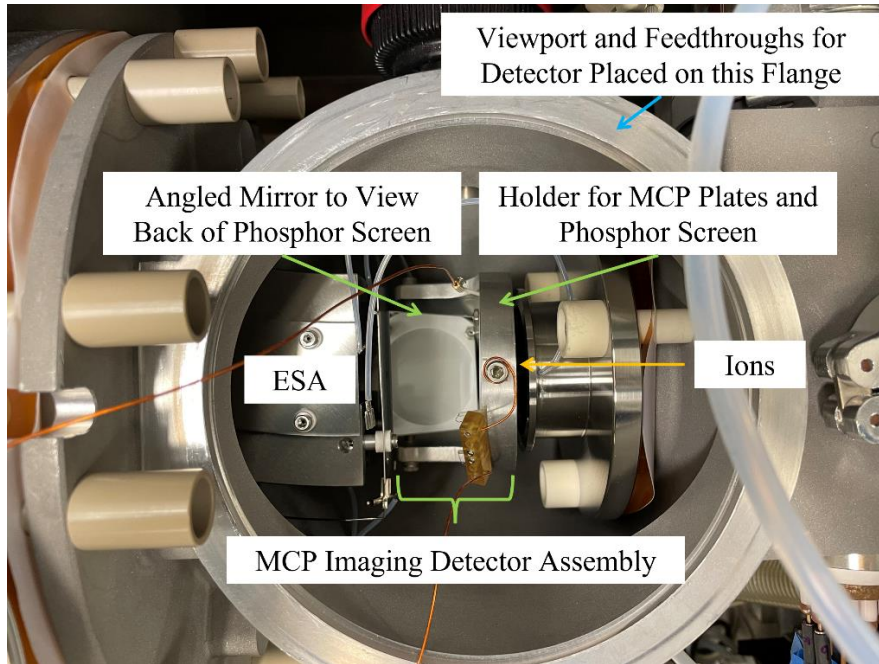


**Figure 5.24** MCP imaging detector installed in the slit lens system region of the Neptune between the transfer lens system and ESA. The holder for the MCP plates and phosphor screen is attached to an optical post and base that interacts with the floor of the vacuum chamber.

To use the mini-MCP detector in the Neptune, the detector was fixed onto the back of the Herzog entrance plate using vacuum compatible Kapton tape. Figure 5.25 shows a photograph of the setup. The mini-MCP detector was electrically isolated from the Herzog plate, which is not shown in Figure 5.25. The mini-MCP detector was biased relative to ground, so the Herzog plate and ESA were unplugged while the mini-MCP detector was operated to avoid arcing since the Herzog and ESA components are biased with reference to (-)5000 V.

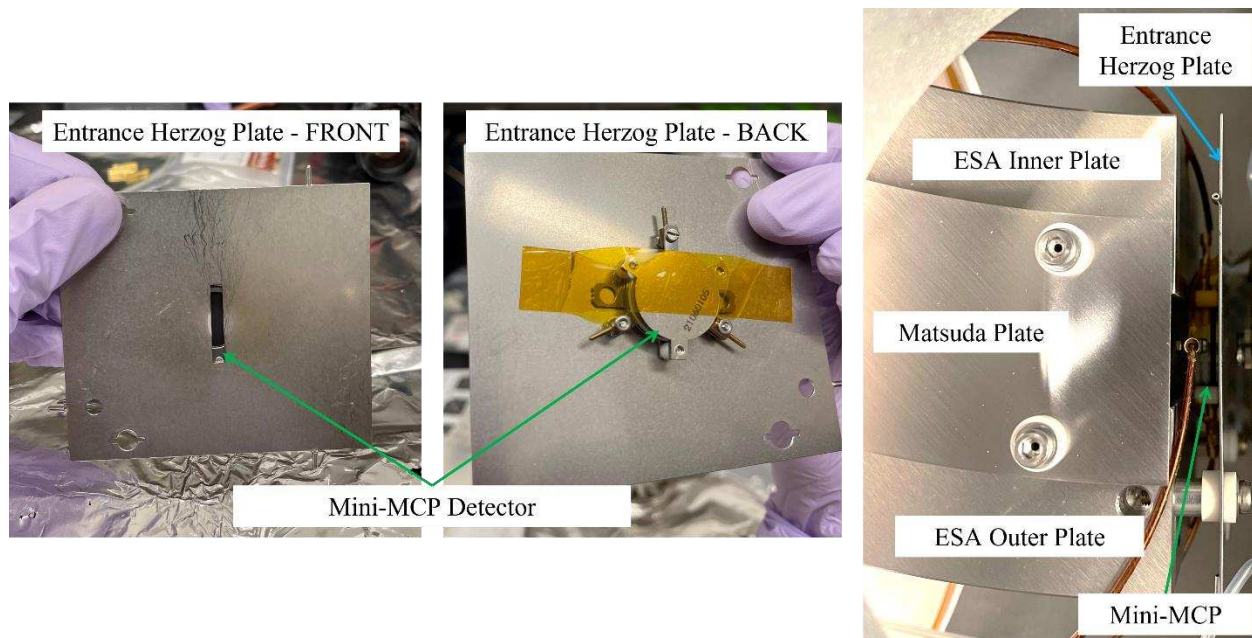


**Figure 5.25** Mini-MCP detector attached to the back of the entrance Herzog plate, marking the entrance of the ESA. The Herzog plate and ESA are unplugged when operating the mini-MCP detector.

Alongside the mini-MCP detector, the MCP imaging detector was also biased with reference to ground using MHV feedthroughs installed on the top flange of the slit lens system region. The MCP detectors were not installed in the Neptune simultaneously. First, the MCP imaging detector was used to observe the shape of the EUV generated ion beam after it travels through the first cross-over point into the Neptune, and confirm if any changes need to be made to either the coupling lens or transfer lens system to aid in focusing or transmission. Then, the mini-MCP detector, placed on the back of the Herzog plate, was used to ensure that the ions were reaching the entrance of the ESA properly in terms of the beam's vertical and horizontal position.

To initially test if the EUV generated ions could be focused through the Neptune's transfer lens system and detected by the MCP imaging detector, the EUV ions made from the ablation and ionization of the Si wafer were accelerated to (+)2160 eV to maximize the ion signal intensity. The ion optics in the Neptune's transfer lens system, which include (in order of appearance) the extraction lens, focus lens, X/Y deflection plates, acceleration lenses 4/5, and the shape quadrupole, were adjusted for initial testing. The extraction lens and acceleration lenses 4/5 were operated at their normal biases of (-)2000 V and (-)5000

V, respectively. Because the EUV ions start with an energy of (+)2160 eV prior to entering the Neptune, the ions will be accelerated to (-)7160 eV upon reaching the MCP imaging detector after traveling through lenses 4/5 in the transfer lens system. The focus lens and X/Y deflection plates were set to 0 V, while the shape quadrupole was disconnected during these experiments because it is biased through a connection on the slit lens system that was removed to install the MCP imaging detector. At these initial transfer lens conditions, the EUV generated ions were successfully detected at the MCP imaging detector, indicating that the EUV generated ions were sufficiently focused past the first cross-over point and through the transfer lens system into the Neptune.

The ion beam profile was then optimized by varying the relative potentials on the focus lens from 0 V to (-)700 V on the instrument software. The X/Y deflection plates remained at 0 V because the beam's horizontal and vertical position were suitable. Figure 5.26 shows the ion beam profiles captured from the MCP imaging detector as the potential on the focusing lens was changed. From 0 V to (-)237 V, the ion beam is shaped into a vertical-like profile. As the potential on the focus lens is increased to (-)500 V, the vertical focus is lost. At (-)700 V, the ion beam's focus is rotated to a more horizontal focus. Beyond a bias of (-)700 V on the focus lens, the ion signal drastically decreased and so is not included in Figure 5.26. Like the Einzel lens in the coupling lens stack, the focus lens in the transfer lens system is used to shape the incoming ions into a narrow vertical line to match the shape of the mass resolution slits that define the second cross-over point.

The results from Figure 5.26 show that some vertical focusing of the EUV generated ions is achieved by optimizing the potential on the focus lens. However, the profile of the EUV ion beam is not ideal when compared to the tightly focused beam generated using the thermal Re filament. Figure 5.26 also shows an image captured from ions generated from the Re filament through the transfer lens system. The Re ions were generated at a much lower starting energy of ~100 eV, which was determined to provide the maximum signal intensity at the detector. As seen in Figure 5.23, the filament ions in Figure 5.26 also result in a much more narrow vertical beam profile compared to the EUV ions. This could be from the lower

velocity dispersion as previously discussed or the fact that the filament ions' starting energy more closely matches the starting conditions of the ICP ions, resulting in better compatibility with the Neptune's ion optics. Unfortunately, when the starting energy of the EUV ions was decreased down to (+)100 eV to replicate the conditions of the ions from the filament, no ions were detected. While more suitable optics could be designed for transmitting and focusing the EUV generated ions through the Neptune, it is promising that the EUV ions can be successfully transferred from the source into the entrance of the Neptune.

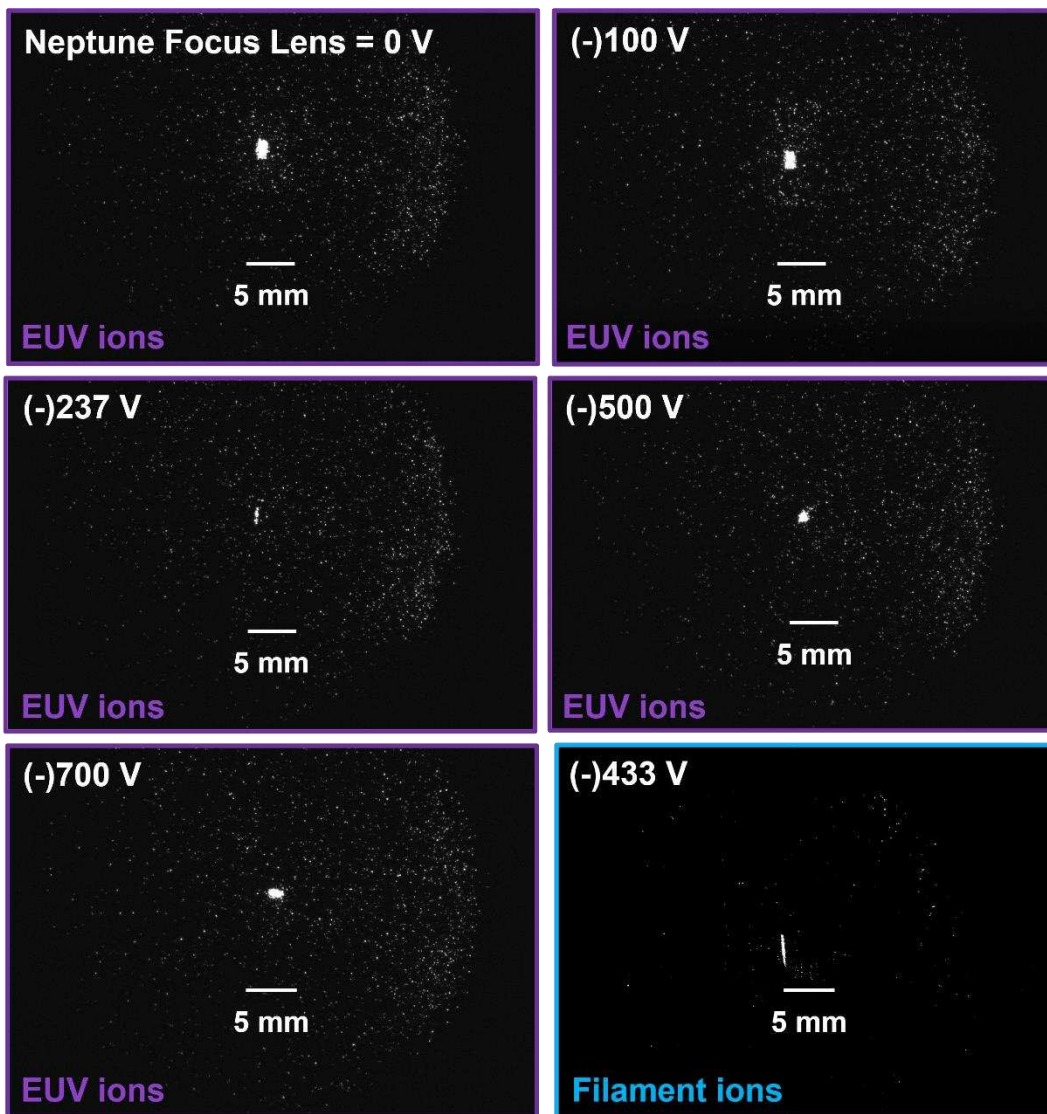


**Figure 5.26** Ion beam profiles collected with the MCP imaging detector after the EUV (purple outlined images) and thermal filament (blue outlined image) ions have traveled through the Neptune's first cross-over point and transfer lens system. The potential on the focus lens in the transfer lens system was varied for each image.

The mini-MCP imaging detector was then used to gain a more quantitative view of the EUV ions after they have traveled through the Neptune's transfer lens system by removing the MCP imaging detector. After removal of the MCP imaging detector, there is sufficient room to re-install the slit lens system because the mini-MCP is installed on the backside of the Herzog entrance plate. However, initial experiments were performed without the slit lens system to maximize the ion signal and ensure that the ions were being properly steered to the center of the ESA entrance defined by the Herzog plate.

Like the prior imaging experiments, all lenses in the transfer lens system were initially set to 0 V, excluding the extraction and acceleration lenses which remained at their normal operating biases of (-)2000 V and (-)5000 V, respectively. Figure 5.27 shows the resulting spectra acquired from the mini-MCP detector with each spectra averaged over 100 EUV laser shots at 10 shots/spot on the Si wafer. The starting ion energy was varied from (+)2160 eV down to (+)660 eV by changing the potential gradient between the sample and zone plate for comparison with the spectra collected prior to the ions entering the Neptune in Figure 5.21. The Einzel lens in the coupling lens stack was optimized according to each ion energy. Ions were detected at the mini-MCP with no adjustments needed to the X/Y deflection plates, indicating that the ion beam's vertical and horizontal position was relatively aligned with the entrance of the ESA. Unlike the imaging results in Figure 5.26, changing the potential of the focus lens did not make an obvious difference in the ion signal intensity or peak shape, so the focus lens remained at 0 V. The focus lens will likely play a larger role in the signal intensity once the slit lens system is re-installed because the ion beam will need to be finely focused through the slits, whereas this is not the case when traveling through the larger opening of the Herzog plate.

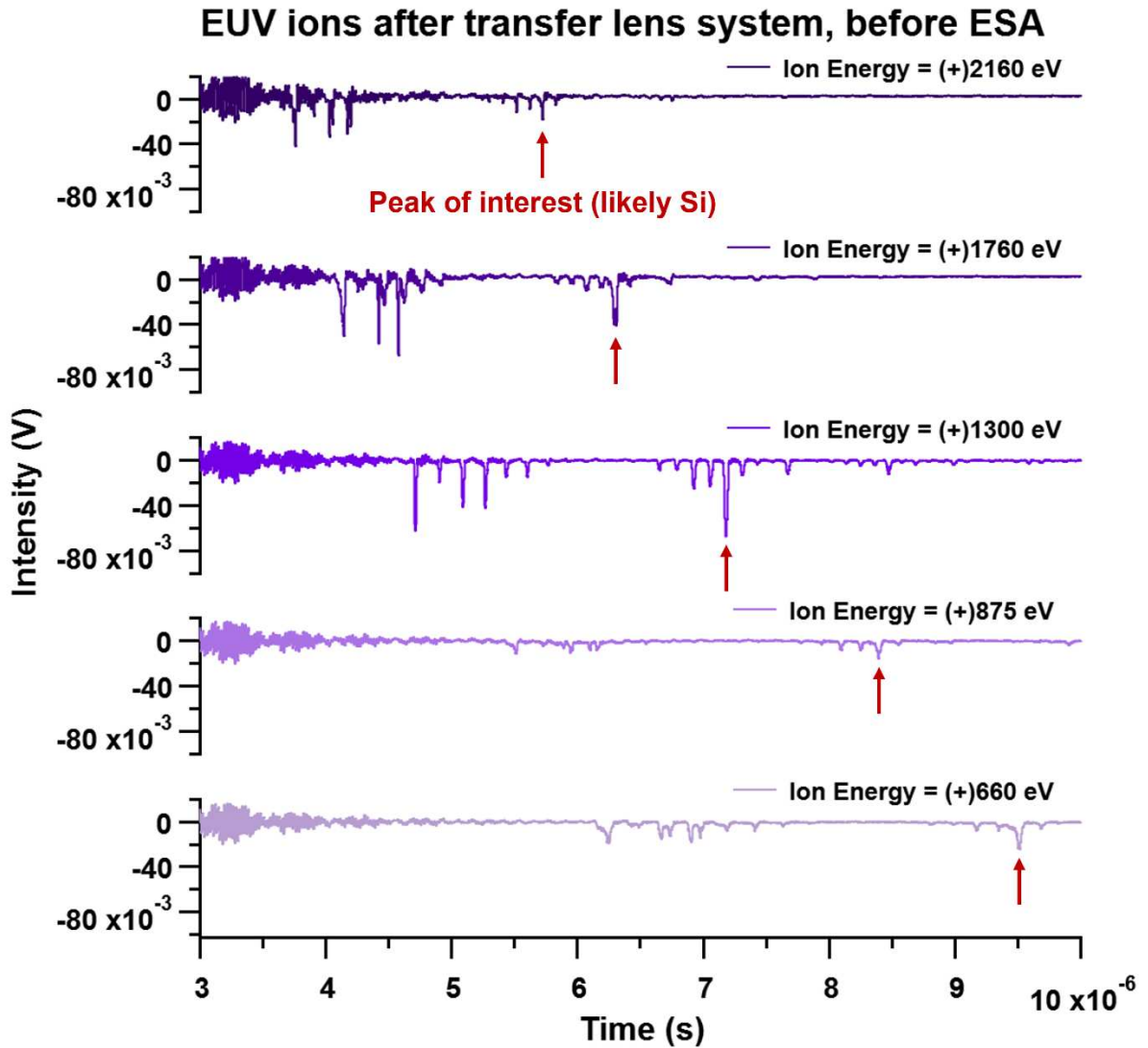


**Figure 5.27** EUV ion signal intensity measured as a function of arrival time with the mini-MCP detector after the ions have traveled through the Neptune's transfer lens system at different starting energies. Each spectrum was acquired using an average of 100 EUV laser shots on the silicon wafer. Ten shots were taken at every spot on the wafer after which the sample was moved 5  $\mu\text{m}$  to ablate a fresh spot. Like the data acquired in Figure 5.21, the ion energy was changed from (+)2160 eV (top plot) down to (+)660 eV (bottom plot) by changing the potential gradient between the sample and zone plate.

Figure 5.27 shows that the maximum peak intensity acquired at each ion energy is >100X lower than that in Figure 5.21. Ions are most likely lost when entering the first cross over point of the Neptune, as explained earlier. Interestingly, Figure 5.27 shows that the ion peak intensities are maximized at an ion energy of (+)1300 eV rather than at an ion energy of (+)2160 eV. Additionally, the peak shape remains more ideal at an energy of (+)1300 eV compared to the abnormal split peaks and broadened peaks

at energies above and below (+)1300 eV, shown in more detail in the zoomed spectra in Figure 5.28. These results indicate that while it would be expected that higher energy ions would result in more intense ion signals, as shown in Figure 5.21, the optimal ion energy after entering the Neptune is dictated by the transfer lens system optics. That is, the extraction and focusing conditions of the transfer lens systems is the most compatible with EUV ions starting at an energy of (+)1300 eV rather than at higher energies. In the future it could be beneficial to further optimize the Neptune's optical components to be more compatible with the higher energy EUV ions to maximize ion transmission.

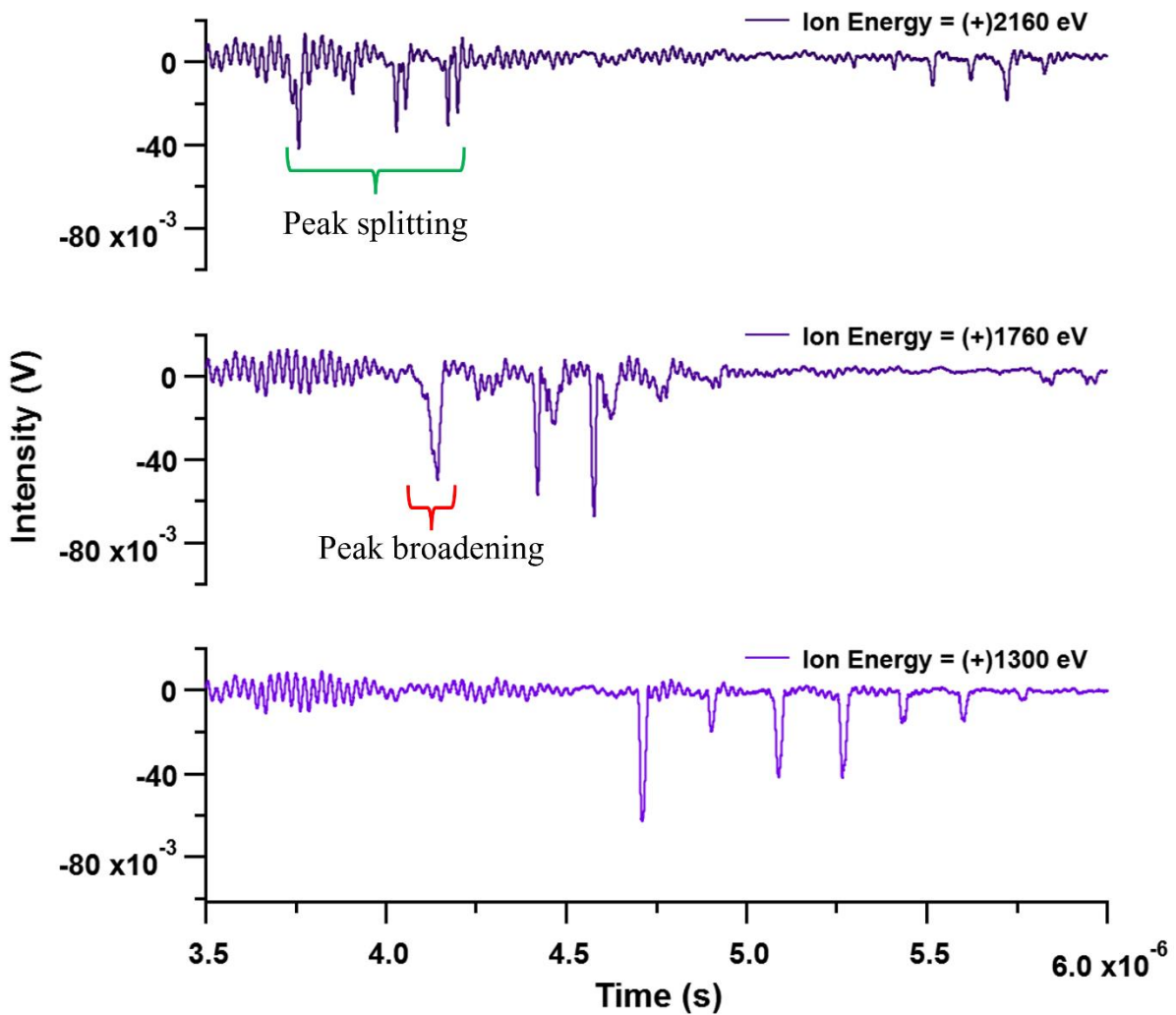


**Figure 5.28** Zoomed in spectra on select peaks for starting EUV ion energies of (+)1300 eV, (+)1760 eV, and (+)2160 eV from Figure 5.27. Examples of the peak abnormalities appearing at higher ion energies have been identified in the spectra.

There are a few other notable differences between the spectra acquired before and after the ions enter the Neptune in Figure 5.21 and Figure 5.27, respectively. Most notably, the spectra in Figure 5.27 show multiple peaks collected in time compared to the one large peak collected in Figure 5.21. This is likely due to the increased flight time that the ions travel from the source into the Neptune, resulting in some mass separation and a TOF-like spectra. The single peak in the spectra in Figure 5.21 was previously identified as Si but based on the results from Figure 5.27, it is possible that the peak is composed of Si but with additional ion masses as well. Additionally, the spectra in Figure 5.27 are an average of 100 EUV laser shots that were taken at 10 shots/spot on the silicon wafer, incorporating the signals of additional ion species formed from multiple laser shots at every spot that are not included in the single shot spectra in Figure 5.21. Nonetheless, the peak identified in Figure 5.27 is likely Si because it remains present and stable even after ablating a single spot with >100 laser shots, while all other peaks drastically decrease. The time scales of the spectra in Figure 5.21 and Figure 5.27 are also different because of the delay applied to the oscilloscope after the laser pulse trigger. Unlike what is shown in the spectra, the arrival time of the ions after entering the Neptune will be later than the ions' arrival time prior to entering the Neptune. Spectra in Figure 5.27 also show more noise at the start of the signal. The source of this noise is from the high voltage pulse of the EUV laser, but it is not known why this noise was not prevalent in the spectra acquired prior to the ions entering the Neptune.

#### **5.e.iv Transmitting EUV ions through cross-over #2 - Experiment**

After the optimal accelerating, focusing, and X/Y plate potentials were determined for the EUV ions entering the Neptune through the first cross over-point and the transfer lens system, the EUV ion beam was further optimized for transmission through the second cross over point. The mass resolution slits in the slit lens system marks the second cross over point, defined by their narrow physical width (see Figure 5.4). The low mass resolution slit has the largest width while the high mass resolution slit has the smallest width, and the slits are placed at the focal point of the focus lens.

To measure the transmission of the EUV ions through the second cross-over point, the mini-MCP detector remained at its position on the back of the Herzog entrance plate at the ESA, and the slit lens system was re-installed. The MCP imaging detector cannot be used with the slit lens system re-installed due to the detector's large size. Because a higher mass resolution results in a lower signal intensity, the lowest mass resolution slit was used for these experiments to maximize the ion signal. The installment of the slit lens system means that the ion beam's horizontal and vertical position needs to be more finely tuned with respect to the narrow width of the low mass resolution slit as opposed to the much wider width of the Herzog entrance plate opening. The focus and shape lenses in the transfer lens system will also play a larger role in optimizing the transmission of the ion beam through the resolution slits.

The EUV ions created from the silicon wafer were accelerated to an energy of (+)1300 eV using the potential gradient between the sample and zone plate. The Einzel lens in the coupling optics was set to (+)700 V and the Neptune extraction lens remained at (-)2000 V. All other lenses in the transfer and slit lens system were initially set to 0 V in the software interface. At these conditions, no ions were detected at the mini-MCP detector, likely indicating that the X/Y deflection, focus, and/or shape lenses need to be adjusted for proper ion transmission through the low resolution slit.

The X/Y deflection plates were varied within the potential limits set in the software until an ion signal was observed on the mini-MCP detector. The X-deflection plate was changed to (+)7.53 V, and the Y-deflection plate was changed to (+)3.45 V in order to center the ion beam through the low mass resolution slit. Additionally, the shape quadrupole was set to (+)200 V for further optimization of the ion signal. Interestingly, the focus lens remained at 0 V for optimal ion signal intensity indicating that the ion beam is sufficiently focused through the slit lens system using the focus lens' base potential. However, the focus lens may need to be adjusted once the mini-MCP is removed from the back of the Herzog plate because the electric fields will change once the Herzog plate (and ESA) are turned on.

Figure 5.29 shows the spectra, zoomed in on the peak of interest (likely Si), acquired from the mini-MCP detector using the optimized lens settings after the ions have traveled through the low mass

resolution slit. For comparison, the (+)1300 eV spectra from Figure 5.27 collected without the slit lens system is also shown. As expected the absolute signal intensity of the ion peak (i.e., the peak area) is ~3X lower after the ions pass through the slit. The peak width of the signals, which directly correlates to mass resolution, is also expectedly more narrow after passing through the low resolution slit as compared to when the slit was absent. The full width of the peak at half of the maximum height (FWHM) is ~26 ns without the slit and ~6 ns with the low mass resolution slit, corresponding to a mass resolution increase from approximately 140 to 535, respectively, using the equation shown in Figure 5.29. The measured low mass resolution of ~535 is in line with the expected mass resolution of the Neptune, which is typically >400 when the ICP ion source is used.

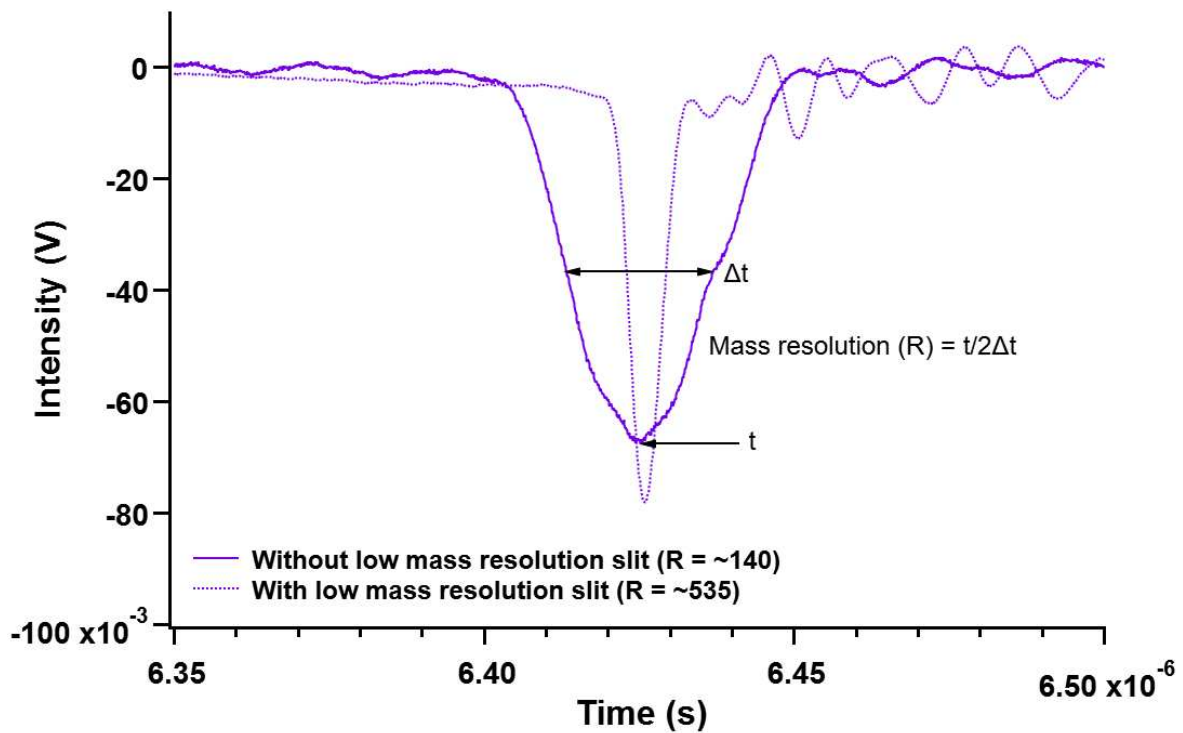


**Figure 5.29** Zoomed in spectra collected with the mini-MCP detector of the EUV ions without (solid purple line) and with (dashed purple line) the low mass resolution slit installed in the Neptune. Each spectrum is an average of 100 EUV laser shots collected with 10 shots/spot on the silicon wafer, and the initial ion energy is (+)1300 eV. The spectrums' timescale has been offset for a direct comparison between the peaks.

Overall, the results shown in Figure 5.29 show the successful transmission of EUV ions through the extraction lens aperture (cross over #1) and through the low mass resolution slit (cross over

#2). The next step is to transmit the EUV ions past the ESA and through the slit prior to the magnet (cross over #3). This will arguably be the most difficult step because the ESA needs to be finely tuned to focus and transmit the ions through the third cross over point prior to their entrance into the magnet. If the potentials applied to the ESA are off by just a few volts, then the ion signal can be severely compromised and/or lost at the third cross over point.

### **5.e.v Transmitting EUV ions through cross-over #3 - Calculation**

To mitigate the challenges associated with experimentally finding the ESA potentials needed to transmit and focus the EUV ions past the third cross over point, the ESA parameters were first theoretically modeled. After modeling the ESA potentials, transmission of the EUV ions through the ESA were measured by placing the mini-MCP detector after the ESA but before the magnet at two different locations.

To model the EUV ions through the Neptune's ESA, recall that the ESA is composed of two concentric plates called the inner and outer plates that focus and filter the ions in terms of their energy and deflects the ions approximately  $90^\circ$  into the magnetic sector. To transmit positive ions, the inner plate is biased more negatively than the outer plate. The DC bias that is applied to each of the plates is directly correlated with the ions' energy. More specifically, the potential difference between the two plates depends on the energy of the incoming ions such that higher energy ions will require a larger potential difference than lower energy ions for proper transmission through the ESA. This relationship between the ions' initial energy ( $U$ ) prior to entering and the electric field strength ( $E$ ) between the ESA plates is seen through Equation 5.4. from above.

As the ion's starting energy ( $U$ ) increases the strength of the electric field ( $E$ ) must also increase accordingly. The electric field strength of the ESA will depend on how the ESA is made in terms of its plate length, distance, radius of curvature, etc. Under normal operating conditions the Neptune's two ESA plates maintain a potential difference of around (-)785 V by biasing the inner and outer plates to

approximately (-)5299 V and (-)4514 V, respectively (see Table 5.4). The inner and outer ESA plates are biased in accordance with the potential of the Herzog plates that are located at the entrance and exit of the ESA, which are biased to approximately (-)4894 V. The potential of the Herzog plates create what is called a “center voltage” in the ESA so that the incoming ions maintain a constant energy as they travel through the electrostatic sector for effective energy focusing and filtering. The Herzog plate potential is set at approximately the same potential as acceleration lens 5 in the transfer lens system. Therefore, because the ions created from the ICP start near ground, the ions’ energy when entering the ESA is approximately equal to the Herzog plate potential. The EUV ions, on the other hand, will have (+)1300 eV more energy when entering the ESA compared to the ICP ions because of the bias applied to the sample. If the ICP ions have an energy around (-)4894 eV in the ESA, the EUV ions are expected to have an energy around (-)6194 eV. The ESA’s center voltage of (-)4894 V can be left unchanged for transmission of the higher energy EUV ions through the ESA. However, the electric field strength created by the potential difference between the two ESA plates must increase according to the higher energy of the EUV ions. For clarification, only after the ions leave the ESA are they further accelerated by a final acceleration potential of approximately (-)10 kV via the acceleration lenses prior to entering the magnetic sector.

To determine the ESA inner and outer plate potentials required to transmit and focus the higher energy EUV ions, a relationship between how the ESA plate potentials change as a function of ion energy was indirectly measured. An indirect measurement was performed because there is not a straight forward route for directly changing the energy of the ICP ions and measuring the corresponding change in the ESA. In the Neptune software with the instrument in a stand-by state, the High Voltage can be varied from its operating potential of (-)10 kV down to approximately (-)500 V. When the High Voltage is changed, the Neptune software automatically changes the potentials on all the ion lenses accordingly, including the Herzog and ESA plates. Because the Herzog plate potential is approximately equal to the energy of the ions in the ESA when using the ICP, the potentials on the Herzog and ESA plates can be measured to establish a relationship of how the ESA’s electric field strength changes as a function of the

ion energy. From this relationship, we can expect to extrapolate the ESA plate potentials required to transmit and filter the EUV ions entering the ESA with approximately (+)1300 eV more energy than the ICP ions. It should be noted that the Neptune's High Voltage can only be varied when the instrument is not operating. As soon as a formal run is started on the instrument, the software automatically sets the High Voltage back to (-)10 kV, and all ion optics also change accordingly.

The Neptune's High Voltage was changed in 500 V steps in the Neptune's software from (-)10 kV down to (-)500 V. A high voltage probe was used to measure the High Voltage, Herzog plate, and ESA plate potentials as the High Voltage was varied. The High Voltage potential was measured by connecting the probe to the outer ESA vacuum chamber (which is floated to the High Voltage potential), while the Herzog and ESA plate potentials were measured by connecting the probe to the corresponding connector pins on Feedthru #2. The probe was referenced to instrument ground for all measurements. Table 5.4 shows the resulting potentials that were measured using the high voltage probe for each component, including the calculated ESA plate difference.

**Table 5.4** High voltage probe measurements of the Neptune's High Voltage, Herzog Plate, ESA Inner Plate, and ESA Outer Plate as the High Voltage is varied from a nominal bias of (-)10 kV down to (-)500 V in 500 V steps. The listed ESA Plate Difference is calculated by subtracting the ESA Outer Plate bias from the ESA Inner Plate bias. Note that the High Voltage measurements from (-)9930 V to (-)6930 V are only accurate to the tens place because of the limited dynamic range of the multi-meter used to record the probe output.

High Voltage (V)	Herzog Plate (V)	ESA Inner Plate (V)	ESA Outer Plate (V)	ESA Plate Difference (V)
-9930	-4894	-5299	-4514	-785
-9430	-4643	-5029	-4282	-747
-8930	-4390	-4758	-4050	-708
-8430	-4138	-4482	-3813	-669
-7930	-3892	-4216	-3585	-631
-7430	-3646	-3949	-3358	-591
-6930	-3400	-3683	-3131	-552
-6493	-3153	-3417	-2904	-513
-5989	-2907	-3150	-2677	-473
-5486	-2661	-2884	-2450	-434
-4982	-2415	-2617	-2223	-394
-4479	-2168	-2351	-1996	-355
-3976	-1922	-2084	-1769	-315
-3472	-1676	-1818	-1542	-276
-2969	-1430	-1551	-1315	-236

-2466	-1183	-1285	-1088	-197
-1963	-937	-1018	- 861	-157
-1460	-691	- 752	- 634	-118
- 956	-441	- 482	- 403	- 79
- 453	-196	- 216	- 177	- 39

Figure 5.30 plots the ESA plate difference as a function of the Herzog plate potentials (i.e., the approximate energy of the ions in the ESA) listed in Table 5.4 as the Neptune's High Voltage is varied. Following the expected relationship from Equation 5.4, Figure 5.30 shows that the electric field strength of the ESA increases linearly as the ion energy increases. Using the linear best fit line through the measured potentials, the calculated ESA plate difference needed to transmit the EUV ions starting with an energy of (+)1300 eV and accelerating to (-)6194 eV prior to entering the ESA is  $(-)996 \pm 11 \text{ V} (2\sigma)$ . Although it is expected that a starting EUV ion energy of (+)1300 eV will produce the most optimal ion signal based off results from Figure 5.27, the ESA conditions that would be expected for EUV ions starting at energies of (+)2160 eV, (+)1760 eV, (+)875 eV, and (+)660 eV are also included in Figure 5.30. These additional ion energies can be used to further compare calculated ESA parameters with experimentally determined parameters as the ion energy is varied.

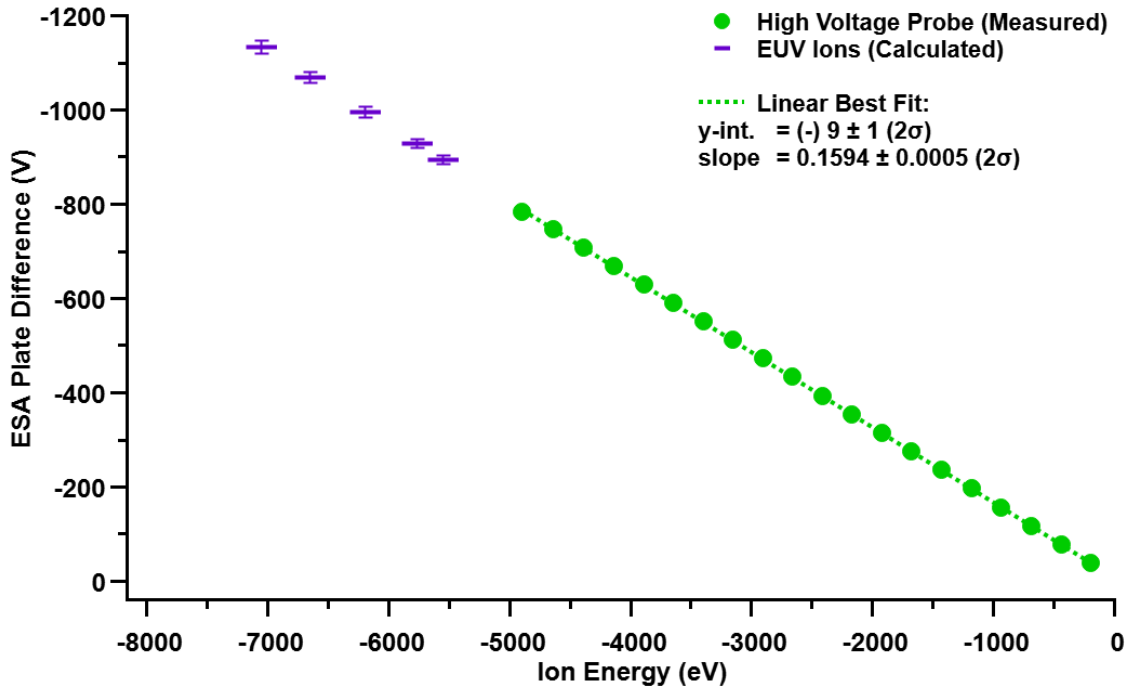


**Figure 5.30** ESA plate difference plotted as a function of ion energy using the high voltage probe measurements listed in Table 5.4 (green circles). The plotted ion energy is assumed to be equivalent to the measured Herzog plate potential. The linear best fit line through the measured points (green dashed line) was used to extrapolate the ESA plate differences needed to transmit the EUV ions (purple solid lines) starting at a higher energy than the ICP ions. The extrapolated points for the EUV ions are shown with  $2\sigma$  error bars, which were propagated using the uncertainty of the slope from linear regression.

After calculating the ESA plate difference that would be expected to transmit the higher energy EUV ions through the ESA, the bias that would be needed on each plate to create the electric field was calculated. The inner and outer ESA plates are not biased equally from the center voltage (i.e., the Herzog plate potential). The inner plate has a higher bias in reference to the center voltage than the outer plate. Therefore, alongside the ESA's electric field strength, it is also important to estimate the potential on each plate that will be needed to create that electric field for proper transmission and focusing of the higher energy EUV ions through the ESA. Because the center voltage of the ESA will remain at (-)4894 V when the (-)6194 eV EUV ions enter the ESA, the potentials on the ESA inner and outer plates will need to change in reference to this center voltage. To determine each plate potential for EUV ion transmission in reference to the center voltage, the offset voltage applied to each ESA plate was measured. The offset voltage is defined here as the potential on each ion optic that is added to its base potential (i.e.,  $U_1$  or  $U_2$ ).

The offset voltage applied to the ESA plates, rather than the absolute potentials (offset + base potential) listed in Table 5.4, is needed because the ESA plate potentials should be changed according to the offset values only, while maintaining the same base potential, to ensure that the center voltage is preserved.

Similar to the prior measurements using the high voltage probe, the offset potentials on the ESA inner and outer plates were measured with the probe while the Neptune's High Voltage was changed. However, unlike when measuring the absolute potentials, measuring the offset potentials requires the High Voltage to be turned off (i.e.,  $U_1$  and  $U_2 = 0$  V). Therefore, even though the value of the High Voltage was varied from (-)10 kV to (-)500 V in the software interface, the only potential applied to the Neptune components were the low voltage offset potentials. Table 5.5 lists the offset potentials recorded for the ESA plates as the corresponding offset potential for the High Voltage is varied, alongside their equivalent absolute values when the High Voltage is turned on, the latter of which is also listed in Table 5.4.

**Table 5.5** Neptune High Voltage and ESA plate offset potentials, in parenthesis, measured with the high voltage probe with the High Voltage off. The corresponding absolute potentials are listed with the High Voltage turned on, which are also listed in Table 5.4.

High Voltage (V), Absolute (Offset)	ESA Inner Plate (V), Absolute (Offset)	ESA Outer Plate (V), Absolute (Offset)
-9930 (- 1)	-5299 (-403)	-4514 (381)
-9430 ( 1)	-5029 (-381)	-4282 (362)
-8930 ( 3)	-4758 (-360)	-4050 (344)
-8430 ( 4)	-4482 (-339)	-3813 (326)
-7930 ( 5)	-4216 (-318)	-3585 (307)
-7430 ( 7)	-3949 (-298)	-3358 (289)
-6930 ( 8)	-3683 (-277)	-3131 (271)
-6493 (10)	-3417 (-256)	-2904 (252)
-5989 (11)	-3150 (-235)	-2677 (234)
-5486 (12)	-2884 (-215)	-2450 (217)
-4982 (14)	-2617 (-193)	-2223 (199)
-4479 (15)	-2351 (-172)	-1996 (182)
-3976 (16)	-2084 (-150)	-1769 (164)
-3472 (18)	-1818 (-129)	-1542 (146)
-2969 (19)	-1551 (-107)	-1315 (129)
-2466 (20)	-1285 (- 85)	-1088 (111)
-1963 (21)	-1018 (- 64)	- 861 ( 93)
-1460 (22)	- 752 (- 42)	- 634 ( 76)
- 956 (24)	- 482 (- 20)	- 403 ( 58)
- 453 (25)	- 216 ( 1)	- 177 ( 40)

Figure 5.31 plots the offset potential for the inner plate as a function of the ESA plate difference to determine the offset potential that will need to be applied to the inner and outer ESA plates to create the expected (-)996 V potential difference to transmit and focus the (-)6194 eV EUV ions with reference to an ESA center voltage of (-)4894 V. Using the linear best fit line through the measured offset potentials, the inner ESA plate is expected have an offset potential of  $(-)516 \pm 5 \text{ V}$  ( $2\sigma$ ) to create a potential difference of (-)996 V between the inner and outer plates for transmission of the EUV ions. Therefore the absolute potential of the ESA inner plate is expected to be  $(-)5412 \pm 27 \text{ V}$  ( $2\sigma$ ), which is calculated as follows:

$$(-)516 \text{ V} - (-)403 \text{ V} = (-)113 \text{ V} + (-)5299 \text{ V} = (-)5412 \text{ V}$$

Where (-)403 V and (-)5299 V are the offset and absolute potentials of the ESA's inner plate at the Neptune's nominal operating voltage of (-)10 kV, listed in the first row in Table 5.5. Therefore, the outer ESA plate's potential is calculated as  $(-)4416 \pm 27 \text{ V}$  ( $2\sigma$ ) to create the expected (-)996 V potential plate difference to transmit the EUV generated ions through the ESA. The ESA inner and outer plate bias was also calculated for EUV generated ions with energies above and below the expected optimal (-)6194 eV ion energy. Table 5.6 provides a compilation of the calculated potentials for the ESA that are expected for focusing and transmitting the higher energy ions created from EUV laser ablation and ionization.

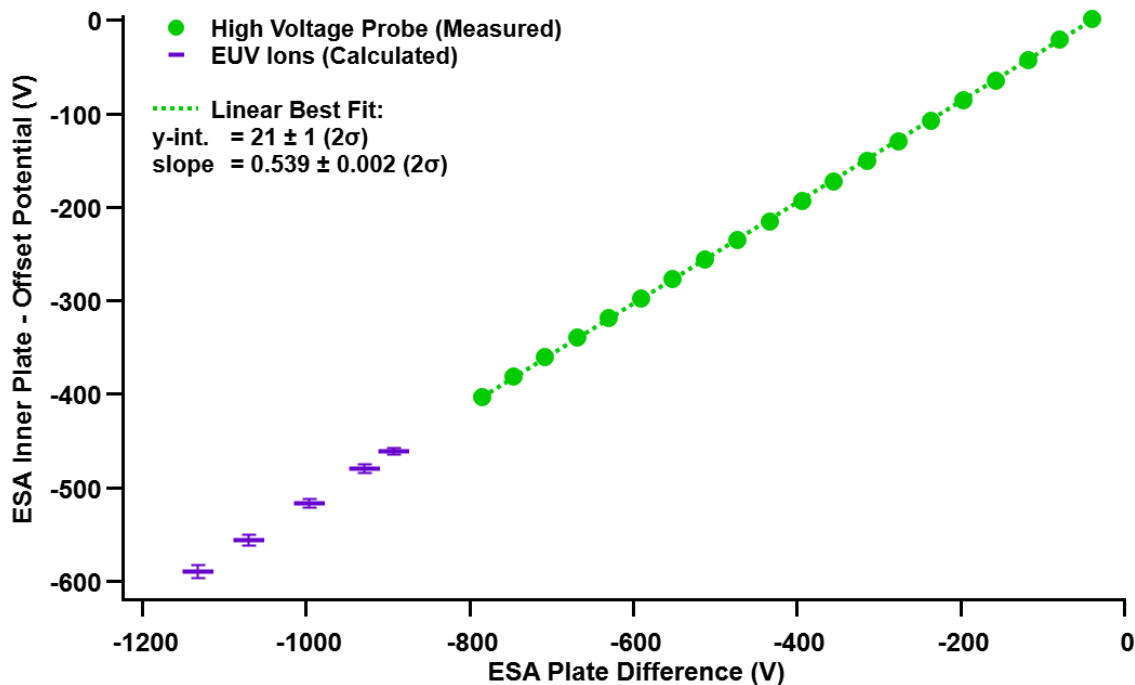


**Figure 5.31** ESA inner plate base potential plotted as a function of ESA plate difference using the high voltage probe measurements listed in Table 5.4 and Table 5.5 (green circles). The linear best fit line through the measured points (green dashed line) was used to extrapolate the ESA inner plate base potentials needed to transmit the EUV ions (purple solid lines) starting at a higher energy than the ICP ions. The extrapolated points for the EUV ions have  $2\sigma$  errors, which were propagated using the uncertainty of the slope from linear regression.

**Table 5.6** Measured ESA conditions for transmission of the ICP ions, representing the Neptune’s normal operating conditions, alongside the calculated/expected ESA conditions for transmission of the higher energy EUV ions. Uncertainties reported for the ESA calculations for the EUV ion source are  $2\sigma$ .

Ion Source	Sample (V)	Ion Energy at ESA (eV)	Herzog Plate/ESA Center Voltage (V)	ESA Inner Plate (V)	ESA Outer Plate (V)	ESA Plate Difference (V)
ICP	0	-4894	-4894	-5299	-4514	-785
EUV	660	-5554	-4894	$-5357 \pm 19$	$-4463 \pm 19$	$-894 \pm 9$
EUV	875	-5769	-4894	$-5376 \pm 22$	$-4447 \pm 22$	$-929 \pm 9$
EUV	1300	-6194	-4894	$-5412 \pm 27$	$-4416 \pm 27$	$-996 \pm 11$
EUV	1760	-6654	-4894	$-5452 \pm 35$	$-4382 \pm 35$	$-1070 \pm 12$
EUV	2160	-7054	-4894	$-5486 \pm 43$	$-4352 \pm 43$	$-1133 \pm 13$

### 5.e.vi Transmitting EUV ions through cross-over #3 – Experiment #1

The theoretical ESA parameters that were calculated for transmitting and focusing the EUV ions according to their energy was then experimentally tested by initially placing the mini-MCP detector at the exit of the ESA, immediately after the exit Herzog plate. Placing the mini-MCP after the Herzog plate

provided more room for error than placing the MCP after the intermediate slit that defines the third cross over because ions are expected to be detected after the ESA within a potential ESA plate range of roughly  $(\pm)50$  V. On the other hand, the ESA plates will need to be tuned within a window of approximately  $(\pm)5$ -10 V when detecting ions after the intermediate slit.

The ions were detected after the ESA, but before traveling through the intermediate slit (i.e., cross over #3), using the experimental set-up shown in Figure 5.32. The mini-MCP was attached to the lens that proceeds the exit Herzog plate on the ESA. These lenses remained disconnected while the mini-MCP was installed. Like in prior set-ups, the mini-MCP was biased with reference to instrument ground.

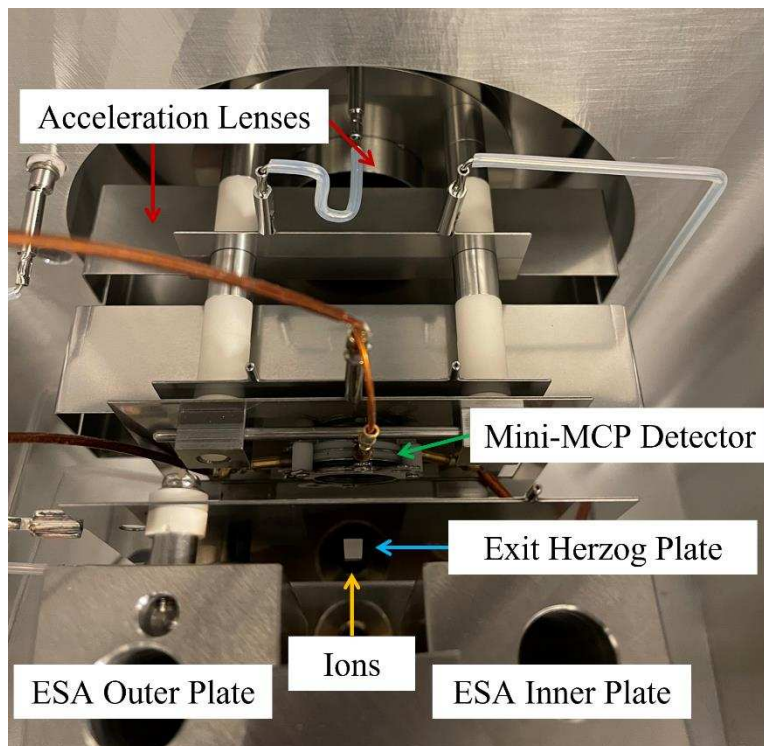


**Figure 5.32** Mini-MCP detector placed immediately after the exit of the Herzog plate to measure the ion signal after the EUV ions leave the ESA. In this set-up, the Herzog plate is biased as normal, but the lens immediately after, to which the mini-MCP is attached, is disconnected for installment of the detector.

To change the potentials applied to the ESA plates, an external power supply and connectors were used to bias the ESA inner and outer plates. The external power supply was operated with reference to instrument ground. To start, the ESA inner plate was set to a bias of  $(-)$ 5412 V and the outer

plate to a bias of (-)4416 V. Initially, the slit lens system was removed for these measurements to maximize the ion yield after the ESA. All other lens potentials remained as they were with the ions accelerated to (+)1300 eV, the Einzel lens set at (+)700 V, and the extraction lens at (-)2000 V. The ESA plates were then separately ramped up and down in 1 V steps from calculated potentials as the laser fired at the silicon wafer until a signal was observed on the mini-MCP detector. The ESA plates were then iteratively optimized until the ion signal was maximized. The ESA plate potentials were determined in this way for EUV ions starting at energies of (+)2160 eV, (+)1760 eV, (+)1300 eV, (+)875 eV, and (+)660 eV. Figure 5.33 shows the resulting ion spectra acquired at these varying ion energies as the ESA plate potentials are changed. Table 5.7 shows the corresponding measured ESA inner and outer plate potentials used to acquire the ion signals. The maximum and minimum potentials for each plate where the ion signal was lost was also determined and is listed next to the measured plate potentials. The potential range for each plate will be useful when fine tuning the ESA to transmit EUV ions through the intermediate slit.

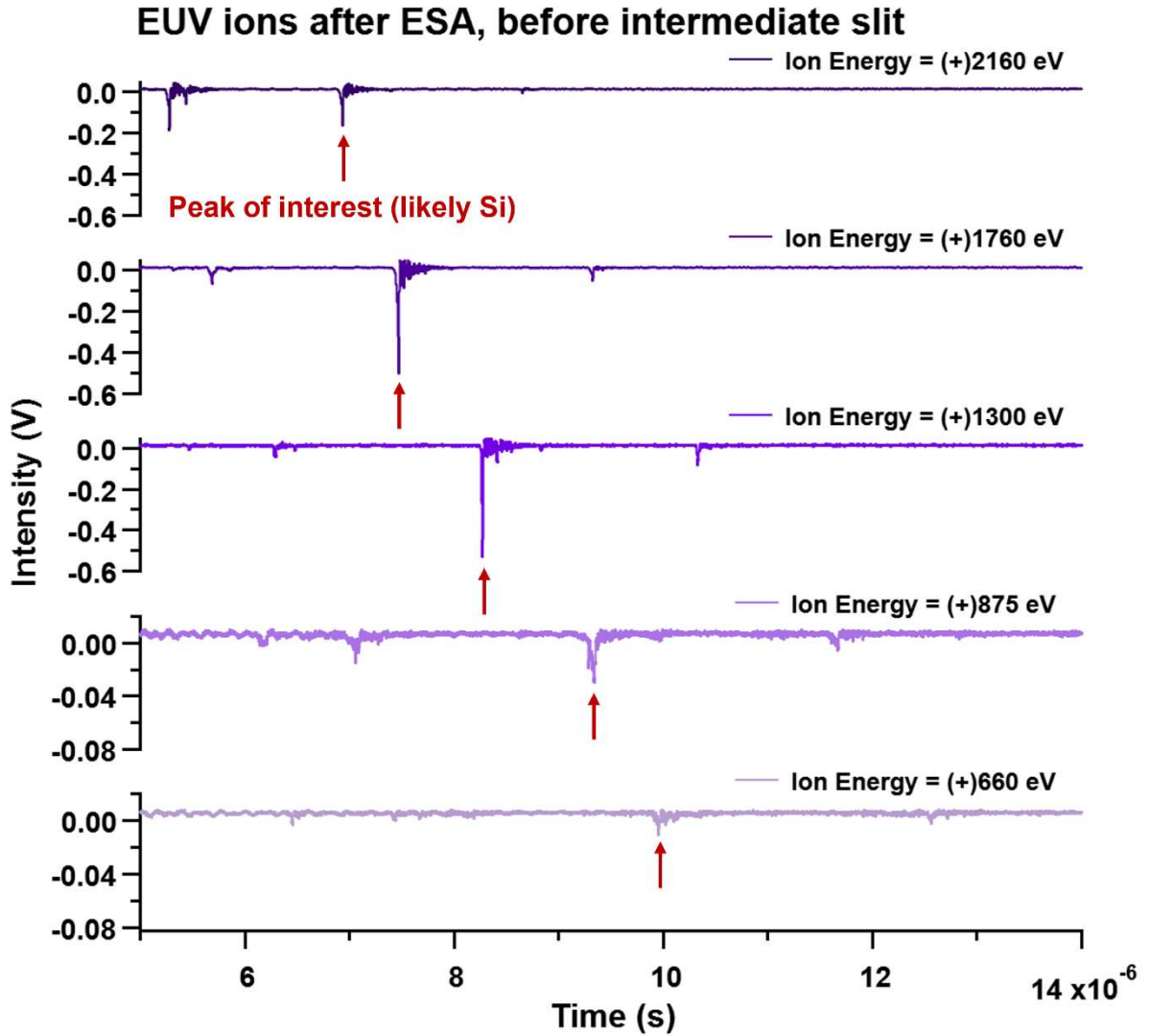


**Figure 5.33** EUV ion signal intensity measured as a function of arrival time with the mini-MCP detector after the ions have traveled through the Neptune’s ESA at different starting energies. Each spectrum was acquired using an average of 60 EUV laser shots at a single spot on the silicon wafer.

**Table 5.7** Measured ESA inner and outer plate biases to transmit EUV ions at variable energies used to collect the ion signals shown in Figure 5.33. The calculated ESA inner and outer plate biases from Table 5.6 are also listed, alongside the percent error between the measured and calculated values.

Sample (V)	Ion Energy at ESA (eV)	ESA Inner Plate (V)			ESA Outer Plate (V)		
		Measured	Calculated	% Error	Measured	Calculated	% Error
660	-5554	-5350 ± 57	-5357	0.13%	-4470 ± 55	-4463	-0.16%
875	-5769	-5367 ± 44	-5376	0.17%	-4437 ± 46	-4447	0.22%
1300	-6194	-5397 ± 35	-5412	0.29%	-4397 ± 31	-4416	0.43%
1760	-6654	-5428 ± 45	-5452	0.44%	-4358 ± 39	-4382	0.55%
2160	-7054	-5456 ± 50	-5486	0.55%	-4318 ± 44	-4352	0.78%

The ESA inner and outer plate potentials that were experimentally determined to transmit the EUV ions are within <1% of the calculated values for all ion energies. These results indicate that the ESA is transmitting the EUV ions as expected based off their initial starting energies. Additionally, Figure 5.33 shows that the optimal starting EUV ion energy, based off of peak intensity and shape, remains at (+)1300 eV. Below and above this starting energy, peak abnormalities appear and the signal starts decreasing. It is not entirely understood why the signal intensities in Figure 5.33 are larger than those in Figure 5.27 by almost an order of magnitude. It is likely that the ion beam is more optimally focused and accelerated in this experimental set-up because the Herzog plates are biased, whereas they were not in the experimental set-up used to collect the data shown in Figure 5.27.

After the ESA potentials in the Neptune were determined for different EUV ion starting energies, the slit lens system was reinstalled to confirm that the ions were sufficiently transmitted through the ESA after passing through the low mass resolution slit. Figure 5.34 shows the acquired Si peaks after the ions have traveled through the ESA with and without the low mass resolution slit installed. The ion signal intensity and peak width expectedly decreased after traveling through the low resolution slit, and the ESA plate potentials were adjusted slightly by ~5-10 V. The focusing, shape, and X/Y deflection plates were also varied to obtain the optimal peak shape. The focusing lens was increased up to (-)680 V to optimize the ion signal intensity, which was a higher bias used than results collected before the ESA. The focus lens likely needed adjustment for ion detection after the ESA because the transfer and slit lens systems are now operating in their normal configuration for these experiments. The calculated mass resolution for the EUV ions starting at an energy of (+)1300 eV remains at ~500 with the low mass resolution slit installed, similar to what was calculated prior to the ions' entrance into the Neptune.

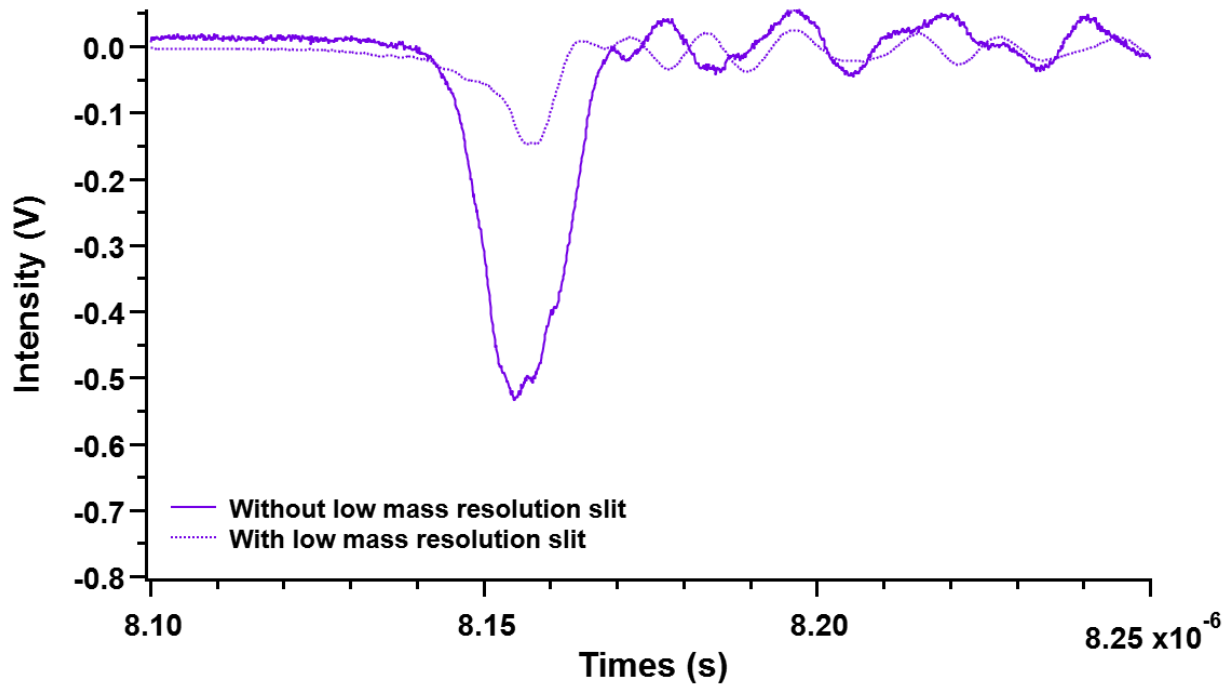


**Figure 5.34** Zoomed in spectra collected with the mini-MCP detector after the ESA of the EUV ions without (solid purple line) and with (dashed purple line) the low mass resolution slit installed in the Neptune. The spectrum collected without the slit is an average of 60 EUV laser shots taken at a single spot on the silicon wafer while the spectrum collected with the slit is an average of 100 shots taken at a single spot on the same sample.

Table 5.8 lists the potentials applied to the EUV and Neptune components to focus and transmit the EUV ions from the source through the Neptune up to the ESA exit. Together, these results indicate that the EUV ions are successfully traveling through the first two cross-over points in the Neptune and are being transmitted through the ESA. However, as to whether the ions are sufficiently focused through the ESA’s intermediate slit (i.e., cross over #3) cannot be directly confirmed with this experimental set-up. The next step is to place the mini-MCP detector immediately after the ESA slit to confirm that the ions are being properly focused into the multi-collector module.

**Table 5.8** EUV and Neptune components used to transmit EUV ions with a starting energy of (+)1300 eV through the Neptune’s transfer lenses, slit lenses, and ESA. The potentials listed in the “HV Supply” column are applied potentials from a high voltage (HV) power supply that is not a part of the Neptune’s electronics. The potentials in the “Neptune Software” column are directly output from the software and do not include the values for the  $U_a$  and  $U_b$  base potentials.

EUV and Neptune Components	HV Supply (V)	Neptune Software (V)
Sample	+1300	--
Zone Plate	Ground	--

Central Electrodes on Beam Deflector	+2000	--
Shim Electrodes on Beam Deflector	+1000	--
Einzel Slits on Beam Deflector	Ground	--
X/Y/Z Plates on Coupling Lens	Ground	--
Einzel Lens on Coupling Lens	+720	--
Source Offset	--	+10
Extraction Lens	--	-2000
Focus Lens	--	-680
Y(+/-) Deflection	--	+9.96
X(+/-) Deflection	--	+10.33
Shape Quadrupole	--	+200
Rotation Quadrupole #1	--	0
Focus Quadrupole #1	--	+10.18
ESA Inner	-5393	--
ESA Outer	-4412	--
Matsuda Plate	--	0
HV Control	--	-9950

### 5.e.vii Transmitting EUV ions through cross-over #3 – Experiment #2

After finding the approximate ESA potentials needed to filter the EUV-generated ions through the exit Herzog plate, the ESA plate potentials needed to filter the ions through the intermediate slit that defines the third cross over was determined. The width of the exit Herzog plate allows ions to be detected when the ESA plates are biased within approximately  $\pm 30$ -50 V of their optimal potentials, while the much more narrow intermediate slit (exact dimensions are not known, see Figure 5.6) is expected to cut that potential range down to  $\pm 5$ -10 V. To perform these experiments, the mini-MCP was placed in the chamber after the intermediate slit but before the magnet. Figure 5.35 shows the experimental set-up, where the mini-MCP detector is attached to a bellows-type transfer rod in a six port vacuum cube and placed inside the chamber after the slit. The transfer rod allows the mini-MCP detector to be pulled in and out of the ions' path, so that the ions can access the magnetic sector after the ESA is finely tuned. To access the chamber after the intermediate slit, the ion getter pump that is typically attached directly to the chamber was removed and placed on the top port of the detector's vacuum cube. While the vacuum cube is a conductance limiting orifice that reduces the flow of gases and particles to the ion getter pump, the pressure achieved in this region was suitable at approximately  $2 \times 10^{-7}$  Torr (typical pressure range is from  $1 \times 10^{-7}$

Torr to  $\leq 10^{-8}$  Torr). The mini-MCP detector was biased as normal with (-)2000 V on the front plate and (-)100 V on the back plate but was biased with reference to the Neptune's High Voltage rather than ground because the chamber to which it is attached is floated to (-)10 kV during operation. The power supply used to bias the detector as well as the oscilloscope used to record the output signal were all floated to (-)10 kV for operation.

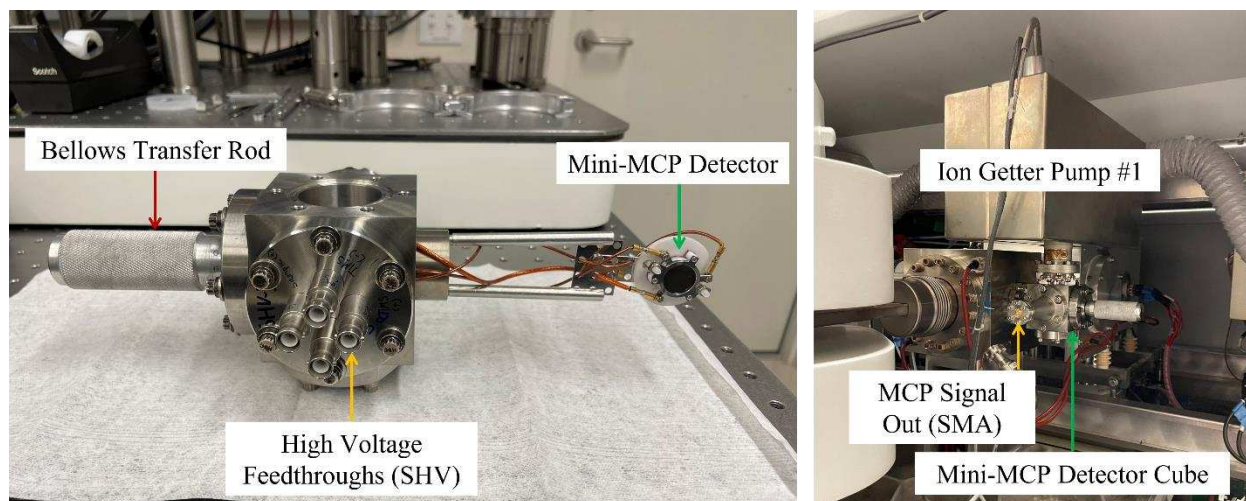


**Figure 5.35** (Left) Mini-MCP detector installed on transfer rod in a six port CF (2.75") vacuum cube for (right) installation in the Neptune after the ESA intermediate slit.

Initially, the Neptune parameters were set to the values listed in Table 5.8, but no ions were detected as the EUV laser fired at the (+)1300 V biased Si wafer at a 1 Hz repetition rate. The ESA plates were separately changed in 1 V increments until ions were detected. The ESA plates were then iteratively optimized until the ion signal was maximized at an ESA inner plate bias of (-)5389 V and outer plate bias of (-)4401 V. As expected, the potential range on the ESA plates where ions are detected is much more narrow after the intermediate slit, ranging between ( $\pm$ )2-7 V versus ( $\pm$ )30-50 V before the slit. Figure 5.36 shows the resulting spectra acquired from the mini-MCP detector after the EUV generated ions from the Si wafer have traveled through the intermediate slit. An additional spectra is also shown of EUV generated ions from a Si wafer that is coated with Au. As expected, the TOF-like spectra show that the Si peak arrives earlier in time than the heavier Au peak. Interestingly, in the Au dominated spectra, the suspected Si peak is still present, albeit at a much lower intensity. A quick mass calibration using  $^{28}\text{Si}$  and  $^{197}\text{Au}$  as reference

peaks show that the other peaks in the Si spectra could be the minor isotopes of Si or the presence of Ca. However, the other peaks in the Au spectra couldn't be identified. It is possible that the smaller peaks that arrive after the larger Si and Au peaks in both spectra are reflections from the transmission line rather than ion signals.

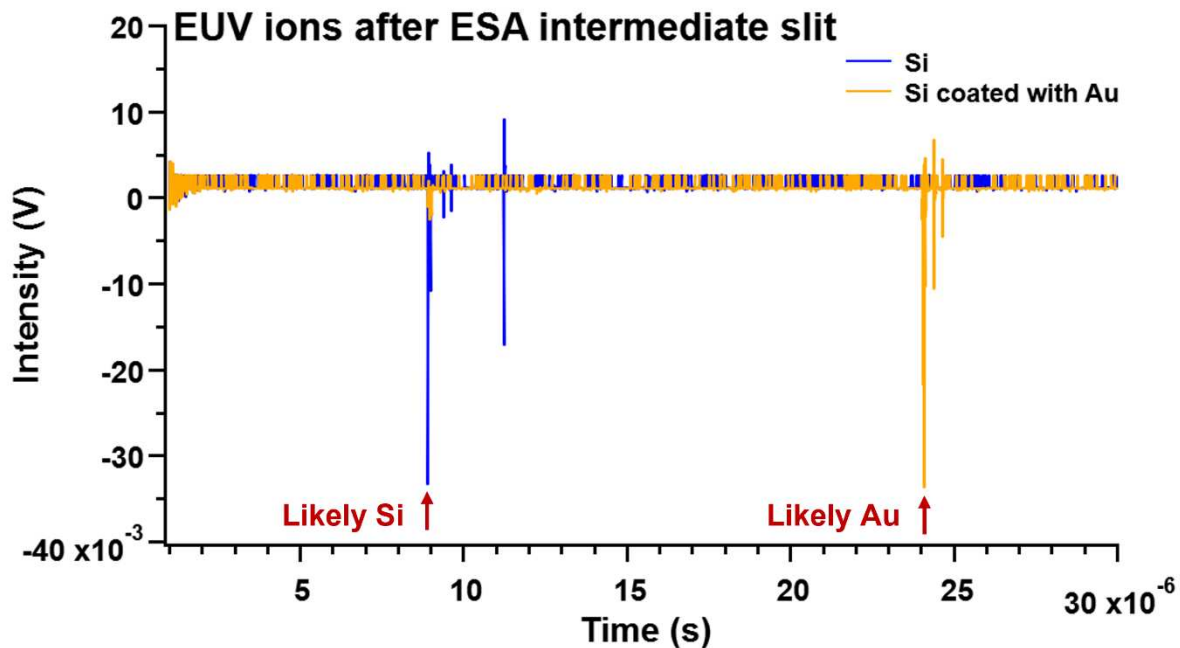


**Figure 5.36** EUV generated ions measured as a function of arrival time with the mini-MCP detector after the ions have been focused through the intermediate slit after the ESA. Each spectrum was acquired using an average of 100 EUV lasers shots at a single spot on a Si wafer (blue trace) and a Si wafer coated with Au (yellow trace).

### 3.e.viii Transmitting EUV ions through cross-over #4 - Calculations

Now that the ESA conditions for the higher energy EUV ions have been both calculated and measured, the proceeding section will discuss how the EUV ions can be transmitted to the Neptune's detector region, which defines cross over #4. Because this will require the ions passing through the magnetic sector, calculations for the required magnetic field were made prior to experimental tests. The magnetic sector in the Neptune is calibrated to the ICP ions that start near ground and are accelerated to approximately (-)10000 eV after the ESA. The magnetic sector has a radius of 23 cm and its field strength can be changed from approximately  $\geq 0.05$  to 1.2 Tesla (T). With the incoming ions from the ICP accelerated to approximately (-)10000 eV, this magnetic field range covers masses from 1 amu up to ~310 amu. The

strength of the magnetic field ( $B$ ) that is needed to separate ions of a certain mass/charge ( $m/q$ ) is dependent on the energy ( $U$ ) of the incoming ions such that higher energy ions (or ions with increased velocity) will require a larger magnetic field to maintain a certain radius ( $r$ ) for a given mass/charge. Recall Equation 5.9 accordingly:

$$r = \sqrt{\frac{m2U}{zB^2}} \quad 5.9$$

Note that to correctly use Equation 5.9, the units of each term should be as follows: radius ( $r$ ) in meters, mass ( $m$ ) in kilograms, energy ( $U$ ) in volts, charge ( $q$ ) in Coloumbs, and magnetic field ( $B$ ) in Tesla.

The dependence of the magnetic field strength on the energy of the ions means that the magnetic field will need to be recalibrated to the higher energy EUV ions. If the radius ( $r$ ), mass ( $m$ ), and charge ( $q = +1$ ) are all kept constant, then the relationship between the magnetic field strength ( $B$ ) and ion energy ( $U$ ) is simplified to Equation 5.13:

$$\frac{B_{ICP\ ions}^2}{U_{ICP\ ions}} = \frac{B_{EUV\ ions}^2}{U_{EUV\ ions}} \quad 5.13$$

Where  $B_{ICP\ ions}$  and  $B_{EUV\ ions}$  are the magnetic fields strengths for the ICP and EUV ion sources, respectively. Similarly,  $U_{ICP\ ions}$  and  $U_{EUV\ ions}$  are the energies for the different ion sources. If, for example, a single charged ( $q = +1$ ) silicon isotope from the ICP with mass 28 amu ( $4.65E-26$  kg) and with (-)10000 eV of energy enters the magnetic sector and is expected to travel a radius of 23 cm to the detector then the required magnetic field is calculated using Equation 5.14:

$$B_{ICP} = \sqrt{\frac{m2U_{ICP}}{zr^2}} = \sqrt{\frac{4.65E-26\ kg * 2 * 10000\ V}{1.60E-19\ C * (0.23\ m)^2}} = 0.33\ T \quad 5.14$$

The magnetic field strength of 0.33 T calibrated for the (-)10000 eV energy ions from the ICP can then be used to calculate the magnetic field strength that would be required for EUV uranium ions starting at (+)1300 eV, and thereby having a nominal energy at the magnet of (-)11300 eV, to traverse the magnetic sector with the same radius ( $r$ ) using Equation 3.13 from above:

$$\frac{B_{ICP\ ions}^2}{V_{ICP\ ions}} = \frac{B_{EUV\ ions}^2}{V_{EUV\ ions}} \rightarrow B_{EUV\ ions} = \sqrt{\frac{B_{ICP\ ions}^2 * V_{EUV\ ions}}{V_{ICP\ ions}}} = \sqrt{\frac{(0.33\ T)^2 * 11300\ V}{10000\ V}} = 0.35\ T$$

The difference in magnetic field strengths between the ICP ions and EUV ions highlights how a larger magnetic field strength in the Neptune will be needed to transmit the EUV ions of the same mass with the same radius but with higher energy through the magnetic sector.

To visualize how the magnetic field strength shifts as the ion energy increases, Figure 5.37 plots the magnetic field strength that was measured from the Neptune to detect each mass at the center detector position when the ions from the ICP are accelerated to a nominal energy of (-)9914 eV. This mass calibration plot provides the magnetic field values for each mass of interest for a set of instrumental parameters (such as detector position, ion energy, etc). A mass calibration curve was then calculated for the higher energy EUV ions that will be entering the magnetic sector with an energy of approximately (-)11214 eV by calculating the magnetic field at each mass using Equation 5.14. When the higher energy EUV ions enter the magnetic sector, this calibration curve can be used to set the initial field strength of the magnet.

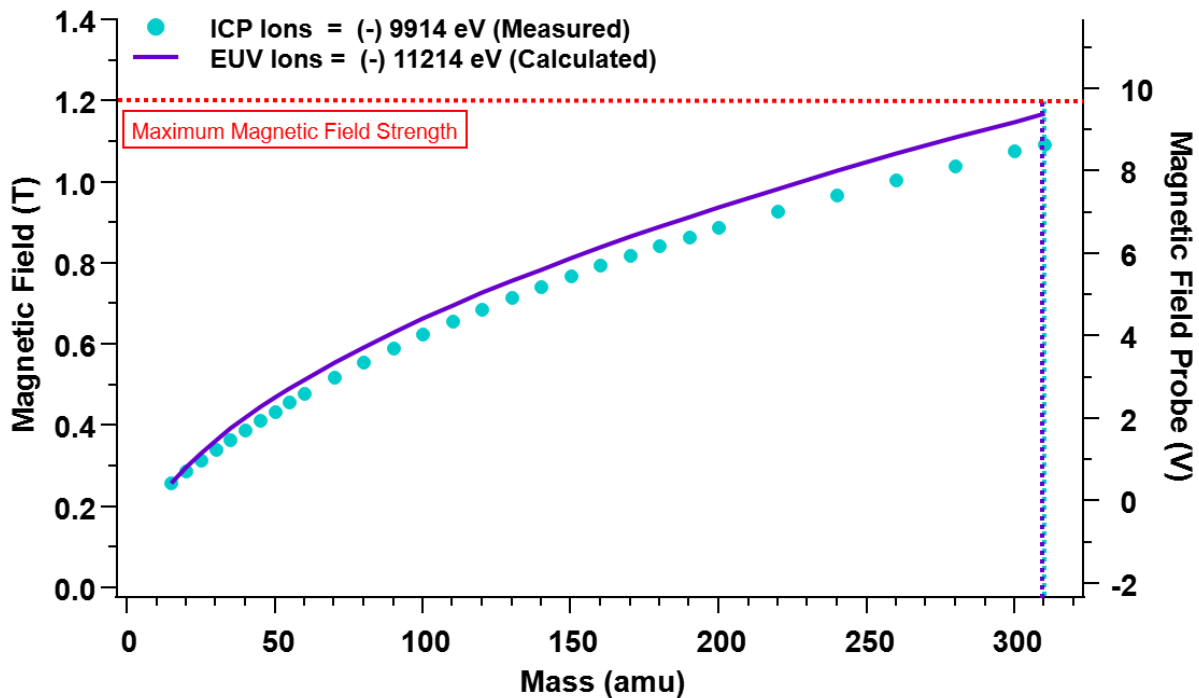


**Figure 5.37** Measured and calculated mass calibration curves for ICP ions entering the magnetic sector of the Neptune with an energy of approximately (-)9914 eV (blue circles) and for the EUV ions with an expected energy of -13000

eV (solid purple line). The magnetic field strength in Teslas is plotted on the left vertical axis and the corresponding magnetic field probe value in volts is plotted on the right vertical axis. Both vertical axes are plotted as a function of mass in atomic mass units. The mass calibration was measured for the ICP ions and calculated for the EUV ions. The red dotted line represents the maximum 1.2 T field, corresponding to ~10 V on the field probe, of the magnetic sector in the Neptune, which corresponds to a mass of 310 amu for the ICP ions (dotted blue line) and 280 amu for the EUV ions (dotted purple line).

It should be noted that the Neptune does not actually output the strength of the magnetic field in Teslas. Rather, the magnetic field regulator that controls the field strength is measured and controlled by the user via a magnetic field probe that is in the air gap of the magnet and whose readout is in volts. In Figure 5.38, the magnetic field and corresponding magnetic field probe values are both plotted on the left and right vertical axes, respectively. For the ICP ions, the magnetic field probe value was directly measured from the Neptune software, which was then converted to the corresponding magnetic field value in Teslas using the linear relationship between the measured field probe values and calculated magnetic field values (using Equation 5.14) shown in Figure 5.38. For the EUV ions, the magnetic field in Teslas was calculated at each mass (using Equation 3.14) and then converted to field probe values in volts using the linear relationship shown in Figure 5.38.

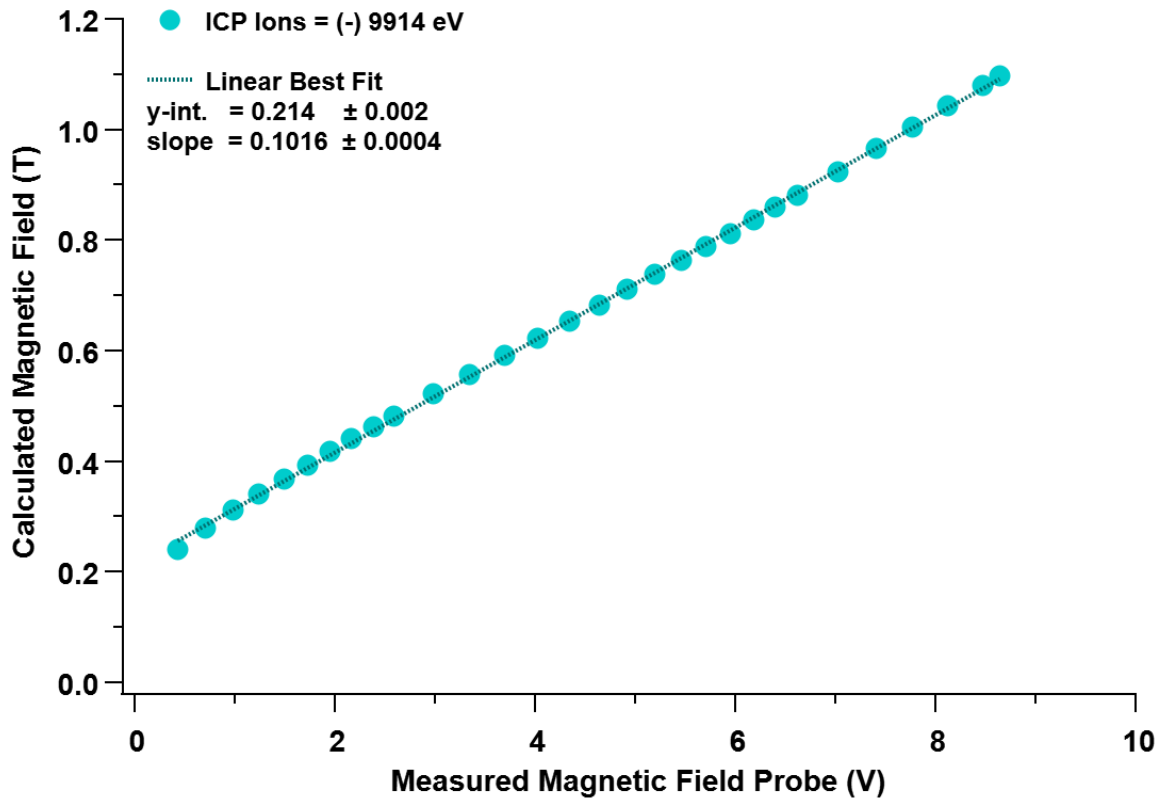


**Figure 5.38** Calculated magnetic field values in Teslas plotted as a function of the measured magnetic field probe values in volts for masses ranging from 15 amu to 310 amu using ICP ions with a nominal final energy of -9914 eV. The linear best fit line is shown as the dark blue dotted line, whose y-intercept and slope values from linear regression are given in the legend.

The maximum 1.2 T magnetic field strength of the Neptune should be equal to approximately 10 V on the magnetic field probe, which should correspond to a maximum mass of 310 amu for the  $\sim (-)10000$  eV ICP ions. However, as can be seen from Figure 5.37, the ICP ions do not cross the 1.2 T maximum field strength at mass 310, indicating that a few higher masses can be detected by increasing the field strength. The higher energy EUV ions are also within the 1.2 T magnetic field range for isotope measurements up to masses of 310 amu. Because we are interested in eventually using the EUV magnetic sector for the analysis of nuclear materials, and specifically for measuring uranium isotopes with masses ranging from 233 to 238 amu (as well as their oxides UO and UO<sub>2</sub> from 249 to 254 amu and 265 to 270 amu, respectively), the magnetic field strength is within the mass range of interest for the higher energy EUV ions.

To verify the calculated changes in the magnetic field of the Neptune's magnetic sector as the ion energy changes, experiments were conducted by slightly changing the energy of the ICP ions. To change the ions' energy, the accelerating potentials were changed in ( $\pm$ )10 V increments up to ( $\pm$ )50 V using the "Source Offset" function in the Neptune software. The source offset changes the initial starting energy of the ions coming from the ICP. For example, if the source offset is set to (+)50 V then the ions will initially have (+)50 eV more energy relative to starting at ground. When the Neptune is operated normally, it will automatically compensate for this higher ion energy by also applying the offset potential to all the ion optics in the transfer lens system, slit lens system, and ESA, including the final accelerating potentials (i.e., the "High Voltage"). This ensures that only ions with a specific energy are filtered and focused into the magnetic sector, regardless of their starting energies, so that the user does not have to adjust the magnetic field strength when the source offset is changed.

To bypass the automatic energy compensation that the Neptune applies to the focusing and accelerating optics so that the magnetic field can be changed as a function of the ion energy, the ESA plates were held at constant potentials using external power supplies while the source offset was varied. Typically, the ESA inner and outer plate potentials are changed by the same value as the source offset, while maintaining the same potential difference between the plates. By keeping the ESA plate potentials constant as the source offset is changed, the ions travel through the ESA with a shifted radial path because the individual plate potentials are no longer correlated with the incoming ion energy. This ultimately results in a change in how the ESA filters the ions, such that ions with an initial higher or lower energy entering the ESA will be refocused to the same energy as if they were starting at a 0 V source offset. The ions leaving the ESA are therefore forced to start at the same energy regardless of the source offset but will be accelerated to different final potentials.

To perform these experiments, the Neptune was initially tuned in its original configuration for the detection of  $^{238}\text{U}^+$  on the central Faraday cup. Since the eventual goal of the new EUV magnetic sector system is to detect U isotopes in nuclear materials, the focus of these experiments was on the

detection of  $^{238}\text{U}^+$ . A NIST 610 glass wafer, with approximately 500 ppm of  $^{238}\text{U}$ , was used for analysis. A fs-laser ablation system (Applied Spectra, J-100, USA) with a 343 nm wavelength (frequency tripled from a 1030 nm fundamental output) and <400 fs pulse duration was used for sample introduction by ablating the glass wafer in line scan mode. The ICP conditions were tuned for a sufficient  $^{238}\text{U}^+$  signal intensity. After the signal was optimized, the connection to the ESA plates from the Neptune were unplugged and replaced with a connection to an external power supply located outside of the Neptune and referenced to the instrument's ground. Leaving all other parameters on the Neptune constant, the ESA plates were slowly ramped up in (-)1 V steps until the  $^{238}\text{U}^+$  signal was recovered at a bias of (-)4472 V ( $\pm 1$  V) on the outer plate and (-)5251 V ( $\pm 1$  V) on the inner plate. The difference between the two ESA plate potentials using the external power supply is (-)779 V, which is relatively close to the (-)785 V difference that was measured previously with the high voltage probe.

Keeping the ESA plate potentials constant, the source offset potential was then changed in 10 V steps up to (+)50 V and down to (-)50 V, which are the maximum and minimum limits of the offset supply, respectively. At a 0 V source offset, the ions' final energy is (-)9914 eV. As the source offset is changed, the ions' final energy changes accordingly such that at a (-)50 V offset corresponds to an ion energy of (-)9962 eV, and at a (+)50 V offset the ion energy is (-)9866 eV. At each source offset, the magnet's field strength was swept over a mass range (i.e., a "mass scan") correlating to approximately 235 to 240 amu to recalibrate the magnetic field strength as a function of the change in energy of the  $^{238}\text{U}^+$  ions. The magnetic field probe voltage that correlated to the center of the  $^{238}\text{U}^+$  peak was recorded for each change in ion energy. The magnetic field probe values were converted to field strengths in Tesla using the linear relationship in Figure 5.38. The intensity of the  $^{238}\text{U}^+$  peak did not change in intensity or shape as the energy and magnetic field strength varied.

Figure 5.39 plots the resulting magnetic field values (and corresponding magnetic field probe values) that were measured for  $^{238}\text{U}^+$  as the energy of the ions was changed by ( $\pm$ )50 eV before entering the magnetic sector. For comparison, Figure 5.39 also shows the calculated magnetic field values

as solid lines for changes in the ion energy when the source offset was changed by (-)50 V, 0 V, and (+)50 V using Equation 5.14. The corresponding measured and calculated values plotted in Figure 5.39 are listed in Table 5.9.

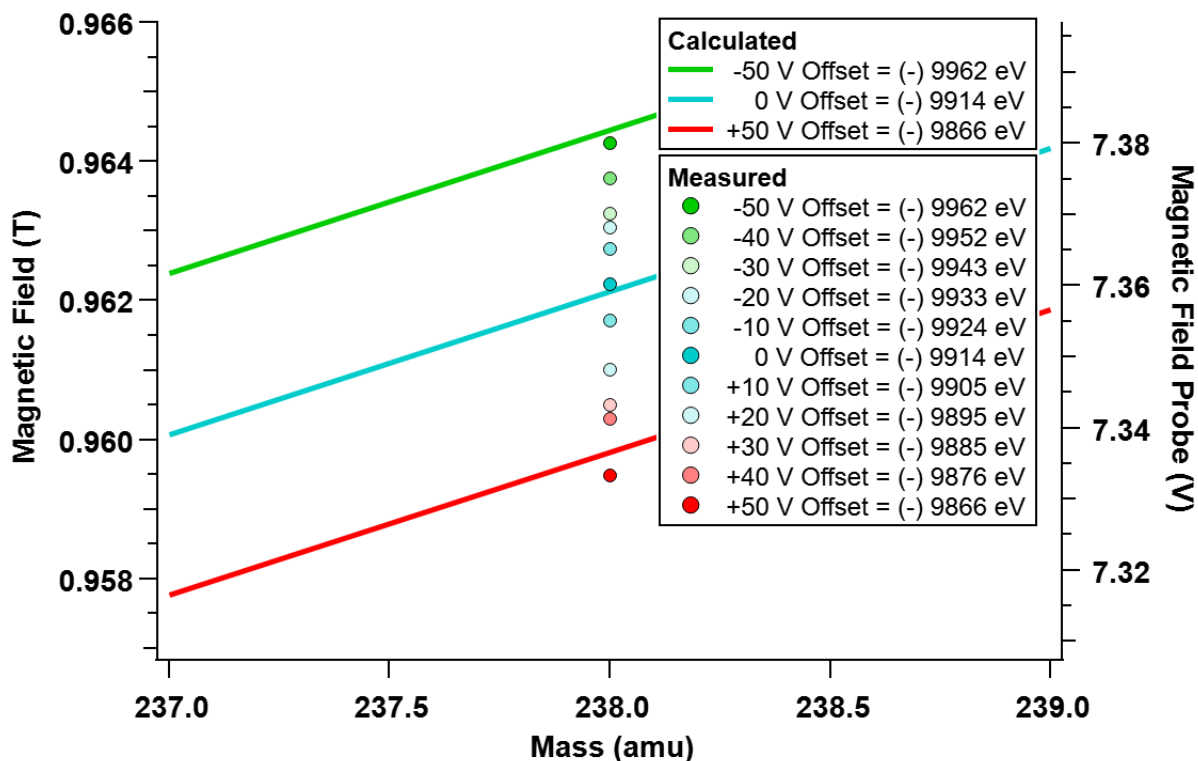


**Figure 5.39** Calculated (solid lines) and measured (circle markers) magnetic field strength in Tesla, and corresponding magnetic field probe value in volts, plotted as a function of mass for  $^{238}\text{U}^+$  as the ion energy is changed via the source offset. The source offset is varied from (-)50 V to (+)50 V in 10 V increments. The solid lines represent the expected magnetic field strength trend for (-)50 V, 0 V, and (+)50 V offsets. The corresponding ion energy for each source offset value is shown in the legend, which was measured as the Neptune’s final acceleration voltage output from the software interface as the “High Voltage.”

**Table 5.9** Calculated and measured magnetic field values for the detection of  $^{238}\text{U}^+$  as the energy of the ions were changed by  $\pm 50$  eV via the Neptune’s source offset. The ion energy is equivalent to the “High Voltage” reading from the Neptune software. The percent difference is calculated using the field probe values using the following equation:  $[(\text{Calculated} - \text{Measured})/\text{Calculated}] * 100\%$ .

Source Offset (V)	Ion Energy (eV)	Mass (amu)	B Field Probe (V)		B Field Strength (T)		% Difference
			Measured	Calculated	Measured	Calculated	
-50	-9961.81	238	7.380	7.383	0.964(26)	0.964(53)	0.03%
-40	-9952.27	238	7.375	7.378	0.963(76)	0.964(07)	0.04%
-30	-9942.72	238	7.370	7.373	0.963(25)	0.963(60)	0.05%
-20	-9931.17	238	7.368	7.369	0.963(05)	0.963(14)	0.01%
-10	-9923.63	238	7.365	7.364	0.962(74)	0.962(68)	-0.01%
0	-9914.08	238	7.360	7.360	0.962(23)	0.962(21)	0.00%
+10	-9904.53	238	7.355	7.355	0.961(72)	0.961(75)	0.00%

+20	-9894.99	238	7.348	7.351	0.961(01)	0.961(29)	0.04%
+30	-9885.44	238	7.343	7.346	0.960(50)	0.960(82)	0.04%
+40	-9875.89	238	7.341	7.342	0.960(30)	0.960(36)	0.01%
+50	-9866.35	238	7.333	7.337	0.959(49)	0.959(89)	0.05%

Figure 5.39 shows that the magnetic field values that were measured as the ion energy was changed is in relatively close agreement with the calculated values. More specifically, the measured values for  $^{238}\text{U}^+$  are all within approximately  $\leq 0.05\%$  of the calculated values. The close agreement between the calculated and measured magnetic field values as a function of the ion energy indicates that the magnetic field values calculated for the higher energy (-)11214 eV EUV ions are expected to be close to the true values for the detection of  $^{238}\text{U}^+$  as well as for other masses of interest, including  $^{28}\text{Si}^+$  and  $^{197}\text{Au}^+$ .

#### 5.e.ix Transmitting EUV ions through cross-over #4 - Experiment

The EUV generated ions from the ablation and ionization of the Si and Au-coated Si wafers were sent through the magnetic sector in these experiments by setting the magnet's field probe to the calculated voltage based on the EUV ions' final (-)11214 eV energy. Prior to the start of these experiments, the Neptune underwent a new mass calibration, slightly changing the values of the expected magnetic field values for EUV ion transmission from the preceding section. However, the equations and plots are easily adapted to take into account a new mass calibration. Figure 5.40 shows the new mass calibration curves for the ICP and EUV ions from Figure 5.37. Using this new mass calibration, the maximum mass range that can be accessed has decreased for both the ICP and EUV ions from 310 amu to ~300 amu and 260 amu, respectively. If higher masses up to 310 amu need to be measured in the future the magnet can be easily recalibrated. The new mass calibration was used to predict the magnetic field values for the experiment in this section. The new mass calibration was not included in the preceding section because the experimental data in Figure 5.39 were not performed with the new calibration values.

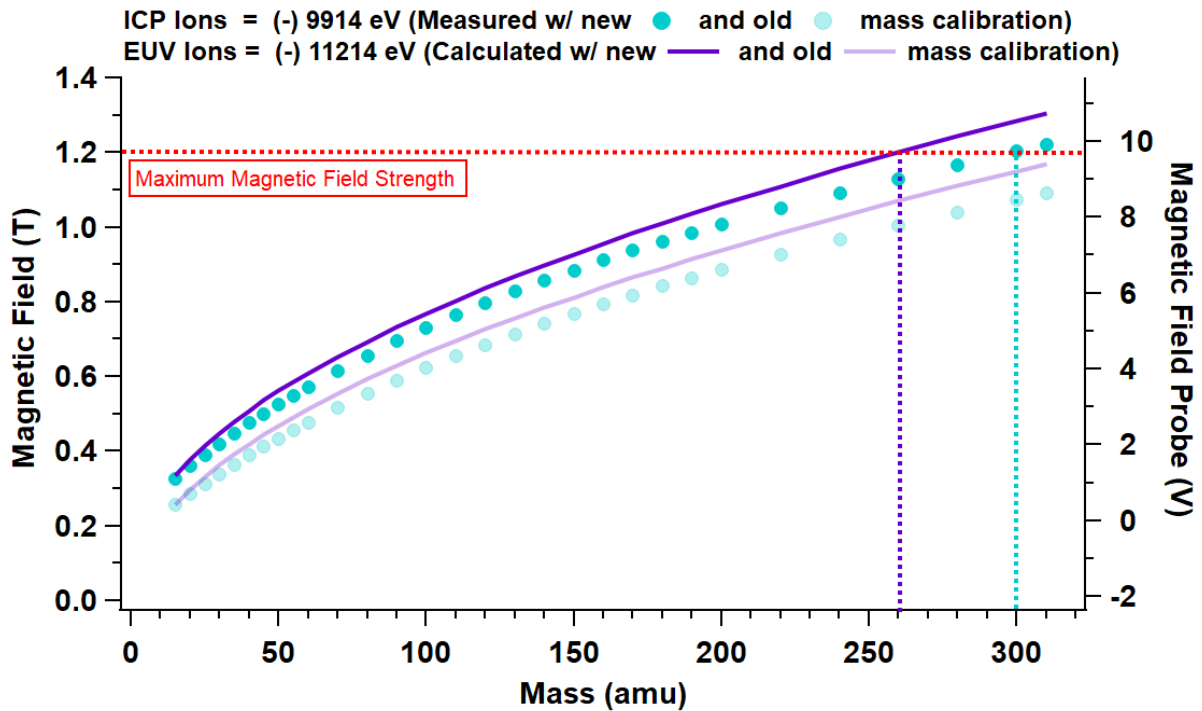


**Figure 5.40** Updated mass calibration curve from Figure 5.37 for the Neptune’s magnetic sector for the measured ICP generated ions (blue dots) and calculated EUV generated ions (purple lines). The new mass calibration curve for the EUV generated ions is used to calculate the required magnetic field probe for transmission of the EUV ions to the Neptune’s detector region.

Using the calculated magnetic field values for the EUV generated ions, the magnetic field probe was set to a value of 2.18 V as well as 8.26 V for the detection of the major isotopes of Si at mass 28 and Au at mass 197, respectively, at a final ion energy of (-)11214 eV. The mini-MCP detector was pulled out of the ions’ path using the transfer rod so that the ions could proceed into the magnetic sector. The Neptune’s central channel secondary electron multiplier (SEM) detector in the multi-collector array was used for ion detection and was biased to (-)2200 V for operation. The current pulse that is output by the SEM was routed directly into an oscilloscope with a 50  $\Omega$  termination, which was placed in the Neptune’s housing and remotely controlled during operation. In the Neptune’s native configuration, the detector’s signal output is sent to an amplifier and discriminator card, which is then passed to an onboard computer that counts the ions per second within a designated integration window. The discriminator was bypassed for the EUV magnetic sector experiments because the laser generates electrical noise that was detected and integrated into the signal output in the Neptune’s software, making it difficult to identify ion signals. Using

the oscilloscope, the laser's electrical noise and ion signals are distinguishable by their different arrival times.

The EUV ions were generated from the same Si and Au-coated Si wafers as the prior experiments by ablating spot sizes  $\leq 2 \mu\text{m}$  in diameter. For the detection of Si and Au ions, the magnetic field was varied in both increasing and decreasing increments that corresponded to 0.1 amu and 1 amu steps, respectively. Each time the magnetic field changed, the magnet was allowed to settle for  $\sim 1$  min. Figure 5.41 shows the successful detection of  $^{28}\text{Si}^+$  and  $^{197}\text{Au}^+$  generated from the EUV laser ionization source using a magnetic field probe bias of 2.115 V (0.345 T) and 8.287 V (0.934 T), respectively. The measured magnetic field values for the EUV generated ions are relatively close to the calculated values. The field probe bias measured for the detection of  $^{28}\text{Si}^+$  was within 3% of the calculated value, while  $^{197}\text{Au}^+$  was within  $<1\%$ . Lighter masses are more sensitive to changes in the magnetic field and are therefore expected to be detected within a more narrow window with more room for error than heavier ions.

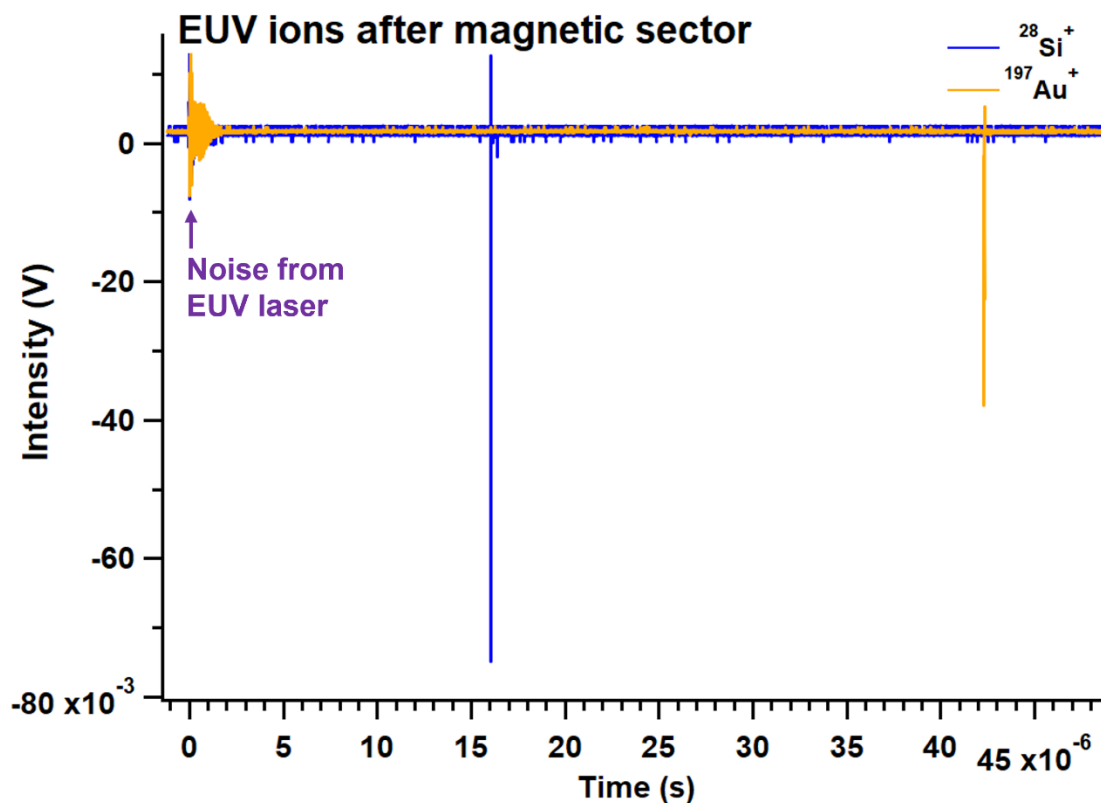


**Figure 5.41** Spectra of EUV generated isotopes detected after the Neptune's magnetic sector using the central channel SEM detector. Each spectrum was acquired using an average of ~50 EUV laser shots at a single spot on a Si wafer (blue trace) and a Si wafer coated with Au (yellow trace).

Unfortunately, isotope ratios could not be measured with the EUV magnetic sector instrument in its current configuration because the EUV ions' ~20-30 ns pulse width is on the order of the SEM detector's dead time. The SEM detectors will need to be replaced by fast recovery detectors that will be able to accurately measure the ion pulses generated by the EUV laser. The next steps towards realizing the full capabilities of the newly built EUV magnetic sector instrument are outlined in the proceeding section.

The detection of EUV generated ions in the Neptune represents the crux of this chapter because it shows that a magnetic sector instrument can be interfaced with a pulsed EUV laser ionization source, which has not been demonstrated until now. However, further development is required on the EUV magnetic sector instrument to obtain accurate and precise isotope ratio measurements. The status of accomplishments in ion detection and subsequent steps for the EUV magnetic sector system is explained in detail below.

### 5.e.x Next steps

An EUV magnetic sector instrument has been successfully demonstrated by connecting a pulsed (1-10 Hz) EUV laser ionization source operating at a 46.9 nm wavelength to Thermo's commercial Neptune sector-field multi-collector mass spectrometer. Major isotopes of silicon ( $^{28}\text{Si}^+$ ) and gold ( $^{197}\text{Au}^+$ ) were independently detected using the central channel SEM detector of the Neptune by ablating Si wafers with spot sizes  $\leq 2 \mu\text{m}$  in diameter. The main challenge of building the EUV magnetic sector system was tuning the Neptune's ion optics, electric sector, and magnetic sector to focus and transmit the incoming EUV ions that were generated with (+)1300 eV more energy than the ions created in the native ICP ion source. The pulsed nature of the EUV ions added an additional layer of complexity to tuning the Neptune's parameters compared to the continuous stream of ions created in an ICP. Alongside calculations of the EUV ions' behavior in the Neptune, the installation of MCP detectors throughout the ions' path in the Neptune aided in properly focusing the EUV ions through the Neptune's cross-over points for sufficient transmission to the detector region. This work is the first known demonstration of an EUV laser ionization source coupled to a magnetic sector mass analyzer and creates opportunities for future high spatial resolution elemental/isotopic analyses that is dominated by ion beam techniques.

However, the proof-of-principle design of the EUV magnetic sector instrument detailed in this dissertation has much room for growth before it reaches a practical application stage. First, as described in the last section, the ion counting SEM detectors, as well as the Faraday detectors, currently used for multi-ion detection in the Neptune have dead times of tens of nanoseconds. The detectors' dead times are on the order of the ions' pulse width generated by the EUV laser. The SEM detector's cannot therefore be used for accurate isotope measurements with the EUV generated ions. Instead, detectors with faster recovery times should be used, such as TOF-like detectors. Perhaps the best suited detector for the EUV magnetic sector instrument are ETP's (now Detector Technology, USA) most recently developed MagneTOF detectors that can achieve FWHM pulse widths on the order of 400 ps, allowing single ions within a tens of nanosecond pulse to be individually detected. Initial work with the Neptune has shown that

the SEM detectors in the multi-collector region can be readily replaced by MagneTOF detectors. An MCP-type detector, like the mini-MCP detector, would also be suitable for EUV generated ion detection in the Neptune, albeit with a larger pulse width. Alternatively, a collision gas cell that spreads the ion pulse width out in time that exceeds the SEM detectors' dead time could be installed in the magnetic sector, potentially allowing the Neptune's native detectors to be used to accurately measure the EUV generated ions. Recently, collision gas cell technology has been built into commercial magnetic sector instruments (like Thermo's Neoma or Nu's Sapphire multi-collector ICP-MS).

Once outfitted with the proper detectors and/or other technology, the EUV magnetic sector's parameters can be accurately characterized. These parameters include the following: (1) efficiency (i.e., volume of material removed from the sample vs the number of ions reaching the detector), (2) accuracy (of isotope ratio measurements), (3), precision (of isotope ratio measurements), (4) sensitivity, and (5) spatial resolution. Fully characterizing the EUV magnetic sector using these parameters will allow comparison to existing mapping techniques that use magnetic sector mass analyzers, like NanoSIMS/SIMS and LA ICP-MS, to identify the new instrument's strengths and weaknesses. Future experiments using the EUV magnetic sector for the detection U isotopes as well as light isotopes (like Li, B, or O) in nuclear materials would be interesting test cases for the new instrument.

While pulsed ionization sources, like the EUV laser, are considered less ideal than ion beam and ICP ionization sources that are more commonly used with "continuous" sector-field analyzers, there may be advantages that could be realized with the pulsed EUV laser source. Alongside the unique ionization properties of the EUV photons that give rise to fewer molecular species than ion beam techniques and the EUV laser's focusability down to the nanoscale, the pulsed nature of the EUV laser could be advantageous for expanding the capabilities of magnetic sector instruments. For example, prior work with pulsed MALDI magnetic sector instruments has shown the simultaneous collection of TOF-like ion spectra alongside higher mass resolution SEM detection at the multi-collection region.<sup>117</sup> It is therefore not far-fetched to imagine that the EUV magnetic sector could be designed to simultaneously collect TOF-like

spectra of low to mid mass ions for elemental analysis as well as the simultaneous detection of, for example, U isotopes at the multi-collector region for isotope ratio analysis using just a single EUV laser shot. That is, the EUV magnetic sector could be designed to perform simultaneous TOF-like and multi-collector analyses, allowing samples to be analyzed over a wide mass range at high spatial scales. This could be especially beneficial for the analysis of micrometer-sized particulate material where the amount of sample available for analysis is limited. It would be more difficult to acquire simultaneous TOF-like and high resolution multi-collector data using a continuous ionization source due to the required pulsed nature of time-of-flight measurements.

Additional modifications that could be made to the demonstrated EUV magnetic sector instrument could involve improving the ion optics in the mass spectrometer that would be more suitable for focusing and transmitting the EUV generated ions. While this work shows that the Neptune's current optics can be modified to adequately transmit the EUV ions, the efficiency of the instrument could surely be improved with specifically designed optics for the EUV ions. Along this same line, transmission of the EUV ions could also be improved by modifying the Neptune's ion extraction conditions so that the EUV ions are accelerated using a 5000 to 10000 V potential at the source rather than 1300 V. That is, EUV ion transmission through a magnetic sector instrument could benefit from floating the source up to an initial high voltage while biasing the other components at a low voltage or ground, representing the opposite configuration of the Neptune. Other magnetic sector mass spectrometers have this configuration, like Thermo's Triton or Nu's Sapphire. Because of the mobility of the EUV laser ionization source, it would be relatively straightforward to attach the EUV laser interface to different magnetic sector mass spectrometer. The work from this dissertation would hopefully aid in decreasing the time and complexity for coupling the EUV laser source to different commercial (or non-commercial) magnetic sector analyzers.

Other improvements that could be made to the demonstrated EUV magnetic sector instrument to increase its widespread use is the choice of EUV laser. The current 46.9 nm capillary discharge EUV laser operates at low 1-10 Hz repetition rates. Practical mapping analyses can require large

areas, on the order of mm's or more, to be scanned. Even at the maximum frequency of 10 Hz, the 46.9 nm capillary discharge EUV laser could take days to complete a full scale mapping analyses. However, laser research is rapidly advancing to produce compact EUV and soft X-ray laser sources with repetitions rates of 100 Hz and greater.<sup>119,120,121</sup> At greater pulse frequencies, it could be possible that EUV lasers are used with magnetic sector instruments for high spatial resolution mapping analyses that is competitive with and/or complementary to NanoSIMS analyses. However, as stated previously, more engineering and research is required to further understand the strengths and weaknesses of using EUV laser sources with magnetic sector mass spectrometers for high spatial resolution isotopic/elemental analyses. Nonetheless, the work in this dissertation highlights some of the advantages of EUV laser light as well as its potential future applications to the analytical chemistry community.

## 6. CONCLUSIONS AND OUTLOOK

This dissertation has described the application and development of a capillary discharge EUV laser ionization source operating at a wavelength of 46.9 nm with mass spectrometry for nuclear and geologic materials analyses down to the nanoscale. The EUV laser's high energy photons and short wavelength make it a unique laser-based ionization source for materials analysis because it can be focused down to spot sizes <100 nm in diameter while simultaneously realizing efficient single photoionization. The unique properties of the EUV laser are exploited here by showing its compatibility with both TOF and magnetic sector mass spectrometers for probing the elemental and isotopic content in solid samples at the micro- and nanoscales.

It was shown that the EUV TOF mass spectrometer that separates EUV generated ions in time according to their mass and charge, was used to measure intra-element U isotope ratios in a non-uniform uranium fuel pellet and to measure inter-element Pb/U and Th/U isotope ratios in different geologic matrices. For the analysis of the uranium fuel sample, the EUV TOF identified 1-2  $\mu\text{m}$  sized areas of  $^{235}\text{U}/^{238}\text{U}$  non-uniformity using 100 nm pixels to map a section of the pellet. The size and distribution of the isotopic non-uniformity mapped by the EUV TOF was similar to that collected with NanoSIMS, indicating that the results collected at the nanoscale with the EUV TOF technique are accurate. The EUV TOF could therefore be a good candidate for other nuclear forensics investigations that require high spatial resolution for accurate assessment of the source material. For the analysis of the geologic samples, the EUV TOF showed that  $^{206}\text{Pb}/^{238}\text{U}$  and  $^{232}\text{Th}/^{238}\text{U}$  could be measured within error in certain geologic matrices that included select silicates, monazites, zircons, and iron manganese samples without the use of matrix matched calibration standards. While the precision of the isotope ratios made with the EUV TOF in these samples typically ranged from 1-10%, disqualifying its use for geologic dating applications, the study shows the versatile use of the EUV laser ionization source for materials analysis.

It was also shown that the EUV laser can be coupled to a commercial magnetic sector mass spectrometer (Thermo's Neptune). The proof-of-principle experiments show that the EUV laser generated ions from the ablation of Si wafers with spot sizes  $\leq 2 \mu\text{m}$  can be detected by modifying the ion optics, electric sector, and magnetic sector of the Neptune to sufficiently focus and transmit the ions. The EUV laser generated  $^{28}\text{Si}^+$  and  $^{197}\text{Au}^+$  isotopes from the wafers were separately detected using the SEM detector in the Neptune's multi-collector region. Further developments are required to be made to the EUV laser magnetic sector before it can be fully characterized in terms of its efficiency, precision, accuracy, sensitivity, and spatial resolution for isotope ratio measurements. The most pertinent modifications involve changing the Neptune's detector region with TOF-like detectors that will have, unlike the SEM detectors, sub-ns recovery times for accurate detection of the EUV generated ions. Additional ion modeling work would be beneficial for designing more suitable ion optics for focusing and steering the EUV ions through the mass spectrometer to increase ion transmission. Optimizing ion transmission will be vital to the future development of the EUV magnetic sector for accurate and precise isotopic mapping studies at the nanoscale, which produce far fewer ions compared to microscale analyses.

The EUV TOF instrument could also benefit from modifications to the detection system. A higher gain MCP detector using three MCP plates (called a Z-gap MCP) could be used to increase the instrument's sensitivity, which is currently limited to  $\sim 50$  ppm using super crater "spot sizes" of  $\sim 8 \mu\text{m}$ . Increasing the instrument's sensitivity would make measuring the less abundant minor isotopes more accessible at the cost of making simultaneous measurements of major isotopes inaccessible without decreasing the gain to avoid detector saturation. The MagneTOF detector (ETP/Detector Technology, USA) with ps pulse widths could also be a good addition to the EUV TOF instrument, which might offer increased precision by offering single ion counting capabilities.

The continual development of EUV laser light as a new probe with mass spectrometry could enable new findings in high spatial resolution materials analysis. The EUV photons can be focused down to the nanoscale, are highly absorbed by any material, and have high energy per photon, all leading

to the ability to efficiently probe materials at the nanoscale. Additionally, these unique EUV laser properties could translate into reduced dependence on the sample chemistry and fewer mass interferences that increase the accuracy of measurements of both low and high mass signatures. Therefore, fields ranging from nuclear forensics, geology, the semiconductor industry, chemistry, biology, and any number of fields that require chemical information to be probed with high spatial resolution could benefit from the continued advancement of EUV laser ionization as a next generation probe for mass spectrometry.

## REFERENCES

1. Rush, L. A., Cliff, J. B., Reilly, D. D., Duffin, A. M. & Menoni, C. S. Isotopic Heterogeneity Imaged in a Uranium Fuel Pellet with Extreme Ultraviolet Laser Ablation and Ionization Time-of-Flight Mass Spectrometry. *Anal. Chem.* **93**, 1016–1024 (2021).
2. Buchberger, A. R., DeLaney, K., Johnson, J. & Li, L. Mass Spectrometry Imaging: A Review of Emerging Advancements and Future Insights. *Anal. Chem.* **90**, 240–265 (2018).
3. Chew, D., Drost, K., Marsh, J. H. & Petrus, J. A. LA-ICP-MS imaging in the geosciences and its applications to geochronology. *Chemical Geology* **559**, 119917 (2021).
4. Varga, Z. *et al.* Trends and perspectives in Nuclear Forensic Science. *TrAC Trends in Analytical Chemistry* **146**, 116503 (2022).
5. Kilburn, M. R. & Clode, P. L. Elemental and Isotopic Imaging of Biological Samples Using NanoSIMS. in *Electron Microscopy: Methods and Protocols* (ed. Kuo, J.) 733–755 (Humana Press, 2014). doi:10.1007/978-1-62703-776-1\_33.
6. Hopkins, M. D., Mojzsis, S. J., Bottke, W. F. & Abramov, O. Micrometer-scale U–Pb age domains in eucrite zircons, impact re-setting, and the thermal history of the HED parent body. *Icarus* **245**, 367–378 (2015).
7. Kautz, E., Burkes, D., Joshi, V., Lavender, C. & Devaraj, A. Nanoscale Spatially Resolved Mapping of Uranium Enrichment. *Sci Rep* **9**, 12302 (2019).
8. Usiobo, O. J. *et al.* Nanoscale Mass-Spectrometry Imaging of Grain Boundaries in Perovskite Semiconductors. *J. Phys. Chem. C* **124**, 23230–23236 (2020).
9. Xu, Z., Hang, L., Lu, Q., Guo, N. & Hang, W. A preliminary comparison of time-of-flight laser ionization and secondary ion mass spectrometry in solids analysis. *Spectrochimica Acta Part B: Atomic Spectroscopy* **167**, 105824 (2020).
10. Messenger, S., Keller, L. P. & Lauretta, D. S. Supernova Olivine from Cometary Dust. *Science* **309**, 737–741 (2005).
11. Heide, P. van der. *Secondary Ion Mass Spectrometry: An Introduction to Principles and Practices*. (John Wiley & Sons, 2014).
12. Hoppe, P., Cohen, S. & Meibom, A. NanoSIMS: Technical Aspects and Applications in Cosmochemistry and Biological Geochemistry. *Geostandards and Geoanalytical Research* **37**, 111–154 (2013).
13. Nuñez, J., Renslow, R., Cliff, J. B., III & Anderton, C. R. NanoSIMS for biological applications: Current practices and analyses. *Biointerphases* **13**, 03B301 (2017).
14. Stevie, F. *Secondary Ion Mass Spectrometry: Applications for Depth Profiling and Surface Characterization*. (Momentum Press, 2015).
15. Wang, Z. *et al.* Nanoscale imaging of Li and B in nuclear waste glass, a comparison of ToF-SIMS, NanoSIMS, and APT. *Surface and Interface Analysis* **48**, 1392–1401 (2016).
16. Riciputi, L. R., Paterson, B. A. & Ripperdan, R. L. Measurement of light stable isotope ratios by SIMS:: Matrix effects for oxygen, carbon, and sulfur isotopes in minerals33Dedicated to the memory of Al Nier. *International Journal of Mass Spectrometry* **178**, 81–112 (1998).
17. Seah, M. P. & Shard, A. G. The matrix effect in secondary ion mass spectrometry. *Applied Surface Science* **439**, 605–611 (2018).
18. Zhu, X.-K., O’Nions, R. K. & Gibb, A. J. SIMS analysis of U–Pb isotopes in monazite: matrix effects. *Chemical Geology* **144**, 305–312 (1998).
19. Pisonero, J., Fernández, B. & Günther, D. Critical revision of GD-MS, LA-ICP-MS and SIMS as inorganic mass spectrometric techniques for direct solid analysis. *J. Anal. At. Spectrom.* **24**, 1145–1160 (2009).
20. Wucher, A., Cheng, J. & Winograd, N. Molecular Depth Profiling Using a C60 Cluster Beam: The Role of Impact Energy. *J. Phys. Chem. C* **112**, 16550–16555 (2008).

21. Malherbe, J. *et al.* A New Radio Frequency Plasma Oxygen Primary Ion Source on Nano Secondary Ion Mass Spectrometry for Improved Lateral Resolution and Detection of Electropositive Elements at Single Cell Level. *Anal. Chem.* **88**, 7130–7136 (2016).
22. Hervig, R. L. *et al.* Useful ion yields for Cameca IMS 3f and 6f SIMS: Limits on quantitative analysis. *Chemical Geology* **227**, 83–99 (2006).
23. Gault, B. *et al.* Atom probe tomography. *Nat Rev Methods Primers* **1**, 1–30 (2021).
24. Barroo, C., Akey, A. J. & Bell, D. C. Atom Probe Tomography for Catalysis Applications: A Review. *Applied Sciences* **9**, 2721 (2019).
25. Limbeck, A. *et al.* Recent advances in quantitative LA-ICP-MS analysis: challenges and solutions in the life sciences and environmental chemistry. *Anal Bioanal Chem* **407**, 6593–6617 (2015).
26. Azov, V. A., Mueller, L. & Makarov, A. A. Laser Ionization Mass Spectrometry at 55: Quo Vadis? *Mass Spectrometry Reviews* **41**, 100–151 (2022).
27. Aichler, M. & Walch, A. MALDI Imaging mass spectrometry: current frontiers and perspectives in pathology research and practice. *Lab Invest* **95**, 422–431 (2015).
28. Poitrasson, F., Mao, X., Mao, S. S., Freydier, R. & Russo, R. E. Comparison of Ultraviolet Femtosecond and Nanosecond Laser Ablation Inductively Coupled Plasma Mass Spectrometry Analysis in Glass, Monazite, and Zircon. *Anal. Chem.* **75**, 6184–6190 (2003).
29. Jochum, K. P. *et al.* Non-Matrix-Matched Calibration for the Multi-Element Analysis of Geological and Environmental Samples Using 200 nm Femtosecond LA-ICP-MS: A Comparison with Nanosecond Lasers. *Geostandards and Geoanalytical Research* **38**, 265–292 (2014).
30. Zhang, B., He, M., Hang, W. & Huang, B. Minimizing Matrix Effect by Femtosecond Laser Ablation and Ionization in Elemental Determination. *Anal. Chem.* **85**, 4507–4511 (2013).
31. Kompauer, M., Heiles, S. & Spengler, B. Atmospheric pressure MALDI mass spectrometry imaging of tissues and cells at 1.4- $\mu\text{m}$  lateral resolution. *Nat Methods* **14**, 90–96 (2017).
32. Niehaus, M., Soltwisch, J., Belov, M. E. & Dreisewerd, K. Transmission-mode MALDI-2 mass spectrometry imaging of cells and tissues at subcellular resolution. *Nat Methods* **16**, 925–931 (2019).
33. Wang, J. *et al.* Vacuum Ultraviolet Laser Desorption/Ionization Mass Spectrometry Imaging of Single Cells with Submicron Craters. *Anal. Chem.* **90**, 10009–10015 (2018).
34. Rocca, J. J. *et al.* Demonstration of a Discharge Pumped Table-Top Soft-X-Ray Laser. *Phys. Rev. Lett.* **73**, 2192–2195 (1994).
35. Heinbuch, S., Grisham, M., Martz, D. & Rocca, J. J. Demonstration of a desk-top size high repetition rate soft x-ray laser. *Opt. Express, OE* **13**, 4050–4055 (2005).
36. Vaschenko, G. *et al.* Nanometer-scale ablation with a table-top soft x-ray laser. *Opt. Lett., OL* **31**, 3615–3617 (2006).
37. Attwood, D. *Soft X-Rays and Extreme Ultraviolet Radiation: Principles and Applications.* (Cambridge University Press, 2000).
38. Gamaly, E. G., Rode, A. V., Luther-Davies, B. & Tikhonchuk, V. T. Ablation of solids by femtosecond lasers: Ablation mechanism and ablation thresholds for metals and dielectrics. *Physics of Plasmas* **9**, 949–957 (2002).
39. Juha, L. *et al.* XUV-laser induced ablation of PMMA with nano-, pico-, and femtosecond pulses. *Journal of Electron Spectroscopy and Related Phenomena* **144–147**, 929–932 (2005).
40. Juha, L. *et al.* Short-wavelength ablation of molecular solids: pulse duration and wavelength effects. *JM3.1* **4**, 033007 (2005).
41. Berrill, M. *et al.* Warm photoionized plasmas created by soft-x-ray laser irradiation of solid targets. *J. Opt. Soc. Am. B, JOSAB* **25**, B32–B38 (2008).
42. Rossall, A. K. *et al.* Ablation of Submicrometer Holes Using an Extreme-Ultraviolet Laser. *Phys. Rev. Applied* **3**, 064013 (2015).
43. Dong, F., Heinbuch, S., Rocca, J. J. & Bernstein, E. R. Dynamics and fragmentation of van der Waals clusters:  $(\text{H}_2\text{O})_n$ ,  $(\text{CH}_3\text{OH})_n$ , and  $(\text{NH}_3)_n$  upon ionization by a 26.5eV soft x-ray laser. *J. Chem. Phys.* **124**, (2006).

44. Kuznetsov, I. *et al.* Three-dimensional nanoscale molecular imaging by extreme ultraviolet laser ablation mass spectrometry. *Nat. Commun.* **6**, 1–6 (2015).
45. Green, T. *et al.* Characterization of extreme ultraviolet laser ablation mass spectrometry for actinide trace analysis and nanoscale isotopic imaging. *J. Anal. At. Spectrom.* **32**, 1092–1100 (2017).
46. Liu, F. *et al.* TOF mass spectra of zircon M257 measured by VUV laser desorption ionization. *J. Anal. At. Spectrom.* **37**, 95–102 (2022).
47. Rush, L. A., Duffin, A. M. & Menoni, C. S. Measuring Pb, Th, and U inter-element ratios in geological materials using extreme ultraviolet laser ablation and ionization mass spectrometry. *J. Anal. At. Spectrom.* **37**, 1902–1914 (2022).
48. Cooper-Shepherd, D. A. *et al.* Novel Hybrid Quadrupole-Multireflecting Time-of-Flight Mass Spectrometry System. *J. Am. Soc. Mass Spectrom.* **34**, 264–272 (2023).
49. Kuznetsov, I. Extreme Ultraviolet Laser Ablation Mass Spectrometer for Molecular Imaging at the Nanoscale. *ProQuest Dissertations and Theses* (Colorado State University, 2018).
50. Gruchola, S. *et al.* Reduction of surface charging effects in laser ablation ionisation mass spectrometry through gold coating. *J. Anal. At. Spectrom.* **38**, 1372–1378 (2023).
51. Rush, L. A., Cliff, J. B., Reilly, D. D., Duffin, A. M. & Menoni, C. S. Imaging isotopic content at the nanoscale using extreme ultraviolet laser ablation and ionization mass spectrometry. in *International Conference on X-Ray Lasers 2020* vol. 11886 267–274 (SPIE, 2021).
52. Gehrels, G. E., Valencia, V. A. & Ruiz, J. Enhanced precision, accuracy, efficiency, and spatial resolution of U-Pb ages by laser ablation–multicollector–inductively coupled plasma–mass spectrometry. *Geochemistry, Geophysics, Geosystems* **9**, (2008).
53. Zimmer, M. M., Kinman, W. S., Kara, A. H. & Steiner, R. E. Evaluation of the Homogeneity of the Uranium Isotope Composition of NIST SRM 610/611 by MC-ICP-MS, MC-TIMS, and SIMS. *Minerals* **4**, 541–552 (2014).
54. Duffin, A. M. *et al.* Femtosecond laser ablation multicollector ICPMS analysis of uranium isotopes in NIST glass. *J. Anal. At. Spectrom.* **30**, 1100–1107 (2015).
55. Krachler, M., Varga, Z., Nicholl, A., Wallenius, M. & Mayer, K. Spatial distribution of uranium isotopes in solid nuclear materials using laser ablation multi-collector ICP-MS. *Microchemical Journal* **140**, 24–30 (2018).
56. Kips, R., Weber, P. K., Kristo, M. J., Jacobsen, B. & Ramon, E. C. Microscale Isotopic Variation in Uranium Fuel Pellets with Implications for Nuclear Forensics. *Anal. Chem.* **91**, 11598–11605 (2019).
57. Fallon, C. M. *et al.* Isotopic and Compositional Variations in Single Nuclear Fuel Pellet Particles Analyzed by Nanoscale Secondary Ion Mass Spectrometry. *ACS Omega* **5**, 296–303 (2020).
58. Reddy, S. M. *et al.* Atom Probe Tomography: Development and Application to the Geosciences. *Geostandards and Geoanalytical Research* **44**, 5–50 (2020).
59. Zoriy, M. V. & Becker, J. S. Near-field laser ablation inductively coupled plasma mass spectrometry: a novel elemental analytical technique at the nanometer scale. *Rapid Communications in Mass Spectrometry* **23**, 23–30 (2009).
60. Liang, Z. *et al.* Tip-enhanced ablation and ionization mass spectrometry for nanoscale chemical analysis. *Science Advances* **3**, eaaq1059 (2017).
61. Wirtz, T. *et al.* Design and performance of a combined secondary ion mass spectrometry-scanning probe microscopy instrument for high sensitivity and high-resolution elemental three-dimensional analysis. *Review of Scientific Instruments* **83**, 063702 (2012).
62. Priebe, A., Pethö, L. & Michler, J. Fluorine Gas Coinjection as a Solution for Enhancing Spatial Resolution of Time-of-Flight Secondary Ion Mass Spectrometry and Separating Mass Interference. *Anal. Chem.* **92**, 2121–2129 (2020).
63. Fukuda, K. *et al.* Magnesium isotope analysis of olivine and pyroxene by SIMS: Evaluation of matrix effects. *Chemical Geology* **540**, 119482 (2020).
64. Varga, Z., Wallenius, M., Nicholl, A. & Mayer, K. Assessment of uranium inhomogeneity and isotope imaging for nuclear forensics. *Spectrochimica Acta Part B: Atomic Spectroscopy* **171**, 105920 (2020).

65. Henke, B. L., Gullikson, E. M. & Davis, J. C. X-Ray Interactions: Photoabsorption, Scattering, Transmission, and Reflection at  $E = 50\text{--}30,000$  eV,  $Z = 1\text{--}92$ . *Atomic Data and Nuclear Data Tables* **54**, 181–342 (1993).
66. Wiesendanger, R. *et al.* The LMS-GT instrument – a new perspective for quantification with the LIMS-TOF measurement technique. *Journal of Analytical Atomic Spectrometry* **34**, 2061–2073 (2019).
67. Lin, Y., Yu, Q., Hang, W. & Huang, B. Progress of laser ionization mass spectrometry for elemental analysis — A review of the past decade. *Spectrochimica Acta Part B: Atomic Spectroscopy* **65**, 871–883 (2010).
68. Reilly, D. D. *et al.* Focused ion beam for improved spatially-resolved mass spectrometry and analysis of radioactive materials for uranium isotopic analysis. *Talanta* **211**, 120720 (2020).
69. Schwantes, J. M., Marsden, O. & Pellegrini, K. L. State of practice and emerging application of analytical techniques of nuclear forensic analysis: highlights from the 4th Collaborative Materials Exercise of the Nuclear Forensics International Technical Working Group (ITWG). *J Radioanal Nucl Chem* **311**, 1441–1452 (2017).
70. State of practice and emerging application of analytical techniques of nuclear forensic analysis: highlights from the 4th Collaborative Materials Exercise of the Nuclear Forensics International Technical Working Group (ITWG) | SpringerLink. <https://link.springer.com/article/10.1007/s10967-016-5037-5>.
71. Mathew, K., Mason, P., Voeks, A. & Narayanan, U. Uranium isotope abundance ratios in natural uranium metal certified reference material 112-A. *International Journal of Mass Spectrometry* **315**, 8–14 (2012).
72. Anderson, E. H. Specialized Electron Beam Nanolithography for EUV and X-Ray Diffractive Optics. *IEEE J. Quantum Electron.* **42**, 27–35 (2006).
73. Zirakparvar, N. A. *et al.* A NanoSIMS 50 L Investigation into Improving the Precision and Accuracy of the  $^{235}\text{U}/^{238}\text{U}$  Ratio Determination by Using the Molecular  $^{235}\text{U}^{16}\text{O}$  and  $^{238}\text{U}^{16}\text{O}$  Secondary Ions. *Minerals* **9**, 307 (2019).
74. Ronzani, A.-L. *et al.* Capabilities of laser ablation – ICP-TOF-MS coupling for isotopic analysis of individual uranium micrometric particles. *Journal of Analytical Atomic Spectrometry* **33**, 1892–1902 (2018).
75. Willingham, D., Naes, B. E. & Fahey, A. J. Validating mass spectrometry measurements of nuclear materials via a non-contact volume analysis method of ion sputter craters. *J Radioanal Nucl Chem* **303**, 655–662 (2015).
76. Ranebo, Y., L. Hedberg, P. M., J. Whitehouse, M., Ingeneri, K. & Littmann, S. Improved isotopic SIMS measurements of uranium particles for nuclear safeguard purposes. *Journal of Analytical Atomic Spectrometry* **24**, 277–287 (2009).
77. W. Sinha, B. & Hoppe, P. Ion microprobe analysis: Basic principles, state-of-the-art instruments and recent applications with emphasis on the geosciences. in *Nanoscope Approaches in Earth and Planetary Sciences* (eds. Brenker, F. E. & Jordan, G.) vol. 8 0 (Mineralogical Society of Great Britain and Ireland, 2010).
78. Zirakparvar, N. A. *et al.* A preliminary investigation into the use of molecular oxide and hydride secondary ion relationships for improvement of the  $^{236}\text{U}/^{238}\text{U}$  determination on a NanoSIMS 50L. *Sci Rep* **10**, 12285 (2020).
79. Schaltegger, U., Schmitt, A. K. & Horstwood, M. S. A. U–Th–Pb zircon geochronology by ID-TIMS, SIMS, and laser ablation ICP-MS: Recipes, interpretations, and opportunities. *Chemical Geology* **402**, 89–110 (2015).
80. Schoene, B. 4.10 - U–Th–Pb Geochronology. in *Treatise on Geochemistry (Second Edition)* (eds. Holland, H. D. & Turekian, K. K.) 341–378 (Elsevier, 2014). doi:10.1016/B978-0-08-095975-7.00310-7.
81. Stern, R. A. Chapter 1: An Introduction to Secondary Ion Mass Spectrometry (SIMS) in Geology. in *Secondary Ion Mass Spectrometry in the Earth Science* (ed. Fayek, M.) vol. 41 1–18 (Mineralogical Association of Canada, 2009).

82. Wang, H. A. O. *et al.* Fast Chemical Imaging at High Spatial Resolution by Laser Ablation Inductively Coupled Plasma Mass Spectrometry. *Anal. Chem.* **85**, 10107–10116 (2013).
83. Hao, J.-L. *et al.* Submicron spatial resolution Pb–Pb and U–Pb dating by using a NanoSIMS equipped with the new radio-frequency ion source. *J. Anal. At. Spectrom.* **36**, 1625–1633 (2021).
84. Kuhn, B. K., Birbaum, K., Luo, Y. & Günther, D. Fundamental studies on the ablation behaviour of Pb/U in NIST 610 and zircon 91500 using laser ablation inductively coupled plasma mass spectrometry with respect to geochronology. *J. Anal. At. Spectrom.* **25**, 21–27 (2009).
85. Krosiakova, I. & Günther, D. Elemental fractionation in laser ablation-inductively coupled plasma-mass spectrometry: evidence for mass load induced matrix effects in the ICP during ablation of a silicate glass. *J. Anal. At. Spectrom.* **22**, 51–62 (2006).
86. Zhang, S. *et al.* Elemental fractionation and matrix effects in laser sampling based spectrometry. *J. Anal. At. Spectrom.* **31**, 358–382 (2016).
87. Günther, D. & Hattendorf, B. Solid sample analysis using laser ablation inductively coupled plasma mass spectrometry. *TrAC Trends in Analytical Chemistry* **24**, 255–265 (2005).
88. Thompson, J. M., Meffre, S. & Danyushevsky, L. Impact of air, laser pulse width and fluence on U–Pb dating of zircons by LA-ICPMS. *J. Anal. At. Spectrom.* **33**, 221–230 (2018).
89. Thompson, J. A. *et al.* Use of Non-Matrix Matched Reference Materials for the Accurate Analysis of Calcium Carbonate by LA-ICP-MS. *Geostandards and Geoanalytical Research* **46**, 97–115 (2022).
90. He, M. *et al.* Three-Dimensional Elemental Imaging of Nantan Meteorite via Femtosecond Laser Ionization Time-of-Flight Mass Spectrometry. *Anal. Chem.* **89**, 565–570 (2017).
91. de Koning, C. P. *et al.* Quantitative elemental analysis with the LMS-GT; a next-generation LIMS-TOF instrument. *International Journal of Mass Spectrometry* **470**, 116662 (2021).
92. Luo, T. *et al.* Water Vapor-Assisted “Universal” Nonmatrix-Matched Analytical Method for the in Situ U–Pb Dating of Zircon, Monazite, Titanite, and Xenotime by Laser Ablation-Inductively Coupled Plasma Mass Spectrometry. *Anal. Chem.* **90**, 9016–9024 (2018).
93. Hang, L., Xu, Z., Yin, Z. & Hang, W. Approaching Standardless Quantitative Elemental Analysis of Solids: Microsecond Pulsed Glow Discharge and Buffer-Gas-Assisted Laser Ionization Time-of-Flight Mass Spectrometry. *Anal. Chem.* **90**, 13222–13228 (2018).
94. Verhoff, B., Harilal, S. S. & Hassanein, A. Angular emission of ions and mass deposition from femtosecond and nanosecond laser-produced plasmas. *Journal of Applied Physics* **111**, 123304 (2012).
95. Zhang, S., Zhang, B., Hang, W. & Huang, B. Chemometrics and theoretical approaches for evaluation of matrix effect in laser ablation and ionization of metal samples. *Spectrochimica Acta Part B: Atomic Spectroscopy* **107**, 17–24 (2015).
96. Jochum, K. P., Stoll, B., Herwig, K. & Willbold, M. Validation of LA-ICP-MS trace element analysis of geological glasses using a new solid-state 193 nm Nd:YAG laser and matrix-matched calibration. *J. Anal. At. Spectrom.* **22**, 112–121 (2007).
97. Huang, R. *et al.* Influence of wavelength, irradiance, and the buffer gas pressure on high irradiance laser ablation and ionization source coupled with an orthogonal Time of Flight Mass Spectrometer. *Spectrochimica Acta Part B: Atomic Spectroscopy* **64**, 255–261 (2009).
98. Juha, L. *et al.* Ablation of organic polymers by 46.9-nm-laser radiation. *Applied Physics Letters* **86**, 034109 (2005).
99. Jochum, K. P. *et al.* Determination of Reference Values for NIST SRM 610–617 Glasses Following ISO Guidelines. *Geostandards and Geoanalytical Research* **35**, 397–429 (2011).
100. Jochum, K. P., Willbold, M., Raczek, I., Stoll, B. & Herwig, K. Chemical Characterisation of the USGS Reference Glasses GSA-1G, GSC-1G, GSD-1G, GSE-1G, BCR-2G, BHVO-2G and BIR-1G Using EPMA, ID-TIMS, ID-ICP-MS and LA-ICP-MS. *Geostandards and Geoanalytical Research* **29**, 285–302 (2005).
101. Klemme, S. *et al.* Synthesis and Preliminary Characterisation of New Silicate, Phosphate and Titanite Reference Glasses. *Geostandards and Geoanalytical Research* **32**, 39–54 (2008).
102. Jochum, K. P. & Stoll, B. Reference materials for elemental and isotopic analyses by LA-(MC)-ICP-MS: Successes and outstanding needs. in *Laser ablation ICP-MS in the Earth sciences: Current*

- practices and outstanding issues* (ed. P., S.) vol. 40 147–168 (Mineralogical Association of Canada, 2008).
103. Jochum, K. P. *et al.* FeMnOx-1: A new microanalytical reference material for the investigation of Mn–Fe rich geological samples. *Chemical Geology* **432**, 34–40 (2016).
  104. Gonçalves, G. O. *et al.* An assessment of monazite from the Itambé pegmatite district for use as U–Pb isotope reference material for microanalysis and implications for the origin of the “Moacyr” monazite. *Chemical Geology* **424**, 30–50 (2016).
  105. Gonçalves, G. O. *et al.* The Diamantina Monazite: A New Low-Th Reference Material for Microanalysis. *Geostandards and Geoanalytical Research* **42**, 25–47 (2018).
  106. Thompson, J. M., Danyushevsky, L. V., Borovinskaya, O. & Tanner, M. Time-of-flight ICP-MS laser ablation zircon geochronology: assessment and comparison against quadrupole ICP-MS. *J. Anal. At. Spectrom.* **35**, 2282–2297 (2020).
  107. Willie, S., Mester, Z. & Sturgeon, R. E. Isotope ratio precision with transient sample introduction using ICP orthogonal acceleration time-of-flight mass spectrometry. *J. Anal. At. Spectrom.* **20**, 1358–1364 (2005).
  108. Vermeesch, P. On the treatment of discordant detrital zircon U–Pb data. *Geochronology* **3**, 247–257 (2021).
  109. Itano, K. & Iizuka, T. Unraveling the mechanism and impact of oxide production in LA-ICP-MS by comprehensive analysis of REE-Th-U phosphates. *J. Anal. At. Spectrom.* **32**, 2003–2010 (2017).
  110. Gilbert, S., Olin, P., Thompson, J., Lounejeva, E. & Danyushevsky, L. Matrix dependency for oxide production rates by LA-ICP-MS. *J. Anal. At. Spectrom.* **32**, 638–646 (2017).
  111. Jeon, H. & Whitehouse, M. J. A Critical Evaluation of U–Pb Calibration Schemes Used in SIMS Zircon Geochronology. *Geostandards and Geoanalytical Research* **39**, 443–452 (2015).
  112. Zong, K. *et al.* In-situ U–Pb dating of uraninite by fs-LA-ICP-MS. *Sci. China Earth Sci.* **58**, 1731–1740 (2015).
  113. Tulej, M. *et al.* Isotope abundance ratio measurements using femtosecond laser ablation ionization mass spectrometry. *Journal of Mass Spectrometry* **55**, e4660 (2020).
  114. He, M. *et al.* Composition analysis of ancient celadon via femtosecond laser ionization time-of-flight mass spectrometry. *Applied Surface Science* **351**, 624–634 (2015).
  115. Bussweiler, Y., Gervasoni, F., Rittner, M., Berndt, J. & Klemme, S. Trace element mapping of high-pressure, high-temperature experimental samples with laser ablation ICP time-of-flight mass spectrometry – Illuminating melt-rock reactions in the lithospheric mantle. *Lithos* **352–353**, 105282 (2020).
  116. Chang, Q., Kimura, J.-I., Miyazaki, T., Sasaki, S. & Kanazawa, N. Microanalysis of Pb isotope ratios of low-Pb glass samples by femtosecond laser ablation-multiple ion counter-ICP-mass spectrometry (fsLA-MIC-ICP-MS). *Geochemical Journal* **48**, 309–320 (2014).
  117. Lennon, J. D., Shinn, D., Vachet, R. W. & Glish, G. L. Strategy for Pulsed Ionization Methods on a Sector Mass Spectrometer. *Anal. Chem.* **68**, 845–849 (1996).
  118. Rush, L. A. *et al.* Collisional dampening for improved quantification in single particle inductively coupled plasma mass spectrometry. *Talanta* **189**, 268–273 (2018).
  119. Reagan, B. A. *et al.* High-average-power, 100-Hz-repetition-rate, tabletop soft-x-ray lasers at sub-15-nm wavelengths. *Phys. Rev. A* **89**, 053820 (2014).
  120. Samokhvalov, A. A. *et al.* Fast capillary discharge device for soft x-ray generation in the “carbon-window” and “water-window” spectral regions. *J. Inst.* **17**, P06002 (2022).
  121. Miaja-Avila, L. *et al.* Extreme Ultraviolet Radiation Pulsed Atom Probe Tomography of III-Nitride Semiconductor Materials. *J. Phys. Chem. C* **125**, 2626–2635 (2021).

## APPENDIX

### A.1 EUV TOF components

**Table A.1.1** Main EUV TOF components alongside their specifications, vendor, and part number.

Component	Specifications	Vendor	Part number
<b>EUV Laser</b>			
EUV laser	Table-top sized	In-house [refs <sup>6,7</sup> ]	N/A
1x high voltage trigger amplifier	2 Ch., 50 kV, 10 V trigger voltage, up to 10 Hz rep rate	Maxwell Technologies	40168
1x DC power supply for laser	+60 kV	General Atomics	CCS Series
<b>Optics</b>			
2x toroidal mirrors	2x1" rectangular mirrors, coated w/ 100 nm of unprotected Au	Blue Ridge Optics, USA	N/A
4x course actuators for mirror movement	25 mm travel range, vacuum rated to 10 <sup>-6</sup> Torr, closed loop	Thorlabs, USA	Z825BV
<b>TOF</b>			
1x TOF	1-meter TOF tube w/ reflectron and ion optics	Jordan TOF Products, USA (no longer in business)	D-850
1x dual MCP detector	40 mm active area	Jordan TOF Products, USA (no longer in business)	C-726
<b>Sample Chamber</b>			
1x zone plate	Numerical aperture = 0.12, 200 nm outer zone width, 0.5 mm outer diameter, 0.05 mm central opening	Center for X-Ray Optics (CXRO), USA	N/A
2x fine piezo stages for X,Y sample movement	26 mm travel range w/ 6 nm min. step size, closed loop	Physik Instrumente, Germany	Q-545.240
3x course actuators for zone plate and microscope movement	26 mm travel w/ 100 μm min. step size, closed loop	Oriel (now Newport)	18046 (18011 controller)
<b>Vacuum</b>			
3x 145 L/s turbo pump	<7.5x10 <sup>-11</sup> Torr min. pressure, ISO-100 port	Leybold, Germany	85635
1x 1100 L/s turbo pump	<7.5x10 <sup>-11</sup> Torr min. pressure, CF-200 port	Leybold, Germany	11764
<b>TOF Power Supplies</b>			
4x ±5 kV power supply: 1x for TOF deflection plates, 1x for TOF MCP,	1 Ch./unit, GPIB interface system	Stanford Research Systems	PS350

2x for EUV photodetectors			
1x +10 kV power supply for TOF-related components (pos. ion mode)	4 Ch. (sample, zone plate, reflectron grids)	In-house	N/A
1x -10 kV power supply for TOF-related components (neg. ion mode)	4 Ch. (sample, zone plate, reflectron grids)	In-house	N/A
<b>Data Acquisition</b>			
1x digitizer/ADC	12-bit, 1 GS/s, 1 Ch., 1.75 GHz	DynamicSignals (now Vitrek)	EON Compuscope CS121G1

## A.2 Supplementary Information (SI) for Chapter 4: Paper #2 on EUV TOF

**Table A.2.1** Concentration values (in  $\mu\text{g/g}$ ) of Pb, Th, and U and their respective 1 standard deviation ( $\pm 1\text{SD}$ ) uncertainties for the samples investigated in this study. The concentrations and their associated uncertainties listed for the synthetic glasses (NIST610, USGS GSE-1G and STDP5) and iron manganese (FeMnOx-1) material were used to calculate the  $^{206}\text{Pb}/^{238}\text{U}$  and  $^{232}\text{Th}/^{238}\text{U}$  ratio values found in Chapter 4 in Table 4.1.

Sample	Pb <sub>total</sub>	$\pm 1\text{SD}$	$^{206}\text{Pb}$	$\pm 1\text{SD}$	$^{232}\text{Th}$	$\pm 1\text{SD}$	U <sub>total</sub>	$\pm 1\text{SD}$	$^{238}\text{U}$	$\pm 1\text{SD}$
<b>NIST610</b>	426	1	102.7*	0.2	457.2	1.2	461.5	1.1	460.4	1.1
<b>USGS GSE-1G</b>	378	12	91*	3	380	20	420	30	417*	30
<b>STDP5</b>	1414	61.5	341*	15	1235	133	1378	5	1368*	5
<b>FeMnOx-1</b>	1624	280	391*	67	534	40	547	17	543*	17
<b>SR1</b>	n/a	n/a	218**	3	185	4	n/a	n/a	2455	35
<b>EA</b>	n/a	n/a	70**	1	292	8	n/a	n/a	803	15
<b>14971</b>										
<b>LA ICP-MS</b>	n/a	n/a	173*	3	37819	2404	n/a	n/a	1141	22
<b>ID-TIMS</b>	1904	94	n/a	n/a	n/a	n/a	1580	90	n/a	n/a
<b>Bananeira†</b>	n/a	n/a	243	40	68252	5574	n/a	n/a	972	179
<b>Diamantina†</b>	n/a	n/a	93	11	3588	1822	n/a	n/a	355	41
<b>SL-B</b>	n/a	n/a	29688**	618	543556	7088	n/a	n/a	277039	5732
<b>Mogok 2A</b>	n/a	n/a	3735**	25	528320	2270	n/a	n/a	341808	2266
<b>Mogok 2C</b>	n/a	n/a	4716**	46	418880	4480	n/a	n/a	450034	4421
<b>Mogok 1</b>	n/a***	n/a	n/a***	n/a	24310	2101	n/a	n/a	290841	3683

\*Calculated  $^{206}\text{Pb}$  and  $^{238}\text{U}$  concentrations from total Pb and U concentrations, respectively, assuming natural isotopic abundance. (Note: The  $^{206}\text{Pb}/^{208}\text{Pb}$  ratio has been measured for USGS GSE-1G using LA ICPMS and SIMS, obtaining a ratio value of approximately 1.96, whereas the natural  $^{206}\text{Pb}/^{208}\text{Pb}$  ratio is 2.17. Nonetheless, the natural Pb abundance was assumed here because isotope concentrations are not available)

\*\*Calculated radiogenic Pb concentrations from direct ratio measurements of  $^{206}\text{Pb}/^{238}\text{U}$  and concentration measurements of  $^{238}\text{U}$

\*\*\*Sample has too high common Pb to give calculated Pb concentrations

†Concentration values measured with LA Q-ICPMS

**Table A.2.2** The ion counts of  $^{206}\text{Pb}$ ,  $^{232}\text{Th}$ ,  $^{238}\text{U}$ ,  $^{232}\text{Th}^{16}\text{O}$ ,  $^{238}\text{U}^{16}\text{O}$ ,  $^{232}\text{Th}^{16}\text{O}_2$ , and  $^{238}\text{U}^{16}\text{O}_2$  measured with the EUV TOF in each super crater ablated on the samples analyzed in this study. The corresponding Pb/U and Th/U ratios for each super crater with its  $\pm 2\sigma$  uncertainty is also listed, where the ratio considers all oxide species detected in the super crater, unless otherwise specified. The weighted average of the Pb/U and Th/U ratios is also shown alongside the  $\pm 2\sigma$  uncertainty, which is calculated using the equations in Table A.2.3.

**Sample: NIST 610 (silicate glass)**

Super crater #	<i>Measured Counts</i>							<i>Measured Ratios</i>			
	$^{206}\text{Pb}$	$^{232}\text{Th}$	$^{238}\text{U}$	$^{232}\text{Th}^{16}\text{O}$	$^{238}\text{U}^{16}\text{O}$	$^{232}\text{Th}^{16}\text{O}_2$	$^{238}\text{U}^{16}\text{O}_2$	Pb/U	$\pm 2\sigma$	Th/U	$\pm 2\sigma$
1*	57	313	251	270	260	n/a	73	0.10	0.03	1.00	0.16
2*	55	317	265	297	277	n/a	68	0.09	0.03	1.01	0.16
3*	56	251	187	243	213	n/a	62	0.12	0.04	1.07	0.20
4*	76	327	246	306	269	n/a	59	0.13	0.04	1.10	0.18
5*	83	381	335	281	264	n/a	67	0.12	0.03	0.99	0.15
6*	82	409	314	268	252	n/a	67	0.13	0.03	1.07	0.16
7	48	184	113	197	180	n/a	84	0.13	0.04	1.01	0.21
8	45	147	67	144	129	n/a	71	0.17	0.06	1.09	0.27
9	51	129	99	134	125	n/a	82	0.17	0.06	0.86	0.22
10	59	116	81	98	93	n/a	74	0.24	0.08	0.86	0.24
11	47	87	61	107	95	n/a	66	0.21	0.08	0.87	0.28
12	40	73	48	59	80	n/a	65	0.21	0.09	0.68	0.25
13	54	66	45	66	63	n/a	55	0.33	0.13	0.81	0.32
14*	119	700	640	524	460	n/a	66	0.10	0.02	1.05	0.12
15*	115	684	621	487	472	n/a	76	0.10	0.02	1.00	0.11
16*	124	625	540	462	463	n/a	87	0.11	0.02	1.00	0.12
17*	166	885	796	650	689	n/a	149	0.10	0.02	0.94	0.08
18*	153	796	741	622	614	n/a	140	0.10	0.02	0.95	0.09
19*	186	846	709	698	649	n/a	141	0.12	0.02	1.03	0.09
<i>Weighted average of ratios</i>								<b>0.108</b>	<b>0.007</b>	<b>0.99</b>	<b>0.03</b>

\*Values in red are those used in the calculated of the Pb/U weighted average ratio because these runs have total U counts >450.

### Sample: USGS GSE-1G (basalt glass)

Super crater #	Measured Counts							Measured Ratios			
	<sup>206</sup> Pb	<sup>232</sup> Th	<sup>238</sup> U	<sup>232</sup> Th <sup>16</sup> O	<sup>238</sup> U <sup>16</sup> O	<sup>232</sup> Th <sup>16</sup> O <sub>2</sub>	<sup>238</sup> U <sup>16</sup> O <sub>2</sub>	Pb/U	±2σ	Th/U	±2σ
1	239	916	918	759	761	n/a	142	0.13	0.02	0.92	0.08
2	212	943	1024	792	750	n/a	152	0.11	0.02	0.90	0.08
3	210	954	929	729	791	n/a	176	0.11	0.02	0.89	0.07
<i>Weighted average of ratios</i>								<b>0.12</b>	<b>0.01</b>	<b>0.90</b>	<b>0.04</b>

### Sample: STDP5 (phosphate glass)

Super crater #	Measured Counts							Measured Ratios			
	<sup>206</sup> Pb	<sup>232</sup> Th	<sup>238</sup> U	<sup>232</sup> Th <sup>16</sup> O	<sup>238</sup> U <sup>16</sup> O	<sup>232</sup> Th <sup>16</sup> O <sub>2</sub>	<sup>238</sup> U <sup>16</sup> O <sub>2</sub>	Pb/U	±2σ	Th/U	±2σ
1	401	1562	1318	1323	1346	n/a	439	0.13	0.01	0.93	0.06
2	359	1544	1199	1329	1294	n/a	440	0.12	0.01	0.98	0.06
3	360	1376	1205	1290	1337	n/a	430	0.12	0.01	0.90	0.06
4	602	n/a*	2222	1769	1730	n/a	339	0.14	0.01	n/a	n/a
5	358	1234	977	986	944	n/a	346	0.16	0.02	0.98	0.07
6	295	1048	931	950	859	n/a	329	0.14	0.02	0.94	0.07
<i>Weighted average of ratios</i>								<b>0.133</b>	<b>0.006</b>	<b>0.94</b>	<b>0.04</b>

\*<sup>232</sup>Th signal could not be resolved from ringing induced by a large peak at m/q = 231

### Sample: FeMnOx-1 (iron manganese oxide powder)

Super crater #	Measured Counts							Measured Ratios			
	<sup>206</sup> Pb	<sup>232</sup> Th	<sup>238</sup> U	<sup>232</sup> Th <sup>16</sup> O	<sup>238</sup> U <sup>16</sup> O	<sup>232</sup> Th <sup>16</sup> O <sub>2</sub>	<sup>238</sup> U <sup>16</sup> O <sub>2</sub>	Pb/U	±2σ	Th/U	±2σ
1	654	1233	1132	444	438	n/a	n/a	0.42	0.04	1.07	0.07
2	501	845	720	432	385	n/a	n/a	0.45	0.04	1.16	0.09
3	434	722	636	423	364	n/a	n/a	0.43	0.05	1.14	0.10
<i>Weighted average of ratios</i>								<b>0.43</b>	<b>0.02</b>	<b>1.11</b>	<b>0.05</b>

### Sample: SR1 (zircon)

Super crater #	Measured Counts							Measured Ratios			
	<sup>206</sup> Pb	<sup>232</sup> Th*	<sup>238</sup> U	<sup>232</sup> Th <sup>16</sup> O	<sup>238</sup> U <sup>16</sup> O	<sup>232</sup> Th <sup>16</sup> O <sub>2</sub>	<sup>238</sup> U <sup>16</sup> O <sub>2</sub>	Pb/U	±2σ	Th/U	±2σ
1	484	n/a	4689	490	6090	n/a	2371	0.037	0.003	0.080	0.008
2	415	n/a	3604	380	5419	n/a	2025	0.038	0.004	0.070	0.007
3	393	n/a	2601	339	4599	n/a	1884	0.043	0.004	0.074	0.008
<i>Weighted average of ratios</i>								<b>0.039</b>	<b>0.002</b>	<b>0.075</b>	<b>0.004</b>

\*<sup>232</sup>Th signal had interference from <sup>92</sup>Zr<sub>2</sub><sup>16</sup>O<sub>3</sub> at m/q = 232, so only <sup>232</sup>Th<sup>16</sup>O and <sup>238</sup>U<sup>16</sup>O signals are used for the Th/U ratio

### Sample: EA (zircon)

Super crater #	Measured Counts							Measured Ratios			
	<sup>206</sup> Pb*	<sup>232</sup> Th*	<sup>238</sup> U	<sup>232</sup> Th <sup>16</sup> O	<sup>238</sup> U <sup>16</sup> O	<sup>232</sup> Th <sup>16</sup> O <sub>2</sub>	<sup>238</sup> U <sup>16</sup> O <sub>2</sub> ***	Pb/U	±2σ	Th/U	±2σ
1	n/a	n/a	257	228	684	n/a	461	n/a	n/a	0.33	0.05
2	n/a	n/a	239	241	652	n/a	483	n/a	n/a	0.37	0.06
3	n/a	n/a	212	177	565	n/a	448	n/a	n/a	0.31	0.05
<i>Weighted average of ratios</i>								<b>n/a</b>	<b>n/a</b>	<b>0.34</b>	<b>0.03</b>

\*<sup>206</sup>Pb was below EUV TOF detection limits; \*\*<sup>232</sup>Th signal had interference from <sup>92</sup>Zr<sub>2</sub><sup>16</sup>O<sub>3</sub>; \*\*\*<sup>238</sup>U<sup>16</sup>O<sub>2</sub> was not used for any ratio measurements, but the detected ion counts are shown here for reference.

### Sample: 14971 (monazite)

Super crater #	Measured Counts							Measured Ratios			
	<sup>206</sup> Pb	<sup>232</sup> Th	<sup>238</sup> U	<sup>232</sup> Th <sup>16</sup> O	<sup>238</sup> U <sup>16</sup> O	<sup>232</sup> Th <sup>16</sup> O <sub>2</sub>	<sup>238</sup> U <sup>16</sup> O <sub>2</sub>	Pb/U	±2σ	Th/U	±2σ
1	106	26666	860	14818	458	210	231	0.07	0.01	26.9	1
2	91	17134	567	10451	348	167	206	0.08	0.02	24.8	1
3	85	24585	711	12595	380	138	135	0.07	0.02	30.4	2
4	103	24688	803	12253	393	129	137	0.08	0.02	27.8	1
5	72	23062	837	11513	385	114	110	0.05	0.01	26.0	1
<i>Weighted average of ratios</i>								<b>0.068</b>	<b>0.007</b>	<b>26.9</b>	<b>0.6</b>

### Sample: Bananeira (monazite)

Super crater #	<i>Measured Counts</i>							<i>Measured Ratios</i>			
	<sup>206</sup> Pb	<sup>232</sup> Th	<sup>238</sup> U	<sup>232</sup> Th <sup>16</sup> O	<sup>238</sup> U <sup>16</sup> O	<sup>232</sup> Th <sup>16</sup> O <sub>2</sub>	<sup>238</sup> U <sup>16</sup> O <sub>2</sub>	Pb/U	±2σ	Th/U	±2σ
1	91	56014	1730	26275	813	201	175	0.034	0.008	30.3	1
2	88	56672	1805	25696	890	173	141	0.031	0.007	29.1	1
3	71	56212	1773	28026	836	174	168	0.026	0.006	30.4	1
<i>Weighted average of ratios</i>								<b>0.030</b>	<b>0.004</b>	<b>30.0</b>	<b>0.6</b>

### Sample: Diamantina-1 (monazite)

Super crater #	<i>Measured Counts</i>							<i>Measured Ratios</i>			
	<sup>206</sup> Pb	<sup>232</sup> Th	<sup>238</sup> U	<sup>232</sup> Th <sup>16</sup> O	<sup>238</sup> U <sup>16</sup> O	<sup>232</sup> Th <sup>16</sup> O <sub>2</sub>	<sup>238</sup> U <sup>16</sup> O <sub>2</sub>	Pb/U	±2σ	Th/U*	±2σ
1	46	1326	844	645	397	n/a	n/a	0.04	0.01	1.6	0.1
2	62	1782	883	964	506	n/a	100	0.04	0.01	1.8	0.1
3	70	1610	914	804	480	n/a	n/a	0.05	0.01	1.7	0.1
<i>Weighted average of ratios</i>								<b>0.042</b>	<b>0.007</b>	<b>1.70</b>	<b>0.06</b>

\*Measured Th/U ratio is shown here only for reference because Th content is not homogenous in this sample (i.e., ID-TIMS measures Th/U ranging from 0.22 to 16.2)

### Sample: SL-B (uraninite)

Super crater #	<i>Measured Counts</i>							<i>Measured Ratios</i>			
	<sup>206</sup> Pb	<sup>232</sup> Th	<sup>238</sup> U	<sup>232</sup> Th <sup>16</sup> O	<sup>238</sup> U <sup>16</sup> O	<sup>232</sup> Th <sup>16</sup> O <sub>2</sub>	<sup>238</sup> U <sup>16</sup> O <sub>2</sub>	Pb/U	±2σ	Th/U	±2σ
1	22476	499537	291801	290996	138805	n/a	48801	0.0469	6E-4	1.649	0.005
2	23605	512072	299667	298655	142179	n/a	49358	0.0481	6E-4	1.650	0.005
3	23837	512877	298471	298080	140141	n/a	49241	0.0489	6E-4	1.662	0.005
<i>Weighted average of ratios</i>								<b>0.0479</b>	<b>4E-4</b>	<b>1.654</b>	<b>0.003</b>

### Sample: Mogok 2A (uraninite)

Super crater #	Measured Counts							Measured Ratios			
	<sup>206</sup> Pb	<sup>232</sup> Th	<sup>238</sup> U	<sup>232</sup> Th <sup>16</sup> O	<sup>238</sup> U <sup>16</sup> O	<sup>232</sup> Th <sup>16</sup> O <sub>2</sub>	<sup>238</sup> U <sup>16</sup> O <sub>2</sub>	Pb/U	±2σ	Th/U	±2σ
1	6126	481597	308223	303577	160397	2584	59793	0.0116	3E-4	1.491	0.006
2	6402	476215	307556	310178	161541	2594	58827	0.0121	3E-4	1.495	0.006
3	6255	517753	325381	317055	158413	2459	55655	0.0116	3E-4	1.552	0.006
<i>Weighted average of ratios</i>								<b>0.0118</b>	<b>2E-4</b>	<b>1.512</b>	<b>0.003</b>

### Sample: Mogok 2C (uraninite)

Super crater #	Measured Counts							Measured Ratios			
	<sup>206</sup> Pb	<sup>232</sup> Th	<sup>238</sup> U	<sup>232</sup> Th <sup>16</sup> O	<sup>238</sup> U <sup>16</sup> O	<sup>232</sup> Th <sup>16</sup> O <sub>2</sub>	<sup>238</sup> U <sup>16</sup> O <sub>2</sub>	Pb/U	±2σ	Th/U	±2σ
1	7784	528540	432768	257623	194196	1430	65757	0.0112	3E-4	1.137	0.005
2	6909	434309	390885	276851	223618	1952	83255	0.0099	2E-4	1.022	0.004
3	7211	449558	398705	266156	217256	1921	78253	0.0104	2E-4	1.034	0.004
<i>Weighted average of ratios</i>								<b>0.0105</b>	<b>1E-4</b>	<b>1.058</b>	<b>0.003</b>

### Sample: Mogok 1 (thorite)

Super crater #	Measured Counts							Measured Ratios			
	<sup>206</sup> Pb	<sup>232</sup> Th	<sup>238</sup> U	<sup>232</sup> Th <sup>16</sup> O	<sup>238</sup> U <sup>16</sup> O	<sup>232</sup> Th <sup>16</sup> O <sub>2</sub>	<sup>238</sup> U <sup>16</sup> O <sub>2</sub>	Pb/U	±2σ	Th/U	±2σ
1	338	18560	201834	21515	234508	n/a	125201	0.00060	7E-5	0.071	0.001
2	284	14610	161212	18304	200153	n/a	117440	0.00059	7E-5	0.069	0.001
3	258	14589	159707	18992	200148	n/a	114763	0.00054	7E-5	0.071	0.001
<i>Weighted average of ratios</i>								<b>0.00058</b>	<b>4E-5</b>	<b>0.0703</b>	<b>6E-4</b>

**Table A.2.3** Equations used for calculating the weighted average of the ratios. The equations below specifically represent calculations for  $^{206}\text{Pb}/^{238}\text{U}$  ratios. For  $^{232}\text{Th}/^{238}\text{U}$  ratio calculations,  $^{206}\text{Pb}$  is replaced with  $^{232}\text{Th}$  ion counts. Eqtns. (5) and (6) are bold and represent the final ratio values  $c$  and their uncertainty  $\sigma$ , respectively, reported in the main text of Chapter 4.

Eqtn. (1) $Ratio = a_n = \frac{[206Pb (counts)]}{[238U (counts)]}$
Eqtn. (2) $Ratio\ uncertainty = \delta_n = \frac{[206Pb (counts)]}{[238U (counts)]} * \sqrt{\left(\frac{1}{206Pb (counts)} + \frac{1}{238U (counts)}\right)}$
Eqtn. (3) $Ratio\ weight = b_n = \frac{\frac{[206Pb (counts)]}{[238U (counts)]}}{\delta_n^2}$
Eqtn. (4) $Ratio\ uncertainty\ weight = \alpha_n = \frac{1}{\delta_n^2}$
<b>Eqtn. (5) <math>Weighted\ average\ ratio = c = \frac{\Sigma(b1,b2...bn)}{\Sigma(\alpha1,\alpha2,...\alpha n)}</math></b>
<b>Eqtn. (6) <math>Weighted\ uncertainty\ of\ ratio = \sigma = \sqrt{\frac{1}{\Sigma(\alpha1,\alpha2,...\alpha n)}}</math></b>

Where  $n = 1,2,3,\dots,n+1$  and represents each ratio measured on the sample.

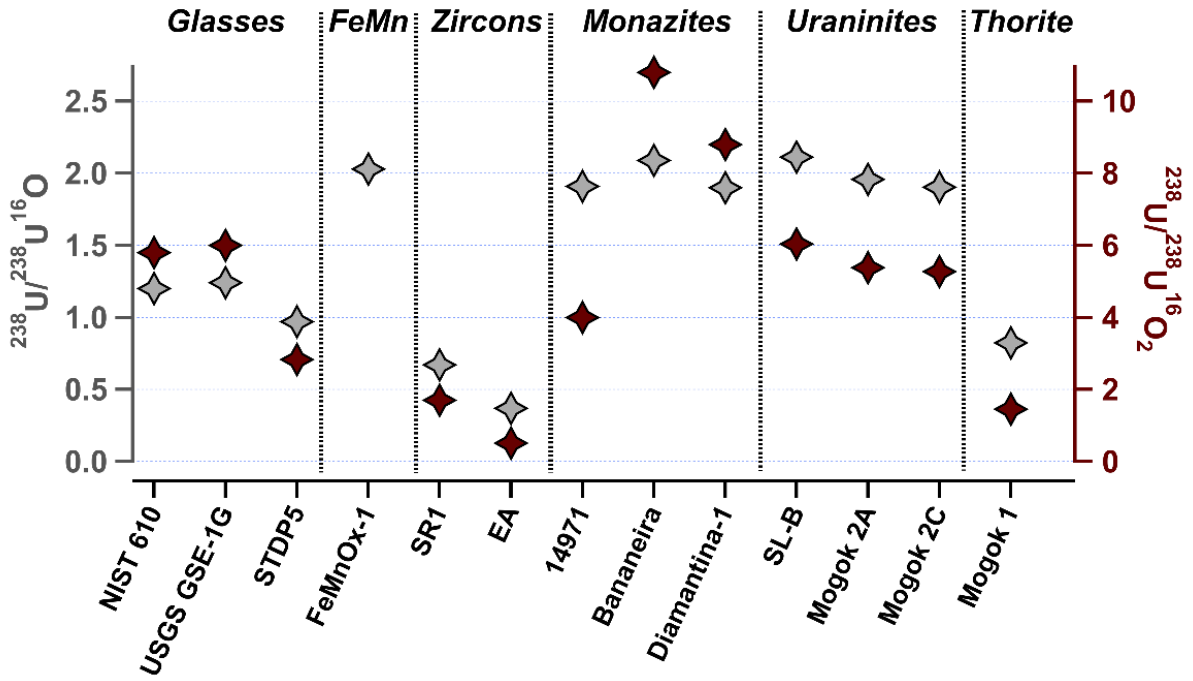
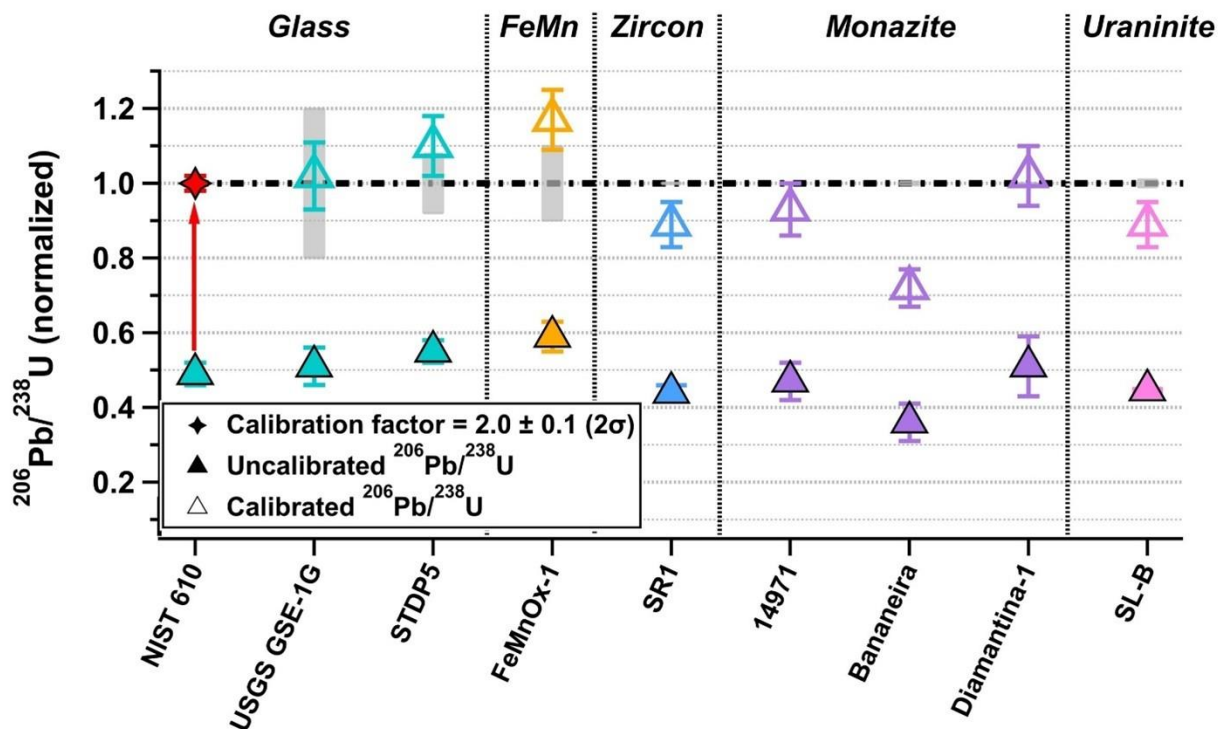


Figure A.2.1  $^{238}\text{U}/^{238}\text{U}^{16}\text{O}$  and  $^{238}\text{U}/^{238}\text{U}^{16}\text{O}_2$  ratios measured with the EUV TOF in the different matrices.



**Figure A.2.2** Uncalibrated and calibrated  $^{206}\text{Pb}/^{238}\text{U}$  ratios (normalized to 1) measured with the EUV TOF. The direct uncalibrated (i.e., raw)  $^{206}\text{Pb}/^{238}\text{U}$  ratios are from Figure 4.4 and are shown as solid triangles. The open triangles represent calibrated  $^{206}\text{Pb}/^{238}\text{U}$  ratios using the NIST 610 CRM as the calibration standard, where the calibration factor is  $2.0 \pm 0.1$  ( $2\sigma$ ). The error bars on each point are  $\pm 2\sigma$ . The black dotted line represents the expected normalized ratios (i.e., 1). The grey shaded region is the corresponding  $\pm 2\sigma$  uncertainty for the expected ratios. The Mogok uraninites and thorite are not shown on this plot because they significantly deviate from the expected values by  $>50\%$  when the calibration factor is applied.

### A.3 EUV magnetic sector components

**Table A.3.2** Main EUV magnetic sector components alongside their specifications, vendor, and part number. For vacuum pump components, see Table A.3.

<b>EUV Laser</b>			
<i>Component</i>	<i>Specifications</i>	<i>Vendor</i>	<i>Part number</i>
EUV laser	$\lambda = 46.9$ nm, 1-10 Hz rep. rate, 1.5 ns pulse duration, 50 $\mu$ J/pulse max., divergence = 5 mrad	XUV Lasers, USA	N/A
1x main controller for EUV laser	User controllable interface for firing EUV laser and adjusting parameters	XUV Lasers, USA	N/A
1x oil pump and thyatron heater supply	Turns on pump for oil circulation and thyatron heater for operation	XUV Lasers, USA	N/A
1x RF power supply	60 MHz	XUV Lasers, USA	N/A
1x DC pre-ionization and low high voltage supply	+8 kV DC	XUV Lasers, USA	N/A
1x Thyatron trigger for main high voltage pulse	N/A	XUV Lasers, USA	N/A
1x controller for main high voltage pulse from DC power supply	User selectable high voltage range from 0 to 42 kV	XUV Lasers, USA	N/A
1x DC power supply for main high voltage pulse	+60 kV DC	TDK-Lambda Americas, USA	N/A
<b>Optical High Vacuum Chamber</b>			
1x 6”(H)x12”(W)x12”(L) vacuum chamber	Aluminum (6061-T6) vacuum chamber frame with modular walls, o-ring sealed, vacuum rated to $<10^{-6}$ Torr	Ideal Vacuum, USA	P109160 (base model)
2x planar mirrors	1”(H)x2”(W)x0.5”(L) rectangular mirrors, coated w/ 100 nm of unprotected Au, surface roughness ( $\lambda$ ) = $<0.7$ nm, edge finish ground = $\lambda/8$	Knight Optical, UK	MQG2105-C
2x mirror mounts	1” mirror mount, clear edge, vacuum compatible	Newport, USA	SN100C-F2H-V6
2x fine actuators for angular mirror movement (installed on 2 <sup>nd</sup> planar mirror)	13 mm travel range w/ 50 nm min. step size, vacuum rated to $10^{-6}$ Torr, closed loop	Physik Instrumente, Germany	N-470.21V (E-872.401 controller)

2x course actuators attached to manual stages for linear mirror movement	12 mm travel range w/ 200 nm min. step size, vacuum rated to $10^{-6}$ Torr, closed loop	Thorlabs, USA	Z812V (KDC101 controller)
2x manual stages for linear mirror movement	12.7 mm travel range, 40 mm x 40 mm platform	Newport, USA	9062-COM
1x gold photodetector for EUV light detection	~25 x 25 mm active area	In-house	N/A
<b>Sample High Vacuum Chamber</b>			
1x 12”(H)x12”(W)x12”(L) vacuum chamber	Aluminum (6061-T6) vacuum chamber frame with modular walls, o-ring sealed, vacuum rated to $<10^{-6}$ Torr	Ideal Vacuum, USA	P108246 (base model)
1x zone plate	Numerical aperture = 0.12, 200 nm outer zone width, 0.5 mm outer diameter, 0.05 mm central opening	ZonePlates, UK	N/A
3x fine piezo stages for X,Y,Z sample movement	13 mm travel range w/ 6 nm min. step size, closed loop	Physik Instrumente, Germany	Q-545.140
1x course stage for X sample movement	50 mm travel range w/ 1.25 $\mu$ m min. step size, closed loop	Standa, Lithuania	8MT30V-50 (8SMC5-USB controller)
1x silicon photodiode for EUV light detection after zone plate	10 mm x 10 mm active area, 0.07 A/W at $\lambda = 46.9$ nm	Opto Diode, USA	SXUV100
1x quadrupole ion beam deflector	90° deflection of positive or negative ions with energy range from 1 eV to 10 keV, 4 points of entry	Beam Imaging Solutions, USA	QID-900
1x steering and focusing ion lens stack with x, y, and z movement and Einzel lenses (coupling lens)	Lens stack taken from Thermo’s Triton Mass Spectrometer	Thermo Scientific, Germany	N/A
<b>Optical Tables</b>			
1x large laser table and frame for EUV laser system	1 m x 2 m x 210 m (3’ x 6’ x 8.3”) table with 6.35 mm (0.25”) mounting holes, and active frame supports	Thorlabs, USA	T36H table with TF1020A7 frame
1x small laser table with vibration isolation for optical and sample chambers	0.61 m x 0.91 m (24” x 36”) table with 6.35 mm (0.25”) mounting holes	Newport, USA	BT-2436-OPT
<b>Sector-Field Multi-Collector Mass Spectrometer</b>			

1x double focusing dual sector-field multi-collector mass spectrometer	Custom detector array for U isotope detection	Thermo Scientific, Germany	Neptune
<b>Detectors</b>			
1x mini-MCP for detecting ions in tight spaces	14.5 mm active area, Chevron type, channel diameter = 12 $\mu\text{m}$ , bias angle = 8°, max. operating pressure = 1 Pa; at 1 kV/MCP gain = 1E6 and R = 400 M $\Omega$	Hamamatsu, Japan	F14884
1x MCP with phosphor screen for positional imaging of ions	40 mm active area, Chevron type, 4.5"-CF (0.11 m) mount w/ glass viewing window, P-43 phosphor screen, MHV input	Beam Imaging Solutions, USA	BOS-40
1x CMOS camera for imaging ions from MCP-phosphor imaging detector	1.6 MP monochromatic camera with F1.4/16 mm fixed focus lens	Thorlabs, USA	CS165MU (MVL16M23 focus lens w/ SM1A10Z adapter)
<b>Power Supplies</b>			
4x $\pm 5$ kV power supply for MCP detectors and EUV photodetectors	1 Ch./unit, 5 kV/50 mA, bipolar, SHV input, GPIB interface system	Stanford Research Systems, USA	PS350
1x $\pm 8$ kV power supply for beam deflector, coupling lens, and ESA	8 Ch., 8 kV/3mA (per Ch.), bipolar, SHV input	CAEN, Italy	R1470ETD
1x $\pm 6$ kV power supply for filament, sample, and zone plate	4 Ch., 6 kV (per Ch.), bipolar, SHV-10 input	UltraVolt, USA	N/A
1x thermal ionization filament current supply with high voltage input	1 Ch, 5 A, 10 kV bias input	In-house	N/A
<b>Data Acquisition</b>			
1x oscilloscope for data acquisition and laser signal monitoring	4 Ch., 500 MHz, 4 GS/s	Teledyne LeCroy, USA	WAVESURFER 3054Z

#### A.4 EUV magnetic sector – Mirror alignment

The EUV laser alignment procedure for the EUV laser interface of the EUV magnetic sector system was adapted from the procedure used with the EUV TOF which was developed by I. Kuznetsov. The procedure is outlined in detail in Kuznetsov's thesis and a simplified diagram is shown in Figure A.4.1. Briefly, PMMA coated glass slides are placed separately at reference positions 1, 2, and 3 (R1, R2, and R3) and the EUV laser is fired for ~1000, ~2000, and ~3000 shots at each slide, respectively. As the reference position moves further away from the capillary, the number of shots increases to account for transmission losses from the gold-coated mirrors (Au1 and Au2) and through the zone plate (ZP) holder (the actual zone plate is removed for the alignment). After the EUV beam has been imaged at each position, a HeNe laser is iteratively aligned externally using mirrors 1 and 2 (M1 and M2) through reference positions R1 and R2, respectively. Once M1 and M2 are aligned through the center of R1 and R2, then the HeNe should also be aligned through R3. Au2 can then be adjusted to position the EUV beam at the desired ZP position.

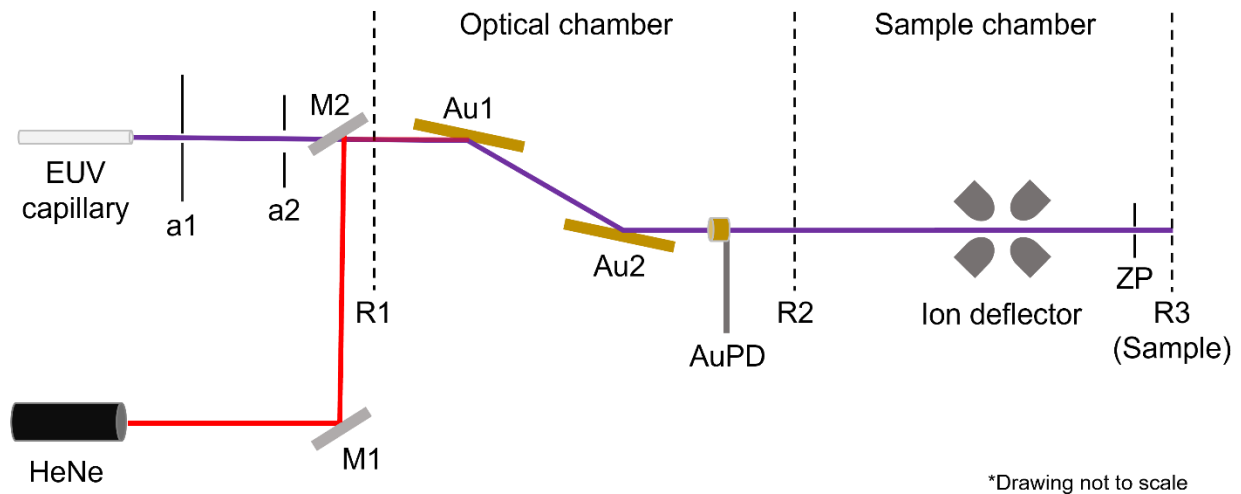


**Figure A.4.1** EUV laser alignment diagram through the optical and sample vacuum chambers for sample ablation and ionization.

## A.5 EUV magnetic sector vacuum schematic

After connecting the EUV laser system to the Neptune, their individual vacuum systems become communal. The vacuum pumps for the EUV laser system include 2 roots pumps, 2 large turbo pumps, 2 small turbo pumps, and 2 small turbo pumps. The Neptune has 2 rotary vane pumps, 2 large turbo pumps, 2 small turbo pumps, and 2 ion getter pumps. Figure A.5.1 diagrams the vacuum system of the EUV magnetic sector instrument in its entirety and Table A.5.1 specifies each vacuum component in the diagram.

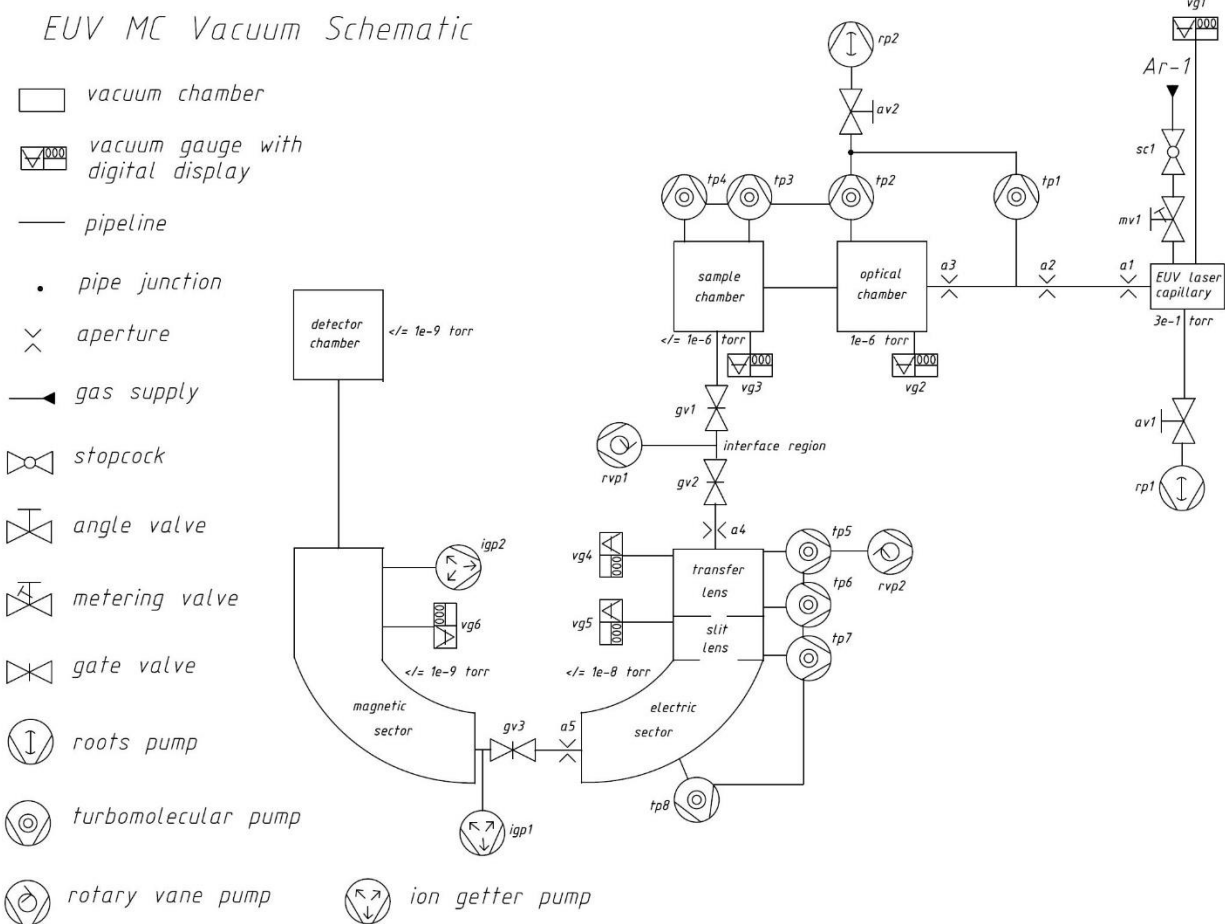


**Figure A.5.1** Vacuum schematic of the EUV magnetic sector system (not drawn to scale). Table A.5.1 specifies the type of vacuum pumps and pressure gauges shown in the diagram.

**Table A.5.1** Vacuum pumps and pressure gauges used in the EUV magnetic sector system corresponding to each vacuum component diagramed in Figure A.5.1.

EUV or Neptune	Component	Pump Speed or Gauge Range	Vendor	Part # / Description
----------------	-----------	---------------------------	--------	----------------------

EUV	Roots pump 1 (rp1)	450 L/min	Pfeiffer	V6SATSFZMF / ACP 28
EUV	Roots pump 2 (rp2)	450 L/min	Pfeiffer	V6SATSFZMF / ACP 28
EUV	Turbo pump 1 (tp1)	60 L/s	Pfeiffer	PMP02800 / TMH 071 P
EUV	Turbo pump 2 (tp2)	260 L/s	Pfeiffer	PMP03901 / HiPace 300
EUV	Turbo pump 3 (tp3)	67 L/s	Pfeiffer	PMP03941 / HiPace 80
EUV	Turbo pump 4 (tp4)	260 L/s	Pfeiffer	PMP03901 / HiPace 300
Neptune	Rotary vane pump 1 (rvp1)	500 L/min	Pfeiffer	PKD54115 / UNO 30B
Neptune	Rotary vane pump 1 (rvp2)	83 L/min	Pfeiffer	PKD61712 / DUO 005
Neptune	Turbo pump 5 (tp5)	210 L/s	Pfeiffer	PMP03110 / TMH 262
Neptune	Turbo pump 6 (tp6)	60 L/s	Pfeiffer	PMP02800 / TMH 071 P
Neptune	Turbo pump 7 (tp7)	60 L/s	Pfeiffer	PMP02800 / TMH 071 P
Neptune	Turbo pump 8 (tp8)	210 L/s	Pfeiffer	PMP03110 / TMH 262
Neptune	Ion getter pump 1 (igp1)	40 L/s	Agilent (Varian)	9191240 / VacIon Plus 40-Starcell
Neptune	Ion getter pump 2 (igp2)	40 L/s	Agilent (Varian)	9191240 / VacIon Plus 40-Starcell
EUV	Vacuum gauge 1 (vg1)	0 to 1 Torr	MKS	626D01TDE / Pressure transducer
EUV	Vacuum gauge 2 (vg2)	750 to $7.5 \times 10^{-10}$ Torr	Pfeiffer	PTT03350010 / PKR 361
EUV	Vacuum gauge 3 (vg3)	750 to $7.5 \times 10^{-10}$ Torr	Pfeiffer	PTT03350010 / PKR 361
Neptune	Vacuum gauge 4 (vg4)	$0.075$ to $7.5 \times 10^{-5}$ Torr	Edwards	D02171000 / Active pirani gauge
Neptune	Vacuum gauge 5 (vg5)	$7.5 \times 10^{-3}$ to $7.5 \times 10^{-9}$ Torr	Edwards	D14645000/ Penning gauge
Neptune	Vacuum gauge 6 (vg6)	$7.5 \times 10^{-5}$ to $7.5 \times 10^{-11}$	Agilent (Varian)	929-500X / MidiVac ion pump controller

To pump down the EUV magnetic sector system, all gate valves throughout the system are initially closed, which includes the following: (1) the gate valve between the EUV laser system and Neptune entrance (“gv1”), (2) the gate valve (i.e., “skimmer valve”) between the interface region and transfer lens region in the Neptune (“gv2”), and (3) the gate valve in the Neptune between the ESA and magnet (“gv3”). The EUV system typically reaches pressures around  $1 \times 10^{-6}$  Torr in 2-3 hours and  $1 \times 10^{-7}$  Torr overnight in both optical and sample vacuum chambers following venting. When 300 mTorr argon is introduced into the EUV laser capillary during operation, the optical vacuum chamber increases to a pressure of  $1 \times 10^{-6}$

Torr, while the sample vacuum chamber remains at  $1 \times 10^{-7}$  Torr. The Neptune's front high vacuum region (i.e., the ESA module), consisting of the transfer and slit lenses as well as the electric sector, is pumped down by four turbo pumps and reaches pressures of  $\leq 1 \times 10^{-7}$  Torr after an overnight pump down following venting. The Neptune's back high vacuum region (i.e., the multi-collector module), consisting of the magnet and detector array, is pumped down by two ion getter pumps and typically reaches pressures down to  $1 \times 10^{-8}$  Torr (but theoretically can reach down to  $1 \times 10^{-9}$  Torr) immediately if the gate valve between the ESA and multi-collector modules remains closed when the former region is vented. If the multi-collector module is vented, it can take  $\geq 1$  week for the pressures to reach back  $\leq 1 \times 10^{-8}$  Torr, typically falling within  $1 \times 10^{-7}$  Torr in the interim. When the Neptune's turbo pumps and ion getter pumps are both turned on, the gate valve between the two modules typically remains open.

Usually, all pumps for the EUV laser system and Neptune remain on except for the Neptune's interface pump ("rvp1"), which is only turned on when actively operating the EUV magnetic sector to increase the pump's lifetime. When the EUV magnetic sector is ready for use, the interface pump is started, followed by opening the skimmer valve ("gv2") that connects the interface region to the rest of the Neptune. Finally, the KF-50 gate valve ("gv1") on the EUV laser sample vacuum chamber is opened, connecting the EUV laser vacuum system with the Neptune's vacuum system. The pressure in the EUV laser's sample vacuum chamber typically increases from approximately  $1 \times 10^{-7}$  Torr to  $1 \times 10^{-6}$  Torr when the KF-50 gate valve is opened. This is likely due to the o-ring groove on the custom flange connecting the two instruments, which could be made to have a better seal. A lower pressure is always better for increasing ion transmission due to a lower pressure equating to a greater mean free path for the ions, so in the future a better flange could be designed. However,  $1 \times 10^{-6}$  Torr is sufficient for transmitting EUV ions into the Neptune. While the EUV laser optical and sample vacuum chambers maintain operating pressures of  $1 \times 10^{-6}$  Torr, the vacuum in the Neptune's ESA and multi-collector modules remains unchanged when the KF-50 gate valve is opened.

## **A.6 EUV Magnetic Sector Custom Connection Vacuum Flange**

The custom flange that was designed to connect the EUV laser sample vacuum chamber to the entrance of the Neptune uses a 2.5 cm (1 in) long KF-50 full nipple vacuum fitting. A sample cone, made from nickel, was welded to one end of the flange, and a ~5.1 cm (2 in) diameter hole was bored in the center of the cone to match the diameter of the KF-50 flange. Additionally, a threaded gasket that is typically used to hold the sample cone in place was welded to the cone, such that the gasket and cone could be screwed into the Neptune entrance as a single piece. The bottom of the welded cone was also machined with an o-ring groove to ensure that high vacuum conditions could be maintained between the EUV laser chamber and Neptune entrance. The other end of the flange was left as its original KF-50 fitting to match the flange size of the exit of the EUV laser sample chamber.

To connect the EUV laser to the Neptune entrance, the welded end of the custom flange that reflects the sample cone is inserted and screwed into the Neptune's entrance. This is followed by the attachment of a bellows flange with KF-50 fittings on both ends to the KF-50 end of the custom flange attached to the Neptune. The bellows flange can be compressed or elongated to adjust the length of the bellows to match the length between the EUV laser system and Neptune. The bellows flange is then attached to a KF-50 gate valve that is directly attached to the EUV laser sample chamber's exit. The KF-50 gate valve allows the EUV laser vacuum system to be isolated from the Neptune's vacuum system when needed, such as for sample loading and unloading.